学位論文

Direct measurement of muonium ground state hyperfine splitting with high-intensity pulsed muon beam

(大強度パルスミューオンビームによる ミューオニウム基底状態超微細構造の直接測定)

平成28年11月　博士(理学)　申請

東京大学大学院理学系研究科

物理学専攻　　神田　聡太郎

Direct measurement of muonium ground state hyperfine splitting with high-intensity pulsed muon beam

by

Sohtaro Kanda

Submitted to the Department of Physics, The University of Tokyo
on November 4, 2016, in partial fulfillment of the
requirements for the degree of
Doctor of Philosophy

Abstract

A hydrogen-like atom consisting of a positive muon and an electron is known as muonium. It is an ideal two-body system for the precision test of bound-state theory and fundamental symmetries. This thesis describes a new precision measurement of the muonium ground state hyperfine splitting. The measuring precision of the muonium hyperfine splitting was statistically limited by a conventional method with the continuous muon beam. The experiment was the first trial of muonium spectroscopy with the high-intensity pulsed muon beam at J-PARC. In order to resolve the problems in the precursor experiments, the world highest intensity pulsed muon beam, a high-rate capable positron detector, two-dimensional and three-dimensional muon beam profile monitors, and a high performance magnetic shield were orchestrated. In the pursuit of evaluation of the systematic uncertainty, a numerical simulation framework was developed. The resonance of hyperfine transition was successfully observed and the muonium hyperfine structure interval of

$$\Delta\nu = 4.463292(22)\ \text{GHz}$$

was obtained with the relative precision of 4.9 ppm. The result was consistent with the previous ones obtained at Los Alamos National Laboratory with the continuous muon beam. Experimental data analysis and estimation of systematic uncertainty demonstrated validity of the new methodology seeking a new frontier of the precision physics with high-intensity pulsed muon beam.

Acknowledgments

I express my heartfelt appreciation for everyone had touched the experiment with concerted efforts. Continuous, wide range cooperation by collaborators has enabled me to work on this experiment. Above all, Prof. Koichiro Shimomura, Prof. Kenji M. Kojima, Dr. Strasser Patrick, Prof. Akihisa Toyoda, Prof. Yasuyuki Matsuda, Prof. Hiroyuki A. Torii, Prof. Kazuo S. Tanaka, Mr. Yasuhiro Ueno, Mr. Yoshitaka Higashi, Mr. Takuya Matsudate, Mr. Toya Tanaka, Mr. Shun Seo, and Mr. Daisuke Yagi helped me at critical moments.

I would like to thank the J-PARC and KEK personnel for scientific, engineering, and technical support. Especially, supports by Prof. Yasuhiro Miyake, Dr. Hiroshi Fujimori, Prof. Yoshiro Irie, Prof. Naritoshi Kawamura, Dr. Akihiro Koda, Dr. Yutaka Ikedo, Dr. Takashi U. Ito, Dr. Wataru Higemoto, Dr. Noriyuki Kurosawa, Dr. Motonobu Tampo, Dr. Taihei Adachi, Mr. Jumpei Nakamura, and Mr. Koji Hamada were essential for the experiment at J-PARC MLF MUSE.

I appreciate assistance in the readout electronics and data acquisition system by Prof. Manobu M. Tanaka, Prof. Tomohisa Uchida, Dr. Satoshi Y. Suzuki, Dr. Masayoshi Shoji, Prof. Isamu Nakamura and Mr. Yuki Matsumoto. I am indebted to Prof. Klaus Jungmann, Prof. David Kawall , and Prof. Akira Ishida for their expert advices about the experiment. I would like to thank Prof. Toichiro Kinoshita, Dr. Makiko Nio, Prof. Takeshi Fukuyama, Prof. Daisuke Nomura, and Prof. Andrzej Czarnecki for valuable theoretical discussions.

Prof. Mitsuhiro Yoshida, Dr. Yasuhiro Kondo, and Dr. Daisuke Sato helped me to manage microwave devices as a key component of the experiment. Prof. Eiko Torikai and Mr. Takuro Fujimaki assisted me to realize a well-controlled zero magnetic field by using a multi-layered magnetic shield. Prof. Kenya M. Kubo supported me to handle high-purity Krypton gas target in the experiment.

I convey a sense of gratitude to Dr. Glen M. Marshall, Prof. Arthur Olin, Prof. George Beer and Mr. Dagobelto Contrelas for cooperation in a detector test at TRIUMF.

Dr. Masahiko Iwasaki, Dr. Katsuhiko Ishida, Prof. Yu Oishi, Dr. Masaharu Sato, Dr. Shinji Okada, Dr. Yue Ma, and Mr. Shuu Aikawa helped me to perform an experiment at RIKEN RAL.

I am grateful to my supervisor, Prof. Naohito Saito and his laboratory colleagues; Prof. Tsutomu Mibe, Prof. Yoshinori Fukao, Prof. Kazuki Ueno, Dr. Masashi Otani, Dr. Yutaro Sato, Mr. Shoichiro Nishimura, Mr. Ryo Kitamura, Mr. Hiromasa Yasuda, and Mr. Li Sirui.

I thank to Mrs. Hisako Ohata and Mrs. Tomoko Iida for office work supports at KEK and J-PARC.

Contents

Chapter 1

Introduction

This chapter describes physics background including a review of the precursor experiment and significance of the study.

1.1 Hyperfine splitting of hydrogen-like atoms

Muonium is a bound state of a positive muon and an electron. In the standard model of particle physics, muonium is a two-body system of structureless leptons which was discovered by Hughes *et al.* [1]. Therefore, a precision measurement of muonium ground state hyperfine splitting (HFS) is the most rigorous validation of bound-state quantum electrodynamics (QED) theory and the most precise method to determine the muon mass via the muon-to-electron mass ratio [2].

QED is the most precise theory in the standard model for the system composed of electrons and photons. The pursuit of precise comparison between the theory and the experiment is primordial question of the physics. The most stringent test of QED was established by measurement of electron spin precession in a penning trap [3]. However, to study the nature of constituent of the world, experimental and theoretical perception of multi-body system is of importance. Spectroscopy of hydrogen-like atom has been one of the most powerful approaches to this subject. For instance, observation of hydrogen HFS interval revealed the existence of electron anomalous magnetic moment. From the viewpoint of bound-state QED validation via

a precision measurement of HFS interval, there are three candidates as a measuring object; hydrogen (p - e^-), positronium(e^+ - e^-), and muonium (μ^+ - e^-).

The most precise experimental result of hydrogen HFS is [4, 5]

$$\Delta\nu_{\mathrm{H_{exp}}} = 1\ 420.405\ 751\ 766\ 7(3)\ \mathrm{MHz} \tag{1.1}$$

and theoretical value is [6]

$$\Delta\nu_{\mathrm{H_{theory}}} = 1\ 420.405\ 11(79)(57)(140)\ \mathrm{MHz} \tag{1.2}$$

where the first error is contribution from finite size effect of the proton, the second error is contribution of proton polarizability, and the last error is summation of remaining contributions. There is a difficulty in improvement of theoretical calculation because the proton is composite particle and understanding of its internal structure is limited.

The most recent experimental result of positronium HFS is [7]

$$\Delta\nu_{\mathrm{Ps_{exp}}} = 203.394\ 2(16)(13)\ \mathrm{GHz} \tag{1.3}$$

where the first error is statistical uncertainty and the second is systematic. Theoretical value is [8]

$$\Delta\nu_{\mathrm{Ps_{theory}}} = 203.391\ 69(41)\ \mathrm{GHz} \tag{1.4}$$

where the error is contribution from unknown non-logarithmic higher-order term.

The muonium HFS was measured by two independent methods; a direct measurement at zero magnetic field and an indirect one utilizing the Zeeman splitting in a high magnetic field. The most precise value of directly-measured muonium HFS interval was

$$\Delta\nu_{\mathrm{Mu_{ZF}}} = 4.463\ 302\ 2(14)\ \mathrm{GHz} \tag{1.5}$$

reported by Casperson *et al.* in 1975 [9]. Note that only statistical uncertainty was considered and systematic uncertainties were not evaluated quantitatively. The de-

tails of the precursor experiment at zero magnetic field is described in the following part of this section.

The most recent experimental result of muonium HFS interval was obtained from the indirect measurement in the presence of a high magnetic field at 1.7 T. The result reported by Liu *et al.*, in 1999 was [10]

$$\Delta\nu_{\mathrm{Mu_{HF}}} = 4.463\ 302\ 765(50)(17)\ \mathrm{GHz} \tag{1.6}$$

where the first error is statistical uncertainty and the second is systematic.

The most precise theoretical value of muonium HFS is obtained as follows [2].

$$\Delta\nu_{\mathrm{Mu_{theory}}} = 4.463\ 302\ 868(271)\ \mathrm{GHz}. \tag{1.7}$$

The details of the theoretical calculation of muonium HFS are discussed in Chapter 2.

In summary, experimental results and theoretical values of HFS interval are listed in Table 1.1 as follows. The most precise comparison between the experiment and

Table 1.1: Experimental and theoretical precision of HFS intervals. Values in column Comparison are defined as the difference between the experimental result and the theoretical one.

Type of atom	Experiment	Theory	Comparison	Reference
Hydrogen	0.2 ppt	1.2 ppm	(0.5 ± 1.2) ppm	[4, 6]
Positronium	10 ppm	2 ppm	(12 ± 10) ppm	[7, 8]
Muonium (Direct)	300 ppb	61 ppb	(150 ± 306) ppb	[9]
Muonium (Indirect)	12 ppb	61 ppb	(23 ± 63) ppb	[10]

the theory is possible with muonium. Furthermore, the precision measurement of muonium HFS interval has profound significance in search for physics beyond the standard model. As an example of application, test for Lorentz symmetry via the measurement of sidereal oscillation, search for a new massive vector boson inspired by proton radius puzzle, and constraint on a long-range spin dependent interaction are discussed in the following chapter. The details of the theoretical background are

discussed in the former half of Chapter 2.

Spectroscopy of the muonium energy levels is performed via measurement of positron angular asymmetry from muonium decays. A muon is obtained from parity violating decay of pion

$$\pi^+ \rightarrow \mu^+ + \nu_\mu \tag{1.8}$$

and its is spin polarized in a direction of its momentum. The muon decay

$$\mu^+ \rightarrow e^+ + \nu_e + \overline{\nu}_\mu \tag{1.9}$$

is also a parity violating process and there is the correlation between the positron momentum and the muon spin direction. Therefore, an averaged muon spin can be obtained by the measurement of decay positron angular asymmetry. Muonium is formed via electron capture in a production target which doubles as a muon stopping target. As a muonium production target, Krypton gas is utilized because of its threshold energy is suitable. In order to measure the energy interval between spin singlet and triplet, muonium spin flip is induced by a microwave resonance. When muonium spin flip occurs, the yield of decay positron which is detected in the downstream side increases since the initial muon spin is aligned in the upstream direction. Experimental observable is an excess of the number of decay positron as a function of the microwave frequency detuning from HFS resonance. The details of the experimental principle are presented in the latter half of Chapter 2.

1.2 Zero field experiment at LAMPF

The precursor experiments of muonium HFS spectroscopy were performed at Los Alamos Meson Physics Facility (LAMPF) in Los Alamos National Laboratory (LANL). Figure 1-1 illustrates the experimental setup. The continuous muon beam was irradiated to the aluminium pressure vessel through the trigger counters. The pressure vessel was filled with Krypton gas and the microwave cavity was installed inside the vessel. Positrons from muonium decay were detected by the proportional chambers

and the scintillation counters. In order to avoid the pileup of muon detection, the beam intensity was limited to 50,000 muons per second.

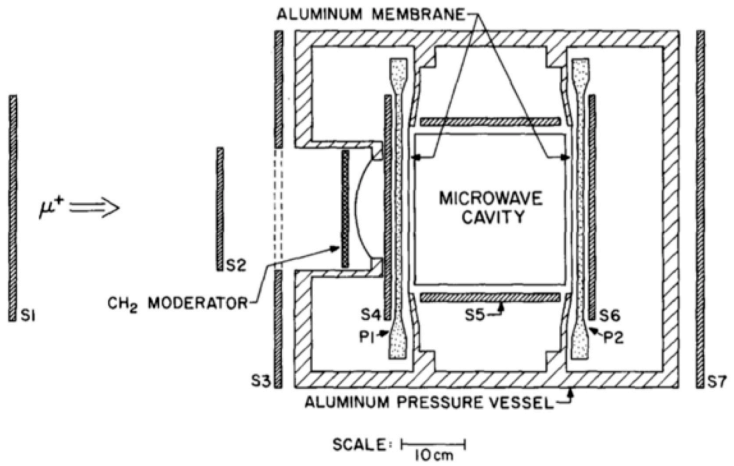

Figure 1-1: Experimental setup of the precursor experiment at LAMPF [9]. Muons and positrons were detected by the proportional chambers and the scintillation counters denoted P1, P2 and S1 through S7 respectively. A muon signal was defined as $\mu_S = \mathrm{S1} \cdot \mathrm{S3} \cdot \mathrm{S4} \cdot \overline{\mathrm{S6}} \cdot \mathrm{P1} \cdot \overline{\mathrm{P2}}$ and a positron signal was defined as $e_S = \overline{\mathrm{S1}} \cdot \mathrm{S3} \cdot \mathrm{S4} \cdot \mathrm{P1} \cdot \overline{\mathrm{P2}}$.

Figure 1-2 shows the muonium HFS resonance curve obtained by the experiment. The vertical axis indicates the muonium HFS signal which was defined as the number of decay positrons normalized by the number of stopped muons. The horizontal axis indicates the microwave frequency. The solid line corresponds to a fitting curve consisting of a Lorenzian function on constant background. This resonance curve was obtained in ten hours of measurement and statistical uncertainty of the frequency center was 9.4 kHz (2 ppm). As a result of the experiment in 600 hours of beam time, the muonium HFS frequency was measured with the precision of 1.4 kHz (300 ppb). Note that only statistical uncertainty was considered and systematic uncertainties were not evaluated quantitatively.

1.3 Objective and significance of the study

The measurement precision of the muonium HFS was mostly statistically limited. This limitation was unavoidable since the continuous muon beam was utilized. The

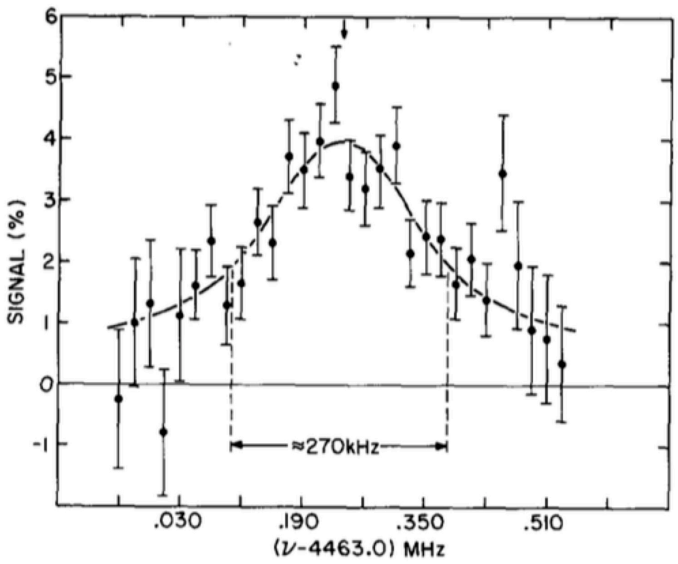

Figure 1-2: Resonance lineshape obtained by the experiment at LAMPF [9]. The muonium spin flip signal was defined as $e_S/\mu_S - 1$ at each microwave frequency where μ_S is the number of muon stopping in the gas target and e_S is the number of decay positron emitted in the downstream direction.

muonium spin flip signal is time dependent and normalized by the number of incident muon. Therefore, for a case of an experiment with the continuous beam, a pair of muon and positron is detected one-by-one. Thus the pileup of muon trigger signal results in serious systematic uncertainty. In order to overcome this limitation in the precursor experiment, a new experiment utilizing the high-intensity pulsed muon beam was proposed. In contrast to the continuous beam, the pulsed beam has a periodic timing structure by nature. For a case of an experiment with pulsed beam, no muon trigger counter is required because an arrival of the muon beam is synchronized to an accelerator repetition. However, this benefit involves the difficulties in the positron detection due to high instantaneous event rate. The novelty and significance of the studies described in this thesis are an application of the high-intensity pulsed muon beam and the development of a high-rate capable positron detection system. Furthermore, a numerical simulation framework for a quantitative estimation of systematic uncertainty which had not been performed in the precursor study was developed. The objective of this thesis is to prove the validity of the new experimental

method.

1.4 Structure of the thesis

This dissertation discusses a new direct measurement of muonium HFS with high-intensity pulsed muon beam at Japan Proton Accelerator Research Complex (J-PARC). The apparatus is described in Chapter 3.

The high intensity pulsed muon beam has a beneficial effect on accumulation of statistics in a limited beam time. On the other hand, the requirements for a detector system is severer than what in the case of continuous beam. Feasibility of the experiment was studied by both numerical simulation and test experiments. The details of simulation study are discussed in Chapter 4.

This thesis has two chapters for the detailed description of detector development. One is for a muon detection system and the other is for a positron detector. Chapter 5 describes the development of a two-dimensional fiber muon beam profile monitor and a three-dimensional muon beam imager. The three-dimensional muon beam imager is utilized to optimize the beam parameters and the target gas condition. Both muon detectors are of service for suppression of systematic uncertainty related to muon beam.

The details of the positron detector development are described in Chapter 6. Because the high-intensity pulsed muon beam is utilized, a number of positrons are emitted at short time intervals and a signal pileup becomes a problem. In order to realize high signal sensitivity and suppression of the signal pileup at the same time, fine segmentation of the detector with an integrated readout electronics is essential.

The experiment was performed in 2016 June at J-PARC Material and Life Science Facility (MLF) Muon Science Establishment (MUSE) D2 area. Experimental setup and data collection summary is presented in Chapter 7.

To determine the muonium HFS interval with a systematic uncertainty as small as possible, a new framework for resonance analysis was developed. Data analysis is described in Chapter 8. The experimental results and evaluation of the systematic

uncertainty are discussed in Chapter 9.

Chapter 2

Physics

This chapter describes a theoretical review of the muonium hyperfine splitting and experimental principle.

2.1 Muonium hyperfine splitting in the standard model

The hyperfine splitting (HFS) of the muonium originates from the interaction of the magnetic moments of the muon and the electron. The most dominant contribution of muonium HFS is the Fermi energy [11]

$$\nu_F = \frac{16}{3}\alpha^2 Z^3 c R_\infty \frac{m_e}{m_\mu}\left[1+\frac{m_e}{m_\mu}\right]^{-3} \tag{2.1}$$

where α is the fine structure constant, Z is the atomic number, c is the speed of the light, R_∞ is the Rydberg constant, m_e and m_μ are the electron and muon masses, respectively.

Formerly, the muonium energy levels up to orders α^2 were obtained from the Breit equation [13]. The Breit equation was not applicable to higher order calculation and it was not Lorentz covariant. Subsequently, the approach based on the Bethe-Salpeter equation has been widely used to the relativistic bound state problem [14]. However, it has difficulty in the calculation of higher order terms due to its complicated structure. To solve the problem with non-relativistic bound state, a suitable QED formulation

named non-relativistic quantum electrodynamics (NRQED) was developed by Caswell and Lepage [16]. NRQED is not a non-relativistic approximation theory of QED but a fully-equivalent theory with the restriction to small momentum transfer defined by the cut-off comparable to the electron mass [21].

Theoretical value of the muonium HFS is obtained by the addition of correction terms to the Fermi energy as follows.

$$\nu = \nu_F + \Delta\nu_{\rm rel} + \Delta\nu_{\rm rad} + \Delta\nu_{\rm rec} + \Delta\nu_{\rm rad-rec} + \Delta\nu_{\rm weak} + \Delta\nu_{\rm had} \tag{2.2}$$

where $\Delta\nu_{\rm rel}$ represents the relativistic correction, $\Delta\nu_{\rm rad}$ is the radiative correction, $\Delta\nu_{\rm rec}$ is the recoil correction, $\Delta\nu_{\rm rad-rec}$ is the radiative recoil correction, $\Delta\nu_{\rm weak}$ is the weak contribution, and $\Delta\nu_{\rm had}$ is the hadronic contribution. There are three small parameters α, $Z\alpha$, and m_e/m_μ for expansion of the theoretical expression of each correction term. For a case of muonium, the atomic number Z equals to one. However, in order to identify the source of the terms, the binding parameter $Z\alpha$ is utilized explicitly.

Relativistic correction

The relativistic correction arises from the vector potential generated by the muon magnetic moment. The leading relativistic correction of order $(Z\alpha)^2$ is calculated by the Breit equation [13]

$$\Delta\nu_{\rm rel} = \frac{1+2\gamma}{\gamma(4\gamma^2-1)}\nu_F \tag{2.3}$$

$$= 356.201 \text{ kHz} \tag{2.4}$$

where $\gamma = \sqrt{1-(Z\alpha)^2}$.

Radiative correction

Leading radiative corrections are attributed to the electron and muon anomalous magnetic moments [12]

$$\Delta\nu_{a_e} = a_e\nu_F \tag{2.5}$$

$$\Delta\nu_{a_\mu} = a_\mu\nu_F \tag{2.6}$$

where a_e and a_μ are the anomalous magnetic moments of the electron and muon.

These radiative corrections depend on α and independent of the binding parameter $Z\alpha$. The main contribution of anomalous magnetic moment is known as the Schwinger term [15]

$$\Delta\nu_{\text{Schwinger}} = \frac{\alpha}{2\pi}\nu_F \tag{2.7}$$

$$= 5178.763 \text{ kHz} \tag{2.8}$$

and total anomalous magnetic moment contributions are calculated as follows

$$\Delta\nu_{a_e} = 5170.926 \text{ kHz} \tag{2.9}$$

$$\Delta\nu_{a_\mu} = 5192.517 \text{ kHz}. \tag{2.10}$$

In addition, there are non-trivial radiative contributions depending on both α and $Z\alpha$. These corrections are mainly induced by the radiative insertions of the electron-line and polarization insertion in the external photons. To improve the theoretical precision of muonium HFS, radiative correction terms of order $\alpha^2(Z\alpha)$ are of importance.

Table 2.1 shows the radiative corrections of each order. The terms of order α^4 are not negligible due to the logarithmic enhancement by the factor $\ln^2(1/Z\alpha)$ or $\ln(1/Z\alpha)$.

Table 2.1: Radiative corrections of order $\alpha^n(Z\alpha)^m$.

Order	Contribution (kHz)	Reference
$\alpha(Z\alpha)$	-428.611(1)	[29]
$\alpha^2(Z\alpha)$	0.4256 (2)	[30]
$\alpha(Z\alpha)^2$	-32.115(3)	[31]
$\alpha(Z\alpha)^3$	-0.542(8)	[20]
$\alpha^2(Z\alpha)^2$	0.193 (24)	[21]
Total	-461.075(39)	

Recoil correction

For radiative correction case, the order of the term was classified by small parameters α and $Z\alpha$. Besides these, recoil corrections have the third small parameter m_e/m_μ as a recoil factor. The leading recoil corrections arise from two-photon exchanges.

The leading recoil correction is [22, 23, 24]

$$\Delta\nu_{\rm rec} = \left(-\frac{3Z\alpha}{\pi}\frac{m_e m_\mu}{m_\mu^2 - m_e^2}\right)\ln\frac{m_\mu}{m_e} \tag{2.11}$$

$$= -800.304 \text{ kHz}. \tag{2.12}$$

Total recoil correction including higher order contribution is calculated as follows [12]

$$\Delta\nu_{\rm rec} = -791.714(80) \text{ kHz}. \tag{2.13}$$

Radiative recoil correction

The leading radiative recoil corrosions are expressed by radiative insertion to the recoil diagrams. Insertions of electron, muon, and photon lines are to be considered. The leading logarithmic electron line contribution in radiative recoil correction is [25]

$$\Delta\nu_{\rm rad-rec} = \frac{15}{4}\frac{\alpha(Z\alpha)}{\pi^2}\frac{m_e}{m_\mu}\ln\frac{m_\mu}{m_e} \tag{2.14}$$

and total radiative recoil correction is calculated as follows [12]

$$\Delta\nu_{\mathrm{rad-rec}} = -3.427(70)\ \mathrm{kHz}. \tag{2.15}$$

Electroweak correction

A contribution from the Z^0 exchange is [26]

$$\begin{aligned}\Delta\nu_{\mathrm{weak}} &= -G_F \frac{3\sqrt{2} m_e m_\mu}{8\alpha\pi} E_F \\ &= -65\ \mathrm{Hz}\end{aligned} \tag{2.16}$$

where G_F is the Fermi coupling constant. A contribution from higher order terms is a small percent of the leading contribution and negligible.

Hadronic correction

A contribution from the hadronic vacuum polarization is [33]

$$\begin{aligned}\Delta\nu_{\mathrm{had_{LO}}} &= -\frac{m_e}{2\pi^3 m_\mu}\nu \int_{4m_\pi^2}^{\infty} ds\ \sigma(s) H(s) \\ &= 232.7(1.4)\ \mathrm{Hz}\end{aligned} \tag{2.17}$$

where m_π is the charged pion mass, s is the center of mass energy squared, $\sigma(s)$ is the total cross section of electron annihilation into hadrons, and $H(s)$ is the QED kernel.

A contribution from the hadronic higher order terms is [27]

$$\Delta\nu_{\mathrm{had_{HO}}} = 5(2)\ \mathrm{Hz} \tag{2.18}$$

and a contribution from the hadronic light-by-light scattering is [28]

$$\Delta\nu_{\mathrm{had_{LBL}}} = -0.0065(10)\ \mathrm{Hz}. \tag{2.19}$$

2.1.1 Theoretical prediction of muonium hyperfine splitting

By adding all contributions as described above, the theoretical prediction of muonium HFS is obtained. In terms of a high precision comparison between theory and experiment, theoretical uncertainty is of importance. Table 2.2 summarizes uncertainties in the theoretical calculation of muonium HFS [2].

Table 2.2: Theoretical uncertainties in muonium hyperfine splitting.

Term	Contribution (Hz)	Major source
Radiative correction	5	Uncalculated contribution
Recoil correction	64	Constant term
Radiative recoil correction	55	Constant term
Hadronic correction	1.4	Vacuum polarization
Total	85	

The theoretical expression contains 85 Hz of uncertainty. This value is relatively small in comparison to uncertainties arising from the physical constants. The Fermi energy is calculated as follows [2]

$$\nu_F = 4\ 453\ 838.995(257)\ \text{kHz} \tag{2.20}$$

with the physical constants

$$\alpha^{-1} = 137.035\ 999\ 139\ (31) \tag{2.21}$$

$$R_\infty c = 3.289\ 841\ 960\ 355\ (19)\ \text{Hz} \tag{2.22}$$

$$\frac{m_e}{m_\mu} = 4.83633170(11) \times 10^{-3}. \tag{2.23}$$

To obtain a unique set of the fundamental constants in the theoretical expression, the least-squares calculations with experimental inputs were performed as follows [2]

$$\nu = \nu(R_\infty, \alpha, \frac{m_e}{m_\mu}, a_\mu) + \delta \tag{2.24}$$

where δ is the uncertainty in the theoretical expression. As a result of calculation,

$$\nu = 4.463\ 302\ 868\ (271)\ \text{Hz} \tag{2.25}$$

was obtained. The uncertainty in this result is dominated by the mass ratio m_e/m_μ.

2.2 Determination of the fundamental physical constants relevant to muon

A precision measurement of the muonium HFS is capable of determination of the fundamental physical constants relevant to muon. This section describes how the muon-to-electron mass ratio and the muon anomalous magnetic moment are determined by the muonium HFS.

2.2.1 Muon-to-electron mass ratio

By comparing the theoretical expression and experimental result of the muonium HFS, the muon-to-electron mass ratio can be extracted. The theoretical expression of muonium HFS is described as follows

$$\nu_{\text{theory}} = \frac{16}{3}\alpha^2 c R_\infty \frac{m_e}{m_\mu}\left[1 + \frac{m_e}{m_\mu}\right]^{-3} + \delta(\alpha,\ m_e/m_\mu) \tag{2.26}$$

where the function δ corresponds to the higher order corrections weakly depending on α and m_e/m_μ. Under the assumption $\nu_{\text{exp.}} = \nu_{\text{theory}}$, the experimental value of the muonium HFS determines the muon-to-electron mass ratio with the precision of 25 ppb. The atomic mass of the electron is measured in a Penning trap with high precision. As of the year 2016, 30 ppt is the highest precision for the electron mass [35]. Therefore, the muon mass can be determined from the mass ratio and the electron mass.

2.2.2 Muon anomalous magnetic moment

The muon anomalous magnetic moment a_μ is considered as a clue to physics beyond the standard model because there is larger than three standard-deviations of discrepancy between experimental result and theoretical calculation [36, 37]

$$a_\mu(\text{Exp.}) = 11\ 659\ 208.9(6.3) \tag{2.27}$$

$$a_\mu(\text{Theory}) = 11\ 659\ 181.8(4.9). \tag{2.28}$$

The muon-to-electon mass ratio is one of the necessities to the experimental determination of the muon anomalous magnetic moment

$$a_\mu = \frac{g_e}{2}\frac{\omega_a}{\omega_p}\frac{\mu_p}{\mu_e}\frac{m_\mu}{m_e} \tag{2.29}$$

where g_e is the electron g-factor, $\mu_{p(e)}$ is the magnetic moment of proton (electron), ω_p is the Larmor frequency of the proton, and ω_a is the difference of the precession frequencies between the muon spin and a cyclotron motion in a storage ring. The relative uncertainty of the muon anomalous magnetic moment is 540 ppb and a contribution from the muonium HFS is 27 ppb.

2.3 Physics beyond standard model relevant to muonium hyperfine splitting

In this section, physics beyond the standard model which can be explored by a precision measurement of the muonium HFS is discussed. In terms of searches for exotic physics, muonium has three key features as follows.

1. Muonium distinguishes the direction in space by relative relationship between its spin polarization and an external magnetic field.

2. Contributions from the weak and the strong interactions are tiny and higher order corrections in small parameter m_e/m_μ are available to calculate electro-

magnetic contribution precisely.

3. High-intensity proton accelerator is capable for massive production of spin polarized muonium.

2.3.1 Lorentz and CPT violation

Lorentz and CPT symmetry are the most fundamental symmetries of the physical laws. A group of effective quantum field theory called the Standard Model Extension (SME) provides a theoretical framework including Lorentz violating terms. The minimal form of the SME in the lepton sector is [38]

$$\begin{aligned}\mathcal{L} = &-a_\alpha^l \overline{\psi}_l \gamma^\alpha \psi_l - b_\alpha^l \overline{\psi}_l \gamma_5 \gamma^\alpha \psi_l \\ &- H_{\alpha\beta}^l \overline{\psi}_l \sigma^{\alpha\beta} \psi_l/2 + i c_{\alpha\beta}^l \overline{\psi}_l \gamma^\alpha \overleftrightarrow{D}^\beta \psi_l/2 \\ &+ i d_{\alpha\beta}^l \overline{\psi}_l \gamma_5 \gamma^\alpha \overleftrightarrow{D}^\beta \psi_l/2. \end{aligned} \tag{2.30}$$

The lepton field ψ is denoted by $l = e^-,\ \mu^-$. Differential operator is defined as $iD_\alpha \equiv i\partial_\alpha + |e|A_\alpha$ where A^α is the vector potential of the electromagnetic field. Parameters a and b are CPT odd coefficients, while H, c, and d are CPT even ones.

Since the muonium hyperfine transition conserves lepton number, the extended Dirac equation can be derived from flavor-diagonal terms in Eq. 2.30 as follows.

$$\begin{aligned}&(i\gamma^\alpha D_\alpha - m_\mu + a_\alpha \gamma^\alpha - b_\alpha \gamma_5 \gamma^\alpha + H_{\alpha\beta}\sigma^{\alpha\beta}/2 \\ &+ i c_{\alpha\beta}\gamma^\alpha D^\beta + i d_{\alpha\beta}\gamma_5 \gamma^\alpha D^\beta)\psi = 0 \end{aligned} \tag{2.31}$$

where ψ is a four-component muon field of mass m_μ, parameters a, b, H, c, k are coefficients of Lorentz violating terms.

With the perturbative treatment of Eq. 2.31, the leading term of Lorentz-violating energy shifts in the muonium HFS is obtained [38]

$$\Delta\nu = \tilde{b}_3^\mu/\pi \tag{2.32}$$

where $\Delta\nu$ is the muonium HFS and $\tilde{b}_3^\mu/\pi$ is the laboratory frame parameter which is defined as $\tilde{b}_3^\mu = b_3^\mu + d_{30}^\mu m_\mu + H_{12}^\mu$.

The SME predicts Lorentz violating observables such as the sidereal oscillation and the annual variation of muonium transition frequency. Due to the rotation of laboratory frame with the Earth, energy shifts oscillate with a period of 23 hours 56 minutes. Applying transformation from the laboratory frame to the non-rotating celestial frame, $\tilde{b}_3^\mu$ is expressed with suitable basis X, Y, and Z as follows

$$\tilde{b}_3^\mu = \tilde{b}_Z^\mu \cos\chi + (\tilde{b}_X^\mu \cos\Omega t + \tilde{b}_Y^\mu \sin\Omega t)\sin\chi \tag{2.33}$$

where $\tilde{b}_J^\mu$ with $J = X, Y, Z$ is the non-rotating frame parameter defined as $\tilde{b}_J^\mu \equiv b_J^\mu + m_\mu d_{J0}^\mu + \epsilon_{JKL} H_{KL}^\mu$, Ω is the Earth's sidereal frequency, and χ is the angle between the quantization axis of muon spin and the Z-direction. In the experiment, the Z-direction is selected along the Earth's axis. These parameters are related to the experimental observable; the muonium transition energy shift by inequality constraint

$$\frac{|\sin\chi|}{\pi}\sqrt{(\tilde{b}_X^\mu)^2 + (\tilde{b}_Y^\mu)^2} \leq \delta\nu_{12}. \tag{2.34}$$

Figure 2-1 is an analysis result by Hughes *et al.* obtained from the most recent experimental data [39]. No significant sidereal oscillation was found and theoretical parameters were constrained

$$\sqrt{(\tilde{b}_X^\mu)^2 + (\tilde{b}_Y^\mu)^2} \leq 2 \times 10^{-23}\ \text{GeV}. \tag{2.35}$$

2.3.2 Massive vector boson inspired by the proton radius puzzle

The charge radius of the proton was measured by two independent techniques; electron-proton scattering and laser spectroscopy of muonic hydrogen. About 4% or seven standard deviations of discrepancy between the results of two experiments was re-

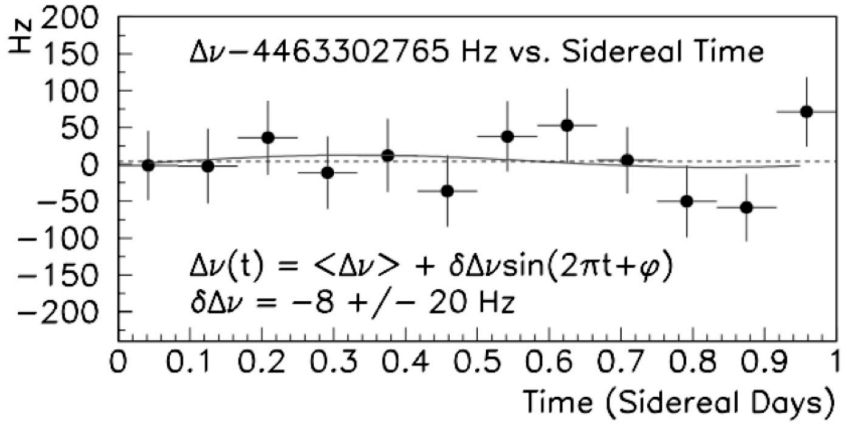

Figure 2-1: Search for the sidereal oscillation of muonium transition frequencies [39]. The amplitude of periodic variations of the muonium HFS frequency was evaluated by fitting the sine curve for data points.

ported by R. Pohl *et al.* [41].

The most precise proton charge radius r_p obtained from the $e - p$ scattering experiment is

$$r_p = 0.8775(51) \text{ fm} \tag{2.36}$$

and one from the laser spectroscopy of the Lamb shift in muonic hydrogen is

$$r_p = 0.84087(39) \text{ fm}. \tag{2.37}$$

This conflict between two experiments is so called the proton radius puzzle and various interpretations were proposed to understand the discrepancy. One of the potential solutions is a contribution of an additional vector force between muons and protons [40].

Phenomenologically, a new vector boson V which mediates the exotic interaction between muons and protons is introduced. This new particle can be regarded as a variation of dark photons. The interaction Lagrangian for this new muon-specific

force carrier V is

$$\begin{aligned}\mathcal{L} &= -V_\nu[\kappa J_\nu^{\mathrm{em}} - \tilde{\psi}_\mu(g_V\gamma_\nu + g_A\gamma_\nu\gamma_5)\psi_\mu] \\ &= -V_\nu[e\kappa\tilde{\psi}_p\gamma_\nu\psi_p - e\kappa\tilde{\psi}_e\gamma_\nu\psi_e] - \tilde{\psi}_\mu((e\kappa + g_V)\gamma_\nu + g_A\gamma_\nu\gamma_5)\psi_\mu]\end{aligned} \tag{2.38}$$

where g_A and g_V are the muon specific couplings, $e = (4\pi\alpha)^{1/2}$, κ is the mixing angle between the photon and V.

A room for exotic corrections to the muonium HFS interval is

$$|\frac{\Delta E_{\mathrm{hfs}}}{E_{\mathrm{hfs}}}| \leq 1.24 \times 10^{-7} \tag{2.39}$$

when it is limited at two standard deviations.

In the limit $m_\mu \gg m_V$ where m_V is the mass of a new particle, the exotic correction obeys

$$\frac{\Delta E_{\mathrm{hfs}}}{E_{\mathrm{hfs}}} \sim \frac{2\alpha m_r}{\pi^2}\int\frac{d^3}{p^4}[\frac{G_E(-p^2)G_M(-p^2)}{\mu_\mu} - 1] \tag{2.40}$$

where p^2 the square of the space-like momentum, m_r is the reduced mass of the muon and electron, G_E and G_M are the electric and magnetic form factors, and μ_μ is the magnetic moment of the muon. The form factor $G_{E(M)}$ is a function of the coupling constant g_V and the mass of a new particle m_V as follows

$$G_{E(M)} - 1 = \frac{\kappa(\kappa + g_V/e)}{p^2 + m_V^2}. \tag{2.41}$$

The coupling constants of muon-specific force are constrained as a function of m_V as shown in the Figure 2-2.

2.3.3 Long-ranged interaction mediated by light pseudo vector boson

As a candidate of the dark matter, a new light pseudo vector boson which induces a spin dependent interaction between atomic constituents can be introduced. This type of interaction results a Yukawa-type correction term to the Coulomb raw as below

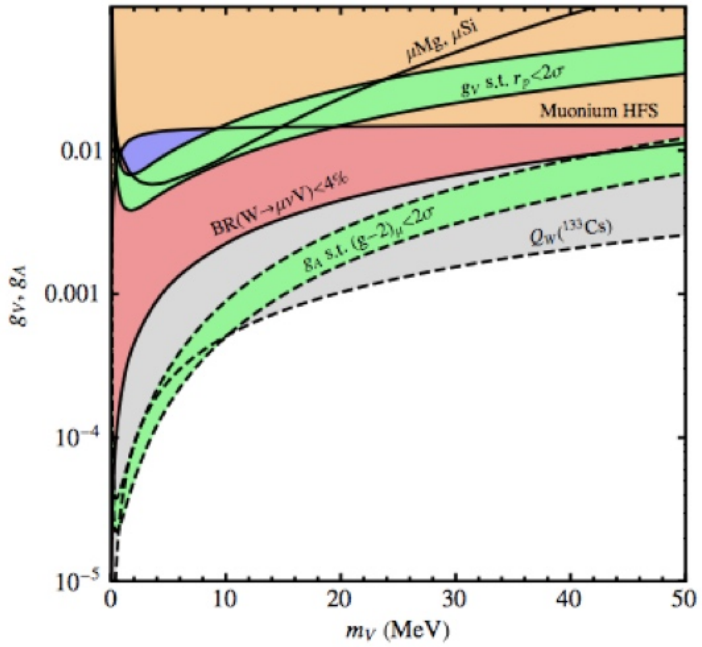

Figure 2-2: Constraints on the mass of massive vector boson m_V and the coupling parameters of the new interaction g_V, g_A [40]. The regions with solid and dashed boundary lines correspond to the allowed regions for a vector and an axial-vector boson, respectively. The orange region represents the parameter constrains from the muonium HFS. Allowed parameter region for a massive vector boson corresponds to the upper green band.

[42]

$$-\frac{\alpha}{r} \to -\frac{\alpha + \alpha''(\boldsymbol{s_1} \cdot \boldsymbol{s_2})e^{\lambda r}}{r} \tag{2.42}$$

where α is the fine structure constant, α'' is a coupling constants of a new boson, $\boldsymbol{s}_1$ and $\boldsymbol{s}_2$ are particle spin vectors, λ is a characteristic range of the interaction, and r is a spacial distance between particles. Figure 2-3 shows constraints on coupling constant α'' as a function of pseudo vector boson mass. The muonium HFS constrains this type of exotic interaction with the strictest limitation.

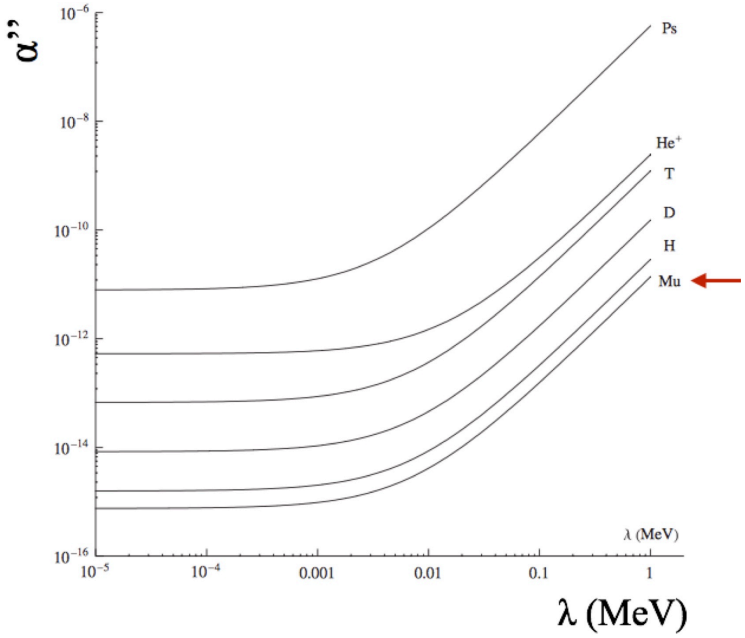

Figure 2-3: Constraints on the mass of light pseudo vector boson λ and the coupling constant of the new interaction α'' [42]. Red arrow indicates the constraint by the muonium HFS. The most severe constraint is given by the muonium HFS.

2.4 Theoretical background of the measurement

This section describes theoretical discussion of muonium energy levels and state amplitudes [43, 44, 45, 46].

2.4.1 Energy levels of muonium

The Hamiltonian of muonium in the presence of magnetic field is

$$\mathcal{H} = h\Delta\nu \boldsymbol{I}\cdot\boldsymbol{J} + \mu_e g_J \boldsymbol{J}\cdot\boldsymbol{H} - \mu_\mu g_\mu \boldsymbol{I}\cdot\boldsymbol{H} \tag{2.43}$$

where h is the Planck constant, $\boldsymbol{I}$ is the muon spin, $\boldsymbol{J}$ is the electron spin. μ_e and μ_μ are the Bohr magnetons of electron and muon, g_J and g_μ are the bound-state g-factors of electron and muon, and $\boldsymbol{H}$ is an external magnetic field. The first term represents a magnetic interaction between electron and muon, the second and the third correspond to the energy of electron and muon in the presence of magnetic field respectively. The energy levels of muonium ground states are obtained as eigenvalues

of this Hamiltonian.

The associated time dependent Hamiltonian is

$$\mathcal{H}' = (\mu_e g_J \boldsymbol{J} - \mu_\mu g_\mu \boldsymbol{I}) \cdot \boldsymbol{H}_{\mathrm{RF}} \cos \omega t \tag{2.44}$$

$$= \mathcal{H}'_0 \cos \omega t \tag{2.45}$$

where H_{RF} is the applied microwave magnetic field and ω is its angular frequency.

Figure 2-4 represents the energy levels of four ground states of muonium as a function of static magnetic field in the unit of hyperfine transition energy $h\Delta\nu$. By taking difference of energy between contiguous states, hyperfine transition frequencies are obtained as shown in Figure 2-5.

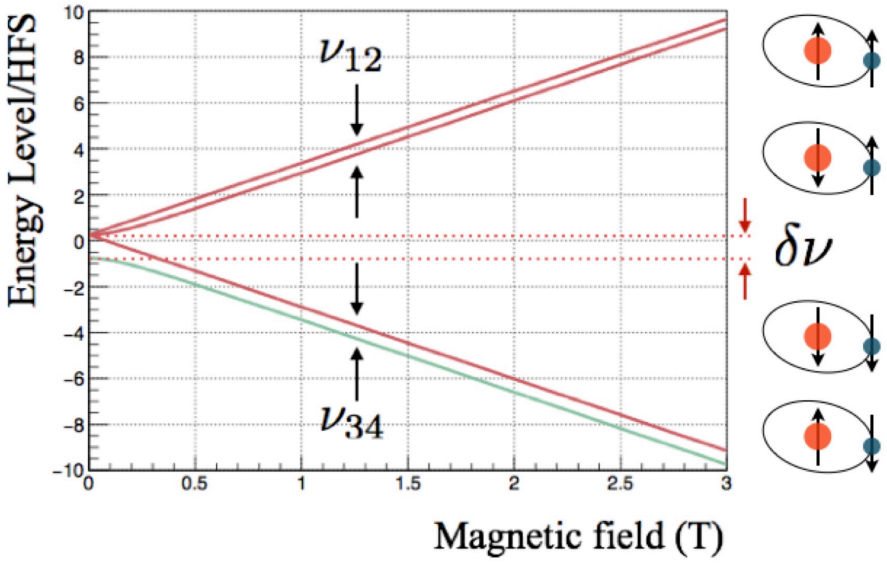

Figure 2-4: Energy levels of the ground state muonium as a function of static magnetic field. Three red lines correspond to the spin triplet states while green line correspond to the spin singlet state. Spin directions of a muon (red) and an electron (blue) in each state are illustrated on the right side. The vertical axis was normalized by the muonium HFS at zero magnetic field of 4.463 GHz.

The four eigenstates of muonium are described by weak and high field quantum numbers as in Table 2.3. In this table, α and β are normalized spin eigenfunctions of

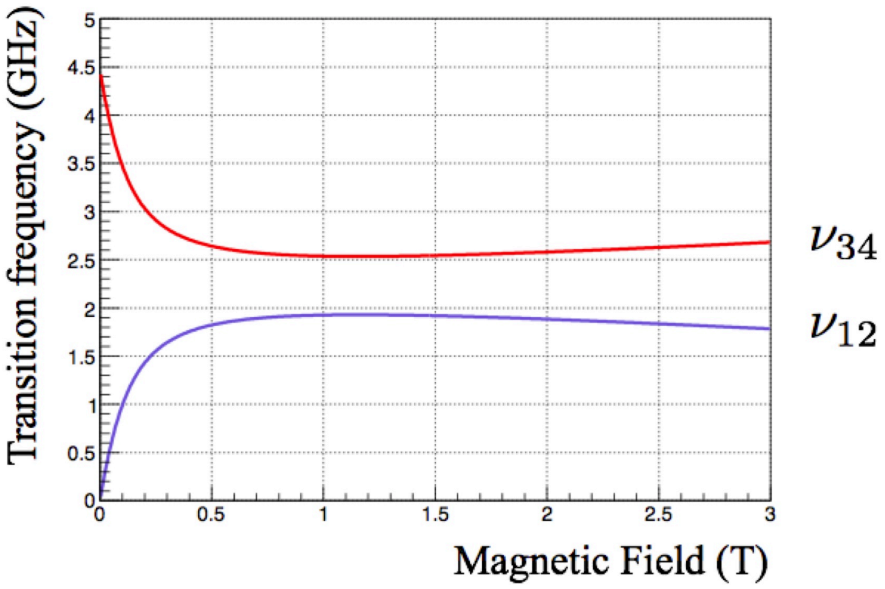

Figure 2-5: Muonium hyperfine transition frequency as a function of a static magnetic field. Red and blue lines correspond to the state transitions $|3\rangle \leftrightarrow |4\rangle$ and $|1\rangle \leftrightarrow |2\rangle$, respectively.

the muon or the electron. The coefficients c and s are

$$s = \frac{1}{\sqrt{2}}\sqrt{1 - \frac{x}{\sqrt{1+x^2}}} \tag{2.46}$$

$$c = \frac{1}{\sqrt{2}}\sqrt{1 + \frac{x}{\sqrt{1+x^2}}} \tag{2.47}$$

with the field parameter defined as follows

$$x = (g_J\mu^e - g_\mu g^\mu)\frac{H}{h\Delta\nu} \tag{2.48}$$

where H is a strength of the external magnetic field.

In the limit of high magnetic field $x \gg 1$, the field parameters s and c are $s \approx 0$ and $c \approx 1$. In the limit of zero magnetic field, the parameters are $s \approx c \approx 1/\sqrt{2}$. In a high magnetic field, the z-components of muon and electron spin; m_μ and m_e are good quantum numbers of the system. On the other hand, in a weak magnetic field, the total angular momentum of muonium F and the associated magnetic quantum number M_F describe the eigenstates.

Table 2.3: Eigenstates of muonium in a weak field and a high field.

Eigenstate	Weak field	High Field
	$(F,\ M_F)$	$(m_\mu,\ m_e)$
$\chi_1 = \alpha_\mu\alpha_e$	(1,1)	(1/2, 1/2)
$\chi_2 = s\alpha_\mu\beta_e + c\beta_\mu\alpha_e$	(1,0)	(-1/2, 1/2)
$\chi_3 = \beta_\mu\beta_e$	(1,-1)	(-1/2, -1/2)
$\chi_4 = c\alpha_\mu\beta_e - s\beta_\mu\alpha_e$	(0,0)	(1/2, -1/2)

The muonium wave function of each state is defined as follows

$$\Psi(r,t) = \phi(r)\sum_{k=1}^{4} a_k(t)\chi_k \exp^{-iW_k/t\hbar} \tag{2.49}$$

where $\phi(r)$ is the spacial component, χ_k is the spin component of the wave function, $a_k(t)$ is the state amplitude, and W_k is the energy eigenvalue.

The energy eigenvalue of muonium is obtained from the equation of

$$W_{F,M_F} = -\frac{1}{4}\Delta\nu - \mu^\mu g_\mu M_F H \pm \frac{1}{2}\Delta\nu\sqrt{1+2M_F x + x^2}. \tag{2.50}$$

Time dependent state amplitudes of muonium are decomposed to two components; muon decay and state transition. Muon decay operator obeys

$$\dot{a}_k(t) = -\frac{1}{2}\gamma a_k(t) \tag{2.51}$$

with the muon decay rate $\gamma = 4.5490(17) \times 10^5$ Hz.

State transition is described as

$$i\hbar\frac{\partial\Psi}{\partial t} = (\mathcal{H} + \mathcal{H}_0')\Psi(t). \tag{2.52}$$

From these equations, the time differential state amplitudes are described as follows

$$\dot{a}_k(t) = -\frac{1}{2}\gamma a_k(t) - i\sum_{i=1}^{4} a_i b_{ik} f_{ik}(t) \tag{2.53}$$

where

$$b_{ik} = \frac{1}{2\hbar}\langle i|\mathcal{H}'_0|k\rangle \tag{2.54}$$

$$f_{ik} = e^{-i(\omega_{ik}-\omega)t} + e^{-i(\omega_{ik}+\omega)t} \tag{2.55}$$

$$\omega_{ik} = \frac{W_i - W_k}{\hbar}. \tag{2.56}$$

For a generalized microwave magnetic field $H = H_x x + H_y y + H_z z$, the matrix element b_{ij} is summarized in the Table 2.4 as follows. The z-axis is defined in parallel with the quantization axis of the muon spin. In the experiment, the initial muon spin is aligned with the beam axis.

Table 2.4: Matrix elements $b_{ij} = \frac{1}{2\hbar}\langle i|\mathcal{H}'_0|k\rangle$. B_J and B_I are the Bohr magneton of an electron and a muon, respectively. The complex magnetic field $H_\pm$ is defined as $H_\pm = H_x \pm iH_y$. The field coefficients c and s are defined in 2.46.

k ╲ i	1	2	3	4
1	$(B_J + B_I)H_z$	$(sB_J + cB_I)H_-$	0	$(cB_J - sB_I)H_-$
2	$(sB_J + cB_I)H_+$	$(c^2 - s^2)(B_J - B_I)H_z$	$(cB_J + sB_I)H_-$	$-2sc(B_J - B_I)H_z$
3	0	$(cB_J + sB_I)H_+$	$-(B_J + B_I)H_+$	$(-sB_J + cB_I)H_+$
4	$(cB_J - sB_I)H_+$	$-2sc(B_J - B_I)H_z$	$(-sB_J + cB_I)H_-$	$(s^2 - c^2)(B_J - B_I)H_z$

2.4.2 State amplitude of muonium states

In general, the state amplitudes of muonium are given as the solutions of Eq. 2.53. This equation can be written in matrix form as follows.

$$\begin{pmatrix} \dot{a}_1 \\ \dot{a}_2 \\ \dot{a}_3 \\ \dot{a}_4 \end{pmatrix} = \begin{pmatrix} -\gamma/2 & -ib_{12}e^{i(\omega_{12}-\omega)t} & -ib_{13}e^{i(\omega_{13}-\omega)t} & -ib_{14}e^{i(\omega_{14}-\omega)t} \\ -ib^*_{12}e^{i(\omega_{12}-\omega)t} & -\gamma/2 & -ib_{23}e^{i(\omega_{23}-\omega)t} & -ib_{24}e^{i(\omega_{24}-\omega)t} \\ -ib^*_{13}e^{i(\omega_{13}-\omega)t} & -ib^*_{23}e^{i(\omega_{23}-\omega)t} & -\gamma/2 & -ib_{34}e^{i(\omega_{34}-\omega)t} \\ -ib^*_{14}e^{i(\omega_{14}-\omega)t} & -ib^*_{24}e^{i(\omega_{24}-\omega)t} & -ib^*_{34}e^{i(\omega_{34}-\omega)t} & -\gamma/2 \end{pmatrix} \begin{pmatrix} a_1 \\ a_2 \\ a_3 \\ a_4 \end{pmatrix} \tag{2.57}$$

The direction of z-axis is selected in parallel with the initial direction of muon

spin. In the experiment, the initial muon spin is fully polarized in the upstream direction. When microwave magnetic field is applied perpendicularly to the z-axis, matrix elements with $\Delta M_F = 0$ are negligible. Hence, Eq. 2.57 can be simplified as

$$\begin{pmatrix} \dot{a}_1 \\ \dot{a}_2 \\ \dot{a}_3 \\ \dot{a}_4 \end{pmatrix} = \begin{pmatrix} -\gamma/2 & 0 & 0 & -ib_{14}e^{i(\omega_{14}-\omega)t} \\ 0 & -\gamma/2 & 0 & 0 \\ 0 & 0 & -\gamma/2 & -ib_{34}e^{i(\omega_{34}-\omega)t} \\ -ib_{14}^{*}e^{i(\omega_{14}-\omega)t} & 0 & -ib_{34}^{*}e^{i(\omega_{34}-\omega)t} & -\gamma/2 \end{pmatrix} \begin{pmatrix} a_1 \\ a_2 \\ a_3 \\ a_4 \end{pmatrix} \tag{2.58}$$

and obviously the state $|2\rangle$ is decoupled from other states.

Linear combinations of state amplitudes

$$a_+ = \frac{1}{2}\sqrt{2}(a_1 + a_3) \tag{2.59}$$

$$a_- = \frac{1}{2}\sqrt{2}(a_1 - a_3) \tag{2.60}$$

obeys the matrix equations as follows.

$$\begin{pmatrix} \dot{a}_+ \\ \dot{a}_- \\ \dot{a}_4 \end{pmatrix} = \begin{pmatrix} -\gamma/2 & 0 & 0 \\ 0 & -\gamma/2 & -i\sqrt{2}be^{i(\omega_0-\omega)t} \\ 0 & -i\sqrt{2}be^{-i(\omega_0-\omega)t} & -\gamma/2 \end{pmatrix} \begin{pmatrix} a_+ \\ a_- \\ a_4 \end{pmatrix} \tag{2.61}$$

Only the states a_- and a_4 are coupled. Therefore, the solution for the state amplitudes is two-level problem

$$a_+(t) = \frac{a_1(0) + a_3(0)}{\sqrt{2}} e^{-\gamma t/2} \tag{2.62}$$

$$a_-(t) = \{\frac{a_1(0) - a_3(0)}{\sqrt{2}}[\cos\frac{\Gamma t}{2} - \frac{i\omega'}{\Gamma}\sin\frac{\Gamma t}{2}] + a_4(0)[-i\frac{2\sqrt{2}b}{\Gamma}\sin\frac{\Gamma t}{2}]\} e^{-\gamma t/2 + i\omega' t/2} \tag{2.63}$$

$$a_4(t) = \{\frac{a_1(0) - a_3(0)}{\sqrt{2}}[\frac{-i2\sqrt{2}b}{\Gamma}\sin\frac{\Gamma t}{2}] + a_4(0)[\cos\frac{\Gamma t}{2} + i\frac{\omega'}{\Gamma}\sin\frac{\Gamma t}{2}]\} e^{-\gamma t/2 + i\omega' t/2} \tag{2.64}$$

where

$$\omega' = \omega_0 - \omega \tag{2.65}$$

$$\Gamma = \sqrt{\omega' + 8|b|^2}. \tag{2.66}$$

When a spin-polarized muon captures an unpolarized electron and forms a muonium, initial state probabilities are as follows.

$$|a_1(0)|^2 = \frac{1}{2} \tag{2.67}$$

$$|a_2(0)|^2 = \frac{1}{4} \tag{2.68}$$

$$|a_3(0)|^2 = 0 \tag{2.69}$$

$$|a_4(0)|^2 = \frac{1}{4} \tag{2.70}$$

From Eq. 2.59, the state amplitudes $a_1(t)$ and $a_3(t)$ are expressed as follows.

$$a_1(t) = \frac{1}{2}\sqrt{2}[a_+(t) + a_-(t)] \tag{2.71}$$

$$a_3(t) = \frac{1}{2}\sqrt{2}[a_+(t) - a_-(t)] \tag{2.72}$$

Figure 2-6 shows calculated state probabilities $|a_+|^2$, $|a_2|^2$, $|a_-|^2$, and $|a_4|^2$.

Figure 2-7 shows calculated state probabilities $|a_1|^2$, $|a_2|^2$, $|a_3|^2$, and $|a_4|^2$.

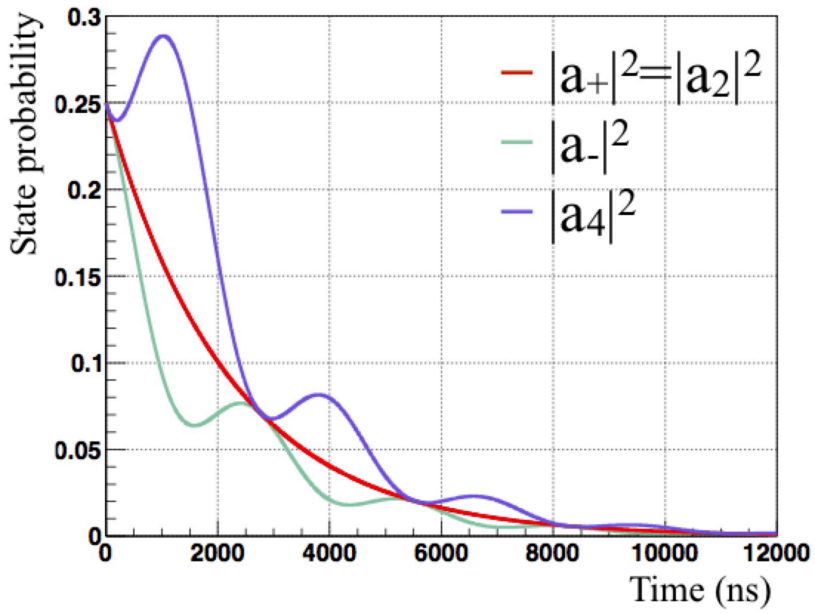

Figure 2-6: State probabilities $|a_+|^2$, $|a_2|^2$, $|a_-|^2$, and $|a_4|^2$. Red line represents $|a_+|^2 = |a_2|^2$, green one represents $|a_-|^2$, and blue one represents $|a_4|^2$. The microwave frequency detuning was set to zero and the microwave power parameter $|b|$ was set to 800 kHz.

2.4.3 Muon polarization

The muon spin polarization equals to the expectation value of the muon spin operator $I_{\mu z}$ in terms of the state amplitudes and the spin eigenfunctions

$$\begin{aligned} P_z(t) &= \langle \Psi(t)|2I_{\mu z}|\Psi(t)\rangle \\ &= \sum_{i,j=1}^{4} a_i^* a_j \langle \chi_i^*|2I_{\mu z}|\chi_j\rangle e^{i\omega_{ij}t} \end{aligned} \tag{2.73}$$

where Ψ is the time dependent muonium states in eq. 2.49 and χ is the spin eigenfunction as in Table 2.3.

The muon spin operator $I_{\mu z}$ has eigenvalue $\pm 1/2$ as follows.

$$I_{\mu z}|\alpha_\mu \alpha_e\rangle = \frac{1}{2}|\alpha_\mu \alpha_e\rangle \tag{2.74}$$

$$I_{\mu z}|\beta_\mu \alpha_e\rangle = -\frac{1}{2}|\beta_\mu \alpha_e\rangle \tag{2.75}$$

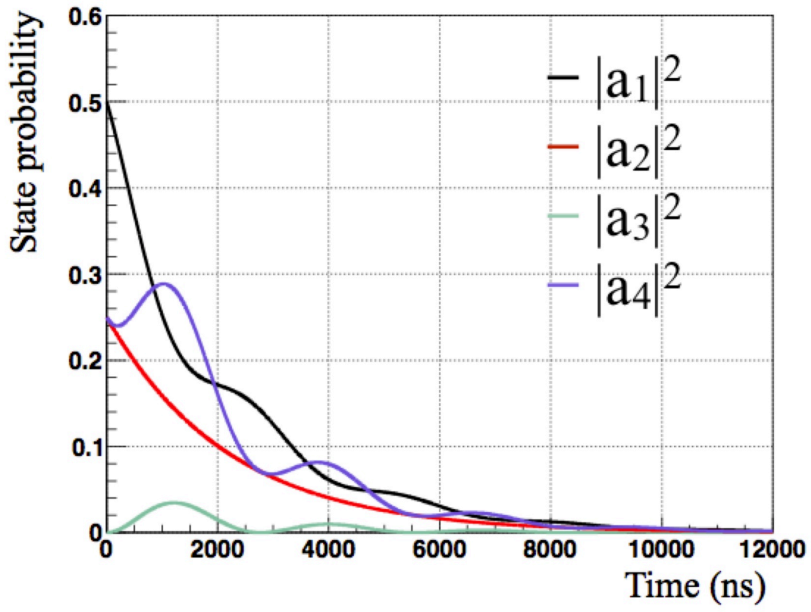

Figure 2-7: Muonium state probabilities $|a_1|^2$, $|a_2|^2$, $|a_3|^2$, and $|a_4|^2$. Black line represents $|a_1|^2$, red one represents $|a_2|^2$, green one represents $|a_3|^2$, and blue one represents $|a_4|^2$. The microwave frequency detuning was set to zero and the microwave power parameter $|b|$ was set to 800 kHz.

For zero magnetic field case, the muon spin polarization is as follows.

$$P_z(t) = |a_1|^2 - |a_3|^2 + a_2^* a_4 e^{i\omega_{24}t} + a_4^* a_2 e^{-i\omega_{24}t} \tag{2.76}$$

Since the muon decay rate $\gamma \approx 455$ kHz is relatively small to the HFS resonance frequency $\omega_{24} \approx 4463$ MHz, the cross product terms in Eq. 2.76 are negligible. Therefore, the muon spin polarization becomes

$$\begin{aligned} P_z(t) &= |a_1|^2 - |a_3|^2 \\ &= 2Re[a_+^*(t)a_-(t)] \\ &= 2Re\{a_+^*(0)e^{-\gamma t + i\omega' t/2} \times [a_-(0)(\cos\frac{\Gamma t}{2} - \frac{i\omega'}{\Gamma}\sin\frac{\Gamma t}{2} + a_4(0)(\frac{-i2\sqrt{2}b}{\Gamma}\sin\frac{\Gamma t}{2})]\}. \end{aligned} \tag{2.77}$$

In Eq. 2.77, b is time dependent oscillating microwave field. To obtain the muon spin polarization which corresponds to an ensemble of muons, the term linear in b does not contribute because of averaging over the arbitrary initial phases. Hence, the

muon spin polarization is represented as follows

$$P_z(t) = 2Re\{a_+^*(0)e^{-\gamma t + i\omega' t/2} \times [a_-(0)(\cos\frac{\Gamma t}{2} - \frac{i\omega'}{\Gamma}\sin\frac{\Gamma t}{2}]\} \tag{2.78}$$
$$= \frac{1}{4}\{\cos\frac{\omega' t}{2}\cos\frac{\Gamma t}{2} + \frac{\omega'}{\Gamma}\sin\frac{\omega' t}{2}\sin\frac{\Gamma t}{2}\}e^{-\gamma t}.$$

To discuss the time dependent muon spin flip signal which is observed in the experiment, the muon polarization in Eq. 2.78 is generalized for the arbitrary initial polarization by taking the ensemble average of muons.

The density matrix for the muon spin is

$$\rho_\mu = \frac{1}{2}\begin{pmatrix} 1+P & 0 \\ 0 & 1-P \end{pmatrix} \tag{2.79}$$

where P is the z-component of the initial polarization. The atomic electrons are unpolarized, so the density matrix for the electrons is

$$\rho_e = \frac{1}{2}\begin{pmatrix} 1 & 0 \\ 0 & 1 \end{pmatrix}. \tag{2.80}$$

From these matrices, the density matrix of muonium at time zero is obtained as follows

$$\rho_{\mathrm{Mu}}(0) = \frac{1}{4}\begin{pmatrix} 1+P & 0 & 0 & 0 \\ 0 & 1 & 0 & P \\ 0 & 0 & 1-P & 0 \\ 0 & P & 0 & 1 \end{pmatrix}. \tag{2.81}$$

The matrix element of $\rho_{\mathrm{Mu}}(0)$ equals to the ensemble average of the state amplitudes as follows

$$\rho_{ij}(0) = \langle a_i^*(0)a_l(0)\rangle. \tag{2.82}$$

Then, the ensemble average of muon spin polarization is

$$\begin{aligned}\langle P_z(t)\rangle &= \frac{P}{4}\{\cos\frac{\omega' t}{2}\cos\frac{\Gamma t}{2} + \frac{\omega'}{\Gamma}\sin\frac{\omega' t}{2}\sin\frac{\Gamma t}{2}\}e^{-\gamma t} \\ &= \frac{P}{4}\{\frac{\Gamma+\omega'}{\Gamma}\cos\frac{\Gamma-\omega'}{2}t + \frac{\Gamma-\omega'}{\Gamma}\cos\frac{\Gamma+\omega'}{2}t\}e^{\gamma t}.\end{aligned} \tag{2.83}$$

2.4.4 Time dependent spin flip signal

The ensemble average of muon spin polarization is proportional to the number of decay positron detection. The time integral of the muon spin polarization gives the theoretical expression of the muonium resonance lineshape.

Time dependent spin flip signal is a periodic function of the microwave power and the frequency detuning. In the experiment, both microwave field and muonium density have spacial dependence. Hence, the signal actually observed is weighted summation of the muon spin polarization with the particular value of microwave power. Figure 2-8 shows calculated time dependent spin flip signals at several microwave frequencies with fixed microwave power. The red line corresponds to the result at resonance, the green and blue ones show that with 500 kHz and 1000 kHz detuned frequencies. When microwave frequency is tuned at the muonium HFS resonance, the spin flip signal is described in a simple sine function. On the other hand, the spectrum with detuned microwave frequency has a complicated dependence.

Figure 2-9 represents calculated spin flip signal at the muonium HFS resonance frequency with several values of microwave power. Each line corresponds to 800 kHz (red), 400 kHz (green), and 1200 kHz (blue) of the microwave power parameter $|b|$, respectively. Figure 2-10 represents the signal at a detuned microwave frequency of 1000 kHz from the HFS resonance. For a case of detuned frequency, the time dependent signal shows the complicated behaviors. However, the first peak of the signal is dominated by a component which corresponds to the highest strength of the microwave field.

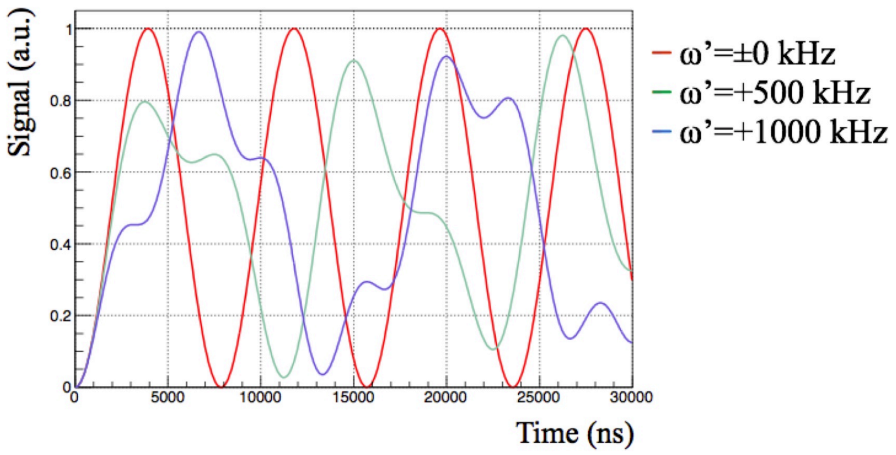

Figure 2-8: Time dependent signal of muonium spin flip. Red, green, and blue lines correspond to the microwave frequency detuning of zero, 500 kHz, and 1000 kHz, respectively. The microwave power parameter $|b|$ was set 800 kHz.

2.4.5 Muon decay positron

The parity violating muon decay causes the correlation between the decay positron energy and the muon spin direction. The distribution of muon decay positron is

$$N(y,\theta,t)dyd\Omega = \frac{\gamma}{2\pi}y^2\lceil(3-2y)+(2y-1)P_{z0}(t)\cos\theta\rceil e^{-\gamma t}dyd\Omega \tag{2.84}$$

where y is the positron energy normalized by its maximum of 52.8 MeV, θ is the polar angle with respect to the z-axis. The muon decay asymmetry is defined as the degree of correlation between positron momentum and muon spin direction. Figure 2-11 represents the positron energy spectrum and the asymmetry as a function of the normalized positron energy. Low energy positron negatively contributes to the angular asymmetry and the sensitivity to the muon spin direction.

When energy threshold y_0 is set, the decay positron spectrum is described as

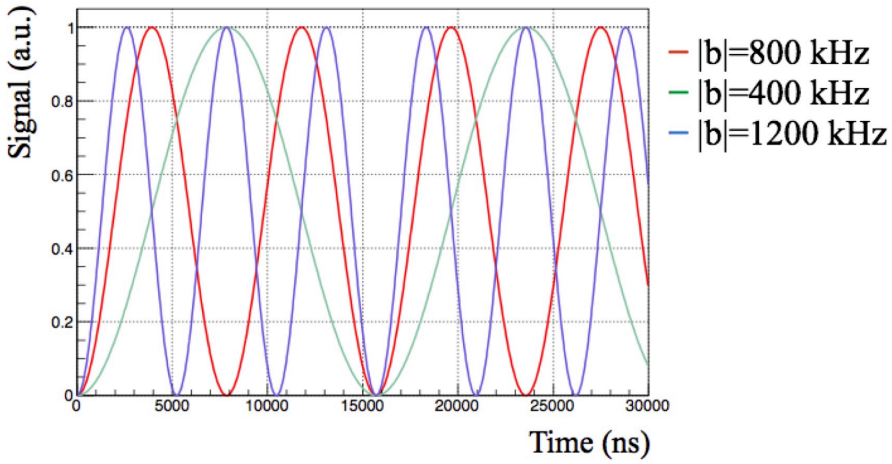

Figure 2-9: Time dependent spin flip signal at the resonance. Red, green, and blue lines correspond to the microwave power parameter $|b|$ of 800 kHz, 400 kHz, and 1200 kHz, respectively. The microwave frequency detuning was set to zero.

follows

$$\begin{aligned} N(y_0,\theta,t)d\Omega &= \int_{y_0}^{1} N(y,\theta,t)dyd\Omega \\ &= \frac{\gamma}{4\pi}[A_1(y_0) + A_2(y_0)P_z(t)\cos\theta]e^{-\gamma t}d\Omega \\ &= \frac{\gamma}{4\pi}A_1(y_0)[1 + a(y_0)P_z(t)\cos\theta]e^{-\gamma t}d\Omega \end{aligned} \tag{2.85}$$

where

$$A_1(y_0) = 1 - (2y_0^3 - y_0^4) \tag{2.86}$$

$$A_2(y_0) = \frac{1}{3} - (y_0^4 - \frac{2}{3}y_0^3) \tag{2.87}$$

$$a(y_0) = \frac{A_2(y_0)}{A_1(y_0)}. \tag{2.88}$$

Figure 2-12 shows the integrated positron asymmetry as a function of the energy threshold. A higher energy threshold gives a large angular asymmetry and less statistics. The angular distribution of the decay positron for several values of the energy threshold is shown in 2-13. An appropriate energy threshold around 40 MeV is effective to enhance the signal sensitivity and suppress the positron counting rate.

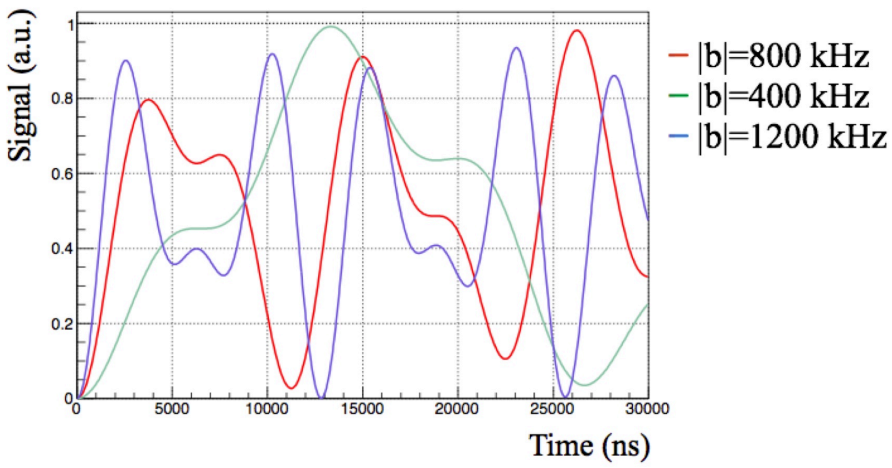

Figure 2-10: Time dependent spin flip signal at the resonance. Red, green, and blue lines correspond to the microwave power parameter $|b|$ of 800 kHz, 400 kHz, and 1200 kHz, respectively. The microwave frequency detuning was set to 1000 kHz.

2.4.6 Resonance lineshape

The resonance lineshape is obtained from the time integration of muon spin flip signal. It corresponds to the positron counting difference with and without microwave magnetic field. The number of detected positrons with the microwave resonance in a finite interval $(t_1,\ t_2)$ is denoted as $N_{\rm ON}(y_0, \theta, t_1, t_2)$ where y_0 is the energy threshold and θ is the polar angle with respect to the z-axis. Similarly, the number of detected positrons without the microwave resonance is denoted as $N_{\rm OFF}(y_0, \theta, t_1, t_2)$. The time integrated muon spin flip signal S is defined as follows

$$\begin{aligned} S &= \frac{N_{\rm ON} - N_{\rm OFF}}{N_{\rm OFF}} \\ &= \frac{N_{\rm ON}}{N_{\rm OFF}} - 1. \end{aligned} \tag{2.89}$$

The calculation of the positron counting ratio is effective to suppress time dependent systematic uncertainties. Most of chronological changes in measurement environment are canceled in the leading order of contribution. In the experiment, switching of microwave output was performed in every minute. Therefore, temporal variations with a time-scale of longer than minutes are highly suppressed.

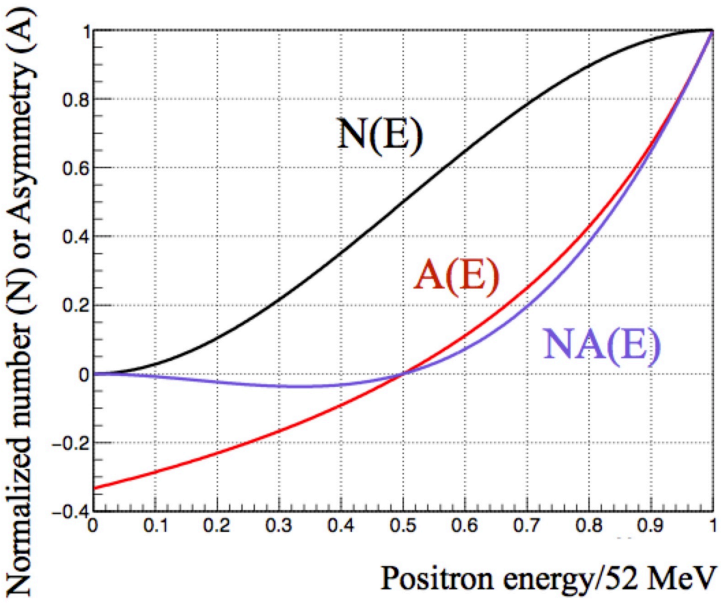

Figure 2-11: Positron angular asymmetry as a function of the energy E. Black, red, and blue lines correspond to the normalized number of positron, the muon decay asymmetry, and the weighted asymmetry as the product of the number and the asymmetry.

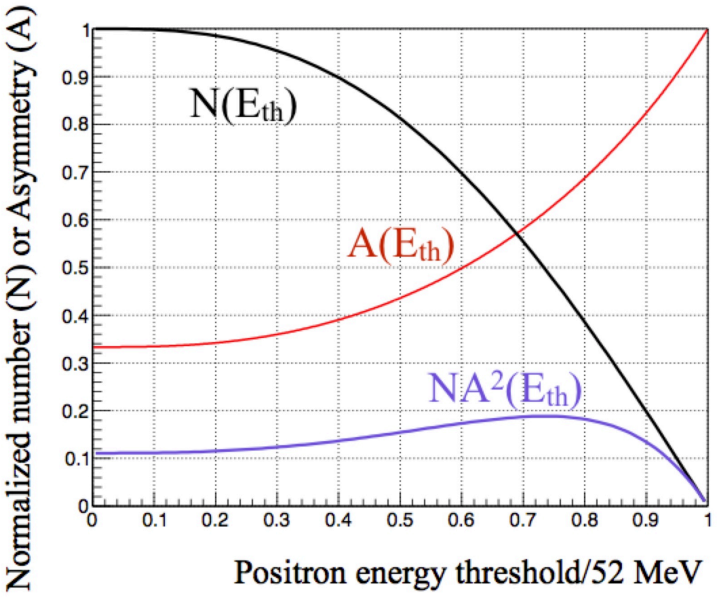

Figure 2-12: Positron angular asymmetry as a function of the energy threshold E_{th}. Black, red, and blue lines correspond to the normalized number of positron, the muon decay asymmetry, and the figure of merit defined as the product of the number and square of the asymmetry.

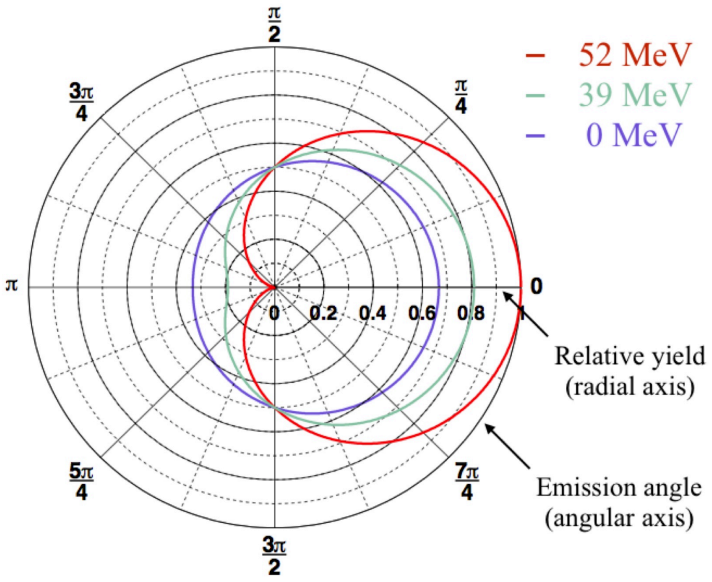

Figure 2-13: Angular distribution of the decay positron emission. The radial axis indicates relative positron yield while the angular axis indicates positron emission angle. Red, green, and blue lines correspond to 52 MeV, 39 MeV, and 0 MeV of the energy threshold, respectively.

The differential signal for a resonance lineshape is defined as follows

$$dS = \frac{a(y_0)\gamma P}{2} \frac{\int_{t_1}^{t_2} \{\frac{\Gamma+\omega'}{2\Gamma} \cos\frac{\Gamma-\omega'}{2}t + \frac{\Gamma-\omega'}{2\Gamma}\cos\frac{\Gamma+\omega'}{2}t - 1\}\cos\theta e^{-\gamma t}dt}{\int_{t_1}^{t_2}(1+\frac{aP}{2}\cos\theta)e^{-\gamma t}dt} \tag{2.90}$$
$$= \frac{\frac{a(y_0)P}{2}\cos\theta}{1+\frac{a(y_0)P}{2}\cos\theta)} L(|b|^2, \omega', t_1, t_2)$$

in which L is the microwave dependency term

$$L(|b|^2, \omega', t_1, t_2) = \frac{1}{e^{\gamma t_1} - e^{-\gamma t_2}} \tag{2.91}$$
$$\left[\frac{\gamma e^{\gamma t}}{\Gamma}\frac{\Gamma+\omega'}{(\Gamma-\omega')^2+4\gamma^2}\{(\Gamma-\omega')\sin\frac{\Gamma-\omega' t}{2} - 2\gamma\cos\frac{\Gamma-\omega' t}{2}\}\right.$$
$$\left. + \frac{\Gamma-\omega'}{(\Gamma+\omega')^2+4\gamma^2}\{(\Gamma+\omega')\sin\frac{\Gamma+\omega' t}{2} - 2\gamma\cos\frac{\Gamma+\omega' t}{2}\} + \frac{\Gamma}{\gamma}\right]_{t_1}^{t_2}.$$

Time integration of dS gives the total signal

$$S = \frac{a(y_0)P}{2\int_V \rho(r)\left[\int_D (1+\frac{a(y_0)P}{2}\cos\theta)d\Omega\right]d\tau} \int_V \rho(r) L(\int_D \cos\theta d\Omega) d\tau \tag{2.92}$$

where $\rho(r)$ is the spacial distribution of muonium, V is the volume of the microwave cavity, $d\tau$ is the volume element, and D is the area of the positron detector.

The integration of the microwave term L over the infinite interval $(0,\ \infty)$ makes the resonance lineshape Lorentzian form as follows

$$L(|b|^2, \omega', 0, \infty) = \frac{-2|b|^2(\gamma^2 + 2|b|^2)}{(\gamma^2 + 2|b|^2)^2 + \gamma^2\omega'^2}. \tag{2.93}$$

Figure 2-14 shows calculated resonance lineshapes for several values of the microwave power. Red line corresponds to a lineshape with $|b| = 800$ kHz. Green and blue ones correspond to $|b| = 400$ kHz and $|b| = 1200$ kHz, respectively. The full width at half

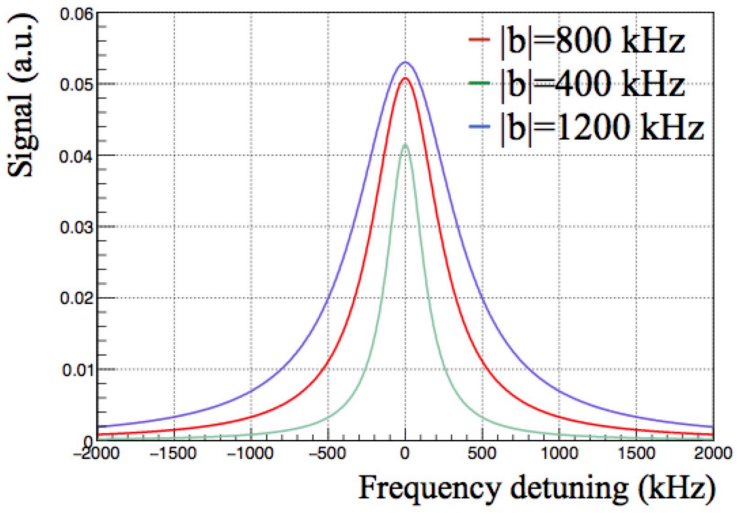

Figure 2-14: Resonance lineshapes of the muonium HFS. Red, green, blue lines correspond to the microwave power parameter $|b|$ of 800 kHz, 400 kHz, and 1200 kHz, respectively.

maximum (FWHM) of the resonance lineshape is

$$\Delta\omega = \frac{2(\gamma^2 + 2|b|^2)}{\gamma}. \tag{2.94}$$

In the zero microwave power limit, the FWHM equals to the natural line width of 145 kHz. The other term of $2|b|^2/\gamma$ represents a contribution of power broadening

effect. The peak height of the resonance lineshape is

$$S_{\max} = \frac{2|b|^2}{\gamma^2 + 2|b|^2}. \tag{2.95}$$

Chapter 3

Experimental Overview

This chapter describes overview of the experiment and the apparatus except for particle detectors. The details of the detectors are described in the following chapters.

3.1 The experimental principle

Figure 3-1 presents the schematic of the experimental apparatus. Spin polarized pulsed muon beam is irradiated to a gas chamber filled with krypton gas. A two-dimensional fiber hodoscope for muon detection is placed in front of the gas chamber to measure the profile and the intensity of the incident muon beam. An injected muon loses its kinetic energy and forms a muonium via an electron capture from krypton atom. A cylindrical microwave cavity is placed inside of the gas chamber. It generates TM110 mode of a microwave resonance at the frequency of 4.463 GHz and induces the muonium HFS transition. The state transition causes a muon spin flip as a function of time. A positron is emitted by parity violating decay of muon and its emission angle is correlated to the muon spin direction. Spectroscopy of the muonium HFS is performed by a measurement of microwave frequency dependence of the number of decay positron from muonium decay. Positron is detected by two layers of segmented scintillation counter. Detectors are placed in the downstream of the target gas chamber.

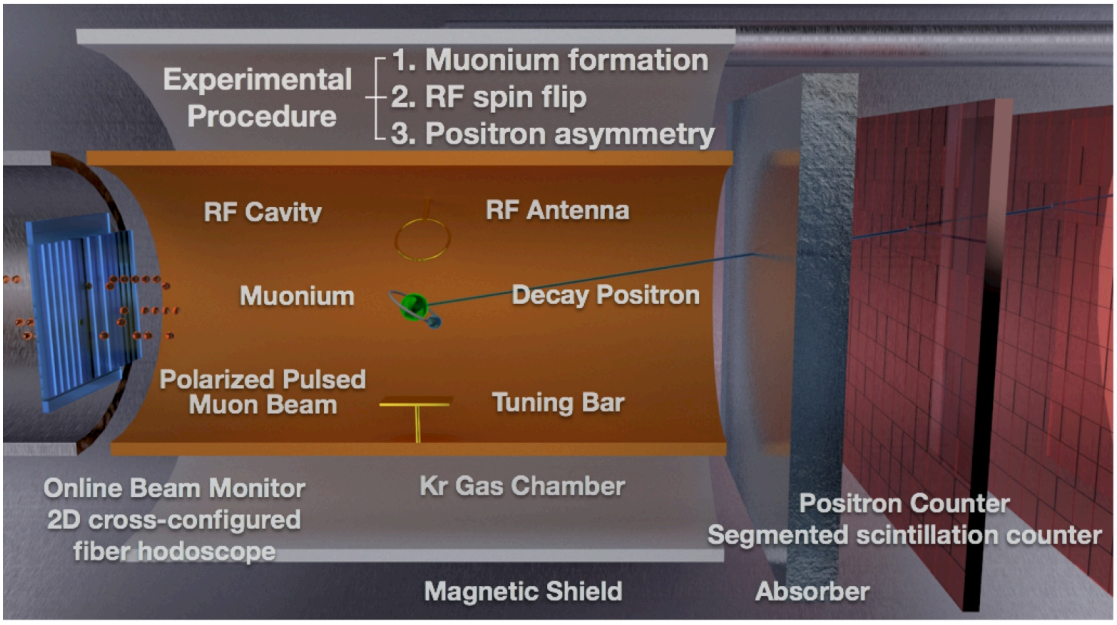

Figure 3-1: Experimental schematic of muonium HFS spectroscopy. Spin polarized pulsed muon beam is irradiated to Kr gas target. Muonium forms by an electron capture from Kr atom. The muonium HFS transition occurs due to the microwave resonance in the cylindrical cavity. Positrons from muonium decay are detected by the positron counter placed behind the gas chamber.

3.2 High-intensity pulsed muon beam

The experiment was performed at the D2 beamline of MUSE facility [48]. Muons are produced by pulsed proton beam irradiation on a graphite target. At J-PARC, protons are produced by charge exchange reaction of hydrogen negative ions from a tungsten filament. Negative hydrogen ions are accelerated to 400 MeV by the linear accelerators. Accelerated hydrogen ions are injected to Rapid Cycle Synchrotron (RCS) and converted to protons by a carbon charge stripping film. Protons are accelerated to 3 GeV and delivered to the target station at MLF [47]. A repetition cycle is 25 Hz and typical proton beam intensity is 20 tera proton per second at 200 kW of RCS operation power. The beam has double or single pulse structure width a FWHM of 100 ns. In the double pulse mode, two bunches have an interval of 600 ns.

At the muon target station of MLF, a rotating graphite disk is placed as a muon

production target [50] . A charged pion is produced by the reaction as follows

$$p + \mathrm{C} \rightarrow \pi^{+} + \mathrm{X}. \tag{3.1}$$

Parity violating decay of a pion produces a spin polarized muon. This process is two-body decay so that the muon has monochromatic kinetic energy of 4.08 MeV. Only muons generated in the vicinity of the target surface are able to escape to the vacuum. As of 2016, five beamline branches had been constructed. D1 and D2 lines are multipurpose beam lines for both particle physics and material science [49]. Figure 3-2 shows the structure of D2 beamline. It has a long superconducting solenoid, a Wien filter for positron separation, two sets of movable slits, three bending magnets, and four sets of quadrupole magnet triplets. Acceptance of the beamline is 50 mSr [48]. Typical muon beam intensity is 3 million muons per second at beam of 200 kW power.

3.3 Experimental area

Figure 3-3 displays a drawing of D2 experimental area. The experimental area has the reinforced baseplate for apparatus mounting, the wall made of stainless steel as a beam dump.

3.3.1 Magnetic field in the experimental area

To perform the experiment with high precision, a static magnetic field in the muonium formation volume should be uniform and close to zero. As a preliminary investigation, magnetic field distribution in the experimental area was measured by using a three-axis fluxgate magnetometer. The details of the magnetometer is discussed in the following section. Figure 3-4 shows measured static magnetic field on the beam axis. The strength of a static magnetic field in the experimental area was generally higher than typical geomagnetism of approximately 50 μT. Hence, the measurement result suggests additional sources of magnetic field around the muonium formation volume.

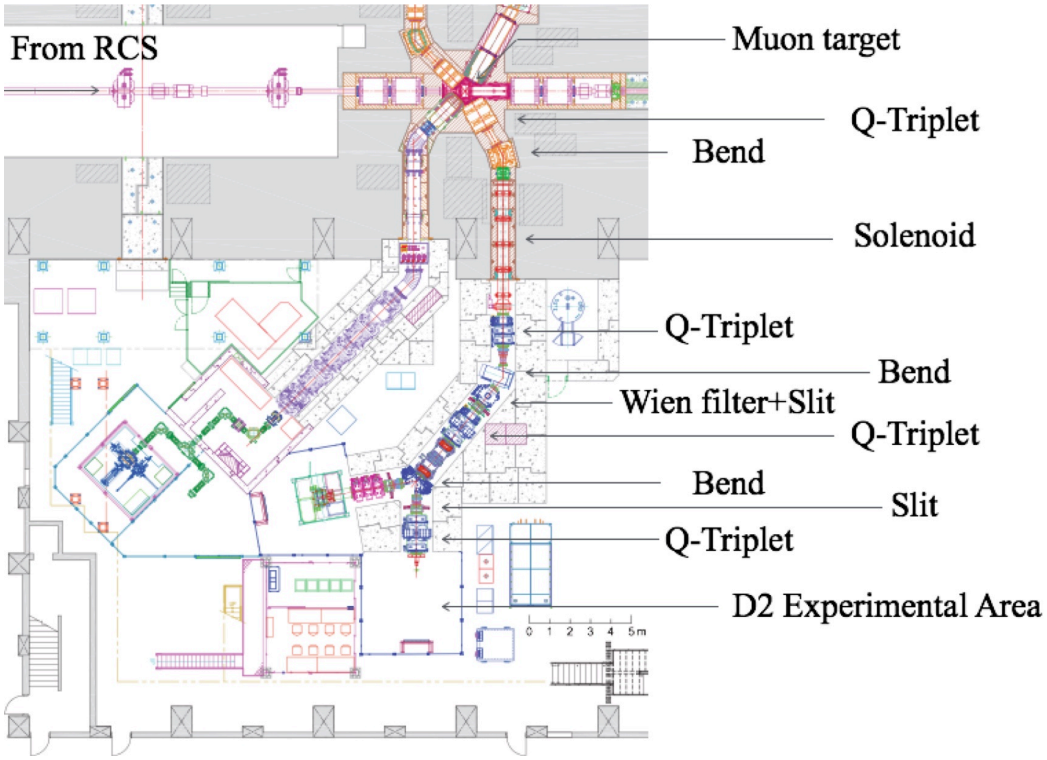

Figure 3-2: Layout of D2 muon beamline at MLF second experimental hall. The pulsed proton beam from RCS is irradiated on the graphite muon production target. Muons from pion decay are transported through the beamline consisting three bending magnets and four sets of quadruple magnet triplets. The Wien filter and the movable slits are utilized for the suppression of beam-associated background.

Further survey revealed that major sources of the magnetic field in the experimental area were the beamline components, and the reinforcement base plate.

By taking a difference in the result where beamline magnets were excited or not, a stray field from the beamline was extracted. Figure 3-5 represents the measured stray field on the beam axis. Even though the apparatus is surrounded by a magnetic shield, magnetic flux on the beam axis is less suppressed because an opening aperture is necessary for muon beam passing. Stray field from a magnet becomes weak as the distance from the magnet increases. Therefore, in order to reduce an influence of stray field from the beamline magnets, an extension of beam duct was developed and placed between the original beam duct and the apparatus. The extended beam duct was placed to minimize the beam loss. In the end of the extended beam duct, a kapton beam window with 75 μm of thickness was placed.

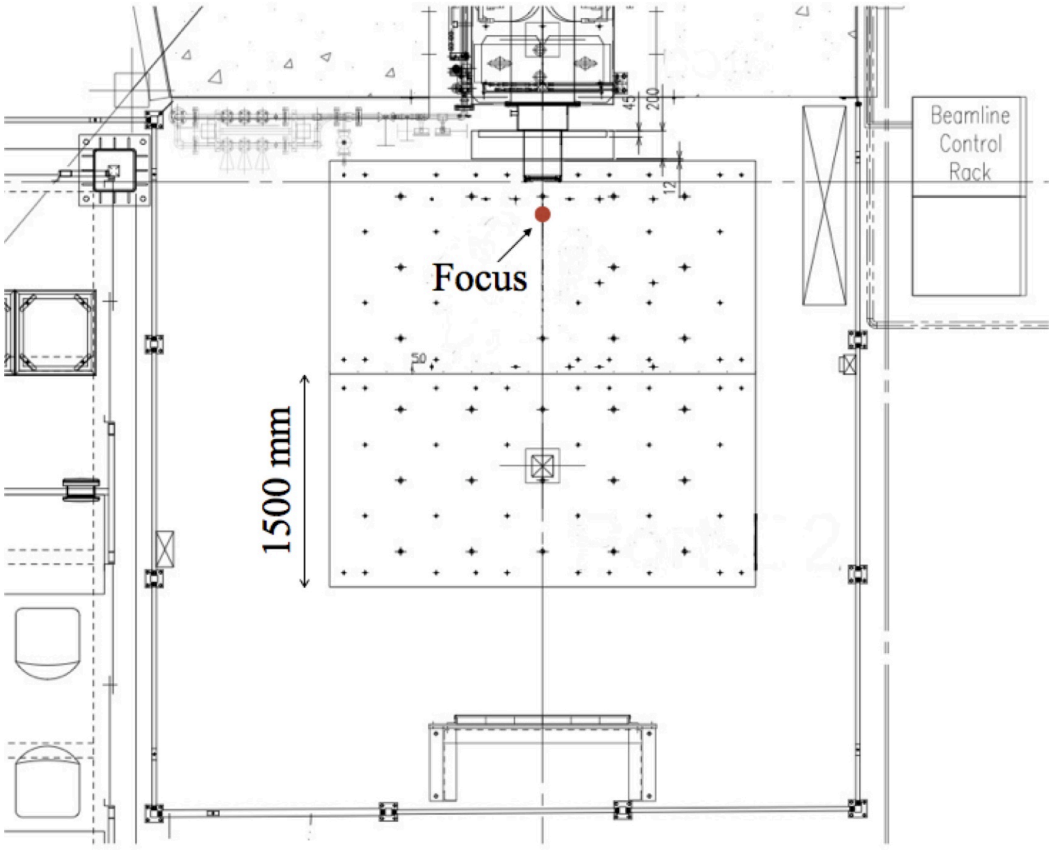

Figure 3-3: Floor plan of D2 experimental area. The focusing point of the muon beam is located 800 mm downstream from the last Q-triplet. The apparatus is placed on the base plate which is three meters squared.

The energy levels of muonium depend on a magnetic field which muonium feels. In the experiement, only the transitions $|1\rangle \leftrightarrow |4\rangle$ and $|3\rangle \leftrightarrow |4\rangle$ can be observed. According to a calculation based on the Breit equation [13], each transition frequency shifts by 14 Hz per nT in opposite directions. This systematic effect broadens the resonance lineshape. This systematic effect on the resonance measurement is discussed in Chapter 4. When static magnetic field is less than 200 nT in the entire microwave cavity volume, systematic uncertainty depending on a static field is negligible.

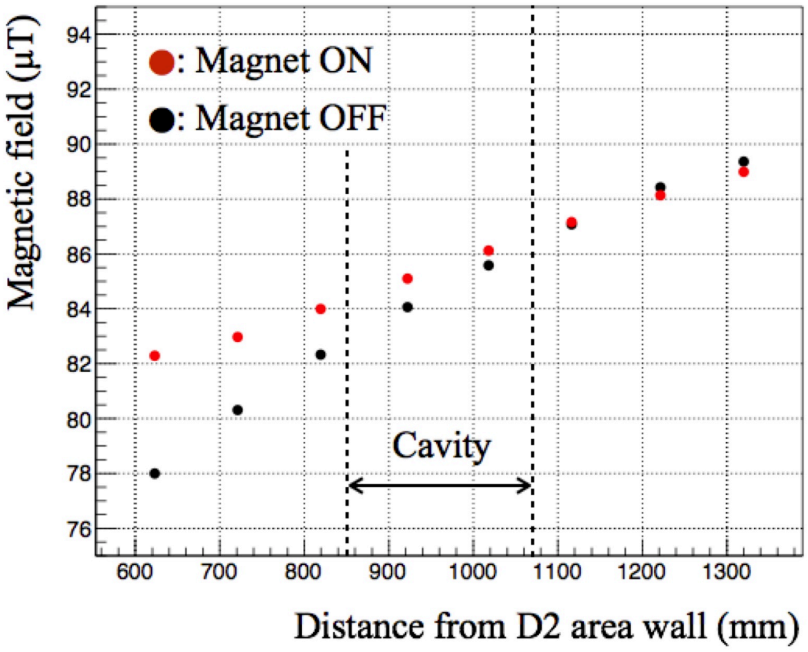

Figure 3-4: Static magnetic field in the experimental area along the beam axis. Red and black circles represent the magnetic field strengths with and without magnet excitation, respectively. Inside of the microwave cavity is indicated by the arrow.

3.4 Magnetic shield

In order to suppress the stray magnetic field in the muonium formation volume, the apparatus was enclosed with a magnetic shield box which made of permalloy; an alloy of nickel and iron [51]. Permalloy has high magnetic permeability and absorbs a magnetic flux from external sources. To enhance the initial permeability, a heat treatment and addition of non-ferromagnetic elements such as copper or molybdenum are highly effective. Typical relative permeability of permalloy after heat treatment is higher than 20,000 [52].

3.4.1 Designing of a magnetic shield

The shield was designed based on the results of a stray field analysis by a finite element method. It comprises a three-layered permalloy box where the layer thickness is 1.5 mm and interlayer distance is 50 mm. Figure 3-6 depicts the drawings of the magnetic

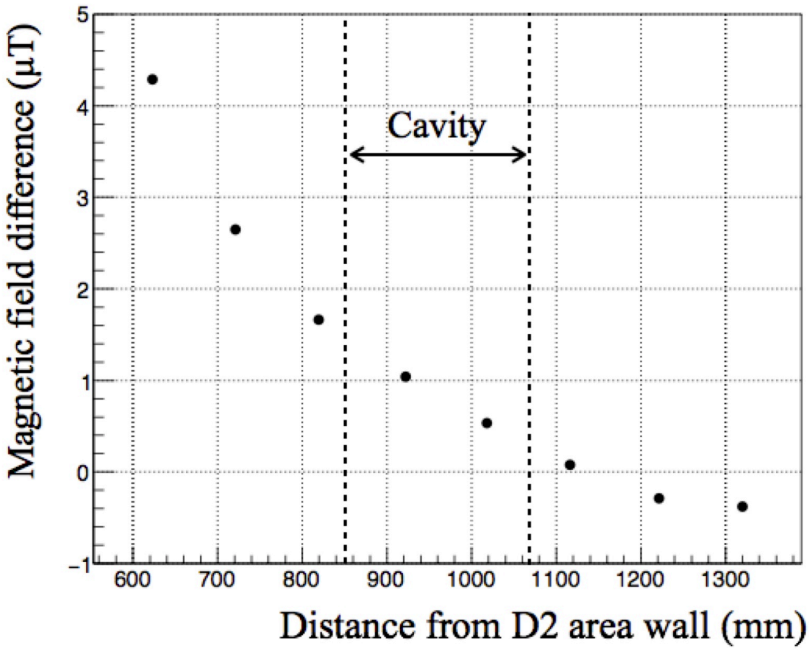

Figure 3-5: Stray field from the beamline along the beam axis. Inside of the microwave cavity, the strength of the stray field between 0.5 μT and 1.5 μT was observed.

shield. Front panels of the shield are divided into the upper and the lower parts where the extended beam duct is installed. In order to minimize magnetic field sources in the shield, material of major metal contents was limited to aluminium, copper, titanium, or austenitic stainless steel (SUS316L).

Figure 3-7 shows simulated magnetic field distribution in the magnetic shield which was designed as described above. The permeability of permalloy was assumed as 12,000. The upper two figures show projected magnetic field strengths at the center of microwave cavity. The lower two figures show field strengths on the beam axis. The z-direction is parallel to the beam axis (the longitudinal axis). A contribution of the z-component of magnetic field is less significant, so the magnetic flux flowing from the apertures on the backplane is no matter of concern.

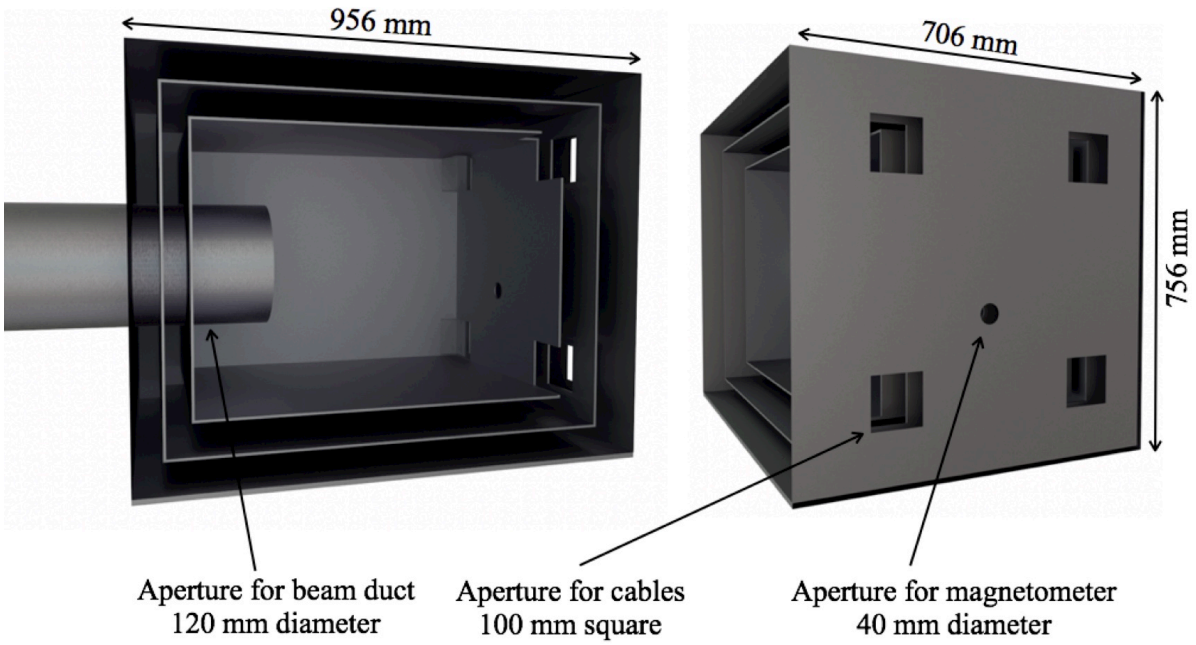

Figure 3-6: Drawings of the magnetic shield: (left) a cross-sectional drawing; (right) a backplane drawing. The magnetic shield consists of a permalloy box having a three-layered structure. The shield has opening apertures for the beam duct, cables for the detector and microwave, and insertion of the magnetometer.

3.4.2 Performance of the magnetic shield

To evaluate the performance of the magnetic shield, the static magnetic field distribution in the shield was measured by using a fluxgate magnetometer. Figure 3-8 shows measured static magnetic field along the beam axis. Black circles indicates a result without magnetic shield, and red ones indicate a result with magnetic shield. The magnetic shield suppressed a static magnetic field in one thousandth approximately. In the entire cavity region, magnetic field strength was less than 100 nT and sufficiently close to zero. Figure 3-9 shows a two-dimensional distribution of measured magnetic field at the center of the microwave cavity. The rotating and eccentric magnetometer helps to find a local magnetization and room to improvement. Asymmetric distribution of the field strength suggests an existence of magnetized component around the microwave cavity.

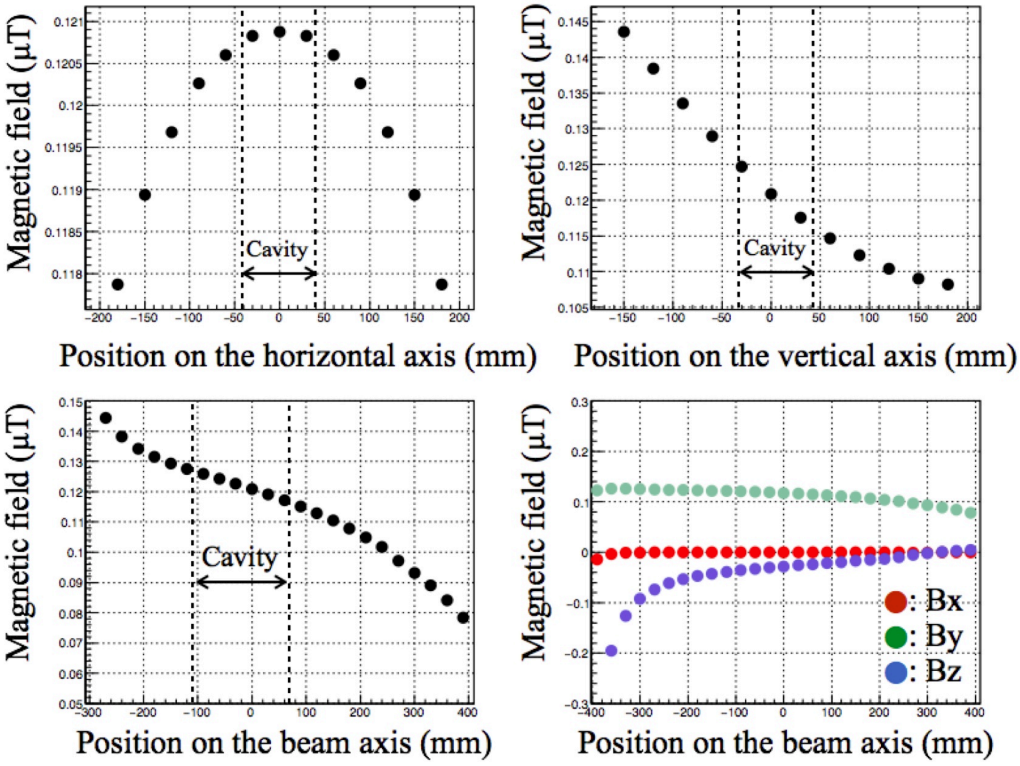

Figure 3-7: Remnant of the magnetic field inside of the shield simulated by a finite element method: (upper left) magnetic field strength on the horizontal axis; (upper right) field strength on the vertical axis; (bottom left) field strength on the longitudinal axis; (bottom right) each component of the magnetic field on the longitudinal axis. Red, green, and blue circles correspond to the horizontal, vertical, and longitudinal components, respectively. The muon beam is injected to a positive direction on the beam axis.

3.5 Magnetometer

The magnetic field strength is measured by a high-precision fluxgate magnetometer (MTI FM3500) with a resolution of 0.5 nT. The magnetometer consists of three sets of a field probe which is described in the following part of this section. Magnetic field measurement was performed before and after the spectroscopy measurement.

3.5.1 Principle of a fluxgate magnetometer

A fluxgate magnetometer utilizes non-linear response of soft magnetic material. Figure 3-10 illustrates the schematic of a parallel-type fluxgate magnetometer. The

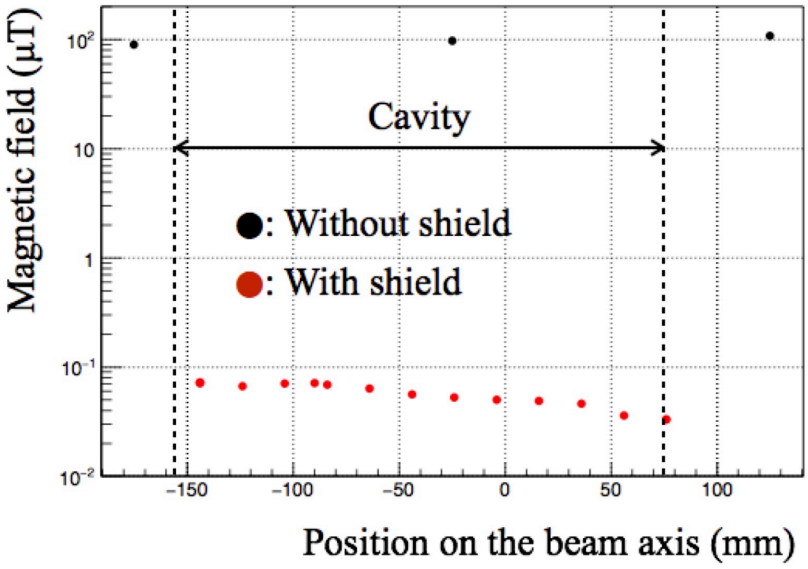

Figure 3-8: Magnetic field strength on the longitudinal axis. Red and black circles correspond to the field strengths with and without shielding, respectively. The muon beam is injected to a positive direction on the axis.

principle of a fluxgate magnetometer is represented in Fig. 3-11. When a modulation field is applied to the first coil (modulation coil), magnetization of the core oscillates and it generates an induction voltage. The second coil (detection coil) detects this induction voltage as indicated by a green solid line in the Figure 3-10. In a presence of external magnetic field, the oscillating voltage becomes asymmetric as a red dashed line in the same figure. This asymmetry contains information of external field strength as the second harmonics of a modulation signal. The detection module consists of a voltmeter with a filter circuit to extract a second harmonics component from the output.

3.5.2 Moving rod for the magnetometer

To measure magnetic field distribution in the magnetic shield, a movable rod for the fluxgate magnetometer was developed. Figure 3-12 illustrates the movable rod and the fluxgate magnetometer. The rod rotates and translates to move the field probe inside the magnetic shield.

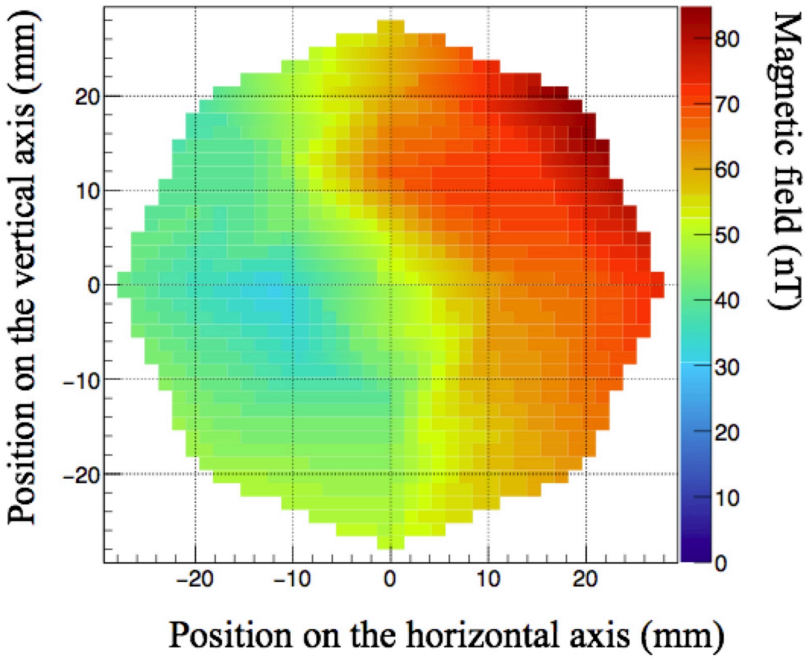

Figure 3-9: Magnetic field distribution at the longitudinal center of the microwave cavity.

Alignment of the probe dominates the uncertainty of the field measurement. In order to optimize a design variable of the moving rod, its vertical displacement against the load by probe was estimated by using an analytic model of flexibility. Figure 3-13 shows calculated displacement as a function of wall thickness of an aluminum pipe. The optimum thickness of the pipe was determined to be 2 mm and the maximum displacement of the probe was estimated to be 0.35 mm. This maximum displacement is small enough for the measurement.

3.6 Gas chamber

A gas chamber was developed to fill a gas target for muonium production. Figure 3-14 is a drawing of the gas chamber. It is a cylindrical vessel made of aluminum with the longitudinal length of 450 mm and the inner diameter of 280 mm. The upstream flange has a thin aluminum beam window with thickness of 100 μm and diameter of 100 mm. The downstream flange has a thin part with thickness of 10 mm

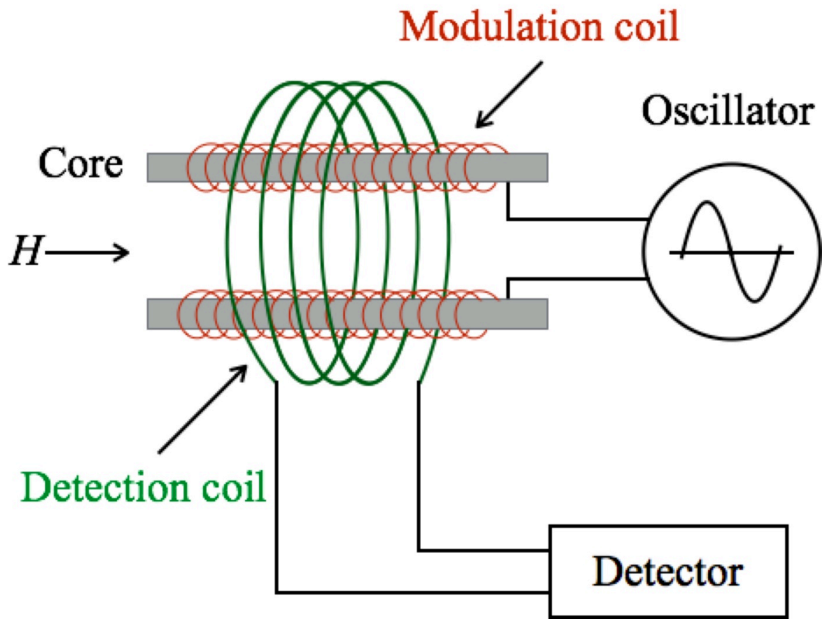

Figure 3-10: Schematic of a parallel fluxgate magnetometer. It consists of a core of soft magnetic material, a modulation coil, and a detection coil. A sinusoidal current flows through the modulation coil and the core is excited.

and diameter of 180 mm for a decay positron to pass through. A beam window was designed to withstand a pressure difference of 1.5 atm or below.

3.6.1 Gas target

Muonium formation in low pressure gases was studied by D. G. Fleming *et al.* [54]. The energy threshold of muonium formation via electron capture is

$$E_{\text{th}} = E_I(\text{Gas}) - E_I(\text{Mu}) \tag{3.2}$$

where E_I(Gas) is the ionization potential of gas and E_I(Mu) is the binding energy of muonium (13.54 MeV). When the threshold energy E_{th} is negative, muonium forms energetically. Table 3.1 summarizes the threshold energy and efficiency of muonium formation in a gas target. Krypton provides high production efficiency and low energy of muonium. As a muonium production target in the experiment, high-purity krypton gas was filled in the gas chamber. It has the research grade purity of 99.999 %. Major

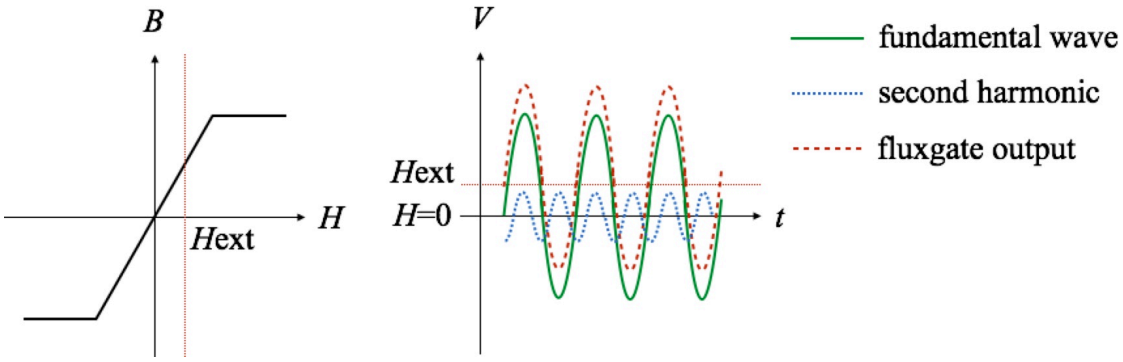

Figure 3-11: Principle of fluxgate magnetometer: (left) magnetization curve of the core; (right) output signal from the detection coil. In a presence of an external magnetic field $H_{\rm ext}$, the core is magnetized. The magnetization of the core oscillates when an oscillating current is applied to the modulation coil. Output signal from the detection coil contains a second order harmonic component which depends on the nonlinear response of the core magnetization.

impurities are Xenon and Argon as the residues in a purification process.

3.7 Gas handling system

Figure 3-15 illustrates a diagram of gas handling system. A scroll pump and turbo molecular pump (TMP) were utilized for evacuation. Degree of vacuum was monitored by a combination of crystal and cold cathode gauge (TOEL CC10). When the pressure is 0.6 Pa or less, cold cathode gauge is operated. Gas pressure was measured by a capacitance gauge (ANELVA M-342DG) with a precision of 0.2% at 300 K.

Before filling the target gas, the gas chamber was heated to bake for removal of impurities. Major expected impurity was the water vapor emitted from the chamber wall and microwave components. The gas chamber was baked for 24 hours continuously at baking temperature of 380 K. Partial pressures of impurities was measured by a quadrupole type mass spectrometer (mks Microvision2).

3.7.1 Degradation in the degree of vacuum

Figure 3-16 shows measured degree of vacuum as a function of elapsed time from chamber containment. Increase in internal pressure was caused by outgas and vac-

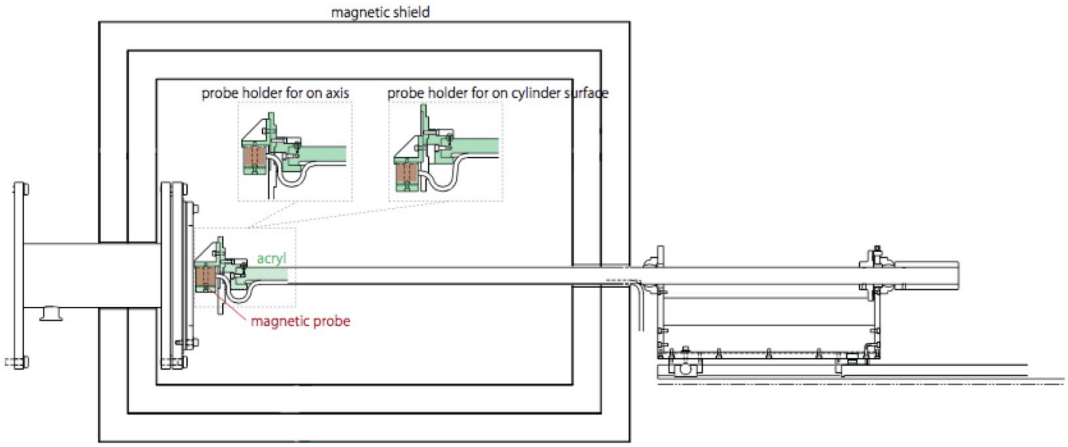

Figure 3-12: Movable rod for the fluxgate magnetometer. The field probe is attached on the edge of an aluminum pipe with the length of 1 m. Two types of attachments were developed to measure the magnetic field both on the longitudinal axis and on the cylindrical surface away from the longitudinal axis. The eccentric distance is selectable from 8 mm or 16 mm.

uum leakage. A rate of pressure increase was evaluated by linear fitting of data points after the gauge switching. Obtained rate was 2×10^{-2} Pa per minutes. To estimate systematic effect caused by this outgas or vacuum leakage, gas component was analyzed by a quadrupole mass spectrometer as discussed in the following part in this section.

3.7.2 Gas purity measurement

Partial pressures of gas component were measured by using quadrupole mass spectrometer. After the pressures reached equilibrium, the content of each impurity was relatively evaluated. Figure 3-17 shows relative pressures for each mass number. Water vapor is a dominant component of the adsorption gas. Nitrogen originates mainly from inflow of the atmospheric air due to vacuum leakage. Carbon dioxide is mostly from stored gas in the inner wall of the gas chamber. According to the atmospheric composition and measured ratio of nitrogen and carbon dioxide, a putative cause of pressure increase is outgas. Oxygen and nitrogen oxide may cause depolarization of the muon spin by spin exchange interaction. Systematic effect by these magnetic

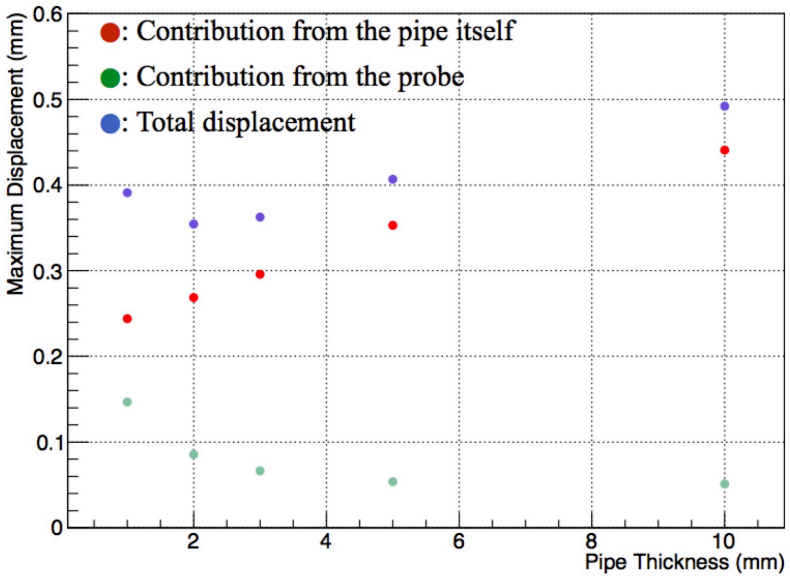

Figure 3-13: Calculated vertical displacement of a fluxgate probe. Red circles indicate a contribution from the pipe itself, green ones indicate a contribution from the probe, and blue ones indicate the total displacement of the probe.

molecules are discussed in the folliwing chapters.

3.8 Microwave cavity

To causing microwave resonance for a muonium state transition, a microwave cavity was developed. It is a cylindrical resonator made of oxygen-free copper. Figure 3-18 shows a drawing of the microwave cavity. The cavity has longitudinal length of 230 mm and inner diameter of 81.8 mm. The front and rear flange have copper thin films with thickness of 20 μm. To improve the resonator characteristics, inner wall of the cavity was electropolished.

3.8.1 Microwave resonance in a cylindrical cavity

The muonium transition probability is proportional to the strength of microwave field. The microwave field component which is perpendicular to the muon spin direction contributes to a muonium spin flip. TM_{mp0} modes of the microwave are suitable for

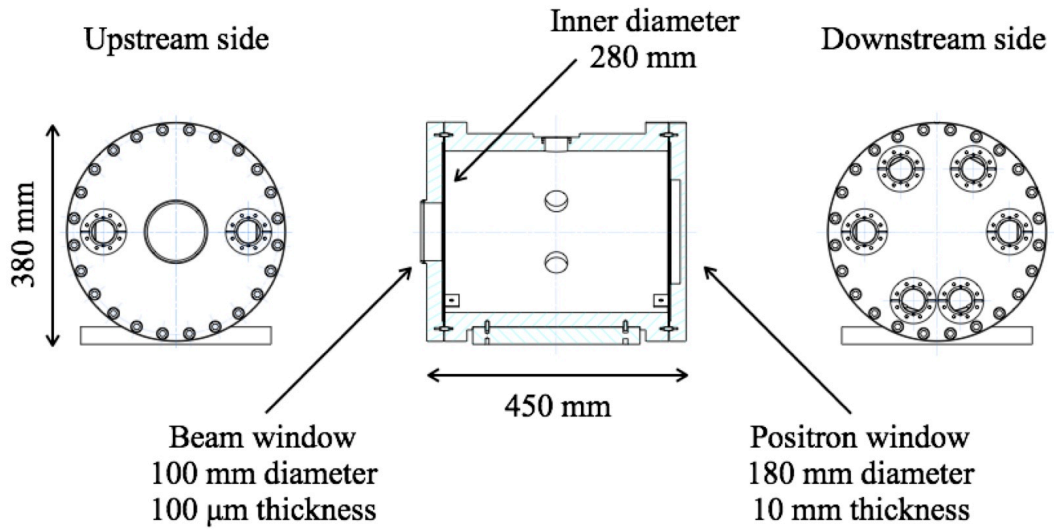

Figure 3-14: Drawing of the gas chamber: (left) view from upstream; (center) cross-sectional view; (right) view from downstream. On the front and rear flanges, thin windows for passing the beam and decay positron are located. Small ports were utilized for target gas injection, vacuum evacuation, microwave input/output, and cavity tuning.

the experiment since no position dependence along the longitudinal axis is desirable. The resonance frequencies of TM_{mn0} modes are

$$f_{mn0} = \frac{c}{n_r}\sqrt{(\frac{j_{mn}}{\pi R})^2 + (\frac{q}{2d})^2} \tag{3.3}$$

where c is the speed of the light, n_r is the reflective index of the medium, R is the cavity radius, d is the cavity length, and j_{mn} is the n-th zero of m-th order Bessel function. For the experiment at zero magnetic field, axial length and radius of a microwave cavity are decided so as to its resonance frequency equals to muonium HFS interval of 4.463 GHz. Furthermore, no other resonance modes should be in the vicinity of frequency sweeping region.

The general expression of TM_{mn0} mode in the cylindrical cavity is derived from

Table 3.1: Threshold energy and efficiency of muonium formation in gases [54]. Threshold energy was calculated by a difference between the ionization potential of each gas and the binding energy of muonium. Production efficiency of muonium was measured by an amplitude of muonium spin precession in a magnetic field.

Gas	Threshold energy (eV)	Efficiency (percent)
He	10.96	0
Ne	8.06	6±5
Ar	2.26	74±4
Kr	0.46	100±5
Xe	-1.44	100±4
N_2	-2.06	84±4

the Maxwell equations with particular boundary conditions.

$$H_r = -A\frac{j\omega\epsilon}{k_c^2}\frac{m}{r}J_m(\frac{j_{mn}r}{R}\sin m\theta) \tag{3.4}$$

$$H_\theta = -A\frac{j\omega\epsilon}{k_c^2}\frac{j_{mn}}{R}J'_m(\frac{j_{mn}r}{R}\cos m\theta) \tag{3.5}$$

$$H_z = 0 \tag{3.6}$$

where $\omega\epsilon\mu = k_c^2 + \beta^2 = (\frac{j_{mn}}{R})^2 + (\frac{p^2}{d^2})^2$, $\beta = \frac{p\pi}{n}$, A is the normalization constant, ω is the microwave resonance frequency.

The maximum field strength of TM_{110} mode depends on the power consumption and the cavity quality factor as follows [55].

$$B_0 = \frac{\sqrt{Q\mu_0 P_{\rm id}}}{\sqrt{2\omega d}aJ_0(j_{11})\pi^2} \tag{3.7}$$

$$\tag{3.8}$$

where Q is the cavity quality factor, μ_0 is the magnetic permeability of vacuum, $P_{\rm id}$ is the power consumption. Figure 3-19 shows the microwave field distribution using design values of the microwave cavity with a radius of 41 mm and a length of 230 mm.

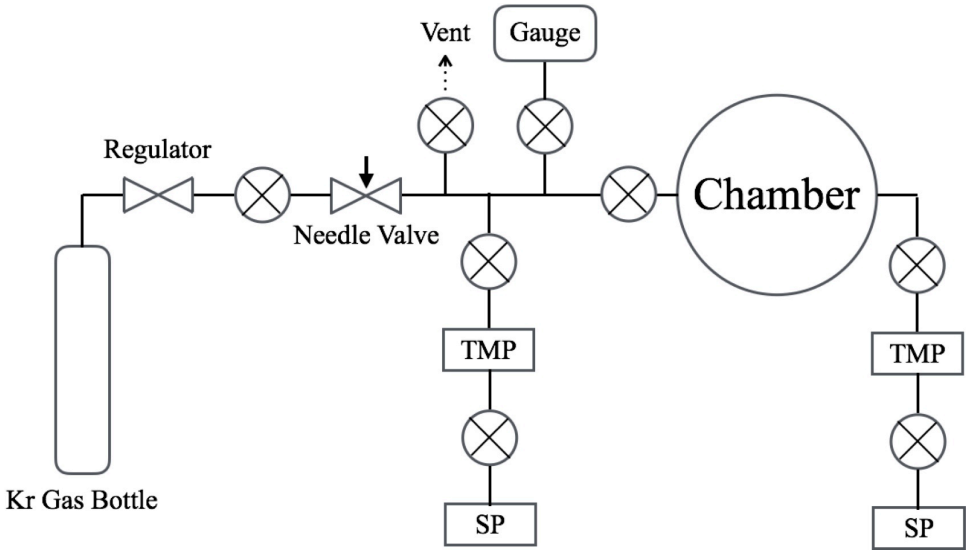

Figure 3-15: Diagram of the gas system. The target gas was injected into the gas chamber via a needle valve. SP and TMP indicate a scroll pump and a turbo molecular pump, respectively. During the spectroscopy measurement, the target gas was sealed and the pressure was monitored by using a capacitance gauge.

3.9 Microwave system

Figure 3-20 illustrates a diagram of microwave system. Microwave signal is generated by a synthesized continuous wave generator (Hewlett-Packard 8671B). The signal is divided into two lines and amplified by two coaxial amplifiers (Mini Circuit ZVE-8G) connected in parallel. The divided signal is merged and transmitted to an input magnetic loop antenna attached to the microwave cavity. To minimize the transmission loss of microwave, high performance coaxial cables (HUBER+SUHNER SUCOFLEX100) and receptacles (HUBER+SUHNER 23-SMA-50-0-1) were adopted.

A magnetic loop antenna resonates when its loop length equals to the integer multiple of the microwave wavelength. In the case of microwave radiation with the frequency of 4463 MHz, the input antenna was designed as a single circular loop with the diameter of 11 mm. It is empirically known that a loop length of the antenna should be sightly shorter than a value derived from the calculation. This is due to the wavelength shortening depending on a finite thickness of wire. In the

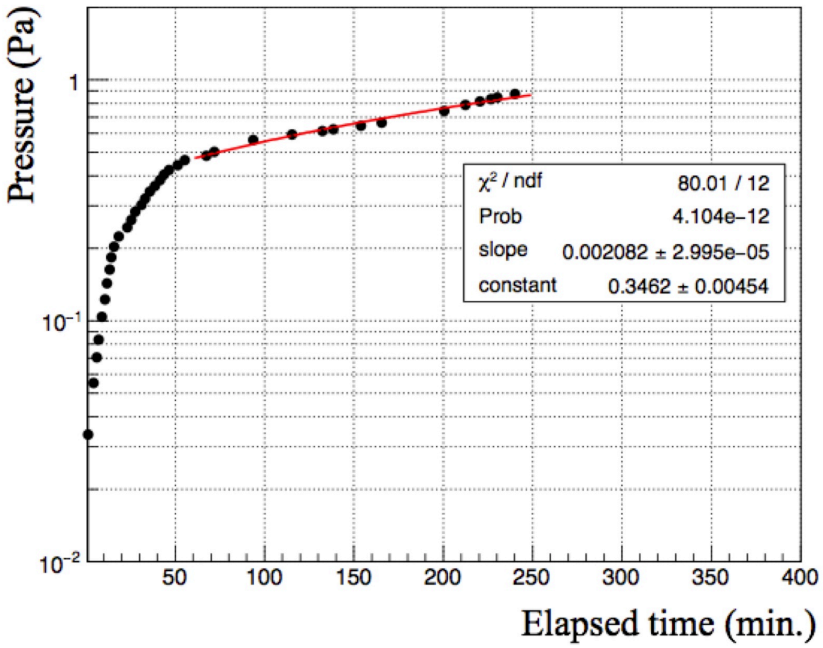

Figure 3-16: Measured degree of vacuum as a function of elapsed time. Red line indicates the fitting result using a linear function. The inflection point at 60 minute corresponds to a switching of the pressure gauge from a crystal gauge to a cold cathode one.

opposite side of the input antenna, a small loop antenna with the diameter of 4 mm for microwave power monitoring was placed. A pickup antenna should be minimized to avoid deformation of microwave magnetic field in the cavity. The signal from the pickup antenna is monitored by the microwave power meters (Giga-tronics 8541C and Rohde&Schwarz NRP-Z51).

A resonance frequency of the microwave cavity is tuned by an aluminum tuning bar with a piezoelectric actuator (attocube ANPz101eXT12). This actuator was remotely controlled by a motion controller (attocube ANC350). The piezo positioner has the resolution of sub-nm and the travel range of 12 mm. A conductive tuning bar increases the resonance frequency when it is inserted.

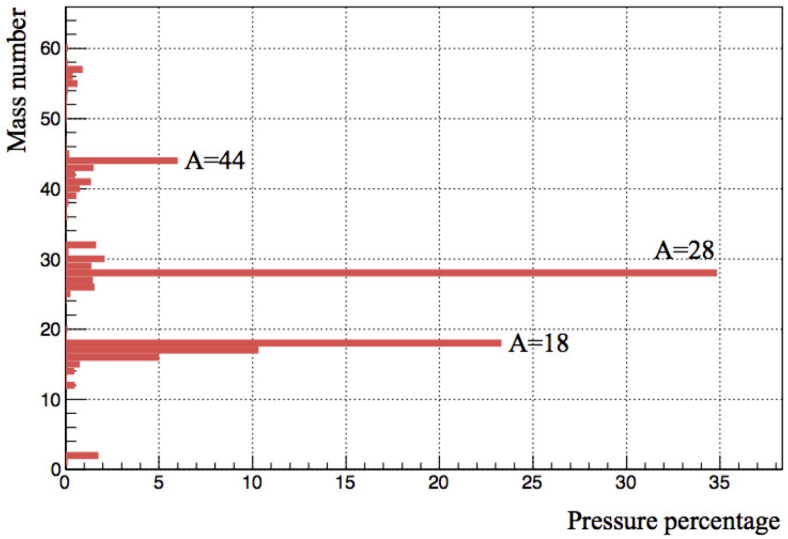

Figure 3-17: Measured gas impurities in the target chamber. Mass number of 18, 28 and 44 indicate water vapor (H_2O), nitrogen molecule (N_2), and carbon dioxide (CO_2), respectively. Mass number of 16 and 17 most likely correspond to the fragments of H_2O molecule.

3.9.1 Performance evaluation of the microwave cavity

Frequency characteristics of the microwave device is described by four S-parameters as the elements of a response characteristic matrix. Figure 3-21 illustrates a schematic of frequency characteristics analysis. S_{11} and S_{22} are the ratio of reflected signal and input signal. S_{21} and S_{12} are the ratio of transmitted signal and input signal. Summation of the signal transmission and the power loss in a device equals to input signal minus the signal reflection. To evaluate the microwave resonator, S_{11} parameter is of importance because it is necessary to estimate the power consumption in the cavity. Each S-parameter was evaluated by a vector network analyzer (Keysight Technologies E5072A-285).

Figure 3-22 shows a resonant absorption spectrum when the microwave at the frequency of 4463.3 MHz is applied. The ordinate indicates S_{11} parameter, namely, the reflecting parts of the microwave. When S_{11} parameter equals to one, the signal is completely reflected.

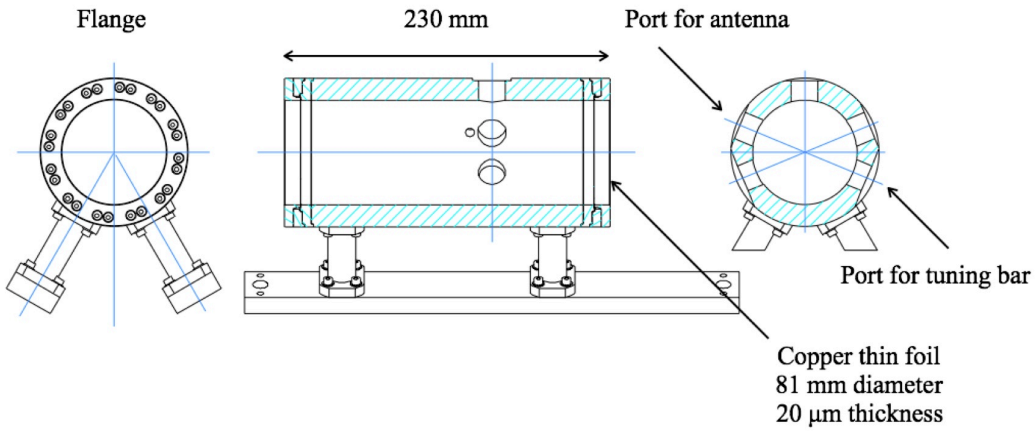

Figure 3-18: Drawing of the microwave cavity: (left) front view; (center) cross-sectional view; (right) cutaway view at the ports. On the front and rear flange, the thin copper foils for particle passing are placed.

The spectrum was fitted to the pseudo-Voigt function [56]

$$y(x) = A[m_\mu \frac{2w}{(x-x_c)^2+w^2} + (1-m_\mu)\frac{\sqrt{4\ln 2}}{\sqrt{\pi}w} e^{-\frac{4\ln 2}{w^2}(x-x_c)^2}] + ax + b \qquad (3.9)$$

where m_μ is the shape parameter, x_c is the resonance frequency, A is the area of the spectrum, w is the width of the resonance line. The coefficients a and b describe a background function which depends on the characteristics of transmission circuit including cables and antenna.

A quality value; an evaluation index for the microwave resonator is defined as

$$Q = \frac{x_c}{w} \qquad (3.10)$$

and obtained from fitting parameters in Eq. 3.9. In Fig. 3-22 case, the quality value was estimated to be 11794 ± 62. The uncertainty is dominated by fitting uncertainty of the resonance width.

Characteristics of the microwave cavity depends on signal frequency. Therefore, to compare the muonium transition probabilities in different microwave frequencies, it is necessary to correct the frequency dependence of microwave magnetic field strength. This systematic effect is corrected by a factor of $Q(1-S_{11})$ relatively. The details

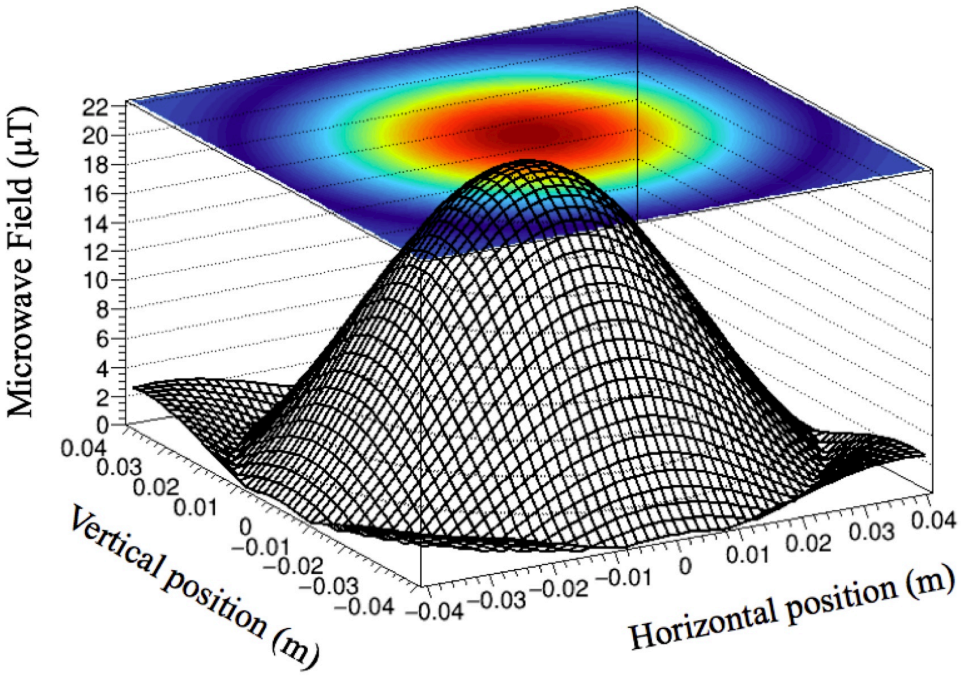

Figure 3-19: Calculated microwave field of TM_{110} mode. The microwave power of 3 W and the cavity quality value of 10,000 were assumed.

of microwave dependent systematics and data corrections are discussed in Chapter 9. Figure 3-23 shows the measured cavity quality value as a function of the resonance frequency.

Figure 3-24 shows measured microwave transmission efficiency which is defined as $1 - S_{11}$ at the input signal frequency center.

Figure 3-25 shows a result of frequency tuning by using the piezo positioner. A red solid line indicates an expected frequency of the muonium HFS transition. Dashed lines indicate target scanning region of microwave frequency. The tunability of the resonator is sufficient to scan the microwave frequency from one end to the other of the resonance lineshape.

3.9.2 Demagnetization of the microwave cavity

During apparatus installation, magnetization of every components in the magnetic shield was surveyed by the magnetometer. Major magnetized components were the screws for flanges and the microwave cavity including the support structure. Magne-

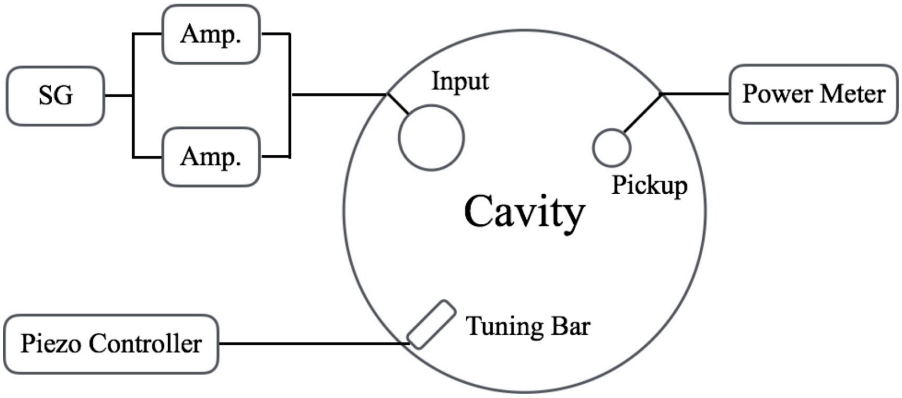

Figure 3-20: Diagram of the microwave system. The microwave is generated by the signal generator which is denoted as SG. The signal is amplified by the parallelized amplifiers and applied to the cavity via the magnetic loop antenna. The resonance condition of the cavity was tuned by the piezo positioner. The stored microwave energy was monitored by the small pickup antenna and the thermal power sensor.

tized screws were replaced and the cavity was demagnetized by an attenuating AC current. Figure 3-26 illustrates the principle of AC demagnetization. A coil generates magnetic field to magnetize an object. When an alternative current reduces gradually, magnetization of the object approaches to zero.

A sequence of demagnetization was as follows; the amplitude of AC current was increased to 10 A and decreased to 0 A in fifteen seconds. After three iterations of magnetization, most of local magnetized parts were disappeared. Figure 3-27 shows a comparison of magnetization survey result before and after demagnetization. Magnetization was measured along the outer surface of the cavity by a fluxgate magnetometer.

3.10 Data acquisition system

A data acquisition (DAQ) trigger is generated from a proton beam kicking pulse at a rate of 25 Hz. The trigger is a coincident logic signal which is bitwise AND of RCS kicker synchronized pulse, MLF beam monitor output, and DAQ state signal. RCS kicker signal indicates a beam pulse injection from RCS to 3NBT; the tunnel connecting to MLF. MLF beam monitor measures a proton beam current and it

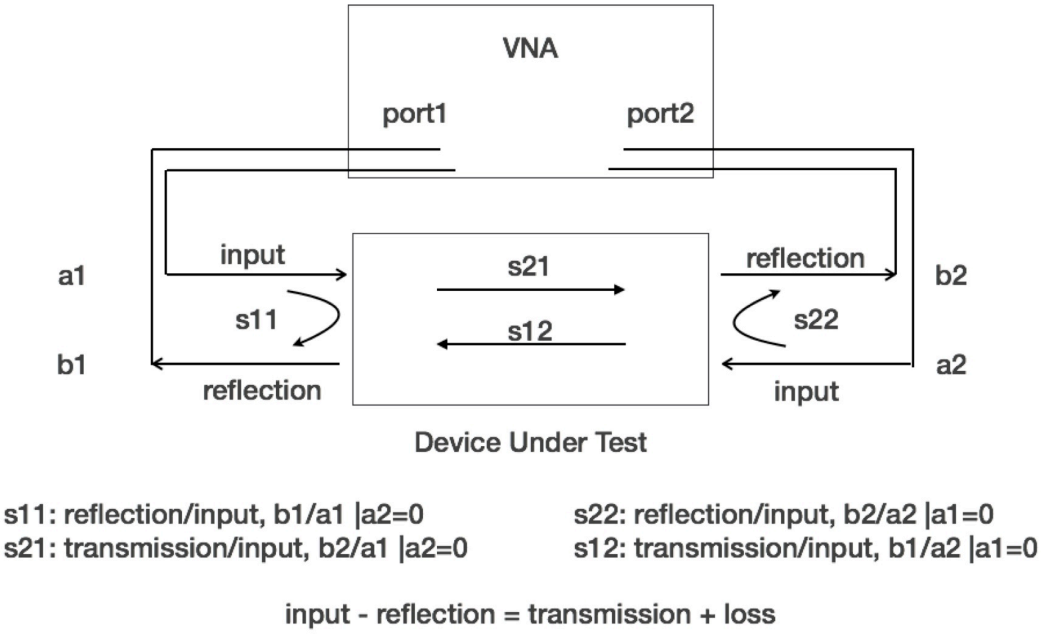

Figure 3-21: Schematic of frequency characteristics measurement by using a vector network analyzer. The phase and the amplitude of reflected wave and transmitted wave were measured.

provides a signal indicates beam arrival. The data taking trigger is distributed to each readout electronics as a common start of a time-to-digital converter (TDC). DAQ state signal indicates the readiness of each FPGA on the readout electronics. To avoid event number mismatch between data acquisition electronics, DAQ readiness signal is required for the trigger signal distribution.

To divide and supply a trigger pulse for each data acquisition electronics, a trigger distributor was developed. Figure 3-29 shows a drawing of the trigger distributor. Timing jitter of the trigger signal was evaluated to be less than 2 ns.

For collecting measurement data, a C++ applications software was developed. Online monitors were implemented on the DAQ framework to confirm the soundness of the detector in operation. Outputs from the magnetometer, the gas pressure gauges, and the microwave power meter were recorded by an application based on Labview by National Instruments [57].

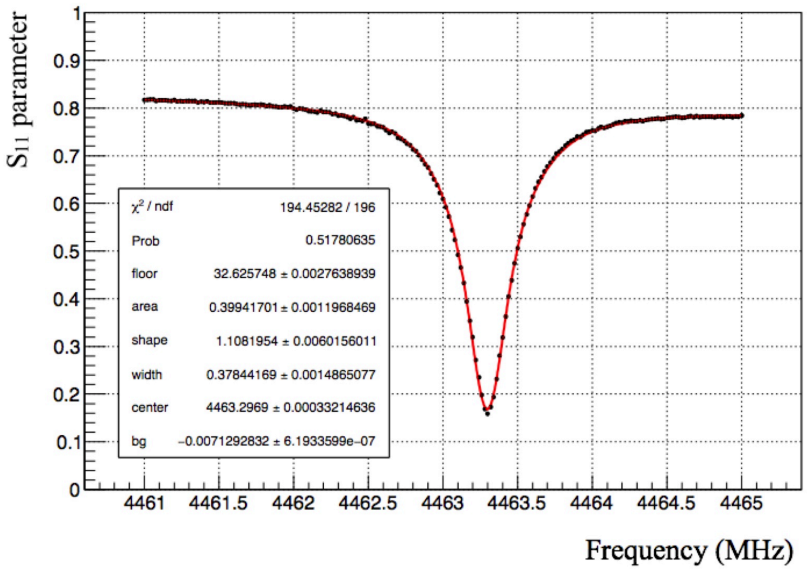

Figure 3-22: Microwave resonance at 4463.3 MHz of the microwave frequency. Fitting was performed by the pseudo-Voigt function to evaluate the cavity quality value. Red line represents the fitting result.

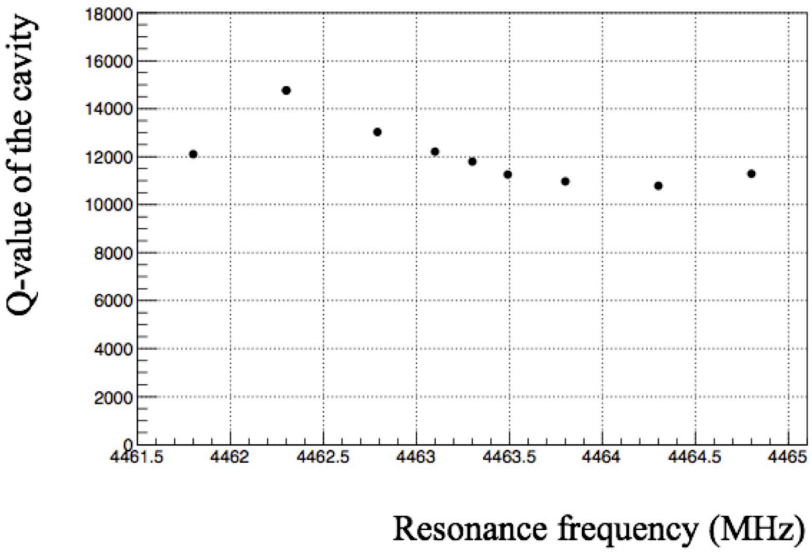

Figure 3-23: Frequency dependence of the cavity quality value. The quality value was defined as $Q = x_c/w$ where x_c is the resonance frequency and w is the resonance linewidth.

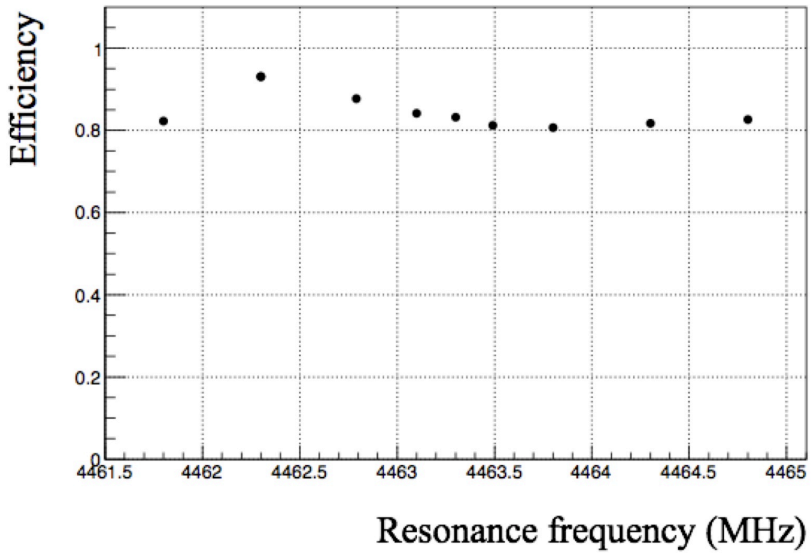

Figure 3-24: Frequency dependence of the maximum microwave transmission at signal frequency. The transmission efficiency of the microwave was defined as $1 - S_{11}$ at the resonance.

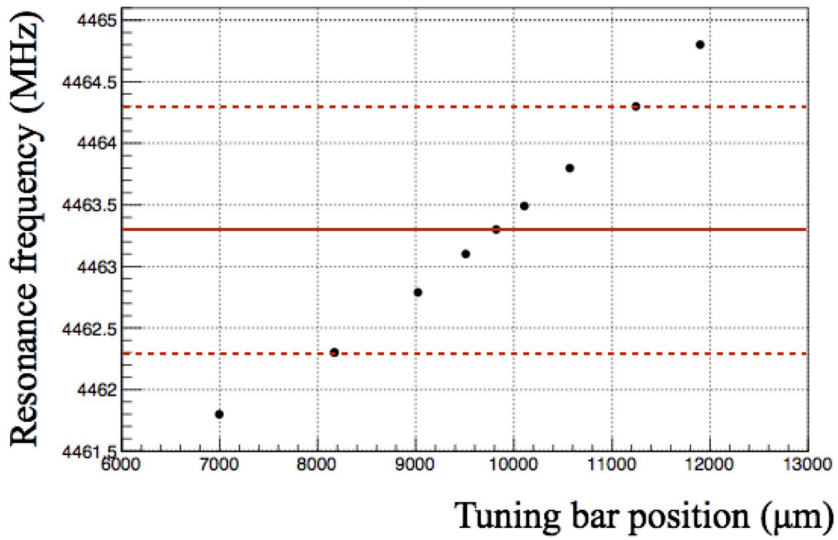

Figure 3-25: Frequency tuning range of the microwave cavity. Red solid line indicates the expected muonium HFS frequency. Two dashed red lines correspond to $\pm$ 1 MHz detuning from the HFS frequency.

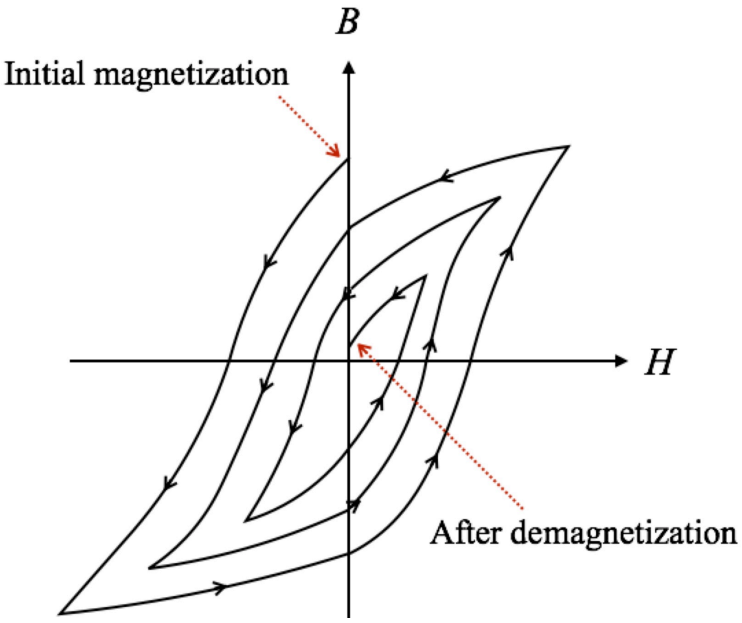

Figure 3-26: Principle of demagnetization. An attenuating current makes the magnetization of the object smaller. The residual magnetism after demagnetization depends on the resolution of current attenuation and coercive force of the material.

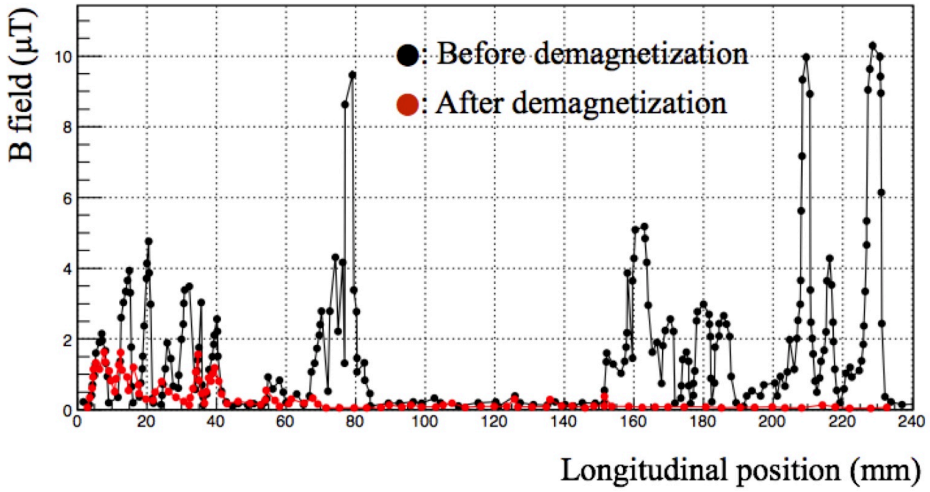

Figure 3-27: Demagnetization of the microwave cavity. Black and red circles represent the cavity magnetization before and after the demagnetization process, respectively.

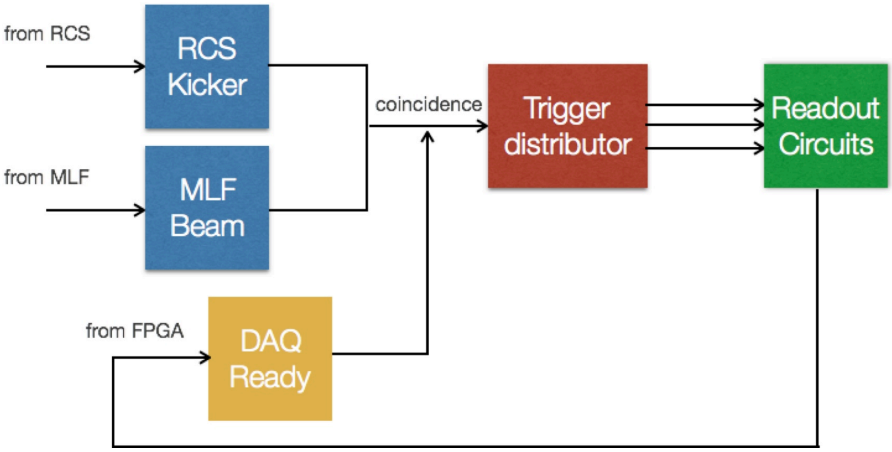

Figure 3-28: Diagram of the data acquisition system. Two-types of the accelerator synchronized pulses at a rate of 25 Hz were utilized to generate the data taking trigger. The signal from the readout electronics indicating the FPGA readiness was added to the trigger logic.

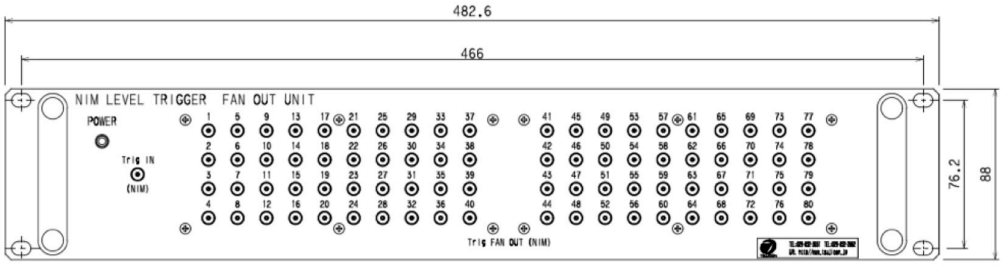

Figure 3-29: Drawing of the trigger distributor. It contains 80 parallel signal lines with equal-length wiring.

Chapter 4

Simulation Study

This chapter describes simulation study for the experiment. The first half of the chapter corresponds to a study for background estimation and apparatus designing. The second half is for the estimation of signal intensity and systematic uncertainties.

4.1 Muon transportation

Muons are produced from a parity violating decay of pions. At MUSE facility of J-PARC, a high-intensity pulsed proton beam is irradiated to a graphite-disk target for muon production. In order to understand the muon beam profile at the experimental area and to predict the beam related backgrounds, muon production on the target and transportation through the beamline were simulated.

4.1.1 Beam profile

Simulation software was developed based on a particle tracking simulator G4beamline [58]. The muon production target and beamline components for particle transportation were implemented with realistic models and parameters. Figure 4-1 shows simulated geometry of the beamline.

Figure 4-2 shows simulated muon beam profile at the focus of the beamline. Beam optics was optimized for transportation of muons with the initial momentum of 29.8

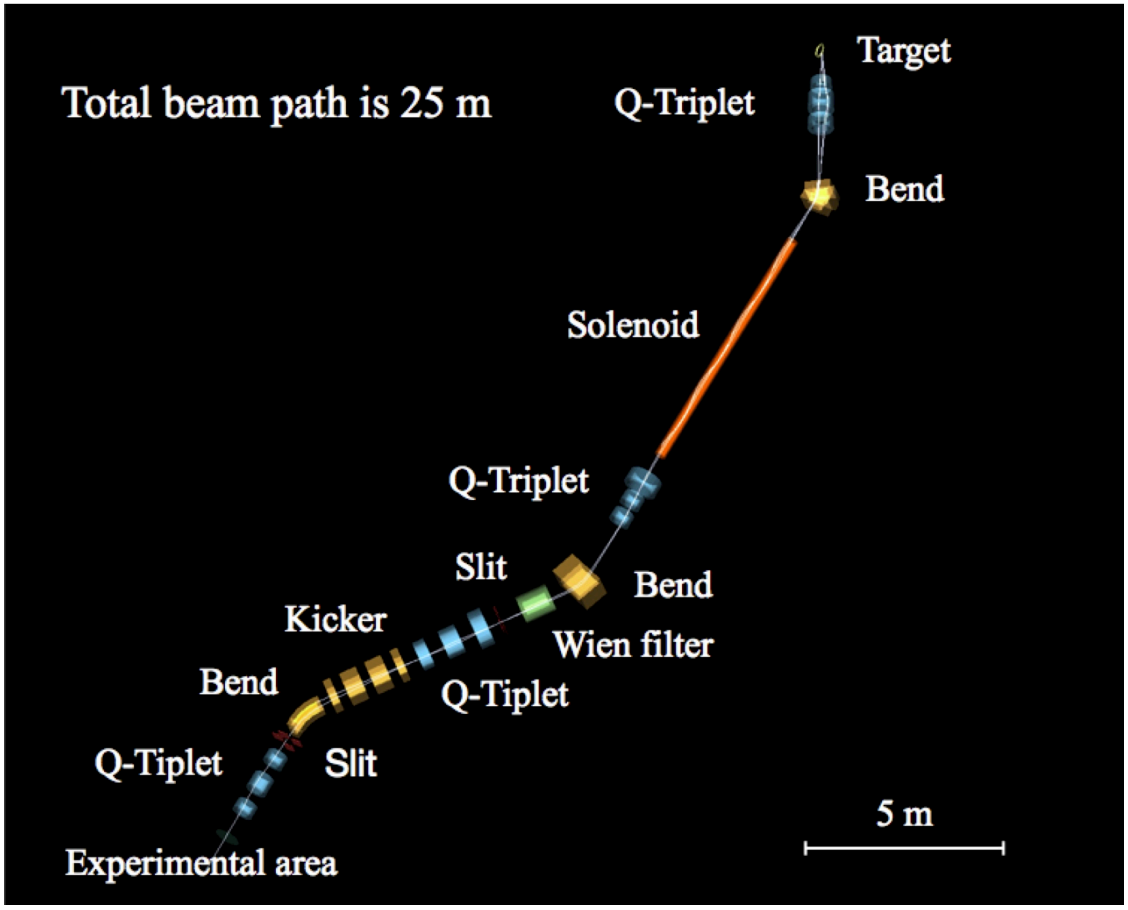

Figure 4-1: Simulated beamline geometry. The production target, the superconducting solenoid, the bending and focusing magnets, and the Wien filter were implemented. The pulse kicker magnet is a beam distributing apparatus for simultaneous operation of D1 and D2 beamline and not used in this simulation.

MeV/c which gives the maximum yield of spin polarized muon from the surface of the production target. According to the result, transportation efficiency of the beamline was estimated to be 1.7%.

Simulated beam profile was compared with measurement result obtained by an imaging plate as shown in Fig. 4-3. The imaging plate contains a phosphor and reacts with charged particles. In the measurement, an imaging plate was placed 60 mm away from the beam duct edge and irradiated with the muon beam for ten seconds. The left figure presents a vertical projection while the right figure presents a horizontal one. Note that the measurement and simulated position was 40 cm upstream from the beamline focus to avoid beam loss in the air. The simulated beam profile involves

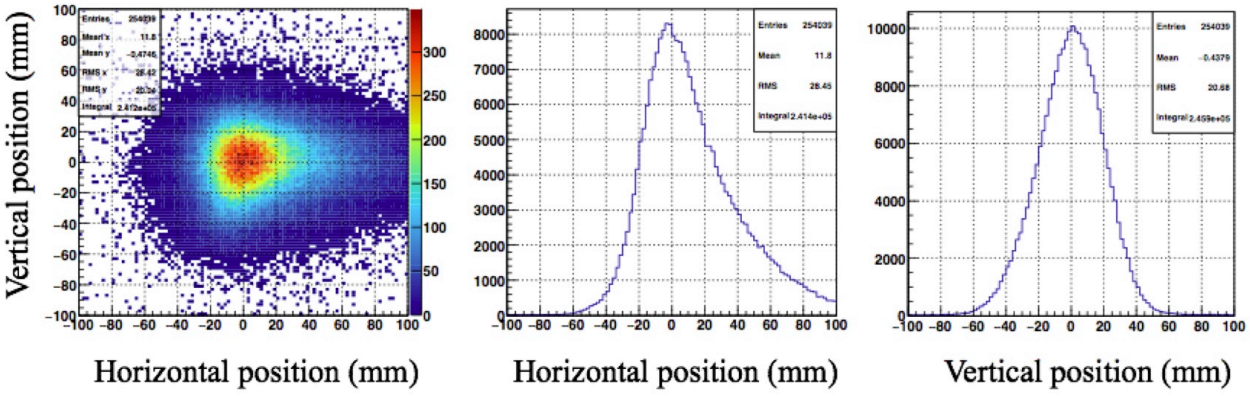

Figure 4-2: Simulated muon beam profile at the focusing point: (left) two-dimensional profile; (center) horizontal projection; (right) vertical projection.

major features of measurement result.

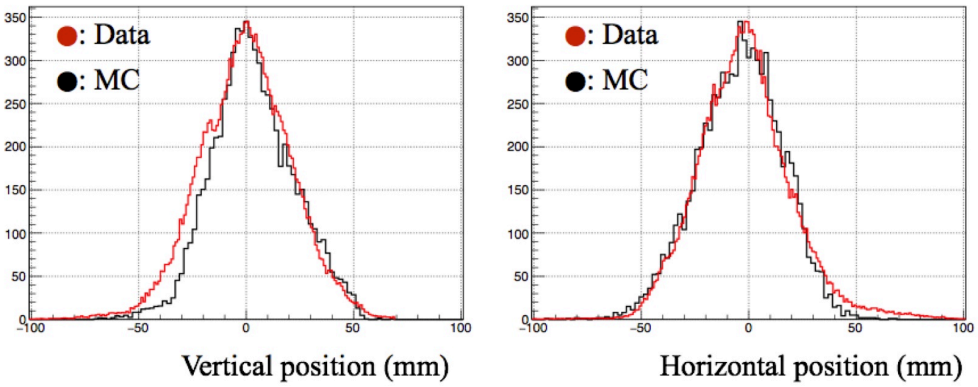

Figure 4-3: Comparison of measured (red) and simulated (black) muon beam profile at the focusing point: (left) vertical projection; (right) horizontal projection.

Figure 4-4 shows simulated phase space of muon beam at the focus. In both figures, an ordinate corresponds to the ratio of momentum vector component in travel direction and in perpendicular direction. The result suggests a slight correlation between spacial position and momentum direction of a particle. The spacial asymmetry and parameter correlations of the beam are caused by the chromatic aberration. To calculate muon stopping distribution in the krypton gas target, simulated beam profile was utilized as input parameters.

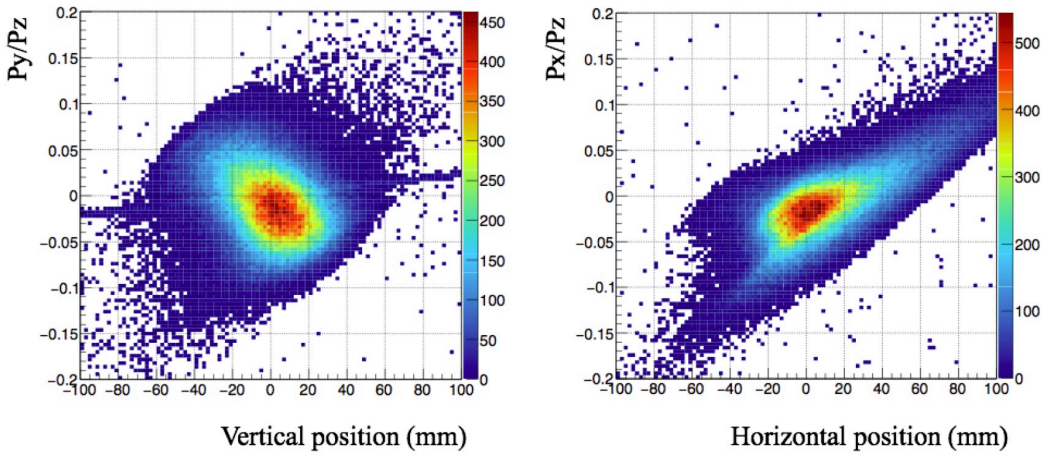

Figure 4-4: Simulated phase space of the muon beam at the focusing point: (left) vertical profile; (right) horizontal profile. Px, Py, and Pz are the components of the momentum vector in the horizontal, vertical, and longitudinal directions, respectively.

4.2 Beam related background

In this section, background sources from beamline are discussed. In the spectroscopy measurement, the prompt and decay positrons produced in the beamline are major sources of background.

4.2.1 Prompt positrons

At the muon production target, a number of positrons are produced concurrently with muons when a proton beam pulse is irradiated. These prompt positrons have similar timing distribution as primary proton beam. They arrive at the experimental area prior to muons in narrow time width of 100 ns FWHM.

Prompt positrons incident to the positron detector and cause an instantaneous large signal resulting in temporary paralyzation of readout electronics and overshoot fake signal. To reduce prompt background, a Wien filter and movable slits were placed in the beamline. Figure 4-5 illustrates the principle of a Wien filter. It provides an orthogonal electric and magnetic fields to separate particles according to their velocity. When a beam passes the Wien filter, particle receives an external force as

$$\boldsymbol{F} = q\boldsymbol{E} + q(\boldsymbol{v} \times \boldsymbol{B}) \tag{4.1}$$

where q is the particle charge, v is the particle velocity, E and B are electric and magnetic fields respectively. When a magnetic field is applied to cancel the displacement of particle due to the electric field, beam travels in the filter straightly. In the case of an interest, a velocity of high-energy positron is almost the speed of light. On the other hand, a muon moves through the beamline at the velocity of 85 m per second corresponding to 28 MeV/c. Therefore, the optimization of the electric and magnetic fields for muon passing leads to positron elimination. To avoid focusing of positron after separation, the movable slits are placed between the filter and the focusing magnet.

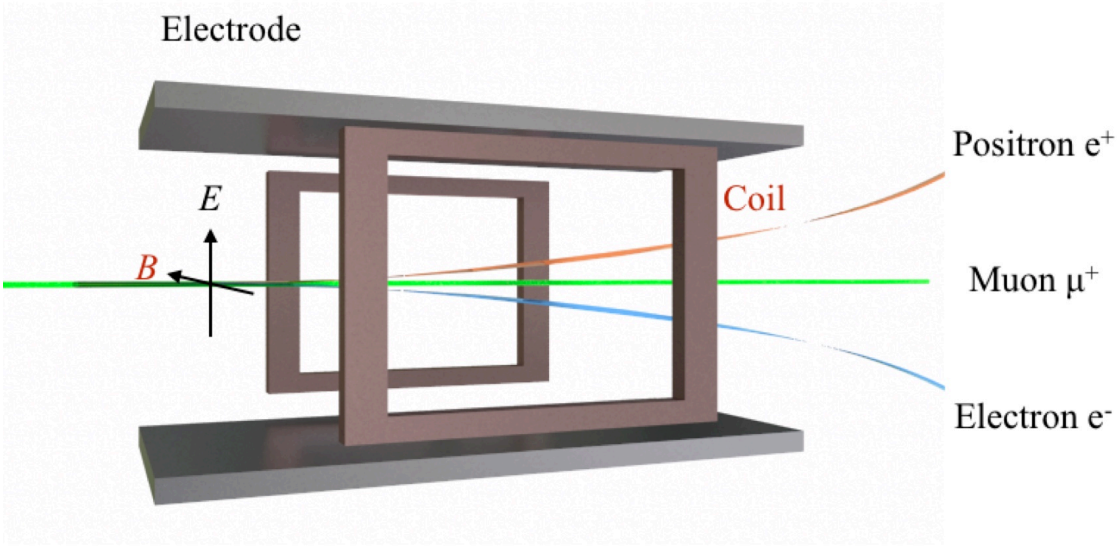

Figure 4-5: Principle of a Wien filter. Intersecting electric and magnetic fields separate the beam particle depending on its velocity.

To realize higher positron reduction efficiency, an applied high voltage should be higher as long as the electrode operates stably. Figure 4-6 shows simulated positron suppression and muon transmission as a function of magnetic field. The vertical axis corresponds to the number of particle reached to the experimental area. Particles were generated at the position of muon production target with the momentum of 29.8 MeV/c. Note that normalizations for muon and positron were arbitrary. Therefore, the result provides relative evaluation based on a strength of magnetic field. High voltage was set to 0.8 MV/m which is the highest avoiding discharge. A Wien

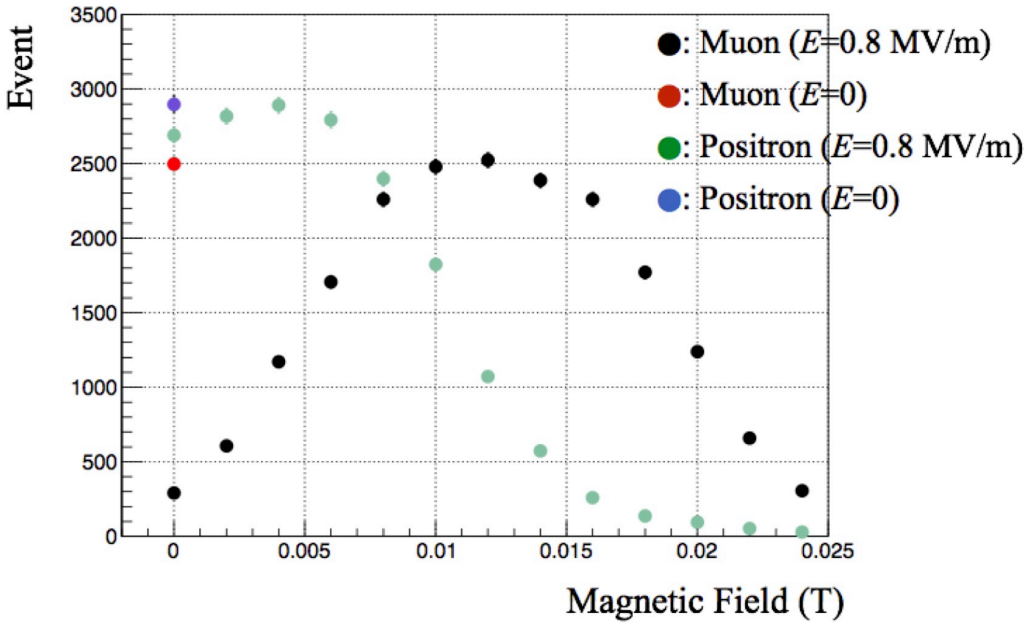

Figure 4-6: Simulated positron and muon separation by the Wien filter. An optimum of a magnetic field was determined to be 12 mT with an electric field of 0.8 MV/m.

filter acts as a spin rotator and causes muon spin depolarization. An optimum of a magnetic field was 12 mT and estimated angle of muon spin inclination was 3 degree on average. This systematic effect does not affects muonium spectroscopy because initial spin polarization contributes only as an arbitrary scaling parameter in the necessary asymmetry measurement.

4.2.2 Duct streaming positrons

During the beam transportation, the muon beam loss causes the decay positron production in the beamline. These duct streaming positrons have the similar timing distribution as signal positrons from muonium decay. Therefore, they are one of the major sources of the beam related background.

Figure 4-7 shows simulated muon beam loss in the beamline. According to the result, more than 80% of beam loss occurs before the last bending magnet which determines momentum acceptance of the beamline. Then, only positrons which have particular momenta are expected to be transported to the experimental area.

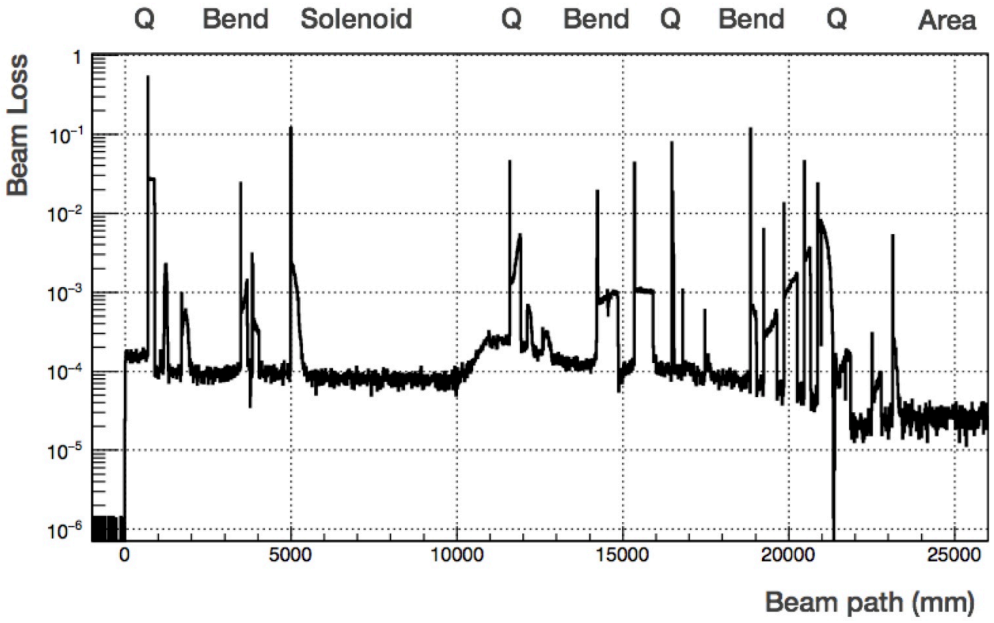

Figure 4-7: Simulated muon beam loss along the beam trajectory central. A zero point corresponds to the position of the muon production target.

Figure 4-8 shows simulated momentum distribution of the duct streaming positrons. Initial momentum distribution was generated uniformly from zero to 52 MeV/c, the highest momentum of positron from muon decay at rest. Red line corresponds to a momentum distribution in the experimental area. A green, blue, and brown lines correspond to momentum distributions at the third, second, and first bending magnet. Only positrons whose kinetic energy is less than 32 MeV/c are able to reach the experimental area. On the other hand, momentum of decay positrons from the gas target follows the Michel spectrum as shown in Fig. 2-11. Therefore, momentum threshold at 32 MeV/c is effective to suppress the duct streaming positron background.

4.3 Muon stopping distribution

In order to estimate the muonium spacial distribution in the krypton gas target, the muon stopping distribution was simulated. A simulator was developed based on GEANT4 [59]. Figure 4-9 shows a simulated geometry and accumulated event display. The muon beam with realistic profile parameters were irradiated to the gas

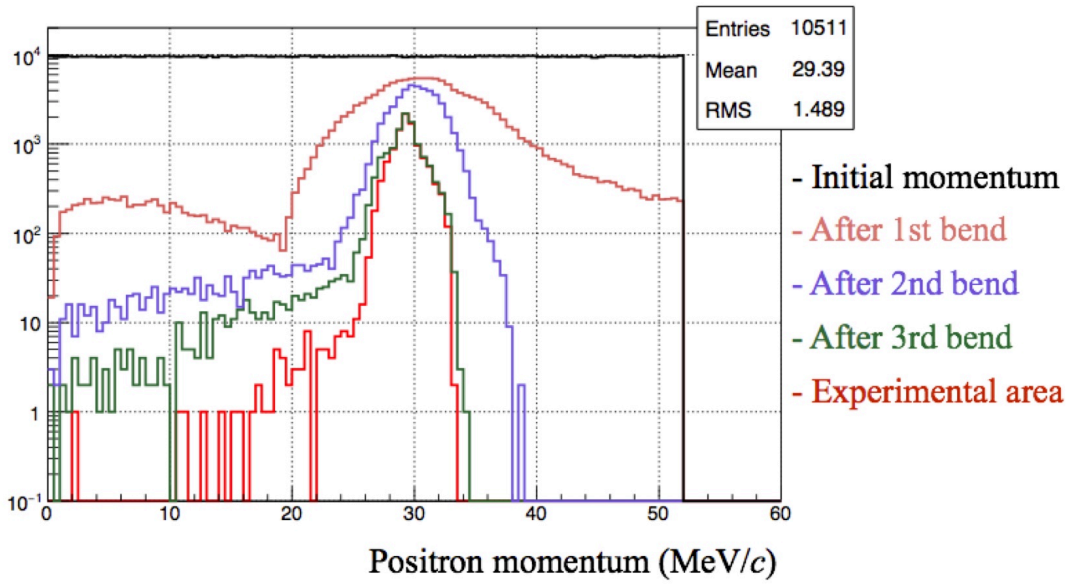

Figure 4-8: Momentum distribution of the duct streaming positron. Initial momentum distributes uniformly between zero and 52 MeV/c. The momentum distribution after each bending magnet is represented in respective color.

target. The pressure of the krypton gas was set to 1.0 atm.

Optimization of the longitudinal length of the microwave cavity

The hyperfine transition frequency of muonium shifts to the lower value due to an atomic collision with krypton. This systematic effect is modeled by a combination of two-body and three-body collisions whose cross-sections depend on the gas pressure. To suppress the systematic uncertainty from this gas pressure dependence, an experiment under lower gas pressure is desirable. A longer gas volume is required to stop muons under low pressure environment. However, a long and narrow microwave cavity acts a particle collimator and causes an disadvantage in the detection solid angle. Therefore, a longitudinal length of the microwave cavity was optimized based on the result of muon stopping simulation. Figure 4-10 shows relative positron statistics as a function of the cavity length. According to the result, the length of the cavity was decided to be 230 mm.

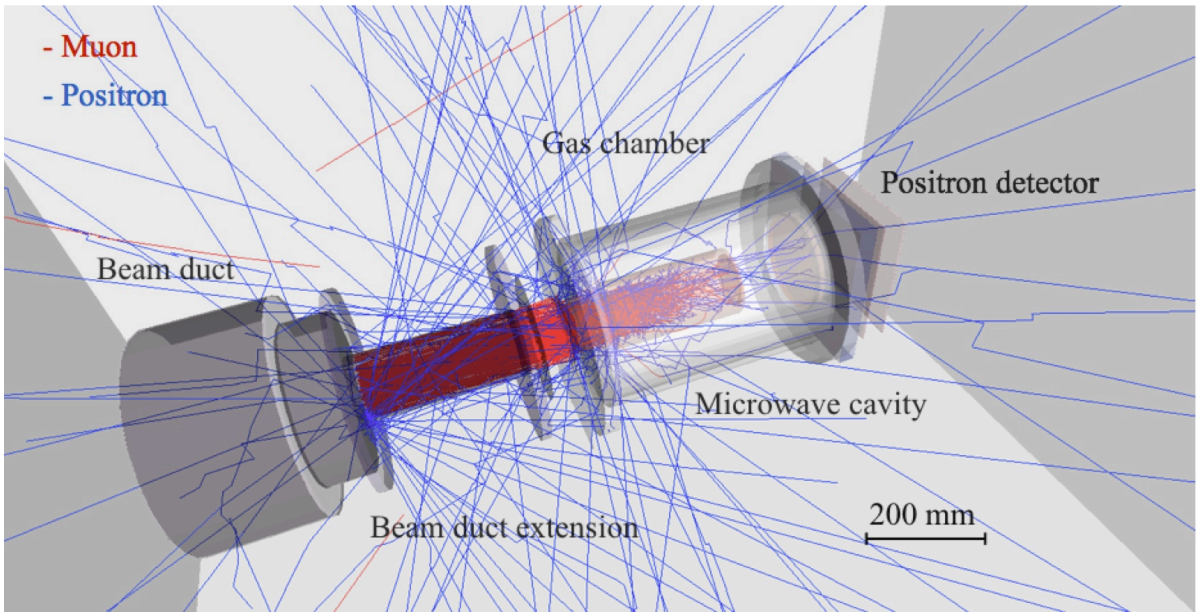

Figure 4-9: The geometry and accumulated event display of the muon stopping simulation. Red and blue lines correspond to the trajectory of the muon and positron, respectively.

Estimation of muonium fraction in the gas volume

Only muons stopped in the gas target form a muonium. Muons stop without electron capture and to be a source of background in the measurement. Figure 4-11 shows a simulated muon stop distribution projected on the beam axis. According to the results, 80% of incident muons stop inside the gas chamber, and 30% stopped inside the microwave cavity. About 1% of total decay positrons were detected by the positron counter.

Figure 4-12 shows a simulated muon stopping distribution projected on the several types of cross-section. The result indicates 46% of detected positrons were from target gas and others are mostly from inner wall of the cavity.

Table 4.1 summarizes the muon stopping distribution. Statistical uncertainty of each value is about 1%.

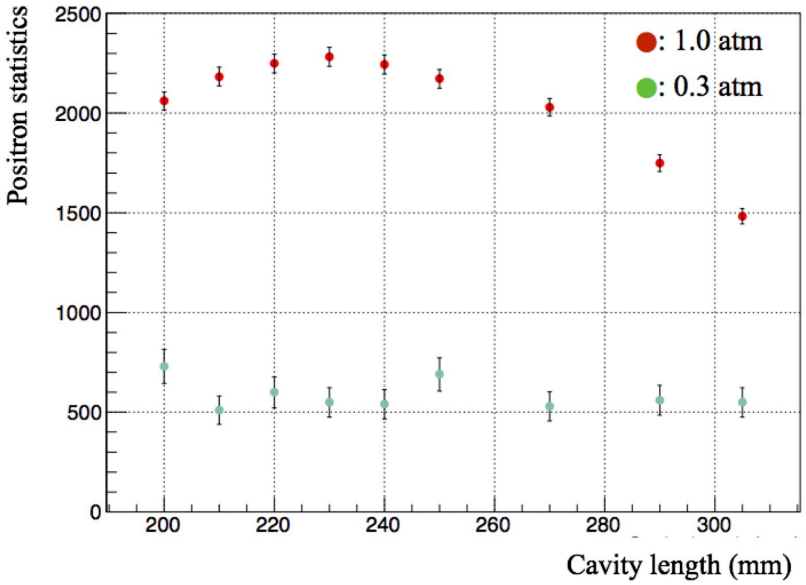

Figure 4-10: Simulated cavity-length dependence of positron statistics. Red and green circles represent the results with 1.0 atm and 0.3 atm Kr gas pressure, respectively.

Table 4.1: Muon stopping fraction whose decay positron was detected. The pressure of the krypton gas was set to 1.0 atm

Stopped object	Percentage	State	Contribution
Krypton gas in the cavity	46.5	Muonium	Signal
Krypton gas outside of the cavity	1.2	Muonium	Background
Cavity wall	47.0	Muon	Background
Cavity flange and others	5.3	Muon	Background

4.4 Muonium spin flip

By using an analytic expression of muonium transition probability, time dependent muonium spin flip was simulated. Muonium spacial distribution and microwave magnetic field were implemented as shown in Fig. 4-13. The microwave power of 3 W and the cavity quality value of 10,000 were assumed. Figure 4-14 shows a histogram of microwave magnetic field which muonium feels. Fitting result was utilized in following calculation of the time dependent spin flip signal. When a muon forms muonium, its kinetic energy is mostly equivalent to temperature of krypton gas. At a room

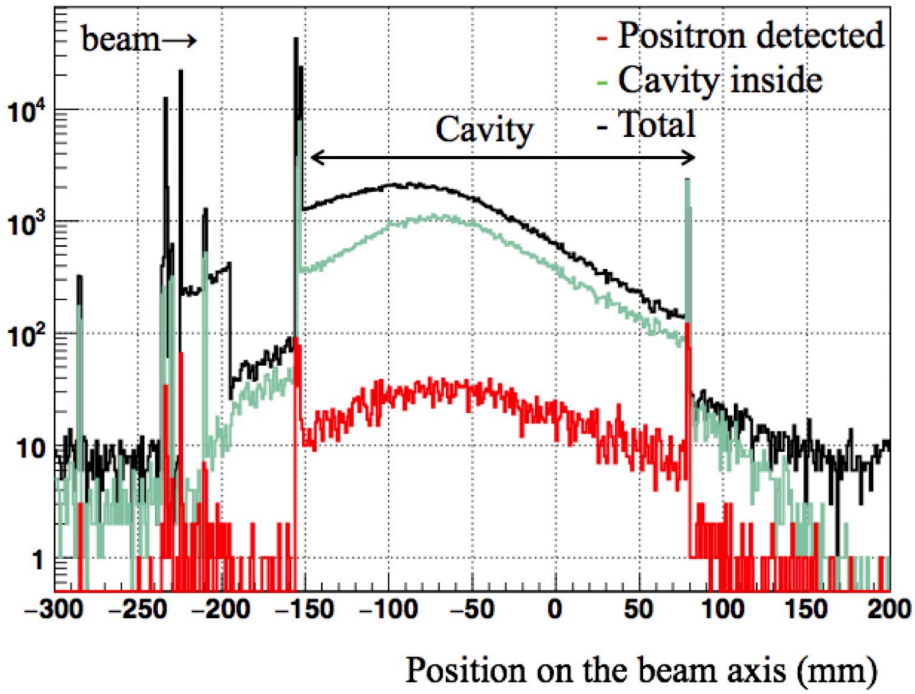

Figure 4-11: Simulated muon stopping distribution projected on the beam axis. The histogram in red line corresponds to the muon stopping distribution only for a case that decay positron was detected by the detectors. The histograms in green and black lines correspond to the muon stopping inside of the cavity, and the total muon stopping, respectively.

temperature of 300 K, thermal velocity of muonium is approximately 7500 m/s. For a case of 1.0 atm gas pressure, a collision between muonium and krypton occurs with the frequency of 10 GHz. A mean free path of muonium is about 65 μm and estimated muonium diffusion was less than 1 mm in a ten-fold of muon mean lifetime. Therefore, changing of the effective microwave power depending on the thermal motion of muonium is negligible.

Time dependent spin flip signal of muonium is calculated from weighted integral of muon spin polarization as follows.

$$S(t) = \int_{b_{\min}}^{b_{\max}} N(b)P(b)db \tag{4.2}$$

where $b_{\min}$ and $b_{\max}$ are the minimum and maximum of microwave power which muonium feels, $N(b)$ is the number density of muonium as a function of the microwave

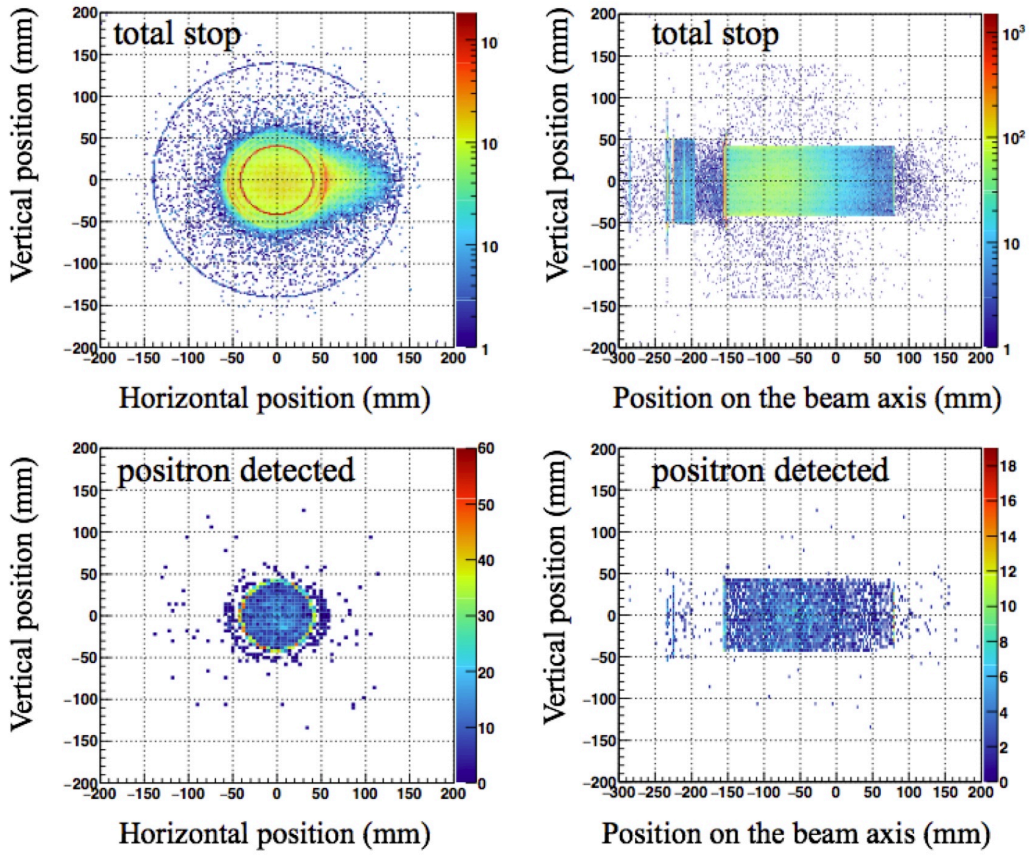

Figure 4-12: Simulated muon stopping distributions projected on the cavity cross sections: (left) projections on the bottom surface; (right) projections on the rectangular surface. The upper figures correspond to total muon stopping. The bottom ones correspond to only muons whose decay positron was detected.

power b, $P(b)$ is a partial contribution corresponds to each microwave power strength. Figure 4-15 represents calculated partial contributions for each strength of the microwave magnetic field.

By taking a summation of each partial contribution, the time dependent spin flip signal is obtained as shown in Fig. 4-16. In the experiment, muon spin relaxation occurs by an inhomogeneity of a static magnetic field and collisions with magnetic gas impurities. When the relaxation time of 15000 ns is assumed, the muonium spin flip signal is calculated as shown in Fig. 4-17. In Chapter 8, data analysis for the time dependent signal utilizing this formulation is discussed.

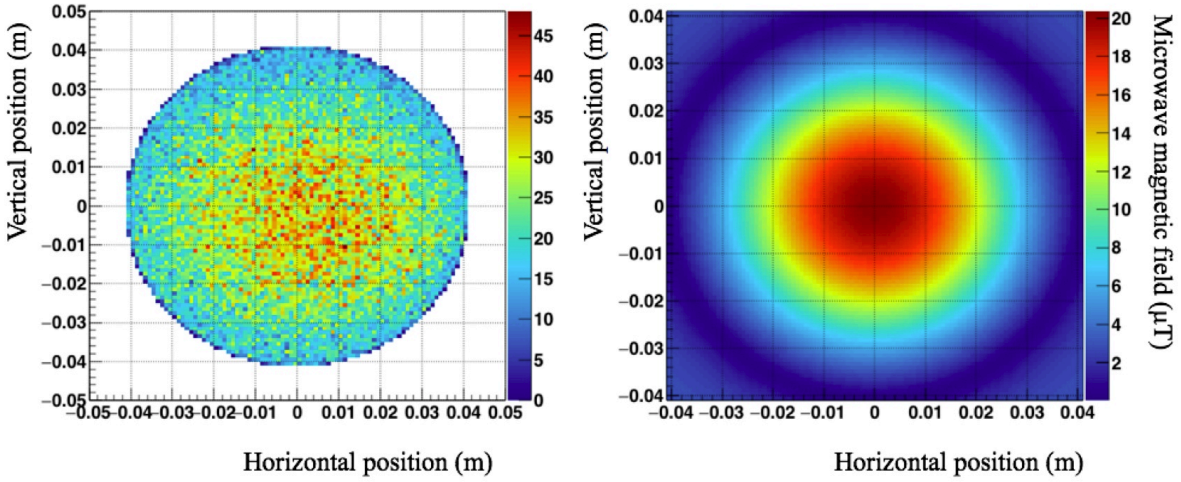

Figure 4-13: Muonium and magnetic field distribution: (left) simulated muonium spacial distribution; (right) calculated microwave magnetic field.

4.5 Muon decay and positron emission

To estimate a counting rate of decay positrons, muon decay and positron emission were simulated. Muon spin polarization and positron angular asymmetry as a function of its kinetic energy were considered. Figure 4-18 shows a correlation between positron emission angle and its kinetic energy.

The trajectory of decay positron was simulated and the position distribution of positron hits on the detector was obtained as shown in Fig. 4-19. Relatively higher event rate was observed at neighboring area of the beam axis because the microwave cavity acts as a collimator.

4.6 Event generator

In order to evaluate a systematic effect related to positron detector response, an event generator for positron detection simulation was developed. An analog circuit response, photon yield, dark noise of photo-sensor were implemented. These parameters were determined based on results of detector specification evaluation which is described in the following chapters. Figure 4-20 shows a typical generated detector signal. Generated events were analyzed in a similar method as the real data. Figure 4-21

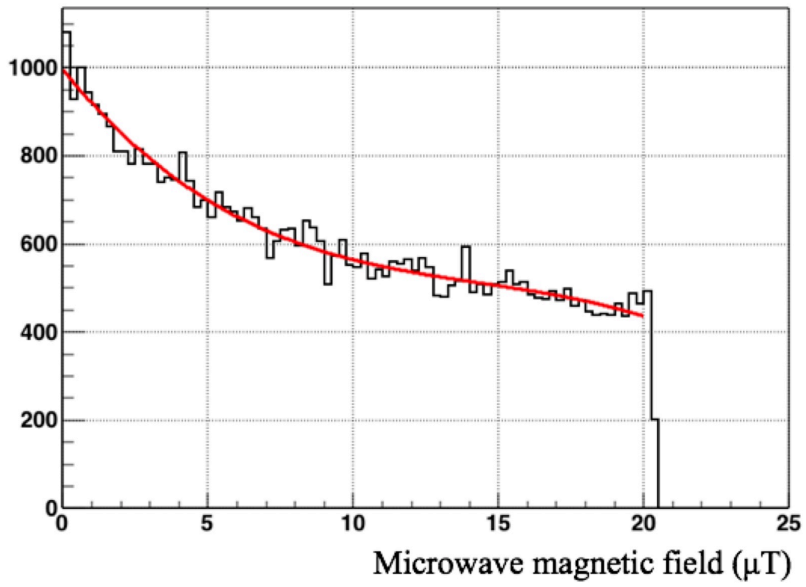

Figure 4-14: Effective microwave field strength obtained by superimposing the spacial distribution of muonium and the microwave field. Red line represents a result of the polynomial fitting.

shows a simulated positron time spectrum. A histogram in black line represents the spectrum without the pileup loss while one in red line represents the ideal time spectrum. The muon beam intensity of 3×10^6 muons per second was assumed. The realistic analog circuit response and characteristics variations of the detector segments were implemented based on the measurement results which are described in Chapter 6. By taking the ratio between the contents of two histograms in Fig. 4-21, the pileup event loss was estimated. Figure 4-22 shows simulated event loss as a function of elapsed time from a muon pulse arrival. The maximum instantaneous event loss was estimated to be 20 %. After 5000 ns elapse from a muon pulse arrival, pileup event loss is deduced down to a negligible level.

4.7 Resonance simulator

To discuss systematic uncertainties in the measurement, a resonance simulator for muonium spectroscopy was developed. It consists of a numerical integrator for positron detection depends on microwave spin flip of muonium. A time-integrated

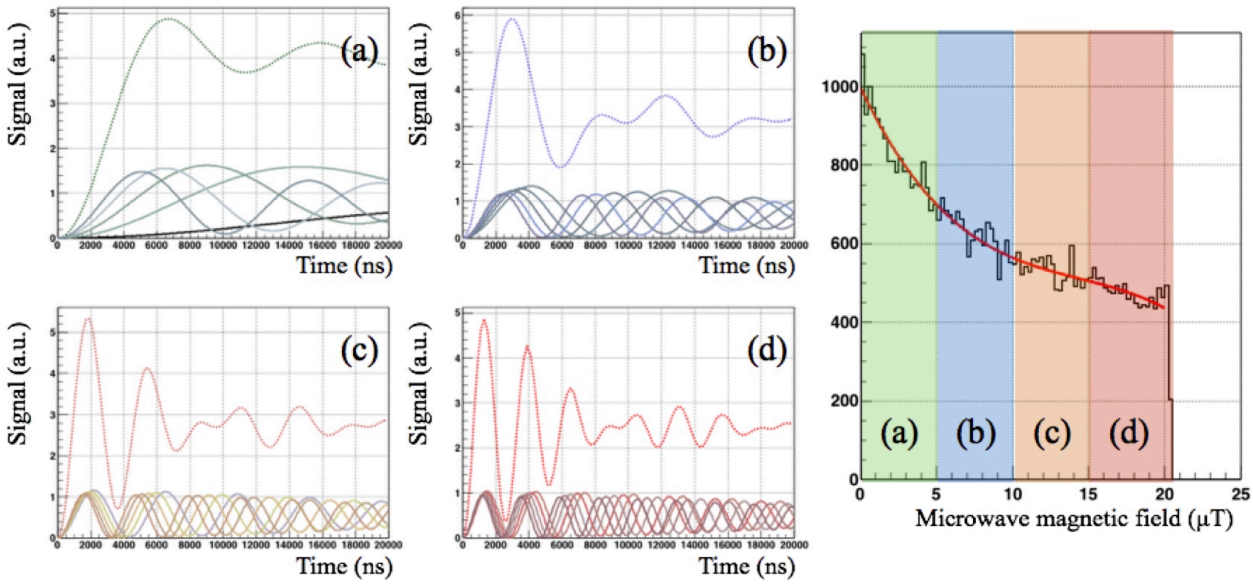

Figure 4-15: Partial contributions for each strength of the microwave field. Solid lines in the left figures correspond to partial contributions divided into four major regions of the microwave field denoted as (a), (b), (c), and (d) in the right figure. Dashed lines indicate summation of the partial contributions in each region.

lineshape was considered based on its analytic expression discussed in Chapter 3. Figure 4-23 shows a simulated resonance lineshape and trends in its frequency center obtained by the iterative simulations. Assumed positron statistics was 3×10^{13}. Obtained frequency detuning of lineshape at the peak was zero-consistent and statistical uncertainty was about 0.2 Hz. This statistical uncertainty is small enough to discuss major systematic uncertainties in the experiment.

4.8 Estimation of systematic uncertainties

In this section, the evaluation of systematic uncertainties are discussed.

4.8.1 Classification of systematic uncertainties

Systematic uncertainties are divided into two major classes. Figure 4-24 summarizes possible systematic uncertainties in the resonance measurement. First category of interest are temporal variations of measurement condition. Both a random fluctuation

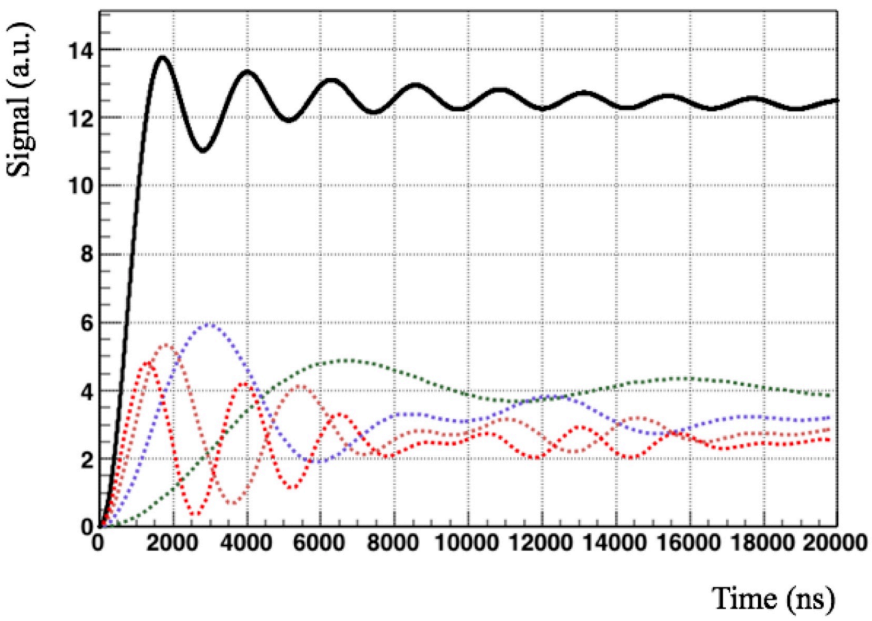

Figure 4-16: Simulated time dependent spin flip signal. Dashed lines correspond to the four partial contributions from each division in the previous figure. The black solid line represents the muonium spin flip signal obtained by summation of each partial contribution.

and a continuous changing during the frequency scan are considered. In most cases, the continuous drift in the measurement sequence causes a systematic shift of the resonance lineshape. This type of effect can be corrected by monitoring of a correspond environmental variable. Gas pressure drift, increase of impurities in the target gas, fluctuation of muon beam intensity, and changing in detection efficiency are highly suppressed by taking the ratio of positron counting with and without microwave resonance. Only the systematic effects related to the microwave power fluctuation are not suppressed by this technique. Other items are static effects arising from the remnant magnetic field, the gas pressure extrapolation to zero, and the event loss due to the detector signal pileup.

4.8.2 Evaluation of time independent systematic uncertainties

The time independent systematic uncertainties are estimated independently and individually.

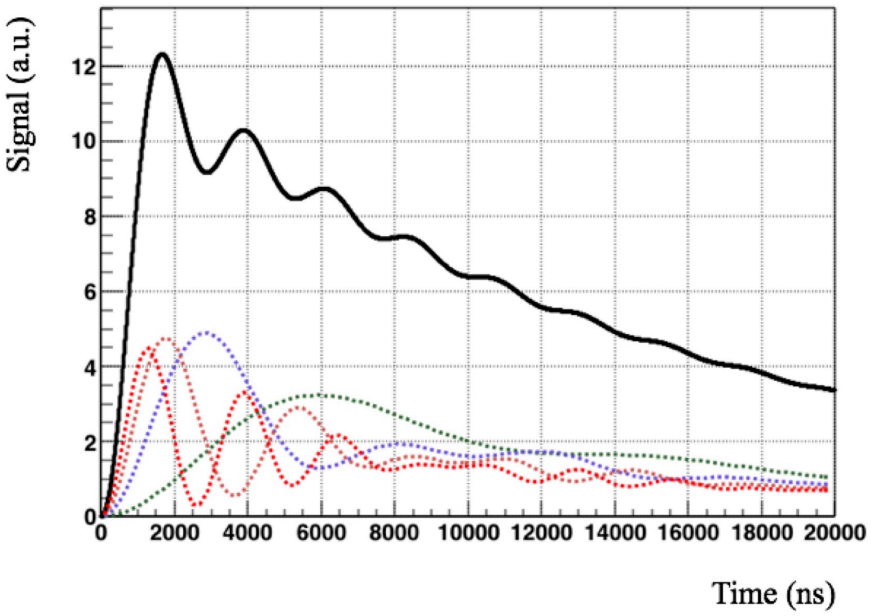

Figure 4-17: Simulated time dependent spin flip signal with spin depolarization. Dashed lines correspond to the four partial contributions from each division which was presented in Fig. 4-15. The black solid line represents the muonium spin flip signal obtained by summation of each partial contributions.

Static magnetic field

In the presence of static magnetic field, each energy level of muonium shifts due to the Zeeman effect. Figure 4-25 shows energy levels of muonium at low magnetic field.

For a case of low magnetic field, the energy levels for only $|1\rangle$ and $|3\rangle$ depend on magnetic field strength as

$$W_1 = \frac{1}{4}\Delta W + (g_J\mu_B^e + g_\mu + \mu_B^\mu)\frac{H}{2} \tag{4.3}$$

$$W_3 = \frac{1}{4}\Delta W - (g_J\mu_B^e + g_\mu + \mu_B^\mu)\frac{H}{2} \tag{4.4}$$

where ΔW is the hyperfine splitting, $g_J(\mu)$ is the gyromagnetic ratio of the electron (muon), $\mu_B^{e(\mu)}$ is the Bohr magneton of the electron (muon), and H is a static magnetic field. According to these equations, shift of each transition frequency was estimated to be 14 Hz per nT in opposite directions. In the experiment, state $|1\rangle$ and $|3\rangle$ are

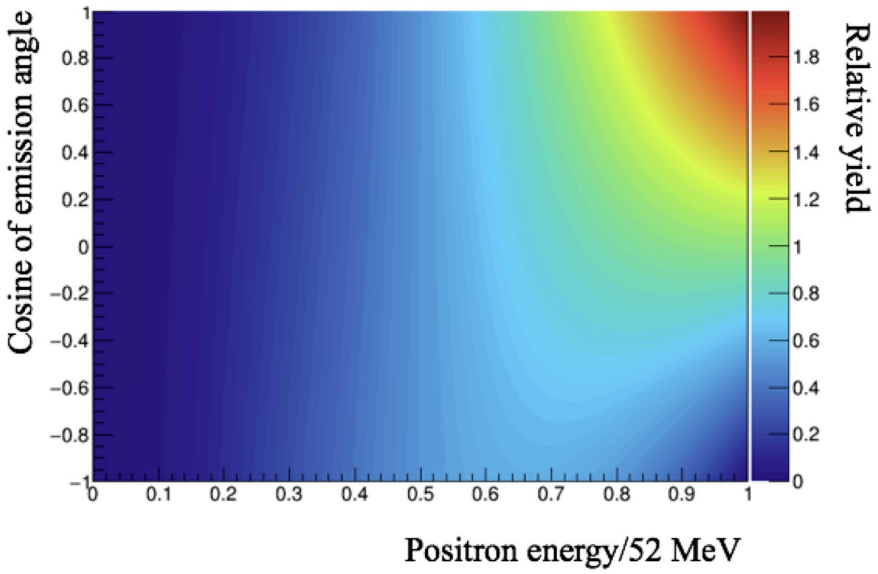

Figure 4-18: Calculated correlation between positron emission angle and kinetic energy. The horizontal axis indicates the positron energy normalized by its maximum energy of 52 MeV. The vertical axis indicates cosine of positron emission angle to the muon spin direction.

degenerated. Then, this systematic effect was evaluated as a summation of two shifted resonance lineshapes by using the resonance simulator. When an uniform magnetic field of 200 nT was assumed, the systematic uncertainty from the static magnetic field was estimated to be negligible.

Gas pressure extrapolation

An atomic collision between muonium and krypton results a shift of transition frequency. This systematic effect can be evaluated as

$$\Delta\nu(p) = (1 + ap + bp^2)\Delta\nu(p = 0) \tag{4.5}$$

where p is the gas pressure, a corresponds to a contribution from two-body collision, and b is a contribution from three-body collision. According to the result of precursor

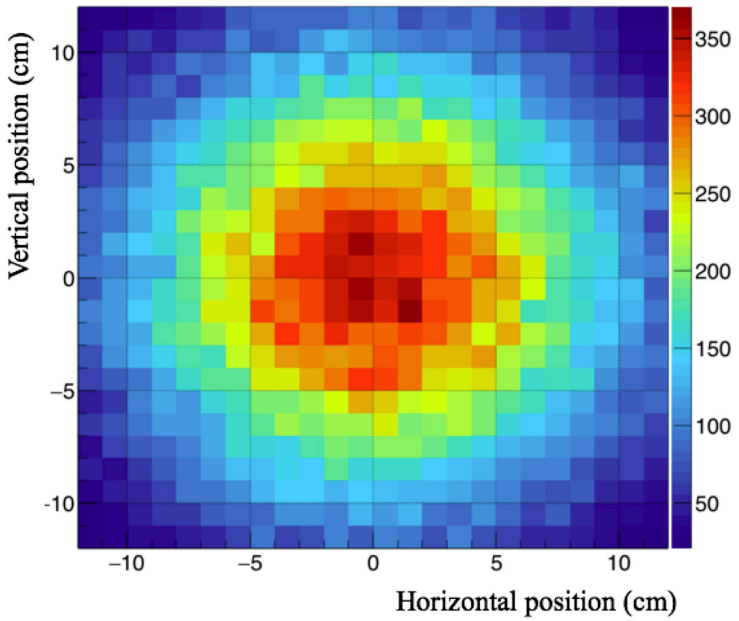

Figure 4-19: Simulated positron hit distribution on the positron detector plane.

experiment, these coefficients were determined as follows [46].

$$a = 7.996(8) \times 10^{-6}/\text{bar} \tag{4.6}$$

$$b = 5.5(1.1) \times 10^{-9}/\text{bar}^2 \tag{4.7}$$

For a gas pressure of 1 atm case, the shift of the resonance frequency is to be 33 kHz. A correction error comes from an uncertainty of the pressure gauge. In the measurement, a capacitance gauge with the precision of 0.2 % was utilized. Therefore, the systematic uncertainty from gas pressure shift was estimated to be 66 Hz.

Detector pileup

Event loss due to the signal pileup depends on positron counting rate. At the leading order, this systematic effect is canceled by taking the ratio of N_{on} and N_{off}. A higher order contribution was estimated by using the event generator and the resonance simulator. For a beam intensity of 3×10^6 case, without pileup correction, the systematic uncertainty from the detector pileup was estimated to be 2 Hz. The details of the estimation are described in Chapter 8.

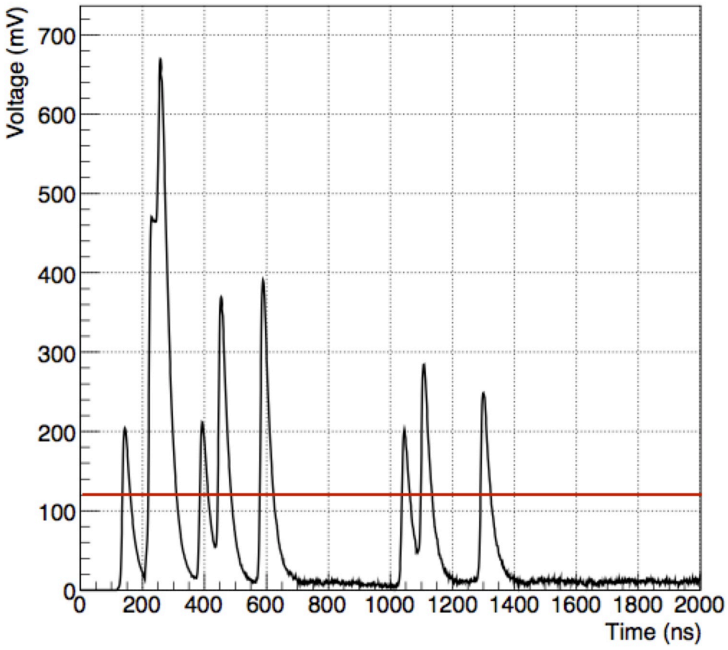

Figure 4-20: Simulated analog signal of the positron detector. Red line indicates the discriminator threshold of 120 mV which corresponds to 3.5 photons equivalent level.

4.8.3 Numerical evaluation of time dependent systematic uncertainties

By iterating the resonance calculation with additional systematic fluctuation of measurement environment, systematic uncertainties in the measurement was evaluated. As the major sources of uncertainty, temporal variations of the microwave power, gas pressure, gas purity, muon beam intensity, and muon beam profile were considered. In terms of the resonance frequency determination, a continuous increase or decrease of the environmental variable causes the most significant systematic effect because it gives an asymmetric resonance lineshape. Randomization of the frequency scan order in the measurement sequence is highly effective to suppress this type of systematic uncertainties.

Figure 4-26 shows examples of iterative calculation of resonance shift caused by the microwave power changing. The left column corresponds to a result with the linear drift of 0.1% during the frequency scan in ascending order. The center column

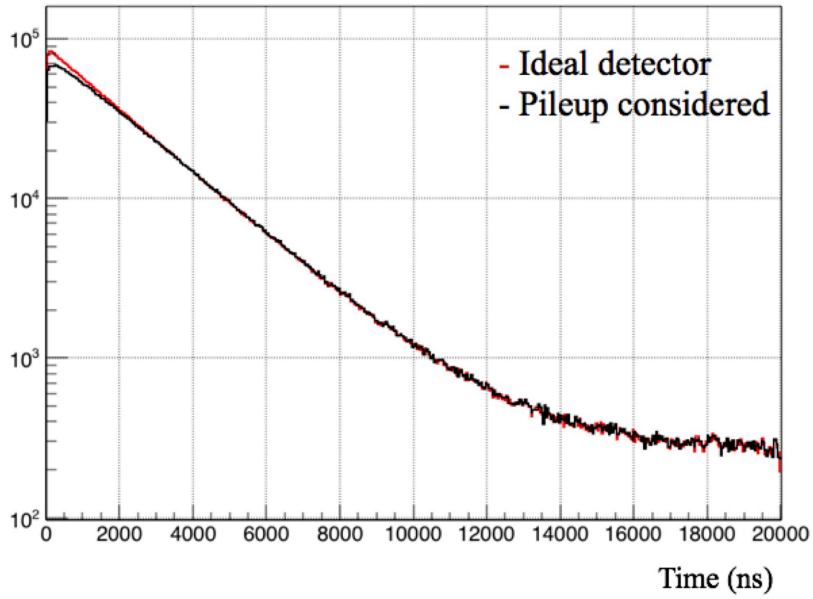

Figure 4-21: Simulated time spectrum of decay positron detection. The histograms in red and black lines indicate the ideal time spectrum and the spectrum with pileup consideration, respectively. The muon beam intensity was set to 3×10^6 muons per second.

corresponds to a result with the linear drift during the frequency scan in randomized order. The right column corresponds to a result with the random fluctuation of 0.1% during the frequency scan in random order. For a case of the linear drift in ascending order, a systematic shift of the frequency center was observed. Contrariwise, only a broadening of the frequency center distribution was observed with the order-randomized frequency scan. For a realistic estimation of the systematic uncertainties, the actual condition of the experiment is to be considered. The details of the evaluation of systematic uncertainties are discussed in Chapter 8.

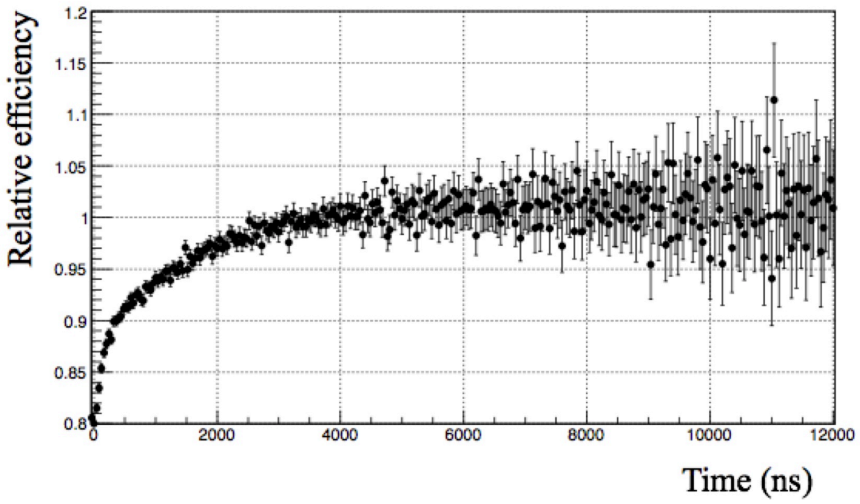

Figure 4-22: Simulated pileup loss as a function of the elapsed time from a muon pulse arrival.

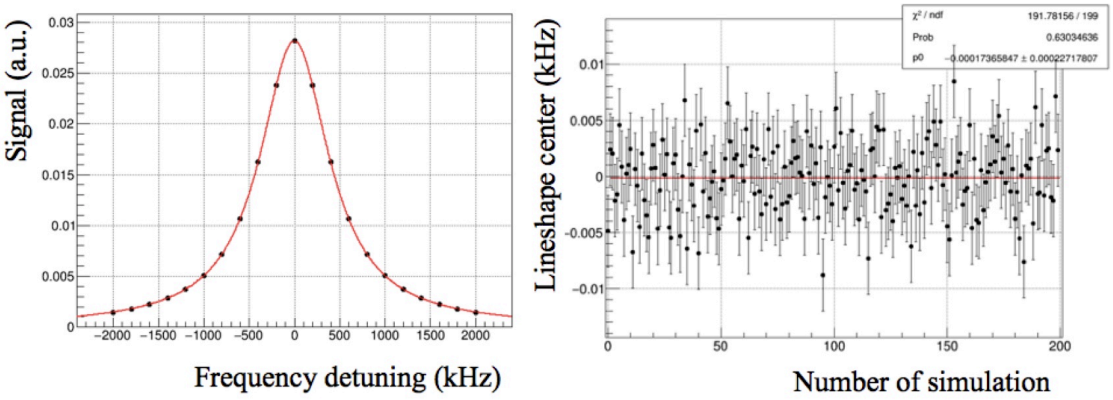

Figure 4-23: Simulated resonance lineshape and iterative virtual experiments. The left figure represents a simulated resonance lineshape with Lorenzian fitting in red solid line. The right one represents the resonance frequency obtained by each virtual experiment. Red line corresponds to the fitting result with a constant function.

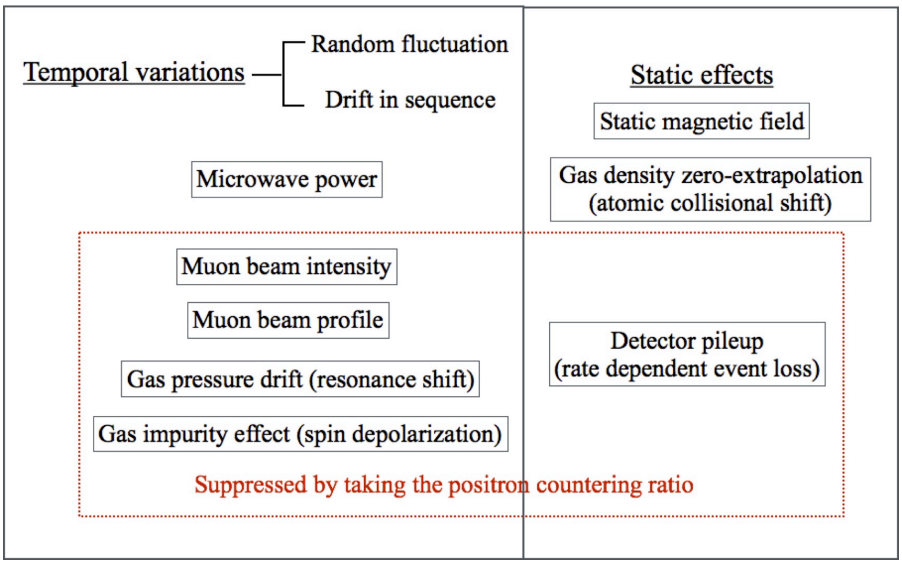

Figure 4-24: Classification of the systematic uncertainties. The systematic uncertainties are classified into the temporal variations of measurement environment (left) and the static effects (right). The uncertainties enclosed by a red frame are highly suppressed due to the microwave switching technique.

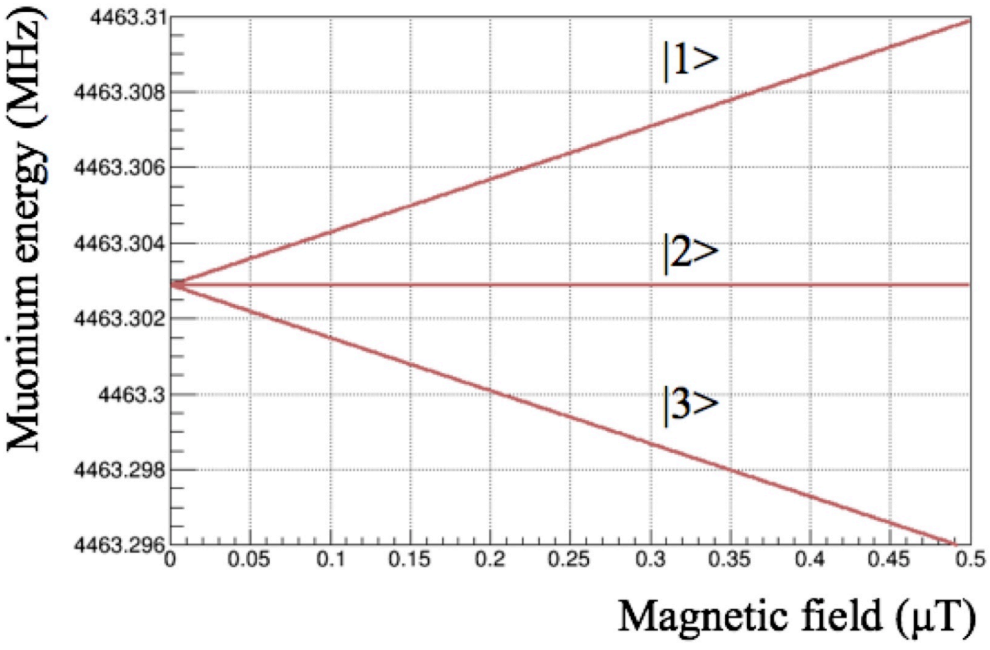

Figure 4-25: Energy levels of muonium at low magnetic field [45]. In a low magnetic field region, the field dependence of the energy levels can be linearly approximated.

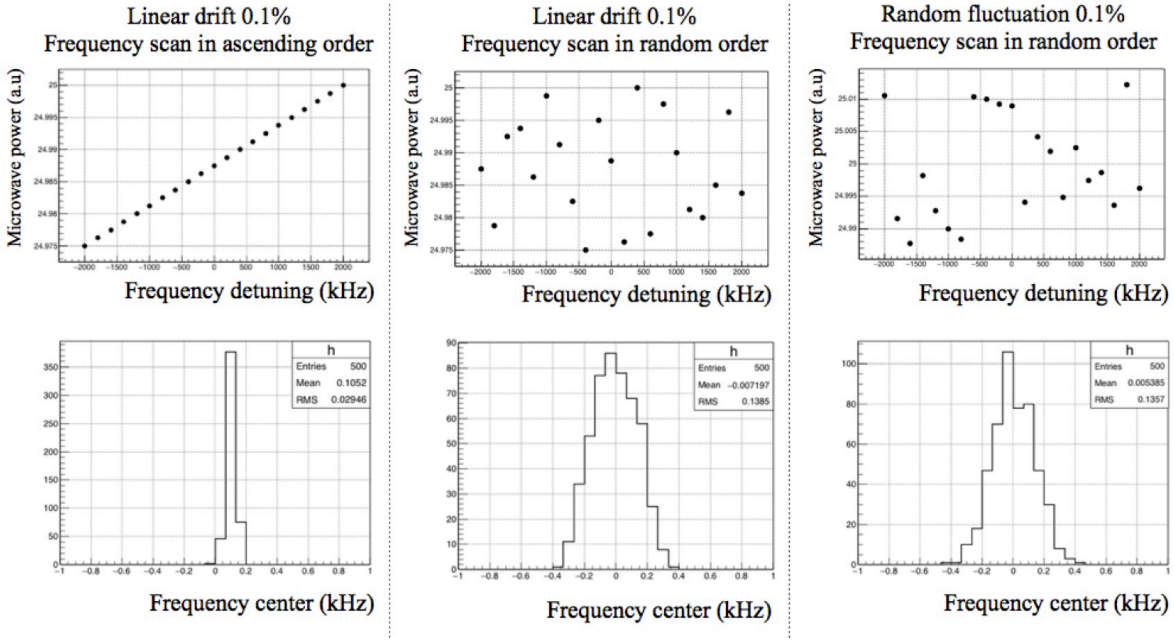

Figure 4-26: Simulated resonance shift caused by the microwave power drift: (left) linear power drift of 0.1% and frequency scan in ascending order; (center) linear power drift of 0.1 % and frequency scan in random order; (right) random power drift of 0.1 %. The upper figures indicate examples of power fluctuation during virtual experiment as a function of microwave frequency detuning. The lower figures indicate distribution of the center of resonance lineshapes.

Chapter 5

Muon detection system

This chapter describes the details of muon detectors. One is a two-dimensional hodoscope for online beam monitoring, the other is a three-dimensional muon beam imager for muon stopping distribution measurement.

5.1 Two-dimensional muon beam profile monitor

To obtain an intensity and profile of incident muon beam, a two-dimensional fiber hodoscope was developed. The detector is placed between an exit of beam duct and an entrance of the gas chamber.

5.1.1 Overview of the detector

The online muon beam profile monitor analyses the muon beam from the aspect of beam shape and relative intensity. Figure 5-1 illustrates a conceptual design of the monitor. The detector consists of a pair of one-dimensional arrays of thin scintillation fiber. Fibers are bound into a bundle and connected to a SiPM. As a readout electronics, EASIROC front-end chip and an external peak holding ADC were utilized [61].

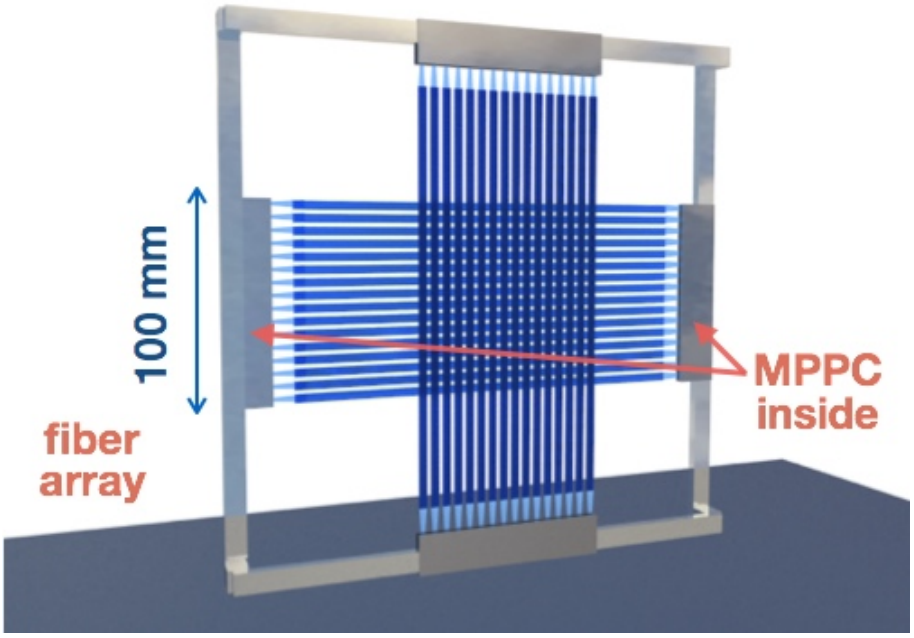

Figure 5-1: Conceptual design of the two-dimensional muon beam profile monitor. One-dimensional array of the scintillation fiber was connected to the SiPMs at both ends. Two layers of the fiber array were placed orthogonal to each other. The detector has an active area of 100 mm in square.

5.1.2 Requirements for the detector

Requirements for the beam profile monitor are minimum destruction and high reconfigurability of the muon beam. As a detector material, thin scintillation fiber and plastic scintillator slab were considered. From the aspects of machining precision and light attenuation, scintillation fiber was adopted. Figure 5-2 shows simulated energy deposit by a muon with kinetic energy of 4 MeV as a function of fiber thickness. The horizontal axis indicates fiber thickness, the left vertical axis indicates energy deposit, and the right vertical axis indicates spacial spread of the beam in target gas. In order to control the muon stopping center at the microwave cavity, total thickness of a beam monitor should be less than 400 μm in total and its uniformity should be better than 20%. In consideration of substrate thickness for fiber array, scintillation fiber with a diameter of 100 μm was developed.

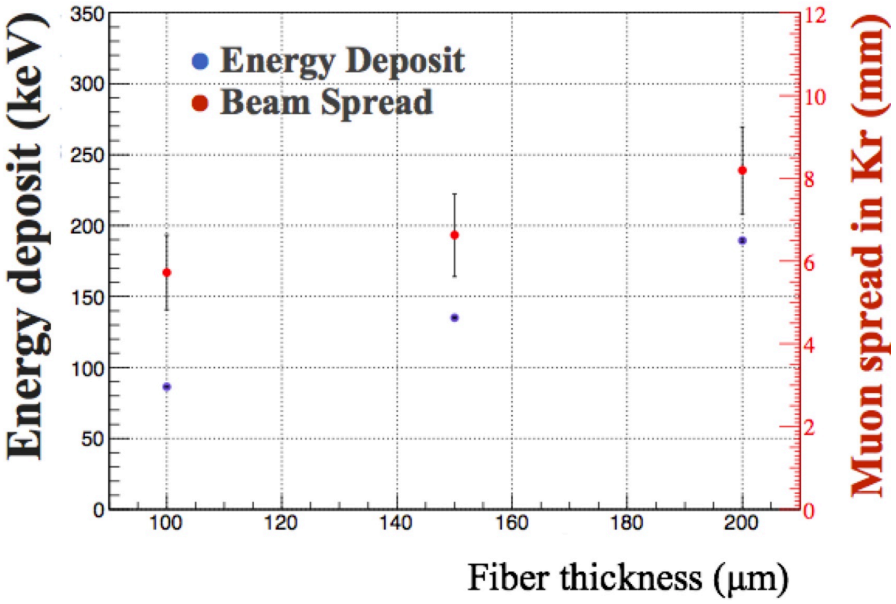

Figure 5-2: Simulated muon energy deposit in a scintillation fiber and muon beam spread in the Krypton gas target. Blue circles correspond to the energy deposit (the right vertical axis). Red circles correspond to the beam longitudinal spread in the gas target. The gas pressure was set to 1.0 atm and the muon energy wa set to 4 MeV.

5.1.3 Detector development

Fibers were arrayed on a polyimide film and hardened by epoxy resin. Figure 5-3 illustrates a conceptual cross section of the fiber layer. On a polyimide sheet with the thickness of 25 μm, scintillation fibers are arrayed one-dimensionally. Thermoplastic resin is poured to fix scintillation fibers on the substrate. To minimize non-uniformity of muon kinetic energy after passing the monitor, thickness of fiber layer was carefully controlled in manufacturing processes. The thermoplastic resin was poured at a plurality of times with precision control of heating temperature.

Figure 5-4 shows photographs of fabricated fiber layer. The left figure is a photograph of the stacked two fiber layers. At both edges of the fiber array, a bundle of 40 scintillation fibers was connected to a SiPM. On the detection plane, each fiber band is 4 mm wide and 100 mm long. To avoid an optical cross talk, an one-millimeter of gap was formed between fiber bands. The right figure is a microscope photograph of the fiber layer. Alignment precision of fiber bundles were evaluated by measuring the

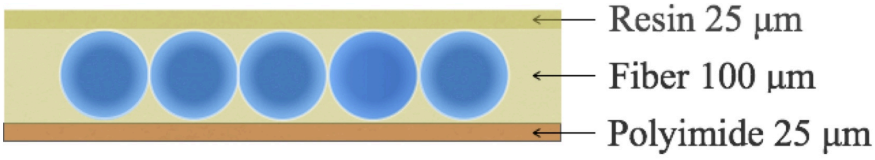

Figure 5-3: Conceptual cross section of the fiber layer. The scintillation fibers are one-dimensionally arrayed on a polyimide substrate. The fibers were fixed by pouring of thermoplastic resin. Total thickness of the layer is 150 μm.

parallelism of bundles. As a result of measurement, alignment precision of 0.5 mm was obtained.

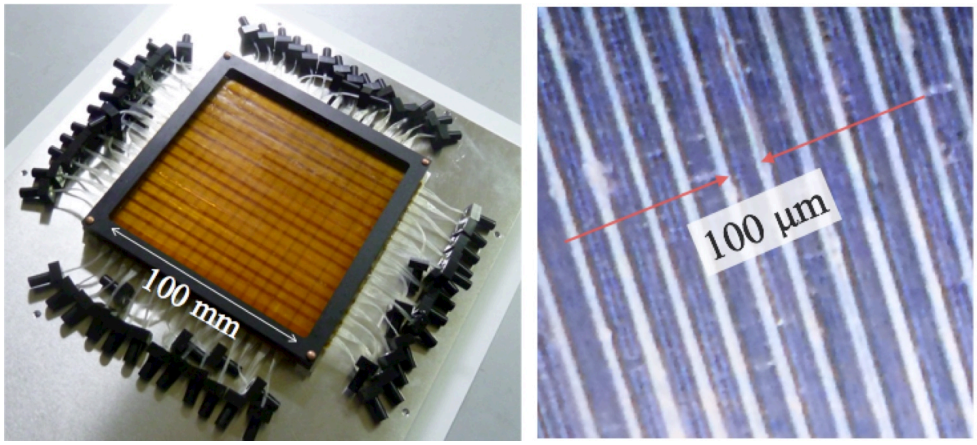

Figure 5-4: The assembled fiber layer (left) overview; (right) microscope view. In the left figure, two fiber layers were stacked.

By using a eddy-current type film thickness gauge, thickness of fiber layers were evaluated as shown in Fig. 5-5. The left figure corresponds to layer thickness distribution. The average thickness of stacked two-layers was 309 μm. Thickness uniformity was evaluated as 10.7 μm by Gaussian fitting. Non-uniformity of the layer thickness was 3.4 % and satisfied the requirement.

As a photo-sensor which is attached to scintillation fibers, SiPM (Hamamatsu Photonics MPPC S12572-015P) was utilized. It has 40,000 pixels of avalanche photo diodes (APD) in 3 mm square photo sensitive area. The photo-sensors were mounted on a printed circuit board (PCB) which is shown in Fig. 5-6. To stabilize optical connection and avoid optical cross-talk between fiber bundles, a supporting frame

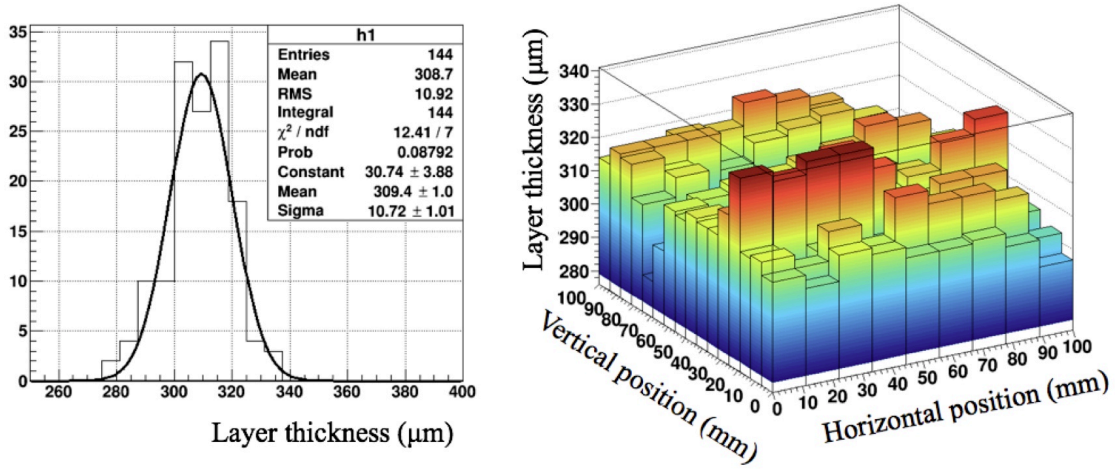

Figure 5-5: Fiber layer thickness distribution: (left) histogram of the layer thickness at each measurement point; (right) layer thickness map. In the left figure, black line corresponds to a result of the Gaussian fitting.

was attached as shown in the lower figure. To provide uniform detection efficiency, operation voltages of SiPM were adjusted in the range of 0.2 V.

Figure 5-7 shows a photograph of the assembled detector. In the experiment, the detector was installed between the beam duct and the gas chamber.

5.1.4 Performance of the detector

Basic performance of the detector was evaluated in laboratory test by using a radiative source and cosmic rays. Figure 5-8 shows a pulse height spectrum of ^{90}Sr-^{90}Y beta source. Discrete peak structure of the photon number distribution was observed and fitted by multiple Gaussian functions. A conversion coefficient from ADC channel to number of photons was obtained by evaluation of the distances among peaks of ADC spectrum.

By integration of each Gaussian peak in Fig. 5-8, the detected photon number distribution was obtained as shown in Fig. 5-9. Red circles indicate the measurement result, the histogram in black line indicates the simulation result with two Poisson distributions corresponding to the beta rays from strontium and yttrium.

Attenuation length of scintillation fiber was evaluated by using an UV lamp which emits the light having wavelength of 255 nm. Light output was measured by a photo-

Figure 5-6: Printed circuit board for SiPM mount and fiber connection: (upper) printed circuit board after SiPM implementation; (lower) circuit board with the aluminum support for fiber bundle connection to the SiPM.

multiplier attached on a fiber section. Figure 5-10 shows measured fiber output attenuation as a function of optical path length. An attenuation length of a fiber was evaluated by fitting of the data points with an empirical function

$$y = Ae^{-x/a} + Be^{-x/b} \tag{5.1}$$

where A and B corresponds to contribution from light through a core and a clad of the fiber. Each of the contributions is characterized by the attenuation length parameters a and b. To perform the muon beam profile analysis, this light attenuation effect was corrected by using this fitting result.

Figure 5-11 shows typical measured photon number distribution when a pulsed muon beam is irradiated to the detector. The histograms correspond to the respective horizontal positions as noted in the figure. Pedestal was subtracted by using beam-off triggered data. As the number of photon becomes larger, the spectrum shapes

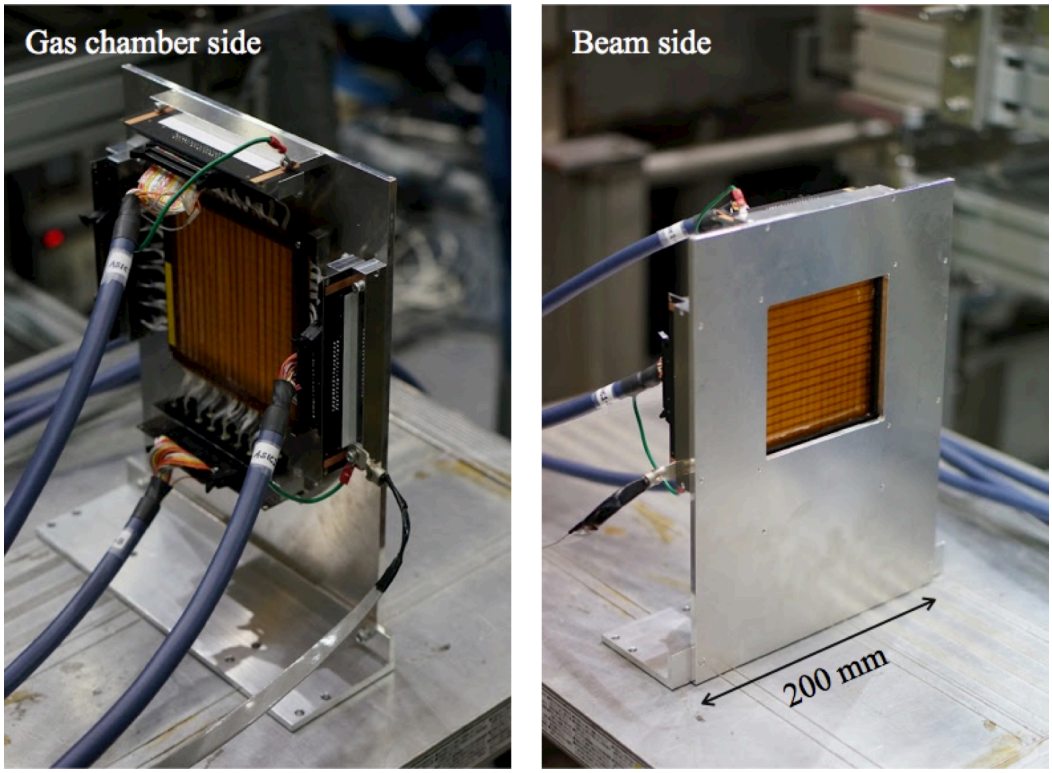

Figure 5-7: Assembled fiber beam profile monitor: (left) gas chamber side; (right) beam injection side. The detection area of the beam monitor is 100 mm square. The supporting structure of the detector was designed so that the horizontal and vertical center meet the beam axis.

asymmetric. This systematic effect can be explained qualitatively by pileup of SiPM pixel. Shapes of each distribution was evaluated by the fitting to a skewed Gaussian function.

A light yield at each fiber band was analyzed to reconstruct a muon beam profile. Figure 5-12 shows a measured muon beam profile at J-PARC MLF MUSE D2-Line. The left figure corresponds to a horizontal projection while the right figure corresponds to a vertical projection. Red solid lines are fitting curves to a Gaussian function on a background. A beam width and a center were obtained pulse-by-pulse.

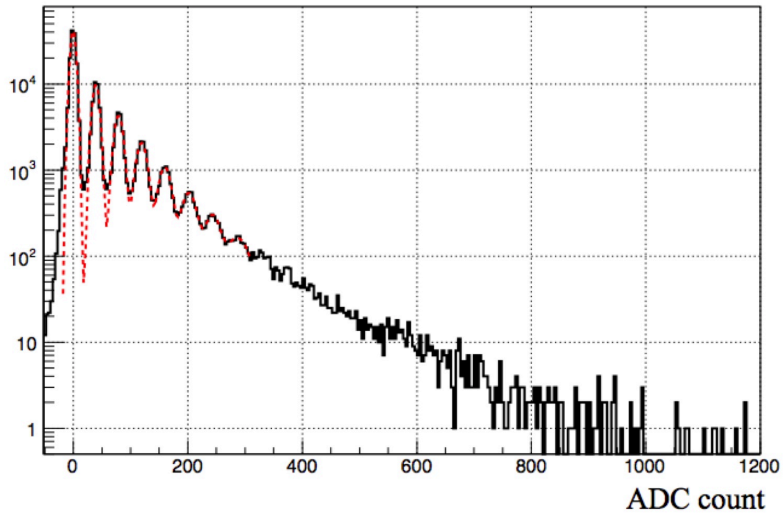

Figure 5-8: Pulse height spectrum of a ^{90}Sr-^{90}Y beta source. Red dashed line correspond to the fitting result with multiple Gaussian functions. Data taking was triggered by a small scintillation counter placed just behind the longitudinal center of the fiber band.

5.2 Three-dimensional muon stopping distribution detector

To measure spacial distribution of muonium in the target gas, a three-dimensional muon beam imager was developed. The details of the detector development are described in this section.

5.2.1 Overview of the detector

A conceptual design of the muon beam imager is shown in Fig. 5-13. A plastic scintillator disk is placed in the gas chamber filled with krypton gas. When the a muon beam is irradiated, a two dimensional image of the beam profile on a scintillator surface is measured. By scanning position of the scintillator, three-dimensional muon stopping distribution is reconstructed.

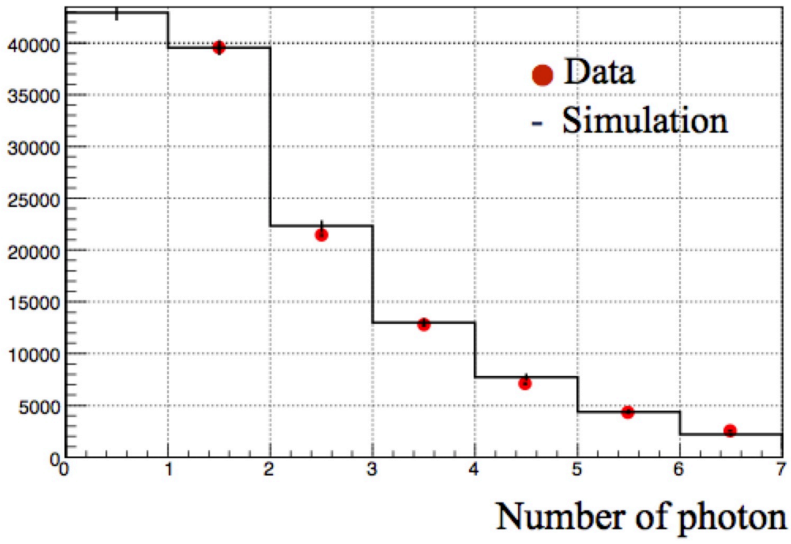

Figure 5-9: Photon number distribution of a ^{90}Sr-^{90}Y beta source. Red circles correspond to the number of photon which was estimated based on the discrete peak structure in the pulse height spectrum shown in Fig. 5-8. The histogram in black line corresponds to the simulated photon number distribution.

5.2.2 Requirements for the detector

To suppress the systematic uncertainty due to the muonium spacial distribution, the beam center and width should be obtained with the precision of 1 mm. Furthermore, remote control operability with good reproducibility is of importance.

5.2.3 Detector development

Figure 5-14 shows a drawing of the detector. As a muon stopping target, a thin disk of plastic scintillator (EJLEN Technology EJ-212) is placed inside of the gas chamber. The fluorescence from the scintillator is amplified by an imaging intensifier (Hamamatsu Photonics C9016-23EXP) and detected by a cooled CCD camera (BITRAN BU-50LN). Cooling of the CCD camera was performed by both an air-cooling fan and a Peltier element cooler.

In order to avoid a reflected light which enters to a CCD camera, a thin black paper was attached on the upstream side of the scintillator. A diameter of the scintillator was 182 mm. The scintillator disk and camera system were remotely controlled by the

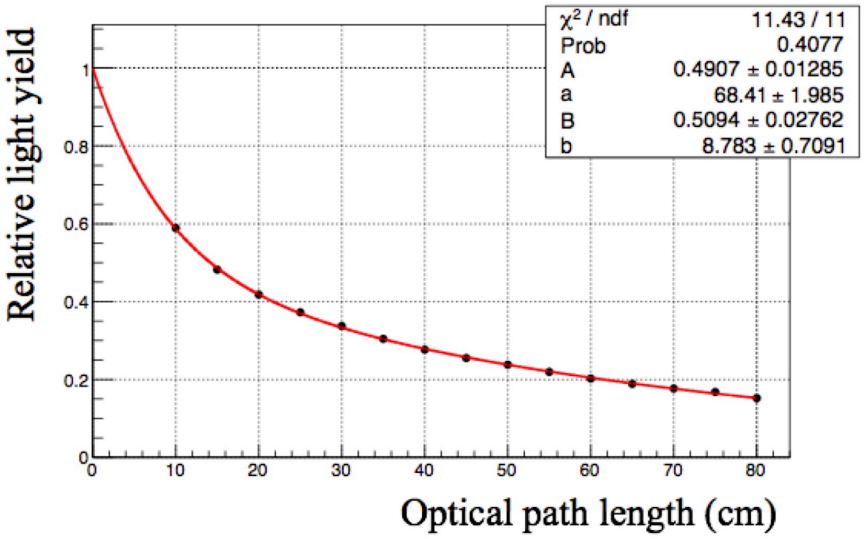

Figure 5-10: Light attenuation in scintillation fiber. Red line corresponds to the fitting result with an empirical function $y = Ae^{-x/a} + Be^{-x/b}$ where a and b are the attenuation length parameters.

linear actuators (Zaber T-NM17A04 for the scintillator, T0NA08A50 for the camera system). Figure 5-15 shows a photograph of the assembled detector system.

To reduce the contribution of thermal noise of a CCD, amplification by an image intensifier was gated by 100 ns of timing window. Gating trigger for the image intensifier was adjusted by a digital delay generator (SRS DG645). By scanning delay amount for a trigger and measuring the light yield, an arrival time of muon pulse was determined.

5.2.4 Performance of the detector

For background subtraction, a thermal noise distribution of CCD output was measured when beam was stopped. Figure 5-16 shows a measured dark frame.

To estimate statistical uncertainty in the measurement, a correlation between CCD signal and its fluctuation was evaluated. The plurality of images under the same measurement condition were analyzed. A root-mean-square of the signal distribution corresponds to uncertainty in photon statistics. A correlation function for statistical uncertainty estimation was obtained by the curve fitting as shown in Fig. 5-17. The

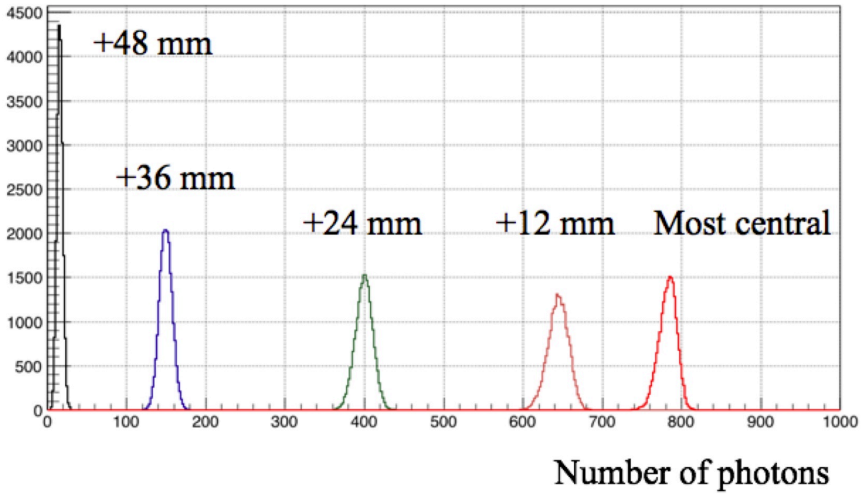

Figure 5-11: Photon number distribution of the pulsed muon beam. Each of the line colors corresponds to the horizontal distance from the beam axis. The measurement was performed with the beam power of 200 kW which corresponds to 3×10^6 muons per second.

function used in the fitting was $y = p_0\sqrt{x}(1+p_1 x)$ where p_0 and p_1 are free parameters. The second parameter in the fitting function corresponds to a non-linearity and that was found to be negligible.

Figure 5-18 shows a typical two-dimensional muon beam profile on the scintillator surface when the scintillator was placed at the entrance of the microwave cavity. Muon beam momentum was 27.4 MeV/c and Krypton gas pressure was 0.3 atm. A conversion coefficient from the CCD pixel to the distance was calibrated by the scintillator diameter. The beam center and width were obtained by the fitting to a two-dimensional Gaussian.

Figure 5-19 shows the beam profile center obtained from the fitting results. Red circles indicate horizontal center while blue circles indicate vertical one. Dashed lines correspond to 1 mm deviation from the mean values. Measurement precision of the beam center was better than 1 mm and satisfied the requirement.

Figure 5-20 shows the beam profile width as a width of two-dimensional Gaussian. As muons go downstream, the beam width increases due to Coulomb multiple scattering and angular spread of the incident beam.

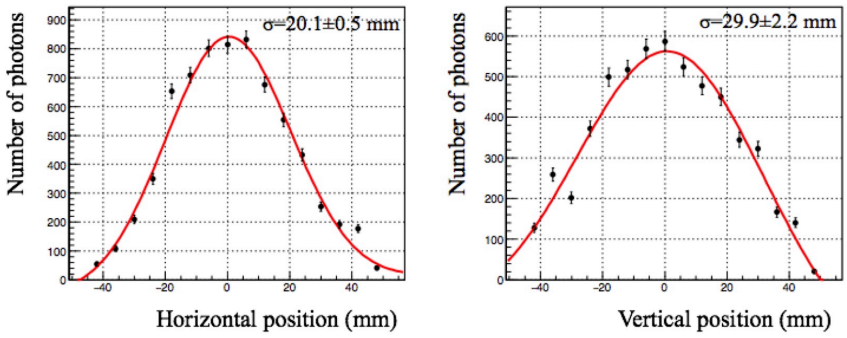

Figure 5-12: Muon beam profile measured by using the fiber beam profile monitor: (left) horizontal projection; (right) vertical projection. Red line corresponds to the fitting result with a Gaussian on a background.

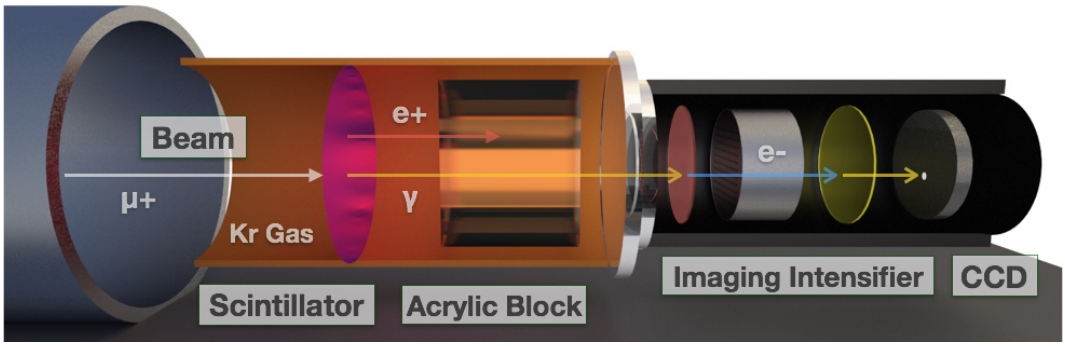

Figure 5-13: Conceptual design of the three-dimensional muon stopping distribution detector. The pulsed muon beam is irradiated to the plastic scintillator which is placed inside the gas chamber. A phosphor in the scintillator is amplified by an image intensifier and detected by a CCD camera. The scintillator is movable on the longitudinal axis.

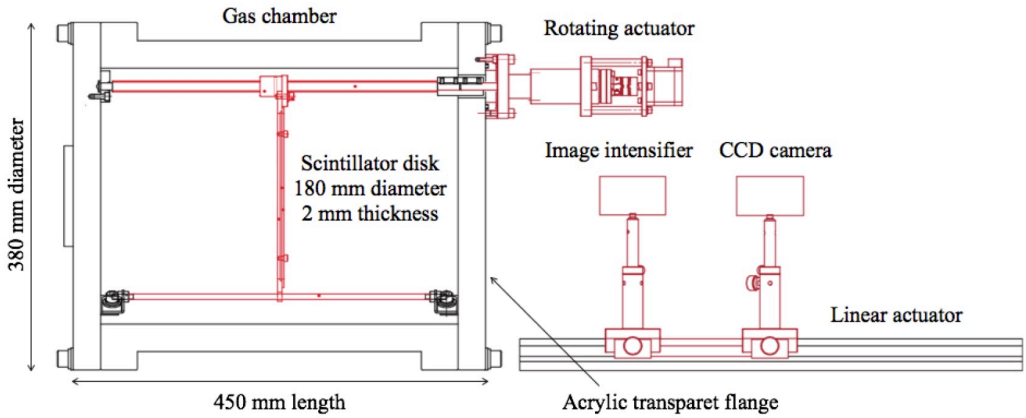

Figure 5-14: Drawing of the three-dimensional muon stopping distribution detector. The plastic scintillator in 180 mm diameter and 2 mm in thickness is installed inside the gas chamber. The longitudinal position of the scintillator is controllable by using the rotating actuator. The translation of the scintillator is synchronized to move of the photo-detection system.

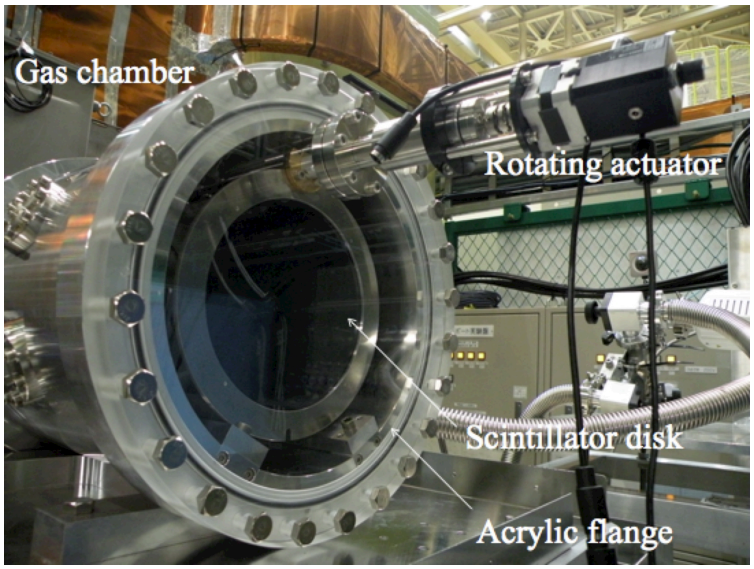

Figure 5-15: Assembled muon beam imager. The thin black paper was attached on the plastic scintillator disk. The acrylic transparent flange was utilized for light transmission.

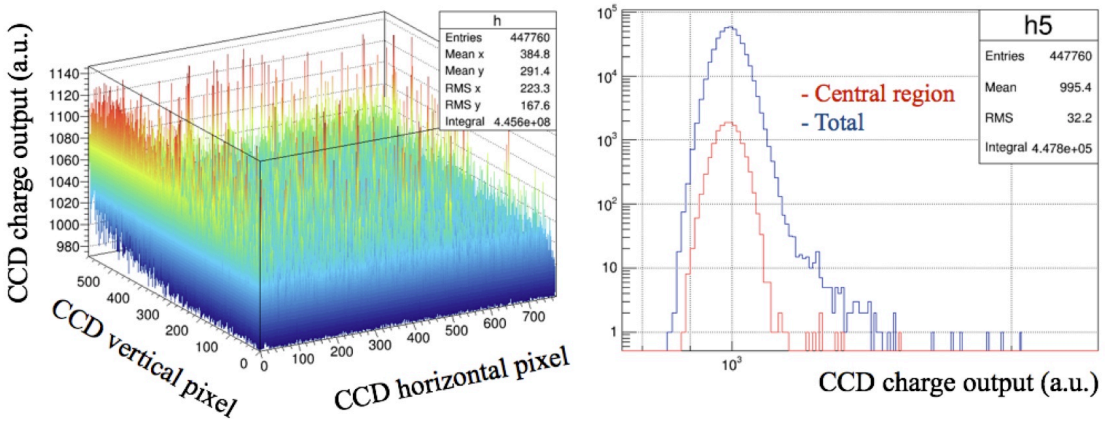

Figure 5-16: Dark frame of the CCD camera: (left) thermal noise rate map ; (right) thermal noise rate distribution. In the right figure, the histograms in red and blue lines correspond to the central region and the entire region of the CCD camera, respectively.

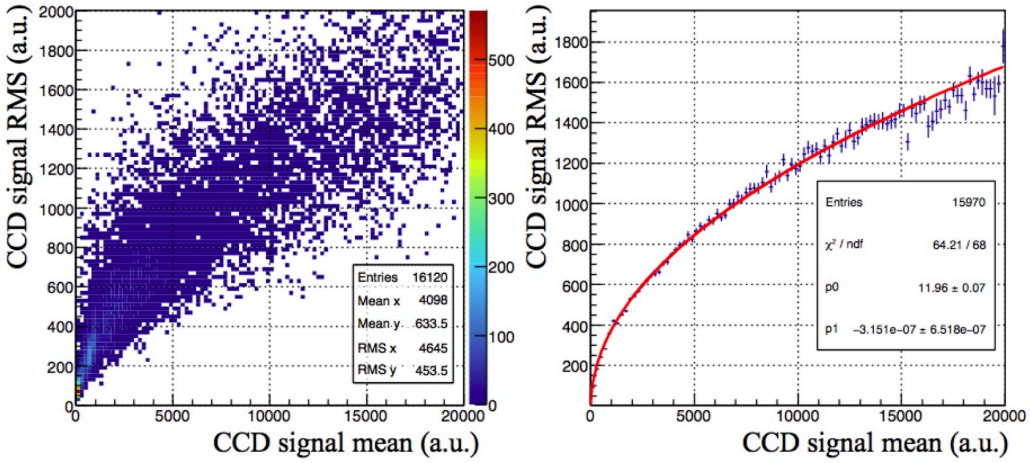

Figure 5-17: Correlation between the CCD signal intensity and its root-mean-square: (left) two-dimensional histogram; (right) one-dimensional projection with a fitting result in red line. The fitting function was defined as $y = p_0\sqrt{x}(1 + p_1 x)$ where p_0 is the conversion factor from the number of photo electron to the CCD charge, p_1 is the non-linearity parameter of the image intensifier response.

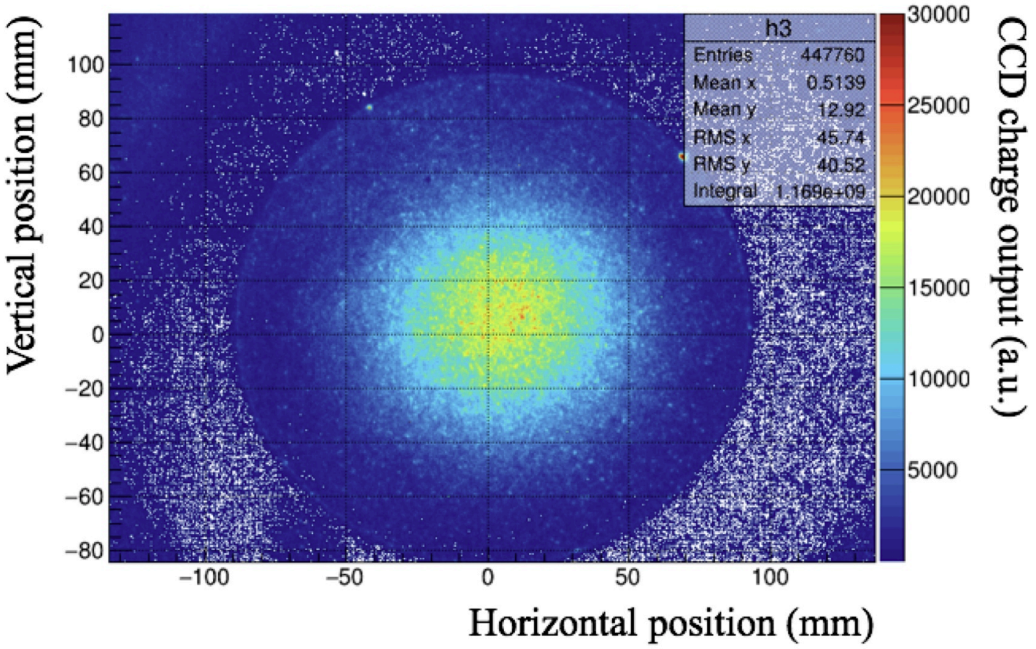

Figure 5-18: Two-dimensional muon beam profile at the entrance of the microwave cavity. The beam momentum was 27.4 MeV/c and the intensity was 3×10^6 muons per second. The exposure time was 75 μs.

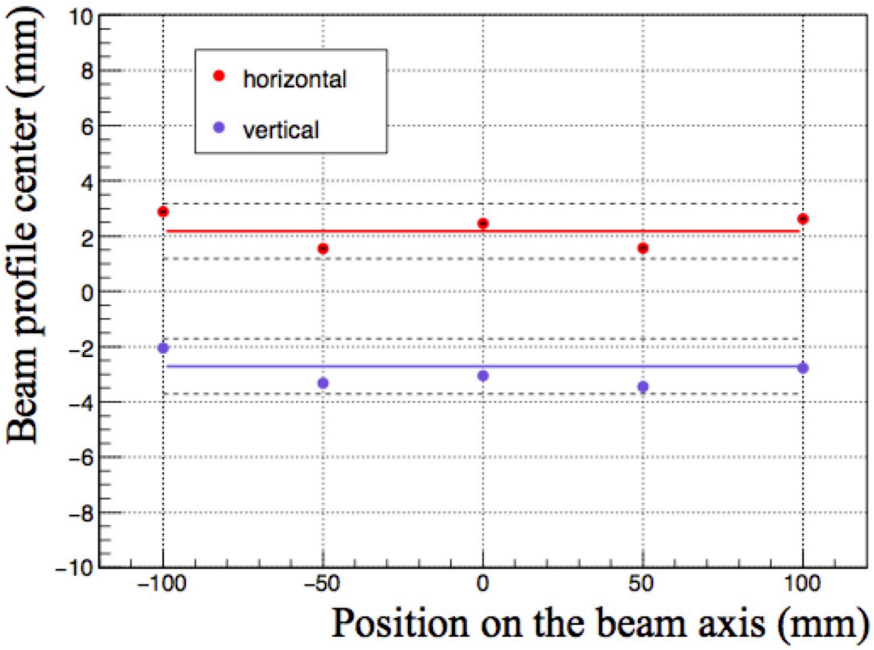

Figure 5-19: Muon beam center measured by the beam imager. Red and blue circles correspond to the horizontal and vertical center, respectively. The fitting result with a constant function is shown in the solid line. Dashed lines indicate the one-millimeter deviation from the average. The target gas pressure was 0.3 atm.

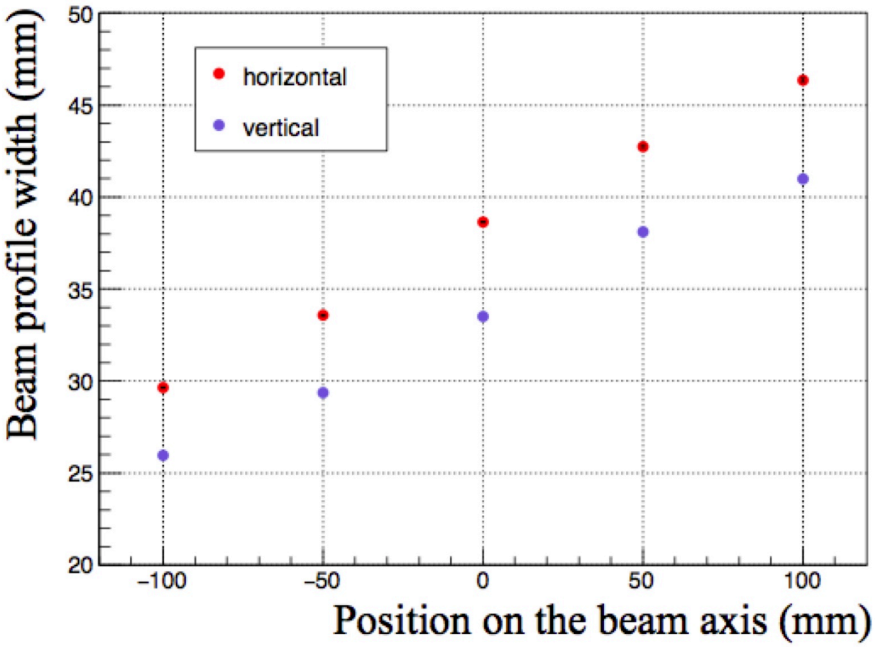

Figure 5-20: Muon beam width measured by the beam imager. Red and blue circles correspond to the horizontal and vertical beam width, respectively. The target gas pressure was 0.3 atm.

Chapter 6

Positron detector

The details of positron detector development are discussed in this chapter. The positron detector is a muon spin spectrometer to analyze the muonium energy state.

6.1 Overview of the detector

Figure 6-1 illustrates a conceptual design of the positron detector. It consists of two layers of segmented scintillation counter with SiPM readout.

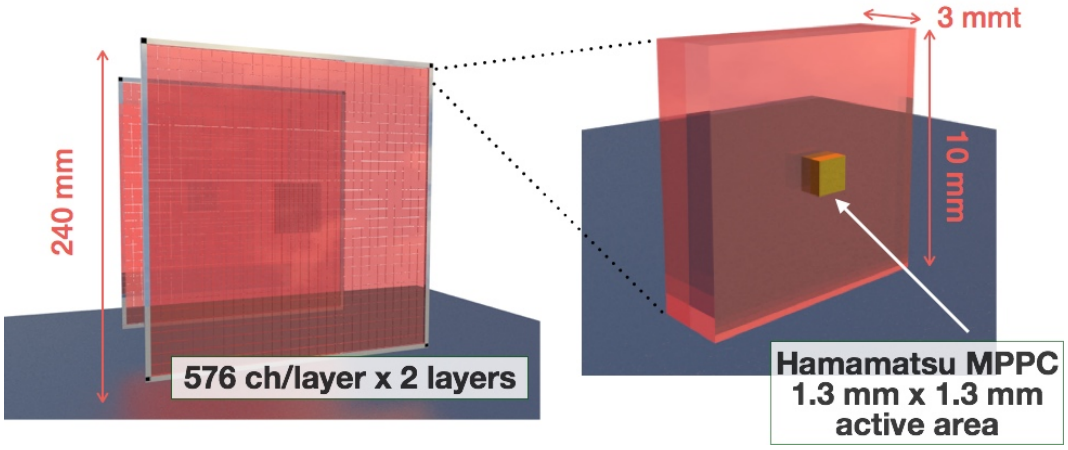

Figure 6-1: Conceptual design of the positron detector. The scintillator pixels with SiPM readout were arranged in a square matrix of 24 rows and columns. Two layers of the detector were placed at the interval of 40 mm. Each element consists of a square scintillator with a side length of 10 mm and a SiPM attached at the center of the scintillator. Thickness of the scintillator is 3 mm and the SiPM has an active area whose size of 1.3 mm square.

6.1.1 Requirements for the detector

The high-intensity pulsed muon beam at J-PARC has a beneficial effect on the accumulation of statistics in a limited beam time. On the other hand, high event rate capability is required for the positron detector. A number of positrons are detected by a positron detector at short intervals and a signal pileup becomes severe. In order to achieve a large solid angle and the suppression of the signal pileup at the same time, fine segmentation of the detector with an integrated readout electronics is essential.

6.2 Development of high-rate capable positron counter

A traditional muon spin spectrometer is a combination of plastic scintillator, PMT, and discrete signal processing electronics. To deal with the unprecedented high intensity pulsed muon beam at J-PARC, a new positron counting system for a muon spin spectrometer was developed. It consists of a fine segment of plastic scintillator, a silicon photomultiplier (SiPM), and fast readout electronics with ASIC based amplifier, shaper, and discriminator (ASD) and multi-hit TDC implemented in FPGA.

6.2.1 Plastic scintillator

A plastic scintillator with a fast decay time constant and an emission wavelength around 450 nm is suitable for a positron detector. EJ212 produced by ELGEN technologies was adopted. The dimension of a scintillator segment was decided based on a simulation study as hereinafter described.

6.2.2 SiPM

As a photo-sensor which is attached to a plastic scintillator, SiPM was utilized for fine segmentation and operation in a place having a spatial limitation. A MPPC (Multi Pixel Photon Counter, Hamamatsu Photonics K.K. S12825-050P-01) was adopted. It has 667 pixels in 1.3 mm $\times$ 1.3 mm active area (50 μm pixel pitch). In order to provide uniform performance of the detector segments, the operation voltages of

SiPMs were carefully selected. Figure 6-2 shows the operation voltage distribution of SiPMs implemented to the detector. The operation voltages are within the range of 2%.

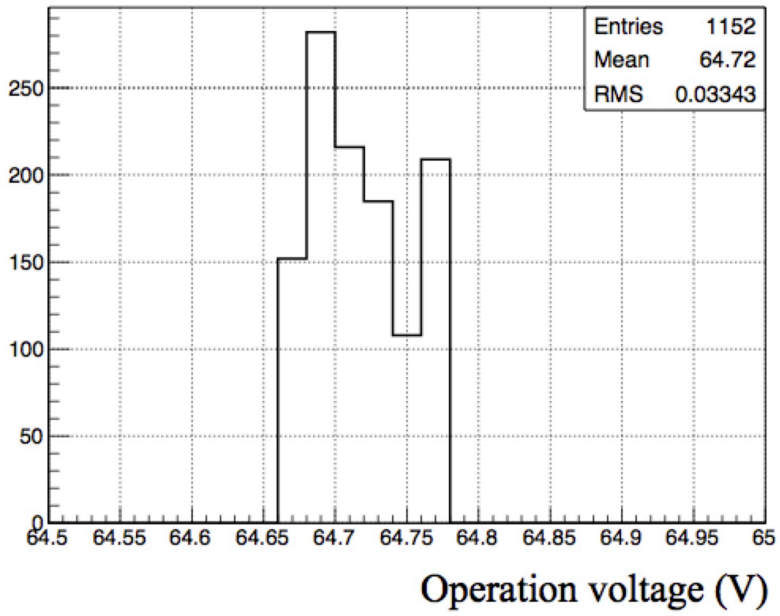

Figure 6-2: Operation voltage distribution of the SiPMs for the positron detector. The operation voltage $V_{\rm op}$ is defined as $V_{\rm op} = V_{\rm br} + 2.0$ V where $V_{\rm br}$ is the breakdown voltage of the SiPM.

6.2.3 Readout electronics

Overview

As a series of readout electronics for SiPM, Kalliope (KEK Advanced Liner and Logic board Integrated Optical detector for Positron and Electron) has been developed by the Electronics Group and Institute of Materials Structure Science (IMSS) of KEK [62]. It consists of an analog signal circuit with an ASIC named VOLUME2012 and a digital circuit with a FPGA.

Analog part

An analog part of the readout electronics is shown in Fig. 6-3. It has two stages of voltage amplifiers and each bias voltage for amplifier is adjusted by the slow control parameters. Slow control parameters are described in 20 bits of register pattern for amplifier gain, amplifier biases, discriminator threshold, and fine tuning of the bias voltages for SiPMs. The specifications of the analog board are summarized in Table 6.1.

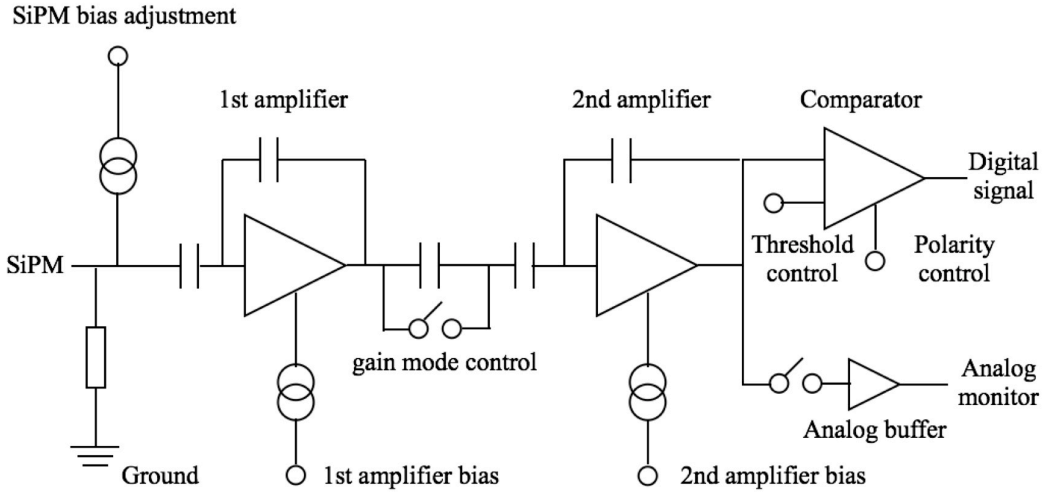

Figure 6-3: Schematic of an analog part of the readout electronics. Signal pulse from the SiPM is amplified by the two stages of voltage amplifiers and digitized by the comparator. The comparator threshold, amplifier gain, and SiPM biases are adjustable by slow control. Analog signal can be monitored through the buffer amplifier.

Table 6.1: Specifications of the analog board for the positron detector.

Specification	Value
Gain	40 dB or 30 dB
Bandwidth	100 MHz
Typical dynamic range	600 mV
Typical pulse width	40 ns
Digital signal logic level	LVCMOS 2.5 V
Channel	32

Digital part

Figure 6-4 depicts a schematic of a digital part of the readout electronics. FPGA firmware contains the implementation of a multi-hit TDC with 1 ns of timing resolution, which is realized by four phase rotating 250 MHz clocks. Figure 6-5 shows a simulated state machine with the phase rotating clocks. The specifications of the digital board are summarized in Table 6.2.

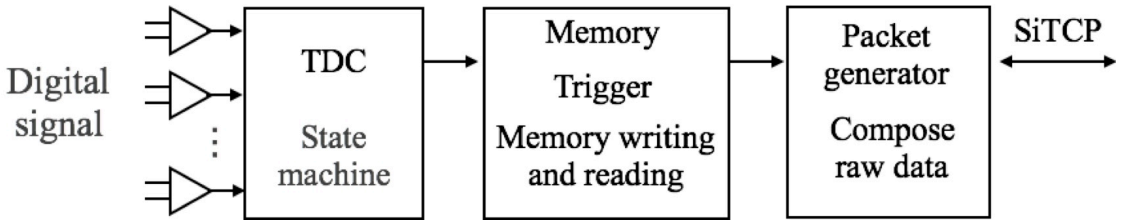

Figure 6-4: Schematic of a digital part. Digital pulse from the analog part are processed by the multi-hit TDC implemented in a FPGA. The FPGA firmware contains the modules for memory reading and writing, data packet generation, and SiTCP communication.

Table 6.2: Specifications of the digital board for the positron detector.

Specification	Value
Clock frequency	250 MHz
Timing resolution	1 ns
Timing window	64 μs
Hit depth	1000
Channel	32

Slow Control

Major parameters of readout electronics are adjustable through a slow control. Table 6.3 is a list of controllable parameters. Amplifier gain is switchable by the number of amplifier stages. Bias for each amplifier dominates the signal pulse height, the dynamic range, and the threshold adjustment range. Not only pulse shape, but an offset voltage for the comparator input and the analog signal dynamic range are

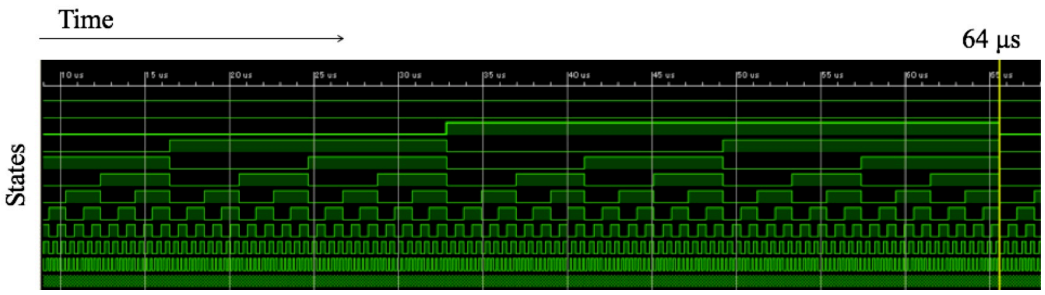

Figure 6-5: Simulated time evolution of the state machine for the multi-hit TDC. Each periodic pulse causes the state transition of the state machine by using the phase rotating four clocks.

correlated to these amplifier parameters. The amplifier parameters were determined based on a result of waveform comparison in the parameter space.

Table 6.3: Slow control parameters of the readout electronics for the positron detector.

Parameter	Tunable range	Control unit
SiPM bias tuning	4 bit	Channel
Amplifier gain	40 dB or 30 dB	ASIC (16 ch.)
First amplifier bias	16 bit	ASIC (16 ch.)
Second amplifier bias	16 bit	ASIC (16 ch.)
Discriminator threshold	4 bit	Channel
DAQ timing window	from zero to 64 μs	FPGA (32 ch.)

6.2.4 SiPM mount board

For implementation of the SiPMs, a printed circuit board was developed. It consists an eight layers of glass epoxy substrate. Signal lines were separated into four layers and ground planes were inserted between each signal layer. Width of microstrip lines and thickness of ground planes were designed to match the characteristic impedance to 50 Ohm. Figure 6-6 shows a photograph and a partial drawing of the printed circuit board for SiPM mount. A display color for each line corresponds to respective layer of the circuit board.

To minimize inactive area on the detector plane, every connector was implemented on the edge of the circuit board. Bypass capacitors were placed to suppress a noise

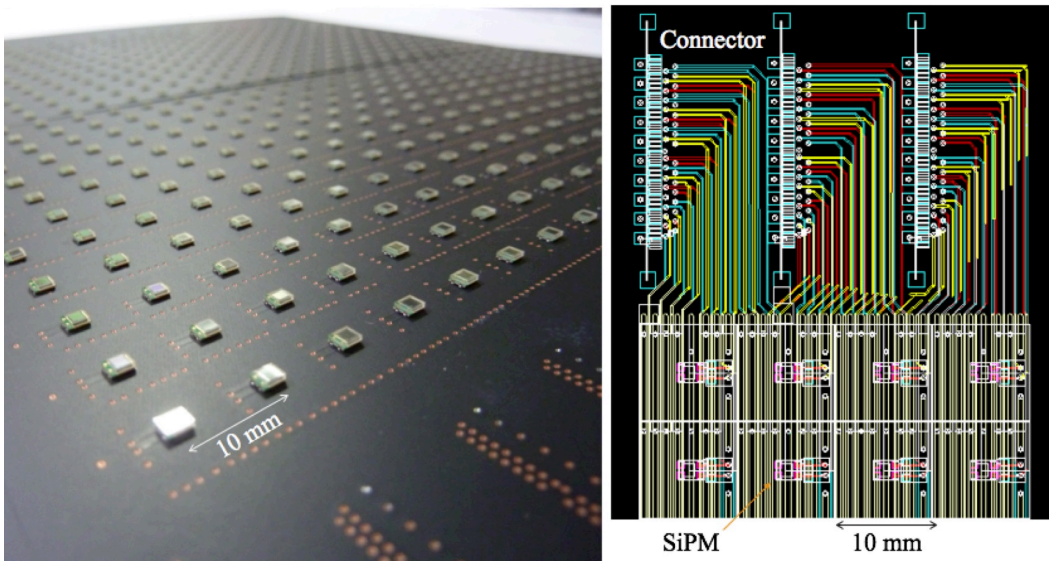

Figure 6-6: Printed circuit board for SiPM mount: (left) photograph of the circuit board after SiPM implementation; (right) partial drawing of the circuit board. The interval between the SiPMs is 10 mm.

from bias voltage lines. The printed circuit board and readout electronics was connected with a fine coaxial cable (KEL AWG40 and SSL20).

6.2.5 Light diffuser

As a light diffuser which doubles an alignment marker, laser patterned white paper mask was developed. Figure 6-7 shows a photograph and a partial drawing of the paper mask.

6.2.6 Reflector film

In order to suppress an optical cross-talk between scintillator segments, a reflector film (3M Enhanced Specular Reflector; ESR) was inserted on the interfaces. To provide the minimum dead-region and gapless insertion of a reflector film at the same time, the reflector ribbons with folds were fabricated [63]. Figure 6-8 illustrates a procedure to assemble scintillators and reflector films. Figure 6-9 shows a photograph of the detector during assembly.

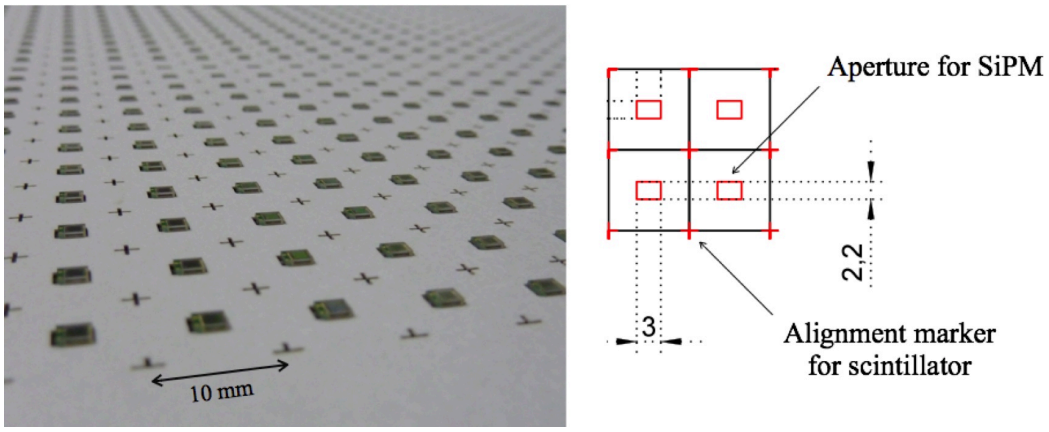

Figure 6-7: White paper mask as a light diffuser and an alignment marker: (left) photograph of the detector after the white paper mask installation; (right) partial drawing of the mask.

6.2.7 Assembly

To eliminate a gap between a reflector film and a printed circuit board, reflector ribbon is slightly wider than scintillator thickness. Scintillators and reflector ribbons were fixed by surrounding acrylic frame and a top board covered with a sheet of reflector film. Figure 6-10 shows the assembled positron detector without the top board. In the experiment, the positron counter was placed at downstream of the gas chamber.

6.2.8 Absorber

As discussed in Chapter 4, placement of an absorber between the gas chamber and the positron detector is effective to suppress positron background both prompt and duct streaming. Figure 6-11 shows simulated positron suppression as a function of absorber thickness. An absorber material which has larger atomic number Z causes particle loss proportional to Z^2 due to bremsstrahlung. For balancing an energy cut and less bremsstrahlung, aluminum was adopted as an absorber material.

Figure 6-12 shows simulated mean kinetic energy of detected positron from stopped muon decay. It has no significant absorber thickness dependence because initial energy of decay positron tends to be higher as shown in Fig. 2-11. Simulation result

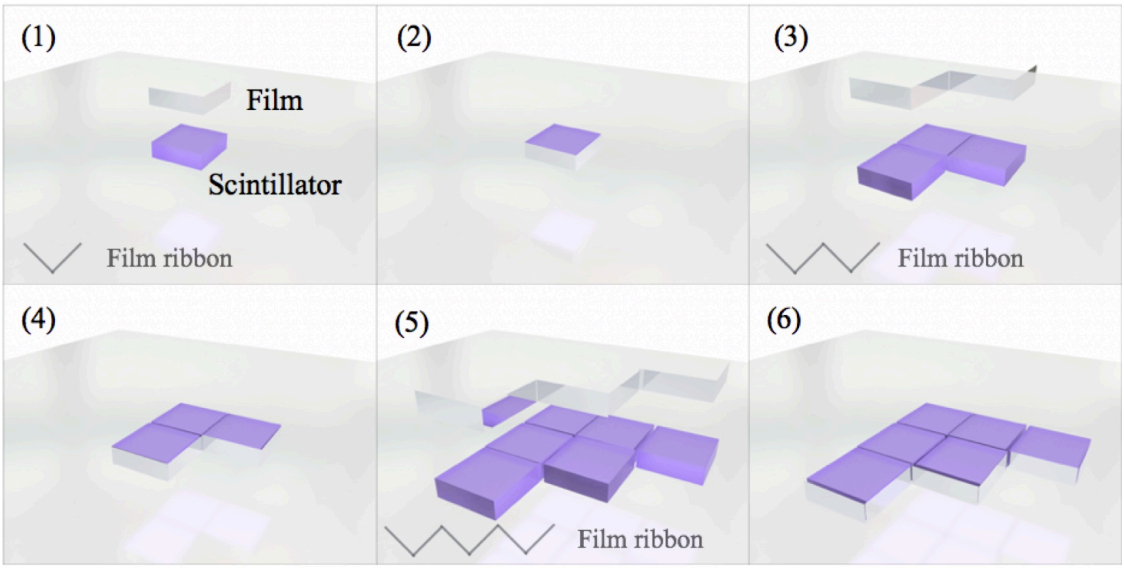

Figure 6-8: Insertion of the reflector films. The ESR ribbons with folds were inserted between the scintillator segments. The detector was assembled from (1) to (6) in order.

suggests larger thickness of an absorber. However, inside of the magnetic shield has severe spacial restriction. At a maximum under spacial constrains, an aluminum plate with the thickness of 30 mm was developed.

6.3 Performance of the detector

Basic specifications of the detector were examined in laboratory test. Characteristics of SiPM were evaluated by using a dark noise. Performance as a particle detector was evaluated by using a ^{90}Sr-^{90}Y radiative source. In order to understand the detector response to a signal positron in the spectroscopy experiment, a beam test with high-intensity pulsed muon beam at J-PARC MLF was performed.

6.3.1 Breakdown voltage of the SiPM

As shown in Fig. 6-2, operation voltages of SiPM were adjusted within the range of 0.2 V. From each detector sub-section, several SiPMs were selected for sampling

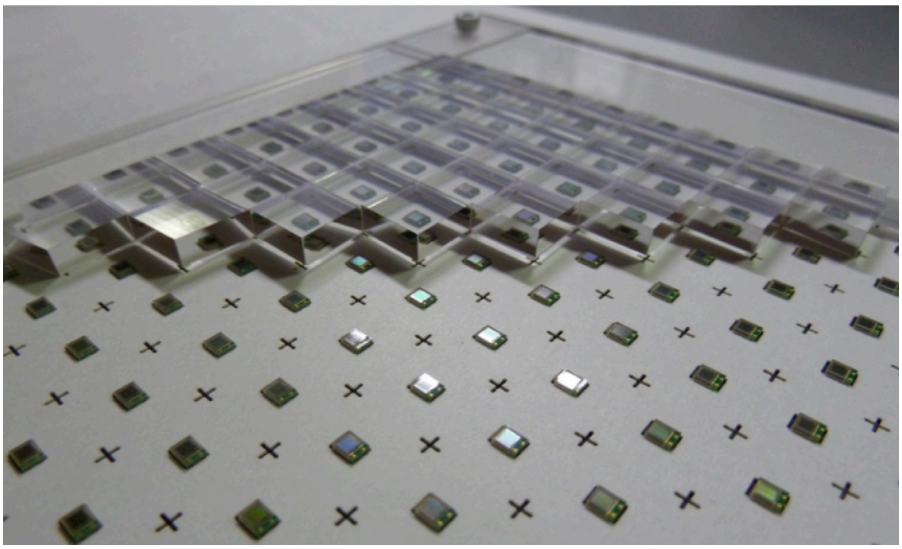

Figure 6-9: Assembly of the scintillators and the reflector ribbons. The scintillators were placed on the board utilizing the alignment cross processed on the white paper mask.

evaluation of the breakdown voltage. The operation voltage V_{op} is defined as 2.0 V plus breakdown voltage V_{br}. Figure 6-13 shows typical result of the measurement. An ordinate axis indicates a distance between one-photon and two-photons pulse height of dark noise. The breakdown voltage was evaluated by the linear fitting as a zero-cross of the fitting line. The measurement results were consistent with expectation from the operation voltage distribution.

6.3.2 Dark noise rate of the SiPM

Figure 6-14 shows measured dark noise rate of the SiPM for all channels of the detector. SiPM bias was set to an operation voltage at a room temperature of 287 K. Discriminator threshold was set to 1.5 photo-electron equivalent level. The result was consistent with specification information provided by a manufacturer. For a case of typical channel with the dark noise rate of 20 kHz, an expected dark count in a data acquisition timing window is 1.3 on average. By taking coincidence between the near layer and the far layer of the positron detector, an accidental coincidence due to the dark counts are safely negligible. Other types of accidental coincidence are discussed in following chapter.

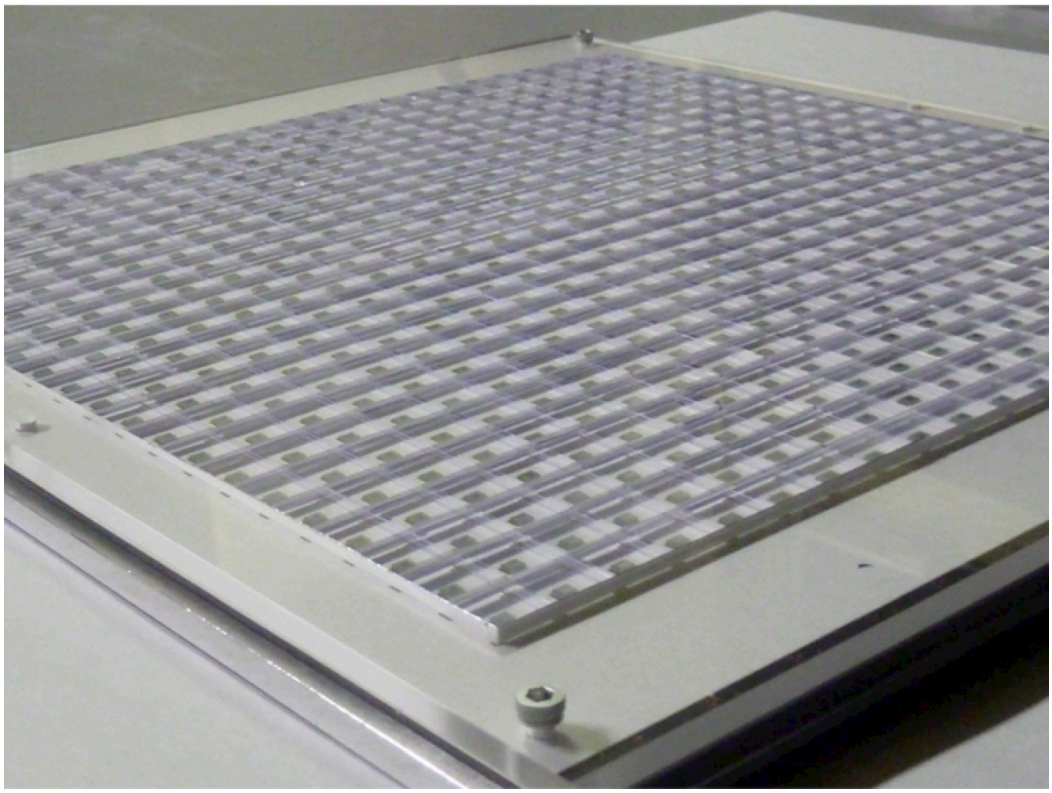

Figure 6-10: The positron counter. The top cover board for protection is not shown. The detector has an active area of 240 mm square.

6.3.3 Signal pulse height

To evaluate an uniformity of detector response one photo-electron signal height was measured in the same manner as the breakdown voltage measurement. Figure 6-15 shows measured typical 1 p.e. signal pulse height in a particular detector module. According to the results, no critical variation of detector performance was observed.

6.3.4 Photon yield

In order to evaluate detection efficiency, photon yield of an electron from Sr-Y beta source, cosmic ray, and muon decay positron were measured. With an objective of high-rate data processing, Kalliope readout system has no ADC for pulse height or charge measurement. Hence, a readout electronics with an external peak holding ADC was utilized to measure photon yield. Note that following results were obtained by using a partial replicant of the full-scale detector which has the same structure

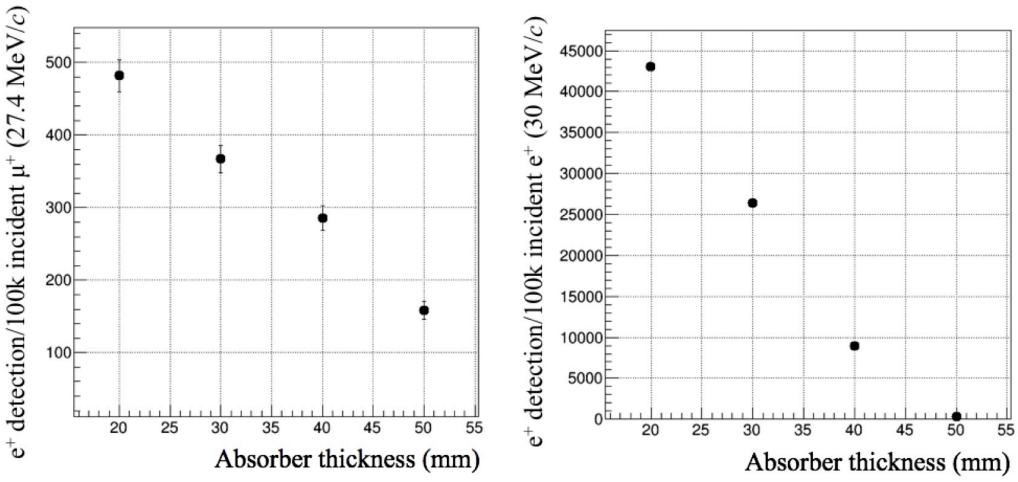

Figure 6-11: Simulated positron suppression as a function of the aluminum absorber thickness: (left) positron relative yield for a case of the positrons from muon decay; (right) positron relative yield for a case of the positrons with the momenta of 30 MeV/c.

and composition related to a scintillator and a SiPM.

Figure 6-16 shows measured photon yield of an electron from a ^{90}Sr-^{90}Y radiative source. To suppress contribution from lower energy electrons from Sr beta decay, the detector was placed between a radiative source and a trigger counter as shown in Fig. 6-17. Only electrons which have the kinetic energy of 1 MeV or higher were selected. SiPM bias was set to an operation voltage at a room temperature. Photon yield distribution was evaluated by fitting to a Landau distribution smeared with a Gaussian.

Figure 6-18 shows measured photon yield of a positron from muon decay at rest. The bias voltage for the SiPM and fitting function were same as the case of radiation source test. A break at the higher edge of the histogram was caused by saturation at the dynamic range of an ADC. Expected energy deposit by a muon-decay positron is about 85% of one by an electron from a ^{90}Sr-^{90}Y radiative source. Therefore, measured photon yield was consistent to each other. When the discriminator threshold is set to 4.5 p.e. level or below, nearly 100% of detection efficiency is expected for a positron from muon decay.

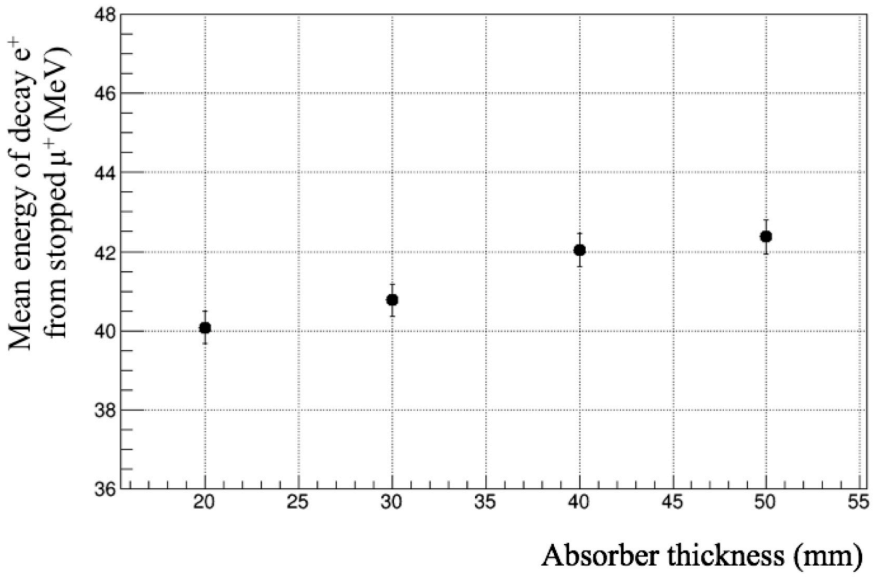

Figure 6-12: Simulated mean kinetic energy of the detected positron from muon decay at rest. An energy threshold around 40 MeV is suitable for the experiment because of a large positron angular asymmetry.

6.3.5 High event-rate capability

To evaluate high-rate capability of the positron detector, a time spectrum of positron from muon decay was measured. The readout electronics parameters and detector configuration were set to same as the muonium spectroscopy measurement. Figure 6-19 shows the time spectra of decay positron measured by each layer of the detector. The left figure corresponds to the near layer, the right figure corresponds to the far layer. A sharp peak at the earliest timing corresponds to the prompt positrons. A mean lifetime of muon was obtained by the fitting to an exponential function on a floor. Fitting range was limited to a lower-rate region to avoid the spectrum deformation due to the signal pileup. Evaluated exponent was consistent to mean lifetime of muon. The details of data analysis are described in Chapter 8.

An approximation curve was extrapolated to the higher-rate region to estimate event loss due to a signal pileup. Figure 6-20 shows an event loss ratio which is defined as normalized difference between the histogram and the approximation curve. The zero-point of the horizontal axis corresponds to a muon pulse arrival. At a maximum event rate, about 20 % of event loss was observed. According to a result of simulation

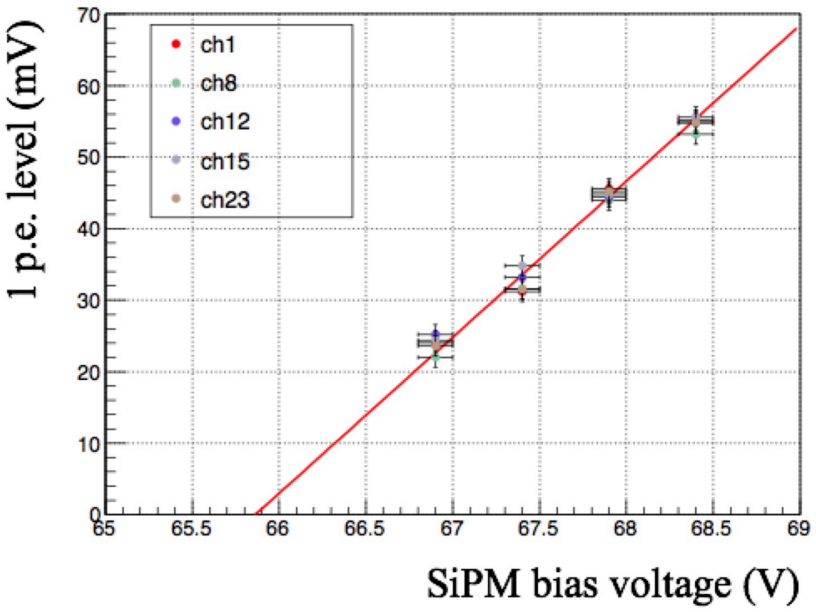

Figure 6-13: Breakdown voltages of the SiPMs. Each of the circle colors corresponds to the sampled channel of the detector. Red line indicates the linear fitting result. The breakdown voltage of the SiPM was obtained by a zero-cross of the fitting function.

study, muonium spin flip signal is not significantly affected by this systematic event loss. The details of the simulation study if this systematic effect are described in Chapter 8.

6.3.6 Timing resolution

Figure 6-21 shows measured hit timing difference between the near and the far layer of the detector when a positron from muon decay is detected. Timing resolution of the detector was evaluated to be 4 ns by the fitting to a Gaussian on a background. A red solid line indicates the fitting result. A red dashed line corresponds to a Gaussian component of the fitting function. The obtained timing resolution was good enough to measure a periodic structure in the time dependent spin flip signal.

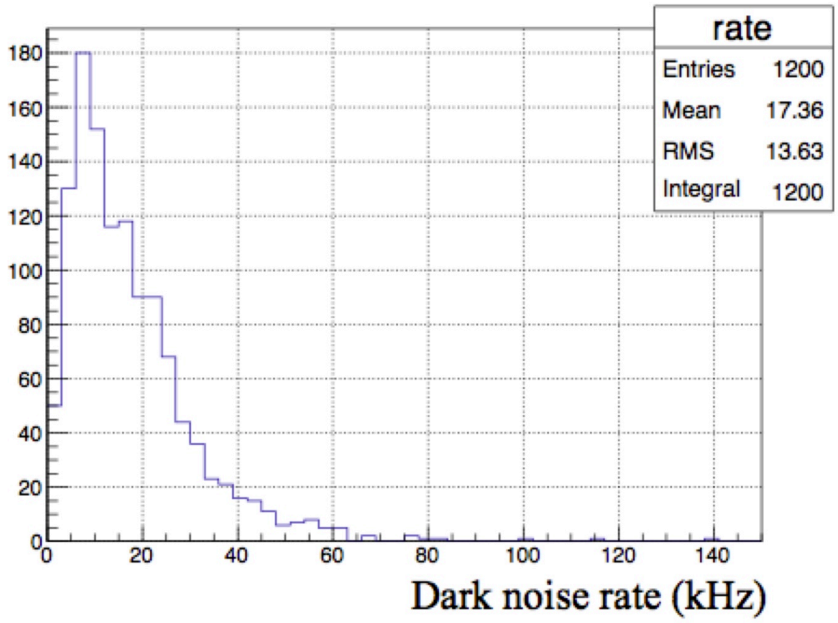

Figure 6-14: Dark noise rate distribution of the SiPMs. Discriminator threshold was set to 1.5 photo-electron equivalent level. The bias voltage for the SiPM was set to the operation voltage.

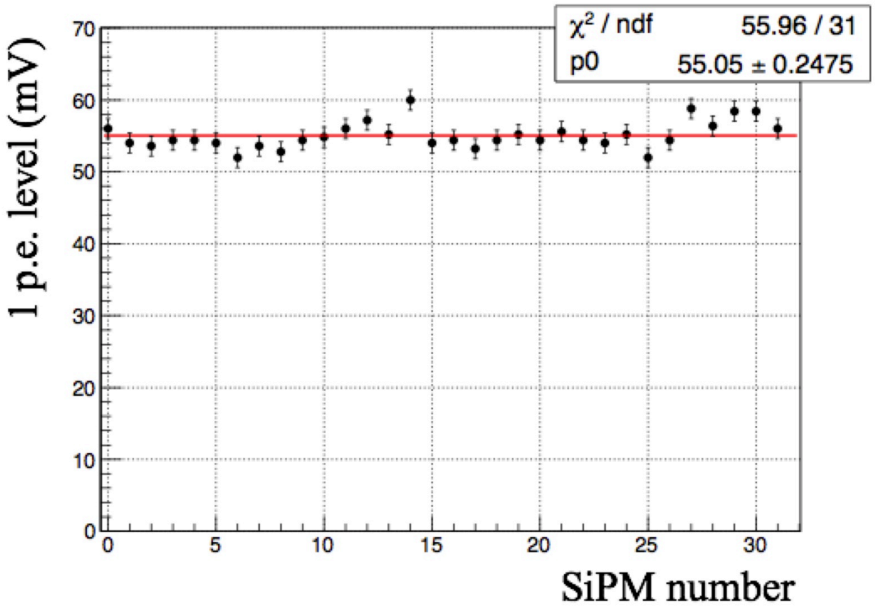

Figure 6-15: Pulse heights of an one-photon equivalent signal of the detector. The horizontal axis indicates the number of channel in the sampled detector module. Red line corresponds to the fitting result with a constant function.

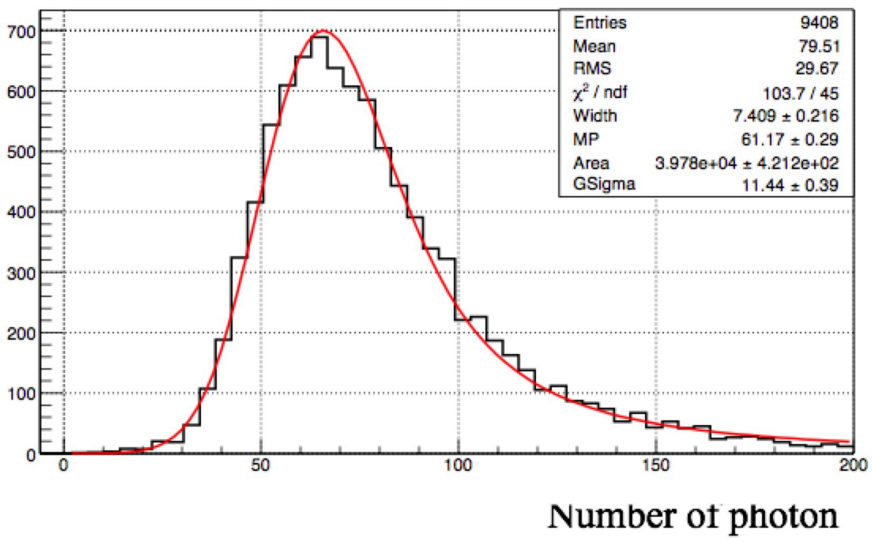

Figure 6-16: Photon yield of a ^{90}Sr-^{90}Y beta source. The bias voltage for the SiPMs was set to the operation voltage. Red line indicates the fitting result with a Landau distribution smeared by a Gaussian. Only electrons with the energy of 1 MeV or higher triggered the data taking.

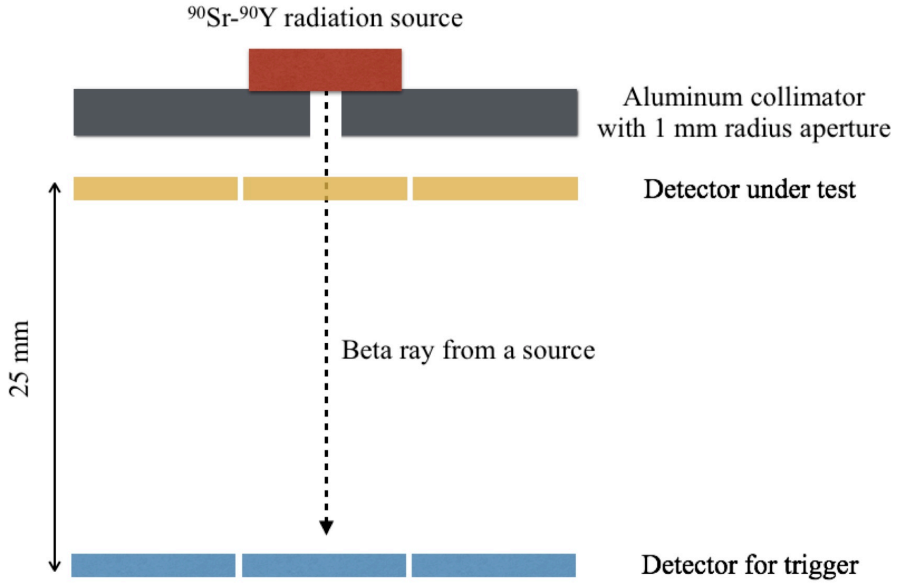

Figure 6-17: Experimental setup for the photon yield measurement. Electrons from a ^{90}Sr-^{90}Y source were irradiated to the detector through the aluminum collimator with an aperture. The detector under test was placed between the source and the trigger detector. Only electrons with the energy of 1 MeV or higher are reachable to the trigger detector.

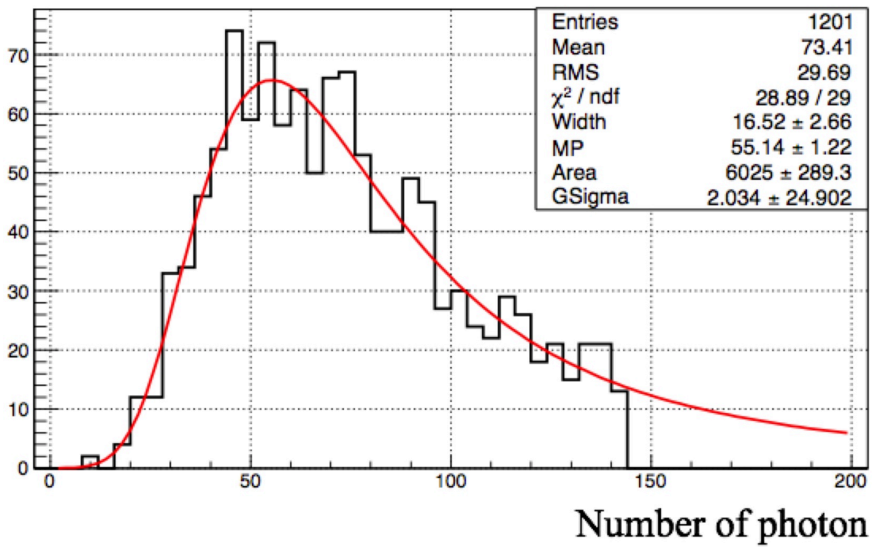

Figure 6-18: Photon yield of a positron from muon decay at rest. Red line indicates the fitting result with a Landau distribution smeared by a Gaussian.

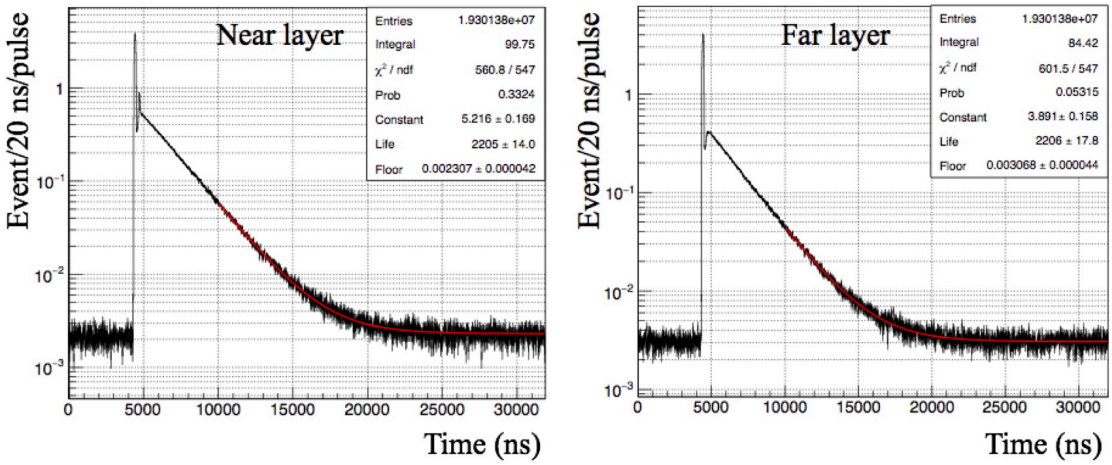

Figure 6-19: Time spectrum of the positrons from muon decay: (left) lear layer data; (right) far layer data. The vertical axis was normalized by the number of muon beam pulse during the measurement. Red line indicates the fitting result with an exponential function on a constant background. The sharp peak at 4800 ns corresponds to the prompt positrons. For a near layer case, the second peak due to a signal overshoot after the prompt incident was observed.

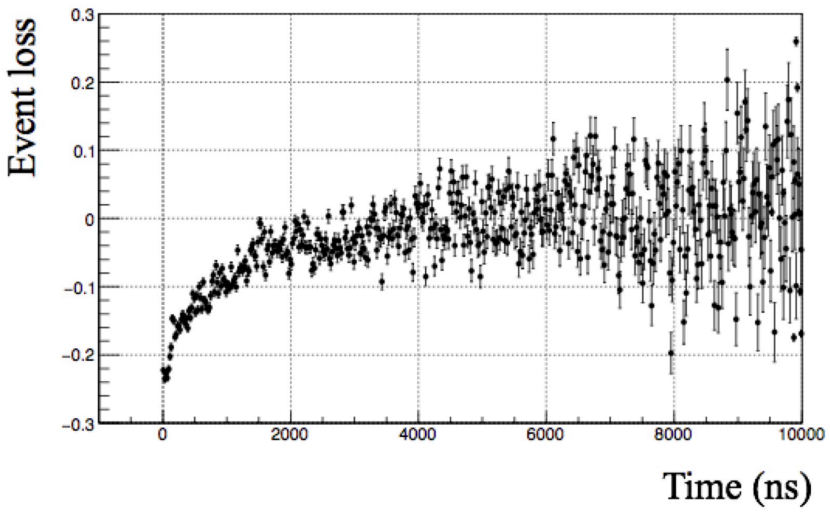

Figure 6-20: Event loss as a function of the elapsed time from muon pulse arrival. The event loss was estimated by a difference between the time spectrum and the extrapolated fitting result in Fig. 6-19. About 20 % of the pileup event loss was observed just after a muon pulse arrival. The measurement was performed with the beam power of 200 kW which corresponds to 3×10^6 muons per second.

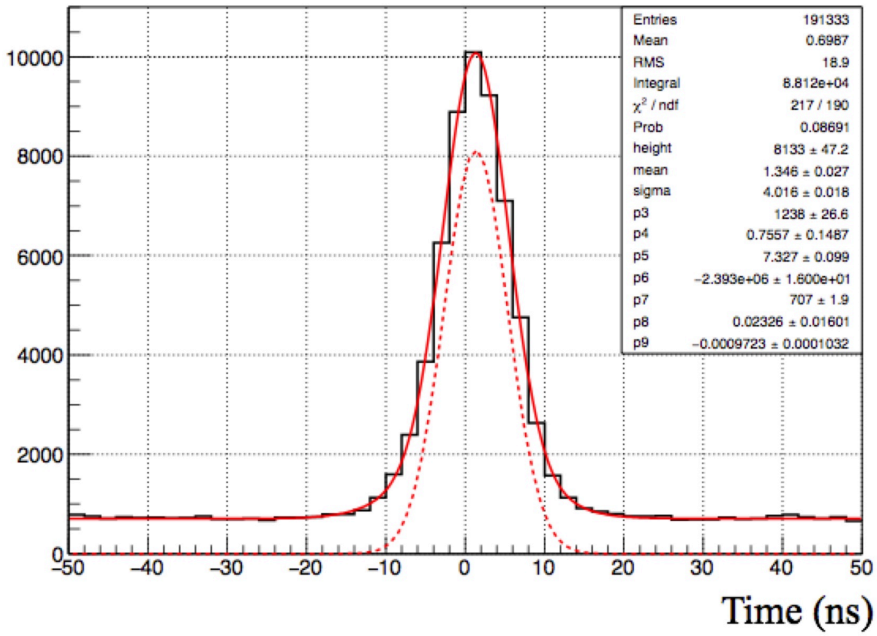

Figure 6-21: Hit timing difference between the near layer and the far layer of the positron detector. Red solid line corresponds to the fitting result with a Gaussian on a background. Red dashed line corresponds to the Gaussian component of the fitting result. The timing resolution of the detector was estimated to be 4 ns based on the width of the Gaussian.

Chapter 7

Experimental setup and data set

This chapter describes the experimental setup for the beam profile measurement and resonance spectroscopy. The experiments were performed at J-PARC MLF MUSE D2 beamline during 2016A operation period in June 2016. Proton accelerator was operated at 200 kW of beam power with a single bunch mode.

7.1 Experimental setup

The experiment was separated into two stages. Firstly, muon stopping distribution in krypton gas target was measured by using the three-dimensional muon beam imager. After a week of interval for setup exchange and baking of the gas chamber, the measurement of muonium HFS resonance was performed. Magnetic field distribution and gas impurity were measured before and after of the resonance measurement. The details of the apparatus are described in Chapter 3.

7.1.1 Muon beam profile measurement

To obtain the spacial distribution of muonium in the target gas, the muon stopping distribution was measured. Figure 7-1 shows an experimental setup. A plastic scintillator disk was placed inside of the gas chamber. A luminescence from the scintillator was amplified by an image intensifier and detected by a CCD camera. The details

of the muon beam imager are described in Chapter 5. The scintillator and imaging detector were remotely controlled in synchronization. To shield an external light, entire setup was covered with a black sheet. Temperature of the CCD was controlled by an air-cooling fun and a Peltier element cooler. At the beginning of the measurement, beamline parameters were tuned to coincide the beam center and the gas chamber center. A current in the last bending magnet and the correction coil at the Wien filter were optimized. After the beam tuning, the measurement was performed at the gas pressure of 0.3 atm, 0.5 atm, and 1.0 atm. After the completion of the

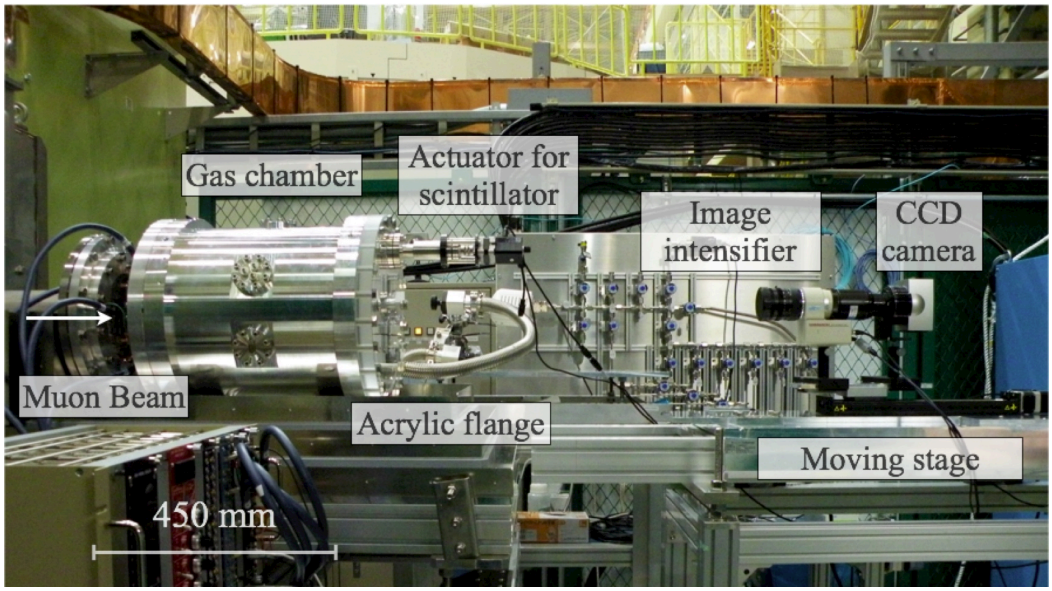

Figure 7-1: Experimental setup of the beam profile measurement. The plastic scintillator was placed inside the gas chamber. The longitudinal positions of the scintillator, the imaging intensifier, and the CCD camera were remotely controlled in synchronization with each other. During the measurement, the entire setup was covered with the black sheet.

beam profile measurement, the beam imager was removed and the magnetic shield was constructed. A baking of the gas chamber was performed to reduce residual gas impurities. The particle detectors were installed after the baking.

7.1.2 Muonium resonance measurement

Figure 7-2 shows an experimental setup of the resonance measurement. Inside of the three-layered magnetic shield, the gas chamber and particle detectors were installed. Temperature inside of the shield was controlled by a local air conditioner (Orion PAP01B). Gas pressure was monitored by a capacitance gauge. Positrons from muonium decay were measured by the positron detector which was placed at downstream of the gas chamber. In order to extract a muonium spin flip signal from decay positron time spectrum, a measurement was performed both with and without microwave resonance.

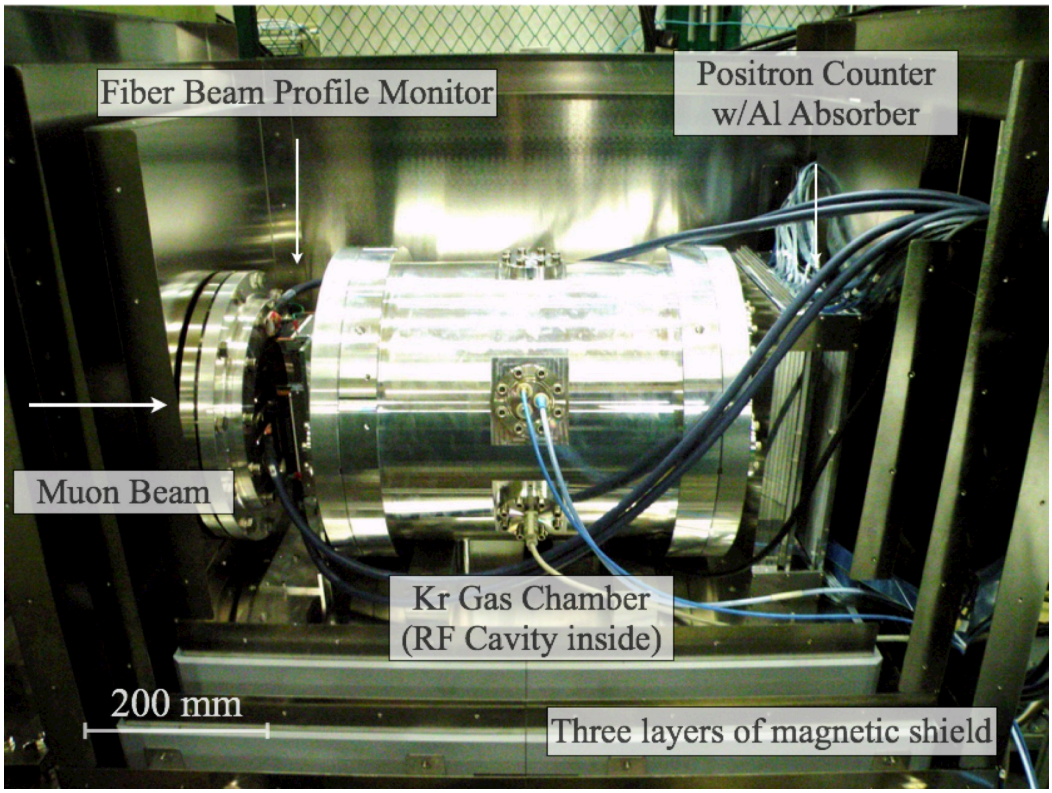

Figure 7-2: Experimental setup of the resonance measurement. The fiber beam profile monitor and the positron detector were placed at front and behind the gas chamber, respectively. The aluminum absorber was placed between the gas chamber and the detector. During the measurement, the entire setup was enclosed by the magnetic shield.

Figure 7-3 shows the microwave cavity after installation. Magnetic loop antennas for microwave input and pickup were installed at upper ports on the cavity. An alu-

minum tuning bar with piezo positioner was attached at lower port of the cavity. Position of the tuning bar was controlled remotely to adjust a resonance frequency of the microwave cavity. Microwave output was controlled remotely and switched ON/OFF every minute to prevent a local temperature rise caused by power consumption at the cavity. This microwave switching is effective to suppress the systematic uncertainties arising from the temporal variations of measurement environment. In principle, the temporal variation with a time scale of longer than minutes are highly suppressed by this technique.

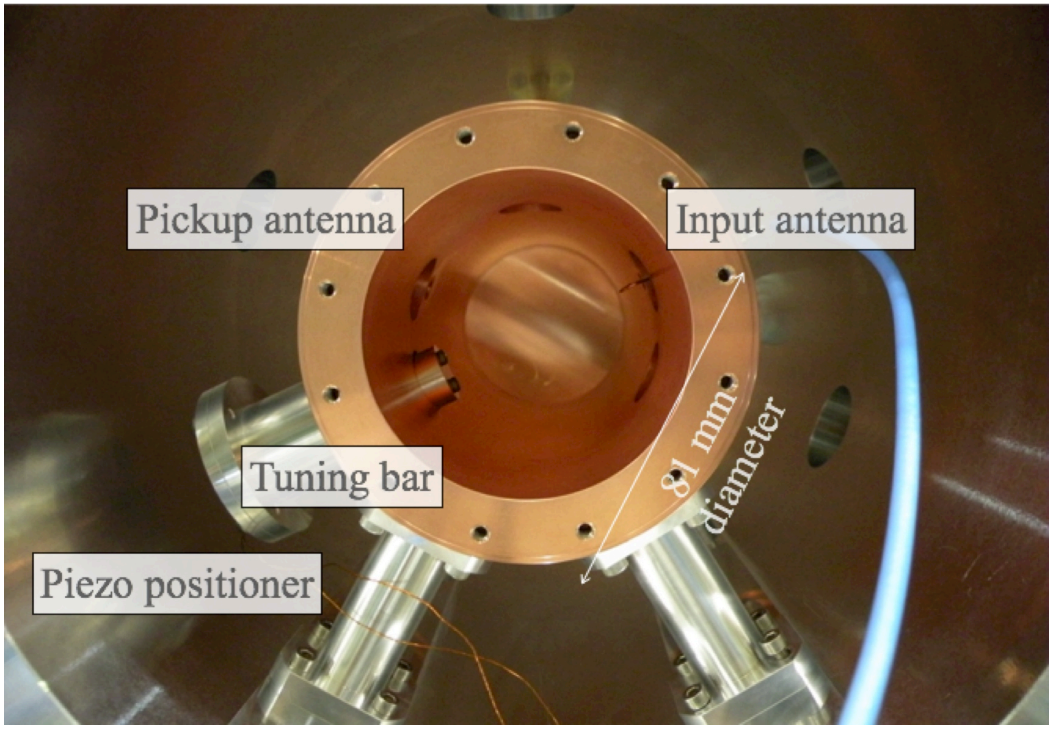

Figure 7-3: Microwave cavity in the gas chamber. The magnetic loop antennas for microwave input and monitoring were attached. The tuning bar with the piezo positioner was utilized for a tuning of the cavity resonance frequency.

Magnetic field survey

Figure 7-4 shows measurement setup for static magnetic field survey. The fluxgate magnetometer was inserted in the microwave cavity and three-dimensional magnetic field was measured. By using an attachment for a probe holder, the magnetometer

Table 7.1: Summary of the experimental conditions for the spectroscopy measurement. The beam conditions and other experimental parameters are shown.

Conditions	Values
Beam intensity	3×10^6 μ^+/s
Beam momentum	27.4 MeV/c
Beam bunching	single pulse, 100 ns FWHM
Beam reputation	25 Hz
Beam duration	8 hours*
Target gas density	1.0 atm
Microwave power	3 W

* Total for the frequency scan

was displaced in radial direction. The magnetometer was rotated around the rod and translated along the longitudinal axis of the cavity.

7.2 Data set

To obtain a resonance lineshape of muonium HFS, the measurement was performed at several values of microwave resonance frequency. Table 7.2 summarizes data set for the microwave frequency scan. In order to confirm a validity of the experiment, a measurement at mismatched frequency tuning between the cavity and the signal generator was performed. This special measurement condition is denoted as off-resonance.

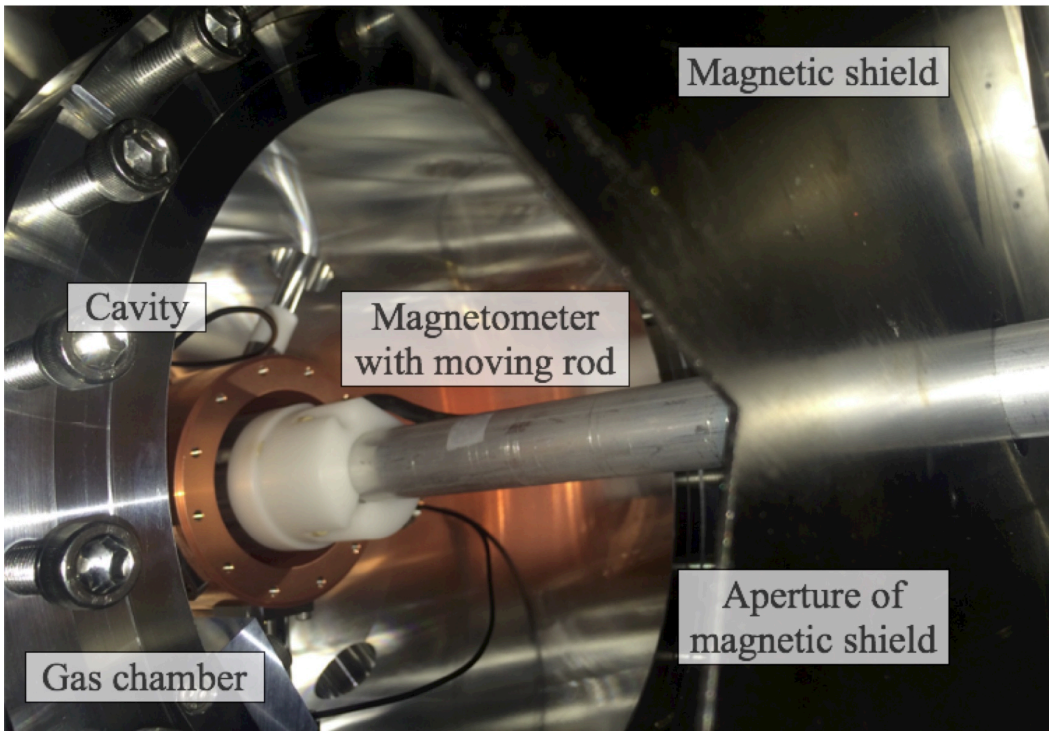

Figure 7-4: Magnetic field survey in the microwave cavity. The fluxgate magnetometer was inserted into the cavity in order to measure the three-dimensional magnetic field map.

Table 7.2: Data set for the microwave frequency scan. The microwave frequency and the time sequential order of the measurement are summarized.

Microwave frequency (MHz)	Frequency detuning from HFS (kHz)	Scan order
4463.3	0	1
4463.5	200	2
4463.8	500	3
4464.3	1000	9
4464.8	1500	4
4463.1	-200	5
4462.8	-500	6
4462.3	-1000	10
4461.8	-1500	8
Off Resonance		7

Chapter 8

Data analysis

This chapter describes data analysis for both beam profile and resonance measurements. The first part of the chapter corresponds to reconstruction of muonium spacial distribution in the krypton gas target. The second part corresponds to determination of the resonance frequency of muonium HFS transition.

8.1 Spacial distribution of muonium

In this section, data analysis of the muonium distribution measurement by using the muon beam imager is discussed. The details of the muon beam imager were described in Chapter 5.

8.1.1 Timing structure of the beam

Light amplification by an image intensifier was triggered by a gating signal with the width of 100 ns. In order to optimize this gating, timing dependence of the light yield was measured. Figure 8-1 shows measured light yield as function of delay amount for gating trigger. The first peak corresponds to the prompt positron, and the second peak corresponds to the pulsed muon. Timing interval between two peaks gives a time of flight difference of muon and prompt positron. It was evaluated as 284 ns and utilized to determine a muon pulse arrival in decay positron analysis. In the

beam profile measurement, the amount of gating delay was set to 101,600 ns as an optimum.

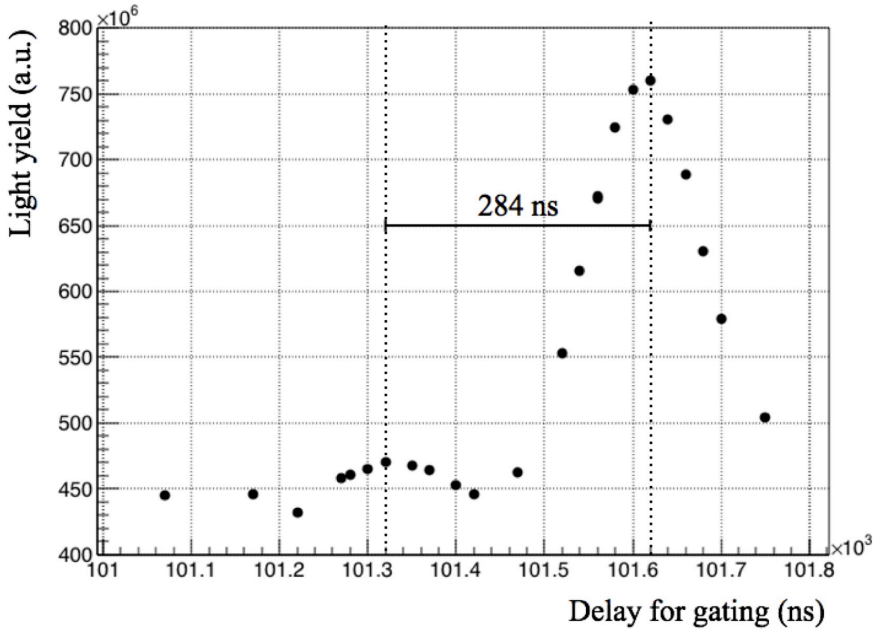

Figure 8-1: Light yield as a function of gate timing for the imaging intensifier. The first and second peaks correspond to the prompt positron and the pulsed muon, respectively.

8.1.2 Profile analysis

As described in the latter half of Chapter 4, the two-dimensional muon beam profile was measured and analyzed. Background arising from CCD thermal noise was subtracted. Photon statistics at each pixel was estimated based on the relation between mean and root-mean square of CCD charge.

Measured beam profile was evaluated by the fitting to a two-dimensional Gaussian on a background. Typical profile and the fitting result are shown in Fig. 8-2. The left figure corresponds to a measured profile, the right figure corresponds to a curved surface obtained by the fitting. Beam width and center were evaluated based on the fitting result. As an alternative approach to evaluate a beam profile, the one-dimensional projections of the beam profile were analyzed. Measured two-dimensional

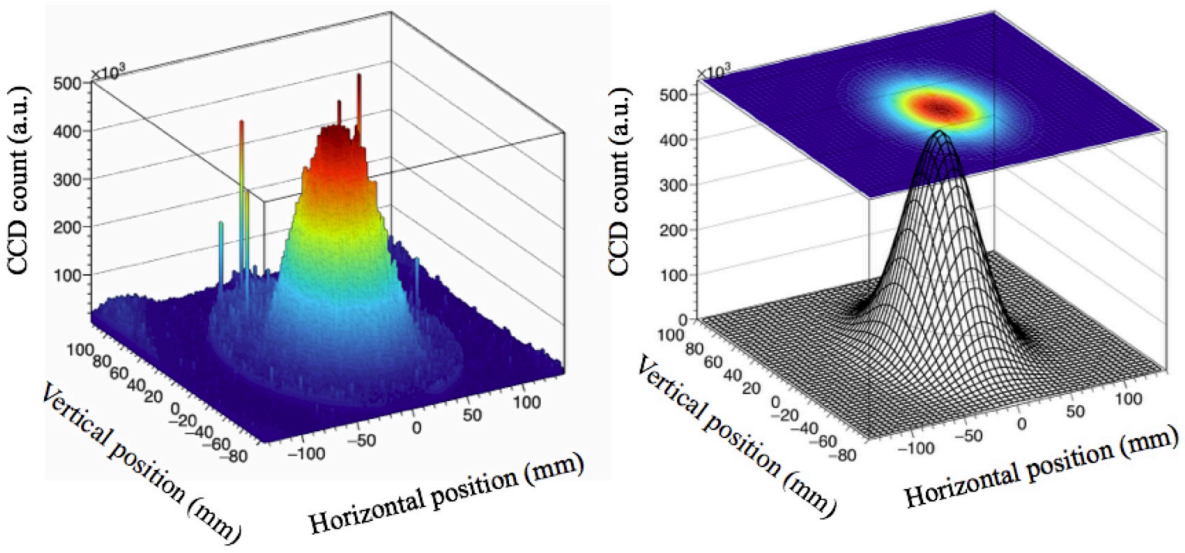

Figure 8-2: Two-dimensional muon beam profile: (left) two-dimensional histogram of CCD charge; (right) fitting result with a two-dimensional Gaussian.

profile was divided into sub-bands whose width was 1.4 mm. Figure 8-3 represents an example of this analysis. A Gaussian fitting was performed to each sub-band.

Figure 8-4 shows obtained beam parameters from each projection. The upper figures correspond to vertical projections, the lower figures correspond to horizontal projections. Red lines indicate beam parameters obtained by two-dimensional fitting aforementioned. At the vicinity of a profile center, there was a good agreement between two approaches. The analysis method was applied to evaluate beam profiles at each longitudinal position.

8.1.3 Evaluation of the beam center and the beam width

As a result of two-dimensional fitting of beam profiles, a muon beam center and a beam width were evaluated as a function of longitudinal position. Figure 8-5 shows a result for beam center for a case of 1.0 atm gas pressure. The left figure corresponds to a horizontal beam center, while the right figure corresponds to a vertical one. Black circles indicate the measurement result while red ones indicate the simulation result. The result suggests systematic uncertainty in the measurement. A putative cause of the systematics is misalignment of the muon beam imager. However, for

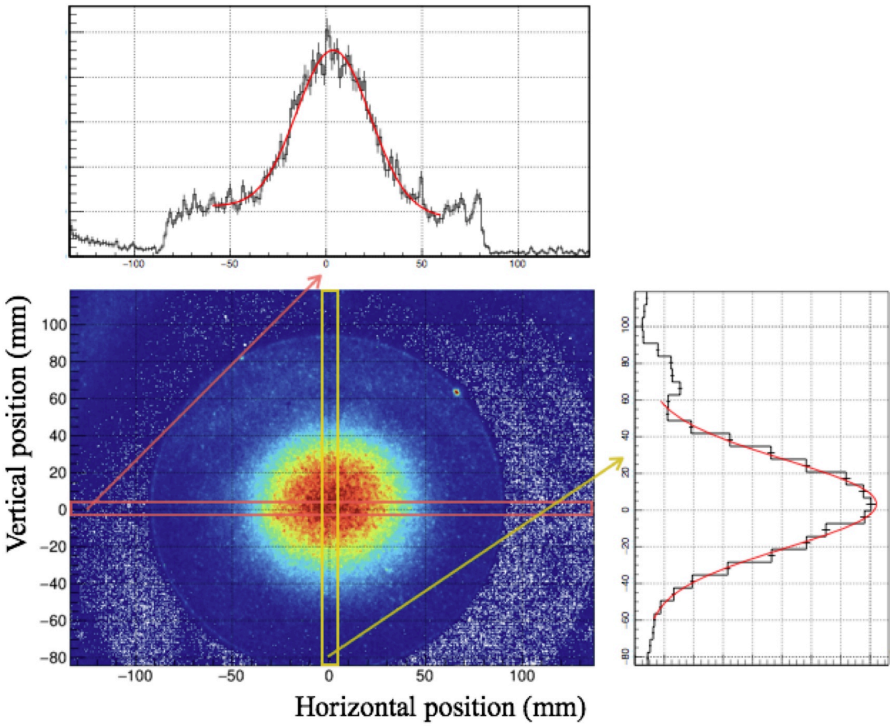

Figure 8-3: One-dimensional projections of the muon beam profile. The two-dimensional beam profile was divided into the plural one-dimensional projections in the horizontal and vertical directions. Each sub-region has the width of 1.4 mm.

both direction cases, this systematic uncertainty is within a range of 1 mm. Fig. 8-6 shows a result for beam width at a gas pressure of 1.0 atm. Black circles correspond to the experimental results, while red ones correspond to the simulation results. A red dashed line is a fitting curve defined as $y = a+bx+c\sqrt{x}$ where a is an initial beam width, b is a contribution from muon momentum direction, and c is a contribution from multiple scattering. Beam spread was mostly dominated by angular spread of the beam.

8.1.4 Stopping distribution

To obtain the muon stopping distribution on the beam axis, longitudinal position dependence of the light yield was evaluated. The number of stopped muon in a short distance is in proportion to a differentials of the light yield. Therefore, muon stopping density at each measurement point is extracted from a difference between the light

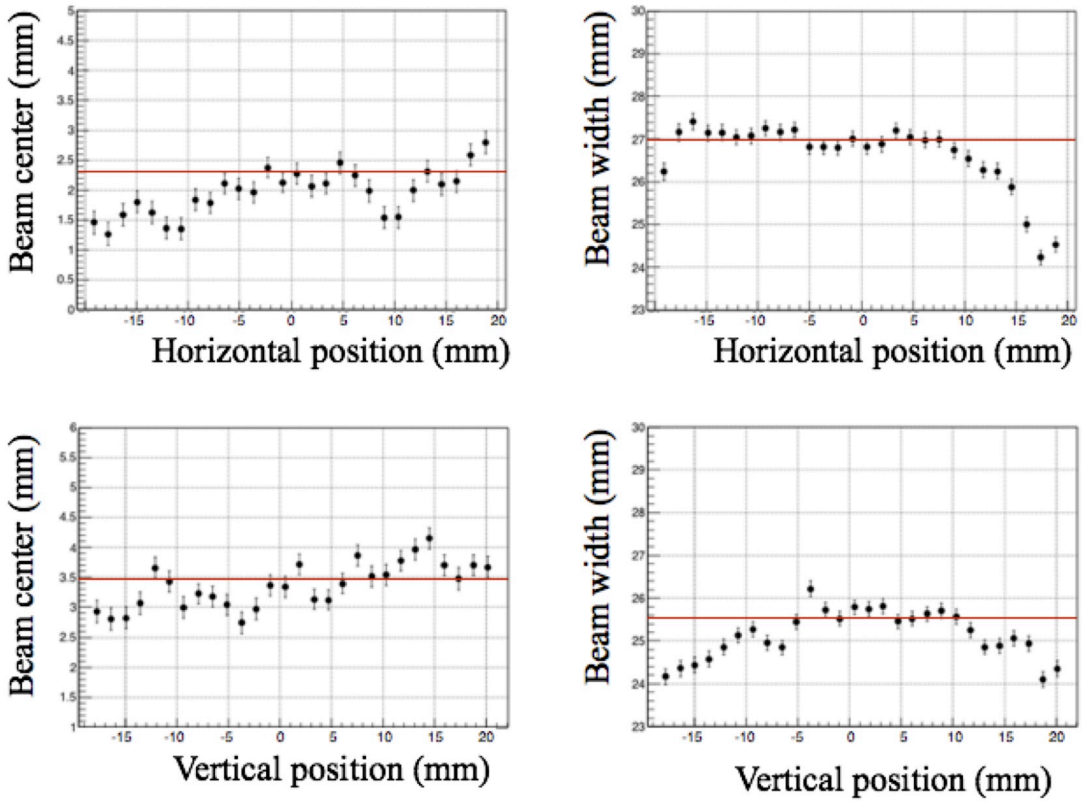

Figure 8-4: Beam parameters obtained from the one-dimensional projections: (upper left) horizontal beam center; (upper right) horizontal beam width; (lower left) vertical beam center; (lower right) vertical beam width. Red lines correspond to the results of two-dimensional fitting.

yields at neighboring measurement points.

Light yield

Figure 8-7 shows a light yield as a function of longitudinal position. Red circles correspond to a result at 1.0 atm gas pressure. Green and blue ones correspond to 0.5 atm and 0.3 atm, respectively. In each case, clear decrease of the light yield as a function of longitudinal position was observed. Note that a thin black paper was attached to the target scintillator. Hence, its contribution to a range of muon should be considered. According to a measured thickness and density of the black paper, a plus-correction to a muon range was about 85 mm. Because the paper was placed in close contact with the scintillator, measurement of beam width was not affected

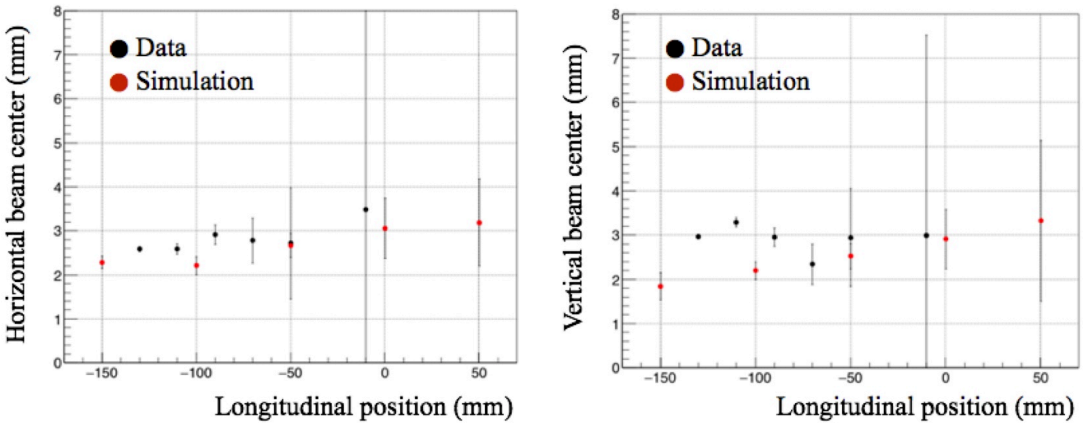

Figure 8-5: Muon beam center as a function of the longitudinal position: (left) horizontal beam center; (right) vertical beam center. The target gas pressure was 1.0 atm. Black and red circles correspond to the experimental and simulation results, respectively. The cavity upstream edge was at -155 mm on the horizontal axis and the downstream one was at 75 mm.

by the attachment. To avoid a background due to a stopped muon in the foil of the cavity, no incident muons should reach the end of the cavity. Considering this range correction, incident muons should stop within a range of 145 mm. Therefore, a gas pressure was set to 1.0 atm in the spectroscopy experiment.

Muon energy correction

Light yield of muon beam is proportional to the number of muon and its kinetic energy. The target scintillator disk was thick enough to stop muons with the kinetic energy of 4 MeV. To compare a muon density at each longitudinal position, variations of muon kinetic energy arising from energy loss in krypton gas should be considered. Figure 8-8 shows simulated muon kinetic energy as a function of longitudinal position. The left figure represents energy distribution, the right figure corresponds to an average of energy. Krypton gas pressure was set to 1.0 atm.

8.1.5 Reconstruction of muonium spacial distribution

In order to obtain a stopping density in upstream region, an experimental result without an attachment was combined. Except for a black paper attachment, beam

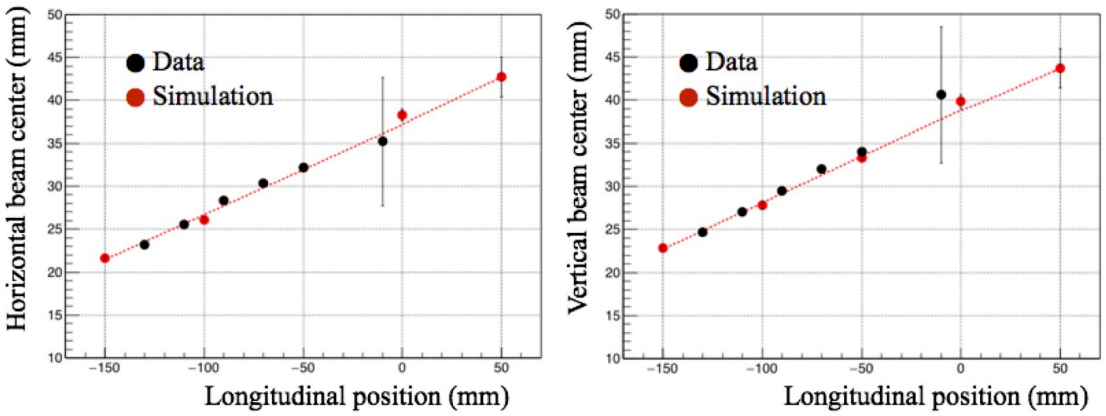

Figure 8-6: Muon beam width as a function of the longitudinal position: (left) horizontal beam width; (right) vertical beam width. The target gas pressure was 1.0 atm. Black and red circles correspond to the experimental and simulation results, respectively. The cavity upstream edge was at -155 mm on the horizontal axis and the downstream one was at 75 mm. In both figures, dashed lines indicate the fitting result.

momentum and amount of material in the beam path for both experiments were equivalent. Figure 8-9 shows a muon stopping distribution projected on the beam axis.

By combining two-dimensional beam profiles and longitudinal stopping density, a three-dimensional muon stopping distribution was reconstructed as shown in Fig. 8-10.

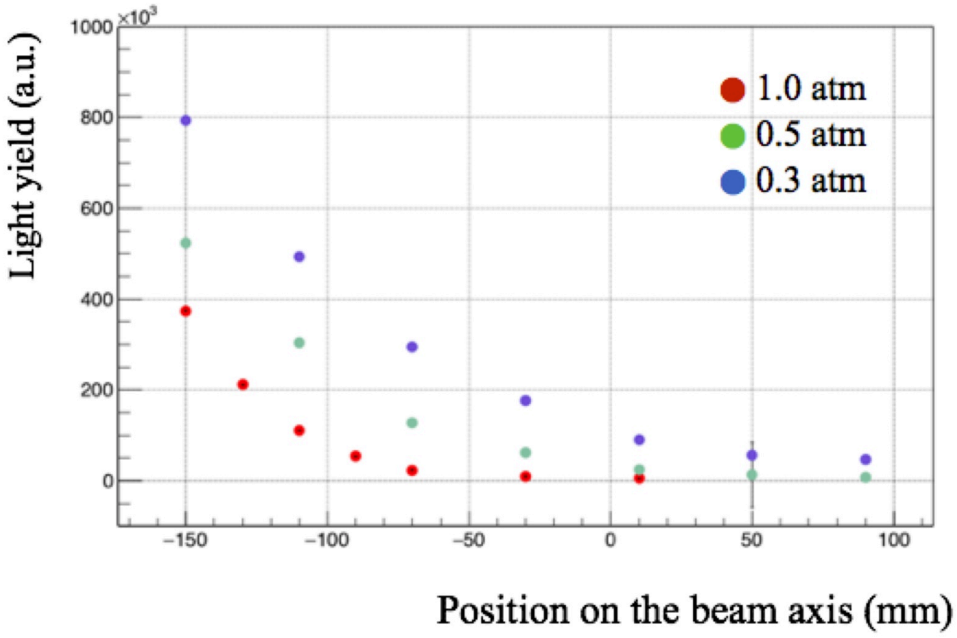

Figure 8-7: Light yield of the pulsed muon beam as a function of longitudinal position. Red, green, and blue circles correspond to the results with the gas pressure of 1.0 atm, 0.5 atm, and 0.3 atm, respectively. The cavity upstream edge was at -155 mm on the horizontal axis. The downstream one was at 75 mm.

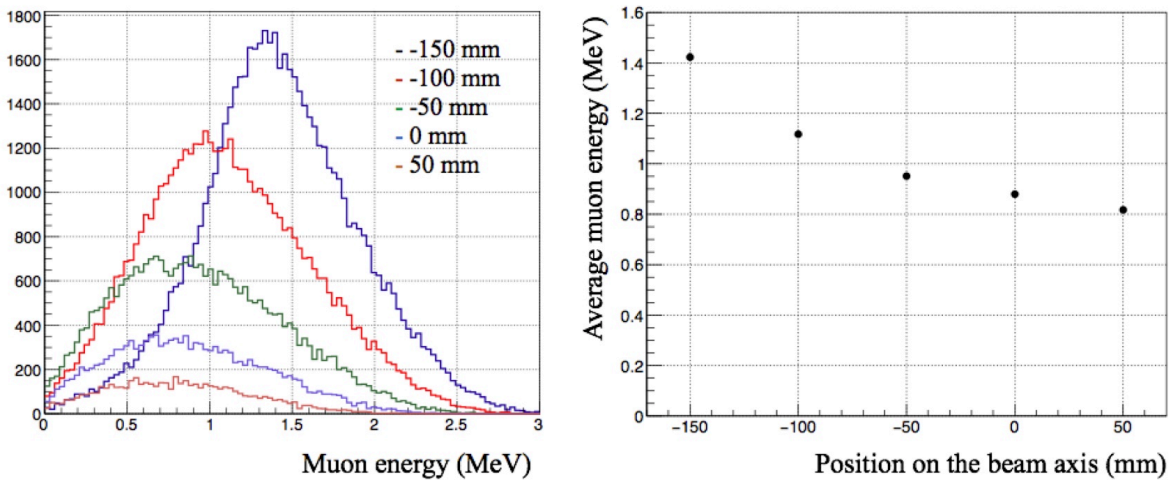

Figure 8-8: Muon kinetic energy as a function of the longitudinal position: (left) energy distribution; (right) average of the energy. The initial muon energy was set to 4 MeV and the target gas pressure was set to 1.0 atm.

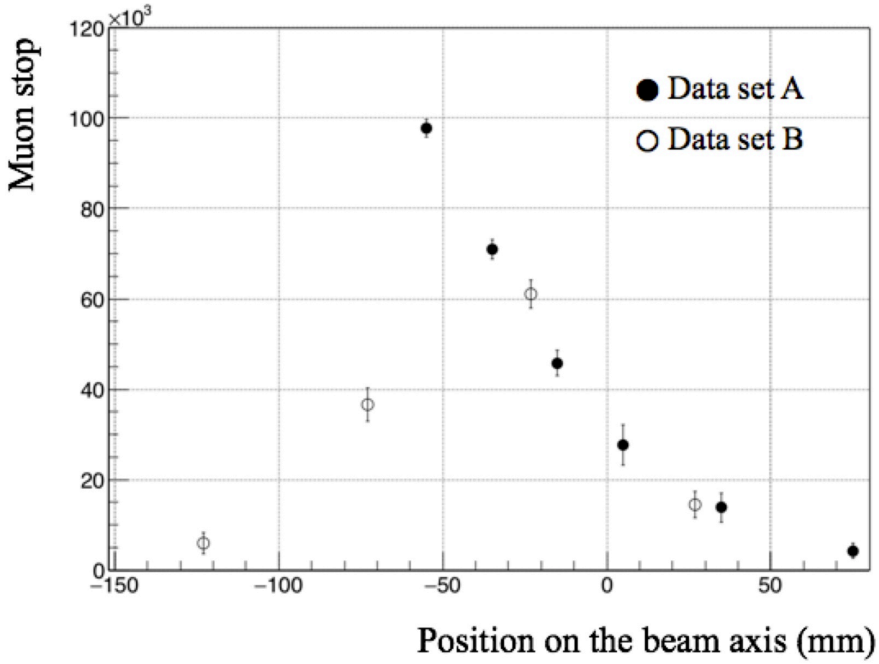

Figure 8-9: Muon stopping distribution on the beam axis. The cavity upstream edge was at -155 mm on the horizontal axis. The downstream one was at 75 mm. Black solid circles indicate the result with the black paper which is denoted as A. Outlined circles indicate one without the paper attachment which is denoted as B.

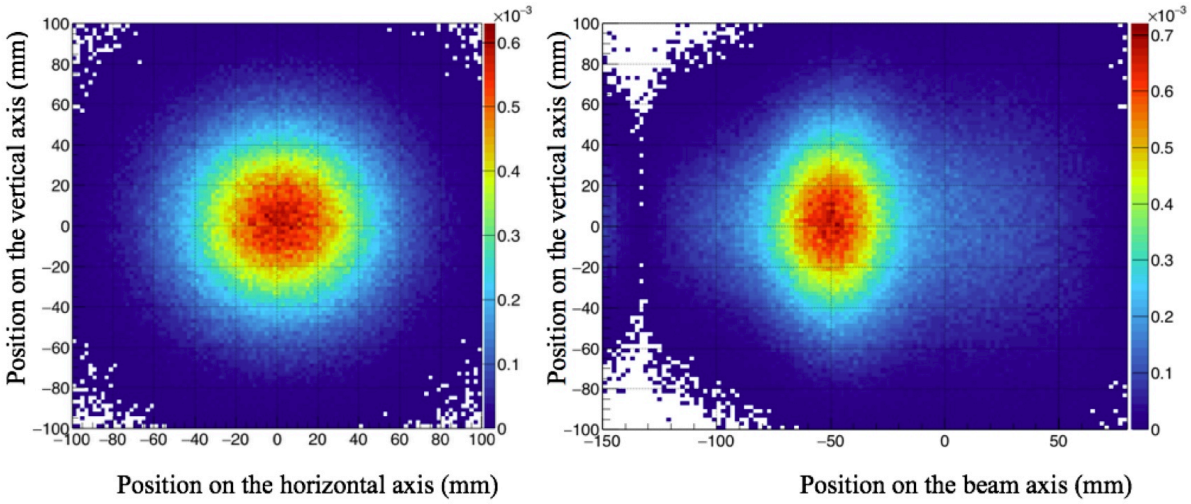

Figure 8-10: Muon stopping distribution in krypton gas at 1.0 atm pressure: (left) view from the longitudinal axis; (right) cross-sectional view.

8.2 Microwave spin flip of muonium

In this section, data analysis of the muonium HFS resonance spectroscopy is discussed. In the measurement, experimental observable is a time dependent counting of positrons from muon and muonium decay. Decay positrons were detected by the positron counter which was placed at the downstream of the gas chamber. The details of the positron detector were described in Chapter 6.

8.2.1 Data analysis procedure

Muonium spin flip signal is extracted from a decay positron time spectrum. Data analysis procedure is as follows.

1. Validation of data taking trigger by using pulse-by-pulse event rate
2. Search for positron hit cluster and cluster merging
3. Coincidence paring between hits on each layer of the detector
4. Extraction of time dependent spin flip signal by taking the counting ratio between microwave ON and OFF

8.2.2 Trigger validation

Data taking trigger for the readout electronics was configured to correspond to a muon pulse arrival one-by-one. Hence, no trigger signal is generated when a proton accelerator stops. However, an accidental failure of beam current monitor may provide a trigger signal even in a case of unexpected beam loss.

Figure 8-11 shows the trends in hit number for each layer of the detector. Red circles corresponds to the number of hit detected by the near layer. Blue circles correspond to one by the far layer. Temporary beam loss was detected and events with no beam were excluded from the following analysis.

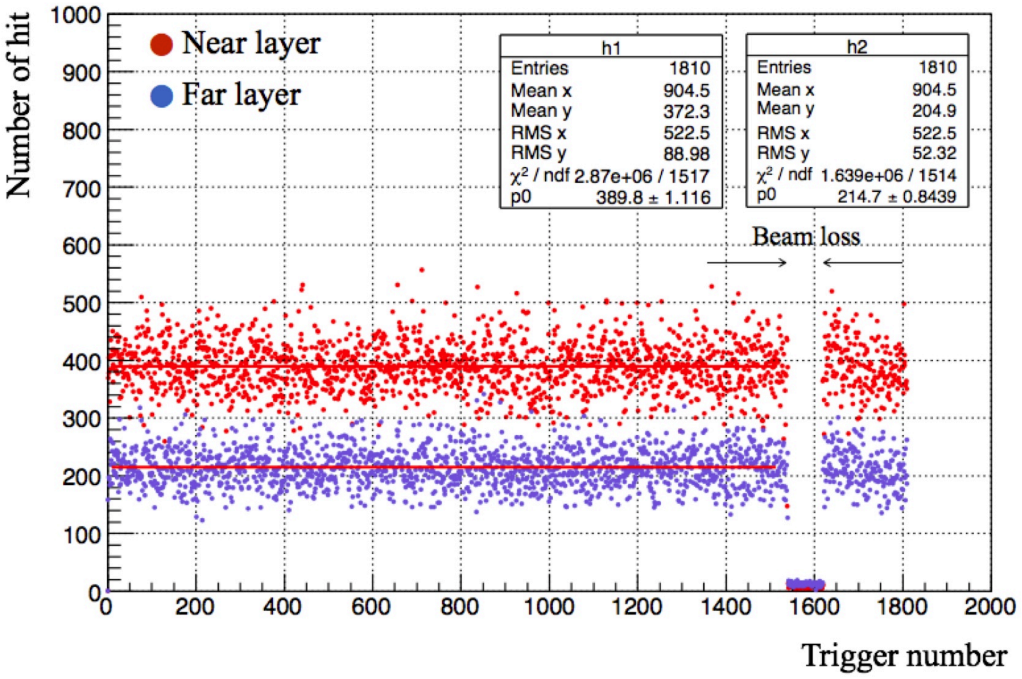

Figure 8-11: The number of hit for each trigger pulse. Red and blue circles represent the number of hit on the near and far layer of the positron detector, respectively. Red solid line indicates an average of the hit number.

8.2.3 Spacial distribution of positron detection

Figure 8-12 shows a hit position distribution on the near layer of the detector. The left figure corresponds to two-dimensional hit map, the right figure corresponds to its projections to horizontal and vertical axises. Similarly to a simulation result shown in Chapter 4, most of positrons were detected by the central region of the detector. This supports that most of positrons were from inside of the cavity along the beam axis as expected by simulation. To check whether the detector is capable of correctly counting the number of positron, temporal and spacial trends in positron hits were investigated by using an event display. Figure 8-13 represents an example of the event display with the 100 ns of timing slices. Spacial position of each hit was displayed on the detector plane. Accordingly, there were some cluster-like hits to be contiguous with other hits. Figure 8-14 shows typical events which were classified to normal hits and cluster hits. Upper figures correspond to a candidate of positron coincidence event which consists of two single hits. At both layers, only one segment detected a hit

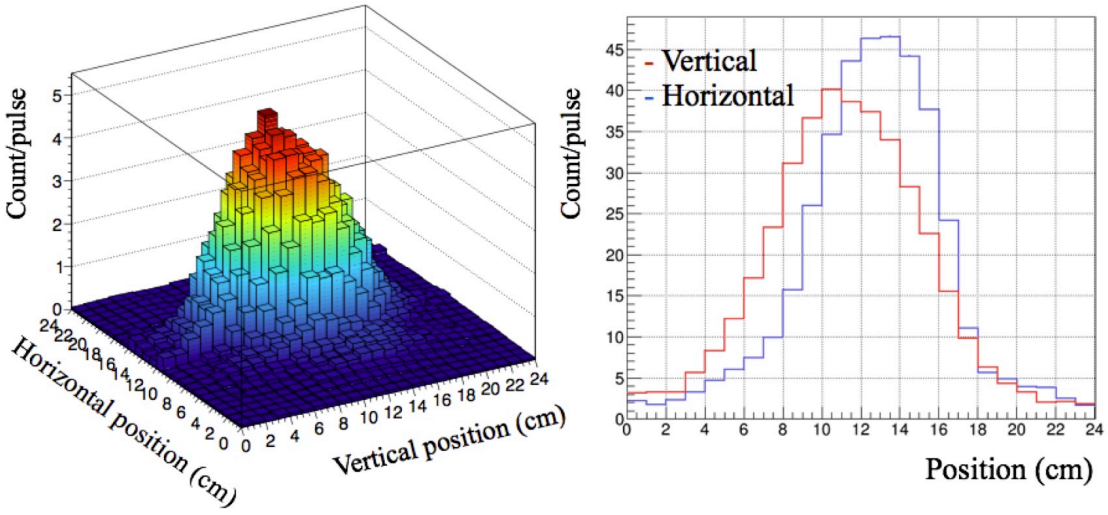

Figure 8-12: Hit map on the detector plane: (left) two-dimensional hit map on the near layer; (right) one-dimensional projections of the hit map. In the right figure, the histograms in red and blue lines correspond to the vertical and horizontal projections, respectively.

in 100 ns of timing window. Lower figures correspond to a possible coincidence event consists of a hit cluster at the near layer and a single hit at the far layer. Probable causes of hit cluster are a electromagnetic cascade, oblique incident positron, and optical or electrical cross-talk. Hit cluster arising from these origins may cause over-counting of positrons. Therefore, the cluster hits should be searched and merged into a single aggregate according to a certain criteria.

8.2.4 Clustering analysis

To distinguish and process a hit cluster, following criteria was implemented in the data analysis. Figure 8-15 illustrates this clustering process.

1. When a hit is found at a particular segment of the detector, eight neighboring of the segment are inquired wether they have a hit in a short time interval.

2. Timing interval between hits are calculated and if it is shorter than a five-fold of timing resolution, these hits are classified into a hit cluster with an identical origin.

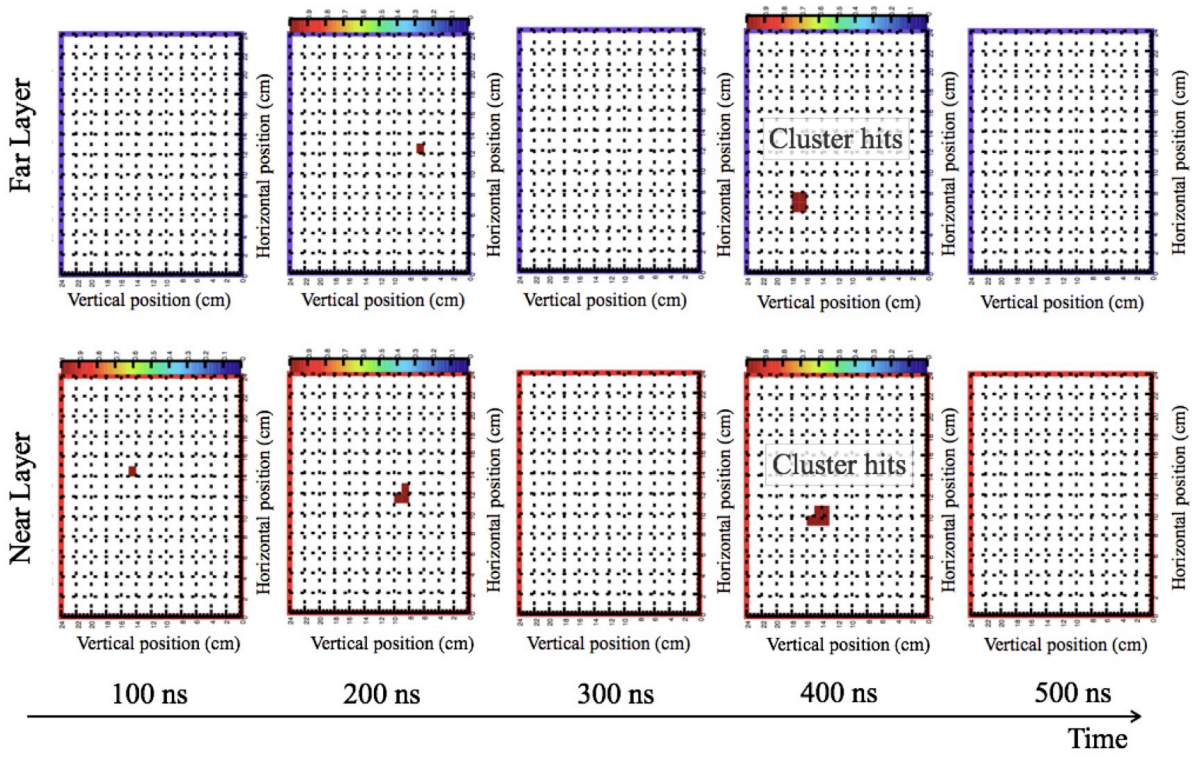

Figure 8-13: Example of an event display. Upper (lower) panels correspond to the hit map on the far (near) layer in every 100 ns. Red squares represent a segment which detected a hit. Multi-hits on neighboring segments were observed and denoted as cluster hits.

3. After a completion of cluster search at a particular segment, a next segment is selected as a target segment.

4. These search and merge processes are iterated for all segments one-by-one.

5. In the end of each event, a central of each hit cluster is determined by calculation of temporal and spacial gravitational center.

Figure 8-16 gives an example of hit clustering. In this example, two independent hit clusters were processed. Figure 8-17 shows a cluster size distribution for each layer of the detector. The histogram in black line corresponds to the result for the near layer. The one in red line corresponds to the far layer. Note that single hit cluster consists of both a positron hit and a SiPM dark count.

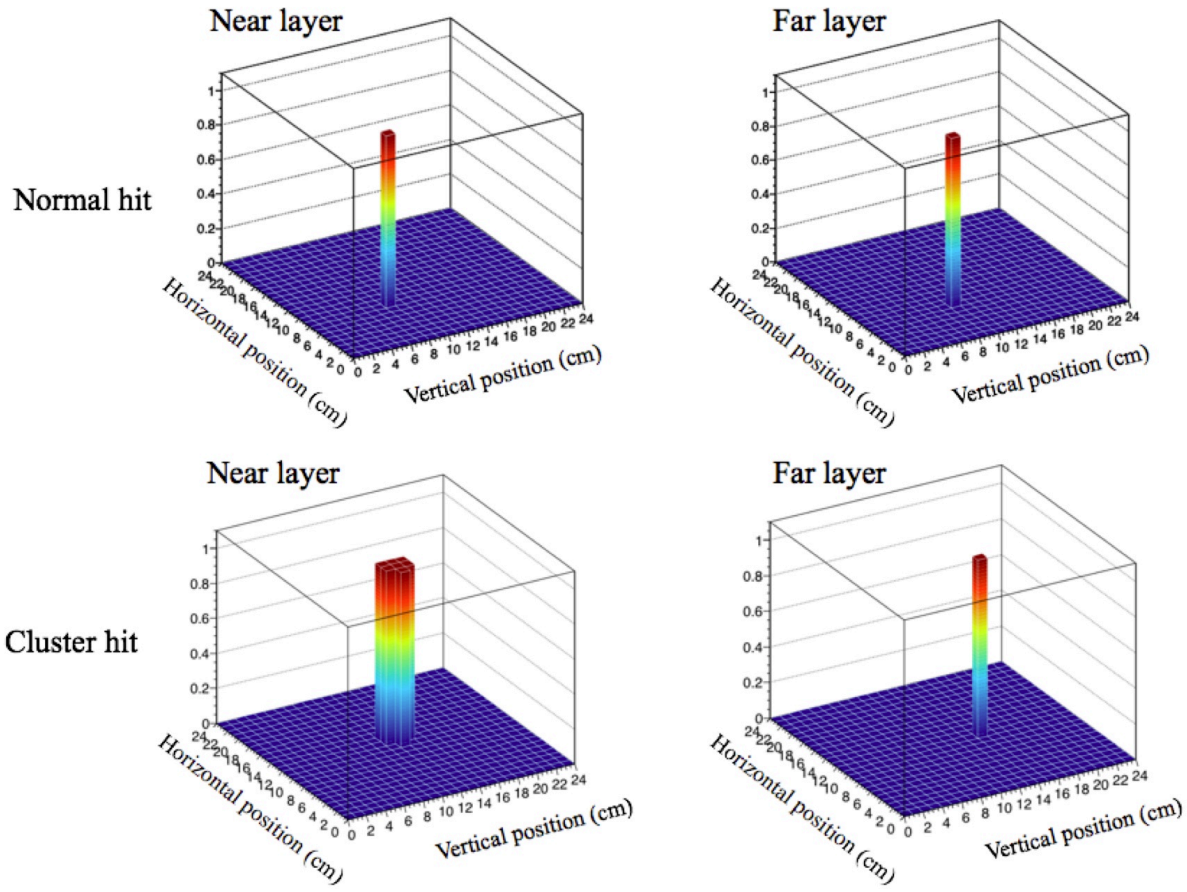

Figure 8-14: Example of cluster hits: (Upper) event display without hit cluster; (Lower) event display with a cluster hit on the near layer.

To estimate the number of uncollected cluster hit, a multiplicity at the near layer was analyzed for a case of single positron event. A single positron like event was selected by a hit on the far layer. Contribution from SiPM dark noise was excluded by a requirement for a cluster size of far layer hit. Figure 8-18 shows the number of hit cluster on the near layer when a single cluster was found on the far layer. The histogram in blue line corresponds to the result with no other event selection, the histograms in green and red lines correspond to the results with event selections in spacial distance between hits on the near layer and the far layer denoted as Δr. Figure 8-19 represents the timing difference distribution between two his clusters on the near layer when a single cluster was found on the far layer. A clear peak structure suggests that multiple clusters on the near layer are uncollected parts of a larger hit

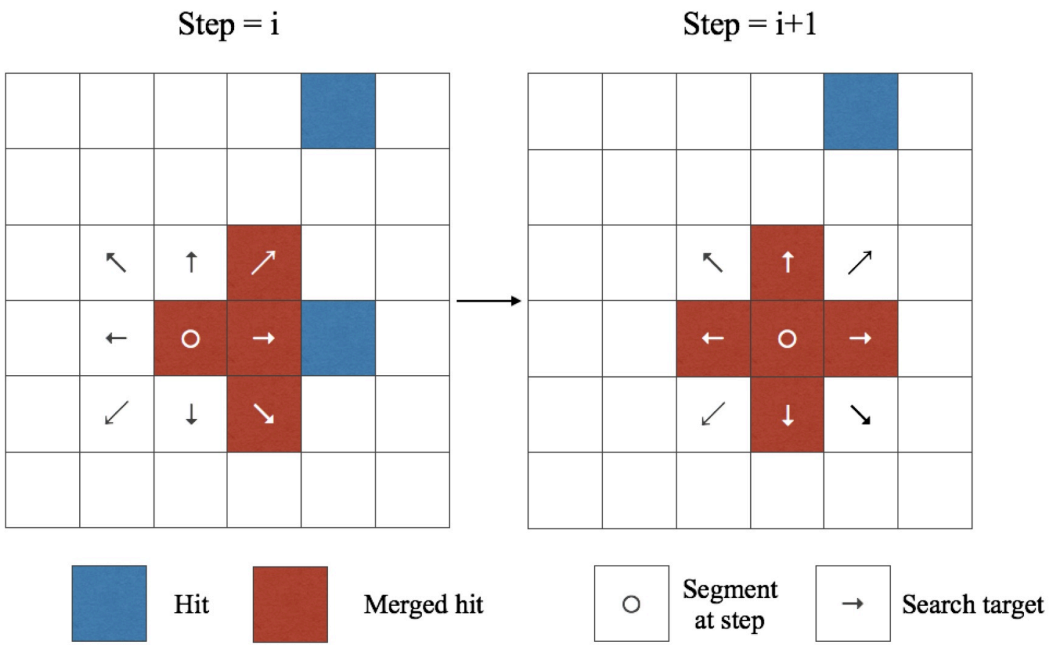

Figure 8-15: Schematic of the hit clustering process. When a hit was found at a detector segment, hits on eight neighboring segments in a short time interval are merged into a hit cluster. Timing window is set to a five-fold of the detector timing resolution. The center of the hit cluster is determined by a gravitational center. This merging process is iterated for all segments.

cluster. According to the cluster-multiplicity shown in Fig. 8-18, uncollected cluster hits rarely contribute to the coincidence analysis when $\Delta r \leq 2$ cm is required. In the following coincidence analysis, this event selection was required. In addition, this event selection in spacial distance is effective to reduce a contribution of accidental coincidence arising from two independent origins. The details of the coincidence analysis are described below.

8.2.5 Coincidence analysis

After a completion of hit clustering, coincidence analysis between two layers were performed. Figure 8-20 shows timing difference between hit clusters on the near layer and the far layer denoted as Δt. Each histogram corresponds to respective timing region which is selected by an elapsed time from a muon pulse arrival which is denoted as t_0. A Gaussian peak on a floor-like background was observed. True coincidence

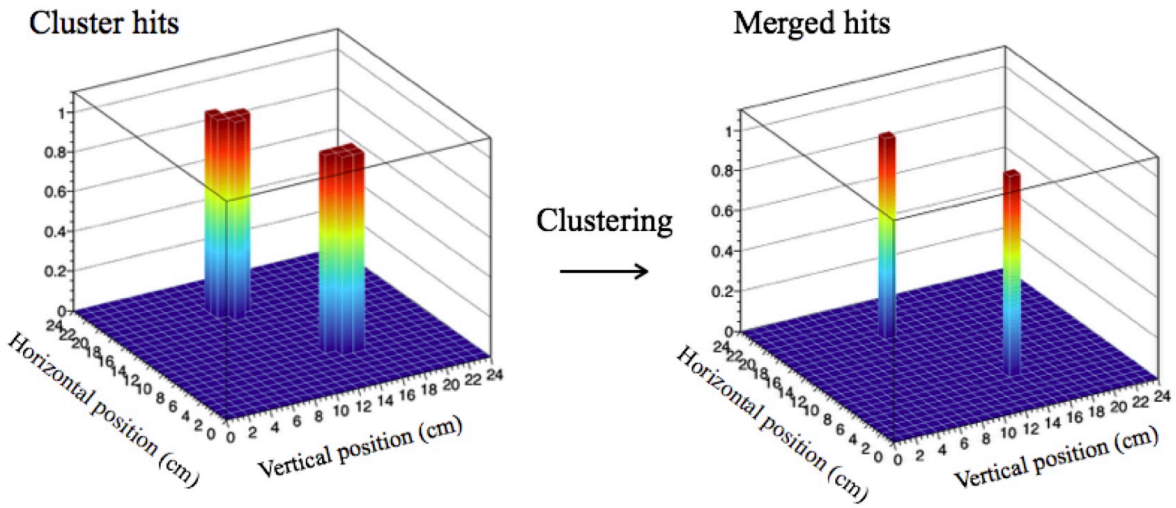

Figure 8-16: Example of the hit clustering: (left) before cluster merging; (right) after cluster merging. Two groups of cluster hits were merged into hit clusters.

event contributes to the peak, on the other hand, accidental coincidence arising from two independent origins contributes to the background. Dashed lines are fitting curves consists of a Gaussian on a background. The fitting was performed to every timing region with the width of 500 ns. Figure 8-21 shows the width of Gaussian peaks at each timing region. In the early timing regions, accidental coincidence contributes to the width of Δt distribution. Once the event rate decreased, the timing width asymptotically approached to a constant. Timing resolution of the detector was estimated to be 4.4 ns.

Figure 8-22 shows a correlation between radial hit positions on each layer. The left figure corresponds to a correlation of true coincidence like events selected by the requirement for timing difference Δt which is less than a three-fold of standard deviation. The right figure corresponds to a correlation of accidental like events. For a case of true-like coincidence events, a clear correlation between hit positions on two layers was observed.

Figure 8-23 represents the radial position difference Δr between coincidence paired hits at each layer. The left figure corresponds to a comparison of Δr for the accidental-like coincident events and the true-like coincident events discriminated by an event selection for the timing difference Δt between hits at each layer. As shown in Fig.

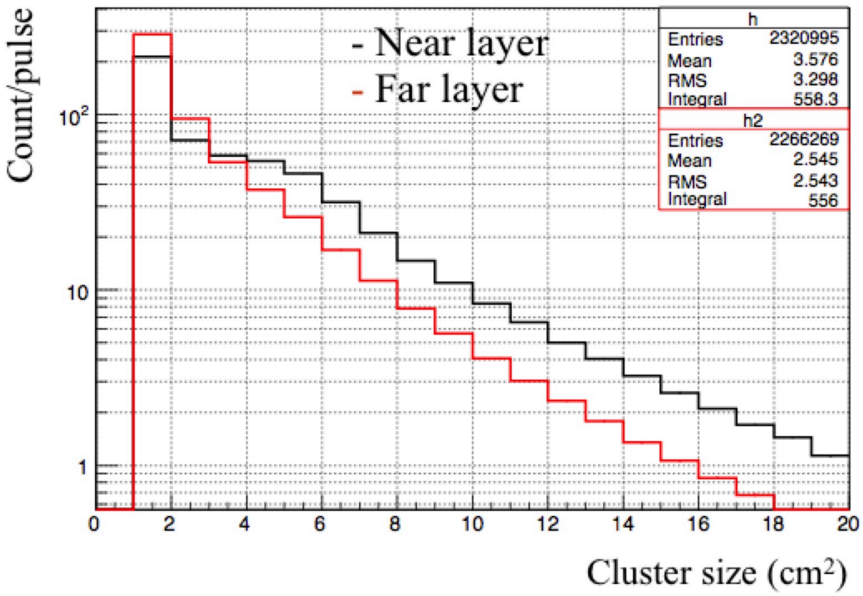

Figure 8-17: Cluster size distribution. The histograms in red and black lines correspond to the cluster size on the near layer and the far layer, respectively.

8-20, even though an event selection for Δt is applied, the sets of true-like coincidence events contain the accidental coincidence events. The right figure indicates a subtracted histogram by taking the difference between two histograms in the left figure. The result suggests that more than 86% of the true coincidence events are in the range of $\Delta r \leq 2$ cm.

8.2.6 Time spectrum analysis

Figure 8-24 shows the time spectra obtained at each step of the analysis. A histogram in blue line corresponds to a spectrum consists of all hits, the one in green line corresponds to clustered hits. The histogram in black line corresponds to a spectrum of coincident events. A red solid line is a fitting curve consists of an exponential function on a floor background. An evaluated exponent was consistent with the mean life time of a positive muon.

Figure 8-25 shows time dependent event loss obtained from a difference between the time spectrum and the fitting curve shown in Fig. 8-24. The maximum event loss due to the signal pileup was estimated to be 20%. It was consistent with the

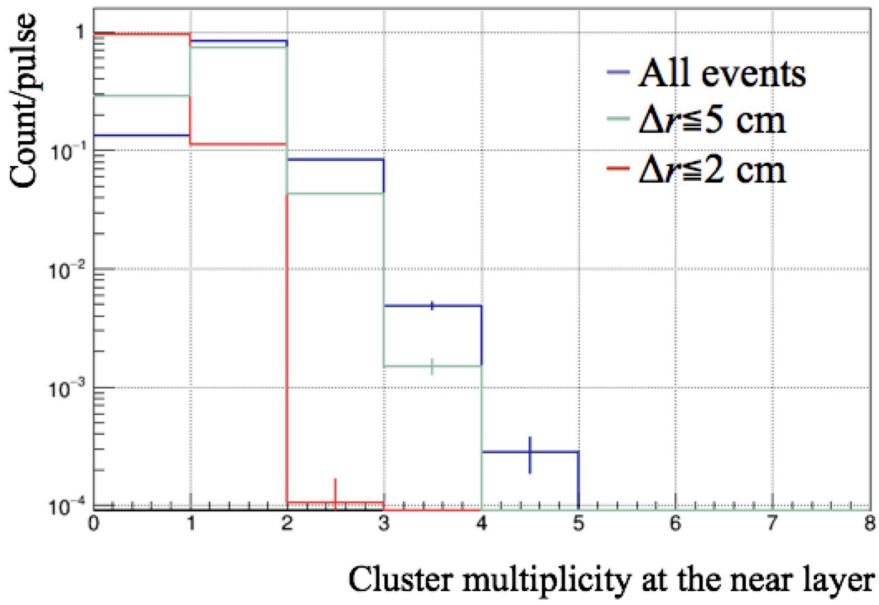

Figure 8-18: Multiplicity distribution after the cluster merging. The histograms in green and red lines correspond to the results with an event selection of $\Delta r \leq 5$ cm and $\Delta r \leq 2$ cm, respectively. The one in blue line corresponds to the result without event selection.

result presented in Chapter 6 which was obtained from the time spectrum of clustered hits. Systematic uncertainty in the resonance measurement arising from this effect is discussed in the following chapter. To consider appropriateness of the coincidence analysis, the finding efficiency of a coincidence hit pair was evaluated. Figure 8-26 shows a fraction of the number of coincidence events relative to the number of hit cluster on the far layer. Black solid circles correspond to the total coincident event, red solid circles correspond to the true-like coincidence, and outlined circles correspond to the accidental-like coincidence. Event selection was the same as the analysis of the coincidence time spectrum shown in Fig. 8-24. While the rate of accidental-like coincidence depends on event rate, true-like coincidence rate is mostly rate independent. This tendency bolsters no significant systematic bias caused by the coincidence analysis.

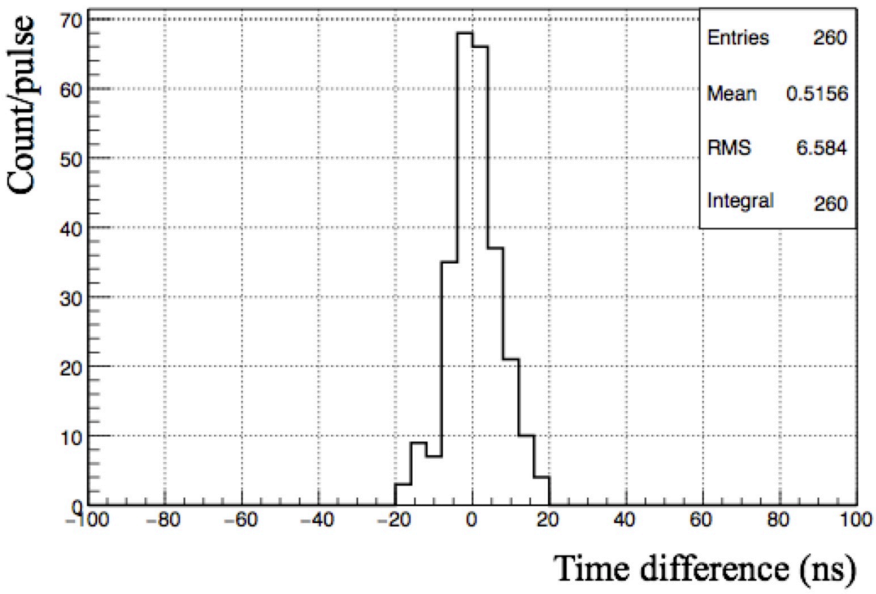

Figure 8-19: Timing difference between two hit clusters which were observed at the same time on the near layer. The peak around zero suggests that two hit clusters have an identical origin e.g. an electromagnetic cascade.

8.2.7 Time dependent spin flip signal

For a validation of the measurement system, microwave off-resonance data was analyzed. A microwave resonance condition was off-tuned to a signal generator output frequency. Figure 8-27 shows an extracted muonium spin flip signal defined by the ratio of the positron counting with microwave $N_{\rm on}$ and one without microwave $N_{\rm off}$. No significant signal was observed. Figure 8-28 shows an extracted time dependent signal of muonium spin flip. A microwave frequency was set to an expected frequency which corresponds to the muonium HFS resonance. The signal definition is the same as the analysis for off-resonance data. Clear oscillating spin flip signal was observed. As discussed in Chapter 2 (Eq. 2.83) and Chapter 4 (Eq. 4.2), the time dependent spin flip signal depends on the microwave strength and the spacial distribution of the muonium. Therefore, the signal is expressed by a summation of partial contributions correspond to different microwave strengths. In Fig. 8-28, red solid line represents a

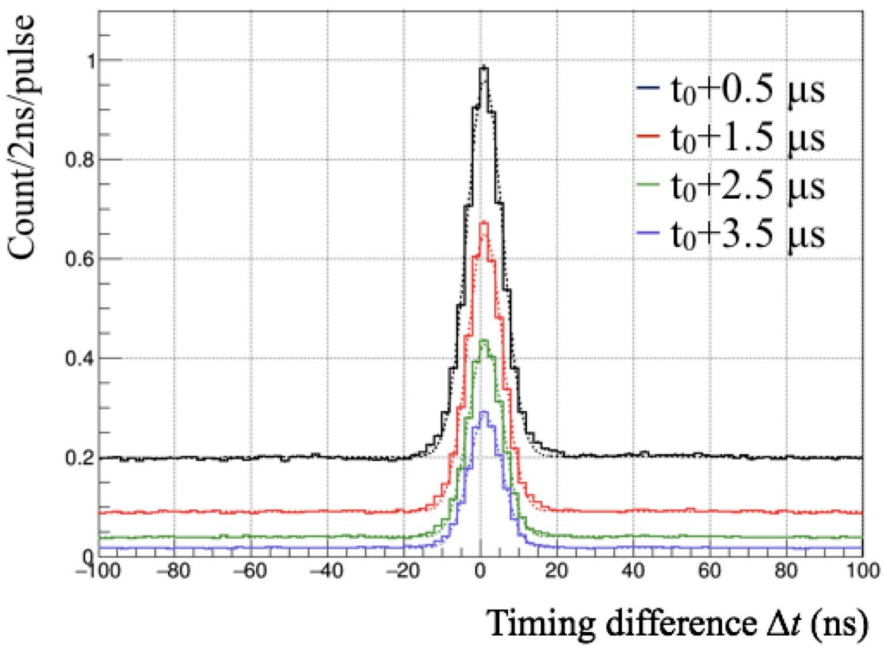

Figure 8-20: Timing difference between the hits on each layer of the detector which is denoted as Δt. Each of the histogram in colors corresponds to the beginning of a timing window. The timing of a muon pulse arrival is denoted as t_0. Dashed lines indicate the fitting results with a Gaussian on a background.

fitting curve which is defined as follows

$$S(t) = \sum_{k=1}^{n} \left[\left\{ \frac{\Gamma_k + \omega'}{\Gamma_k} \cos \frac{\Gamma_k - \omega'}{2} t + \frac{\Gamma_k - \omega'}{\Gamma_k} \cos \frac{\Gamma_k + \omega'}{2} t \right\} N(b_k) \right] A e^{-\lambda t} \tag{8.1}$$

$$\Gamma_k = \sqrt{\omega' + 8|b_k|^2} \tag{8.2}$$

where ω' is the microwave frequency detuning, n is the number of partial contribution, b_k is the microwave power parameter of each contribution, $N(b_k)$ is the number of muonium in each partial contribution, A is the arbitrary scaling parameter, and λ is the spin relaxation time constant. The microwave frequency detuning, the number of muonium in each partial contribution, the spin relaxation time constant, and the arbitrary scaling factor were set as free parameters. The number of partial contribution was set to four from the viewpoint of convergence of the parameters. Dashed lines correspond to the contributions from respective microwave strengths. As a result of the fitting, a microwave frequency detuning was obtained to be 65 ± 223 kHz.

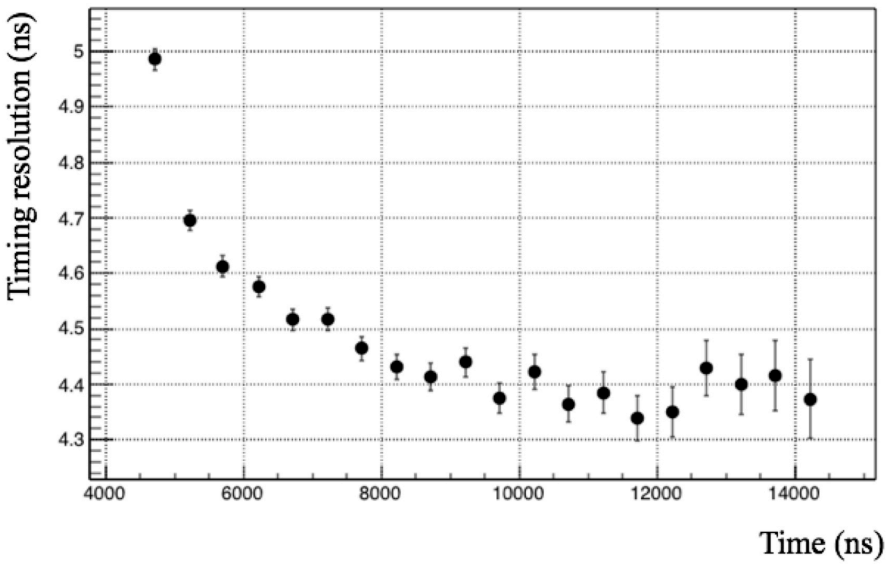

Figure 8-21: Width of the Δt distribution as a function of elapsed time from a muon pulse arrival. In the early timing region, an accidental coincidence contributes to broadening of the width.

The effective microwave strength distribution was obtained by the fitting of the time dependent spin flip signal. Figure 8-29 represents a comparison of the observed data with the simulation result and it shows good agreement.

Figure 8-30 shows a time dependent spin flip signal for a case of 200 kHz detuned from the resonance frequency. A red line corresponds to a fitting curve. All parameters except for an arbitrary scaling factor were fixed. The microwave power and the spin relaxation parameter were set to the fitting result for the on-resonance signal. A microwave frequency detuning was set to 200 kHz. Major features of the time dependent signal was represented by the fitting curve.

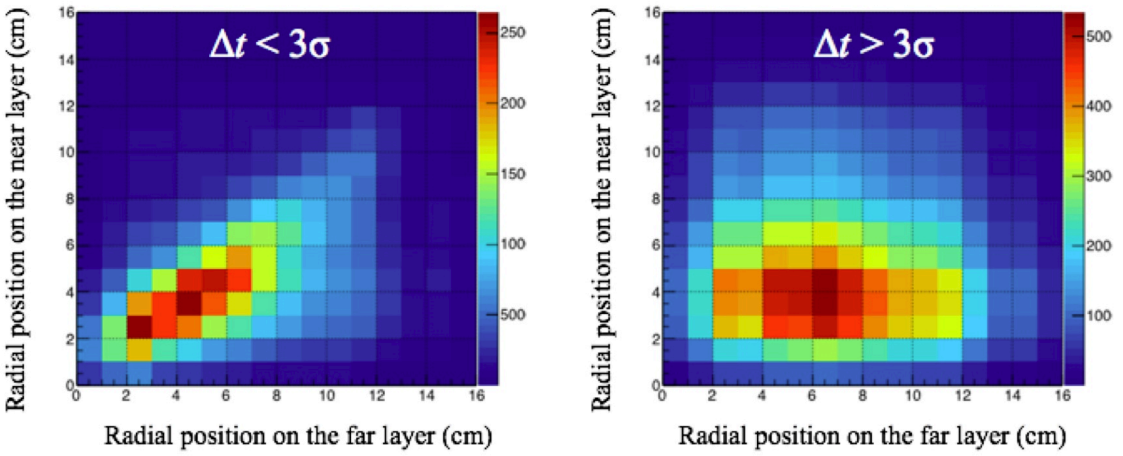

Figure 8-22: Hit correlation in the interlayer coincidence hits: (left) true-like coincidence; (right) accidental-like coincidence. The event selection criteria was $\Delta t < 3\sigma$ for the true-like coincidence where Δt is the interlayer timing difference and σ is the timing resolution of the positron detector.

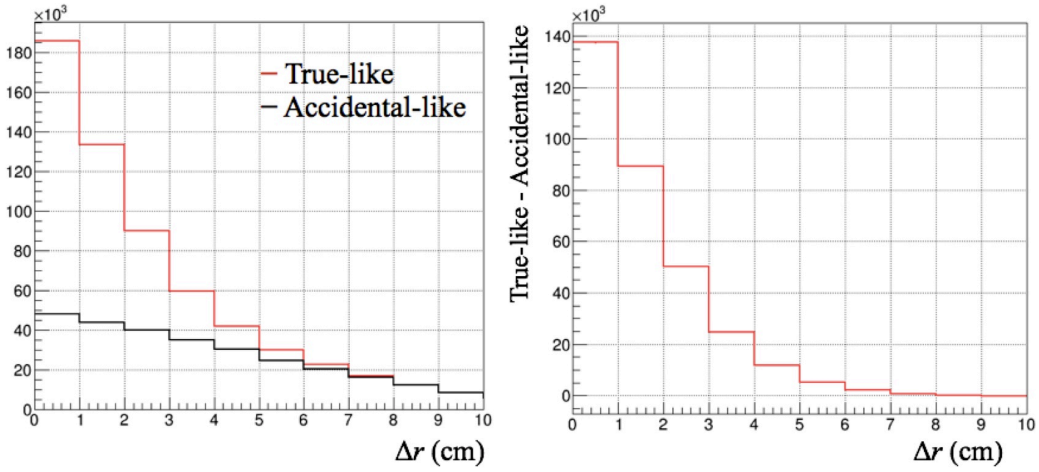

Figure 8-23: Radial position difference between the hits on each layer of the detector which is denoted as Δr. In the left figure, the histograms in red and black lines correspond to true-like and accidental-like events, respectively. The subtracted histogram is represented in the right figure.

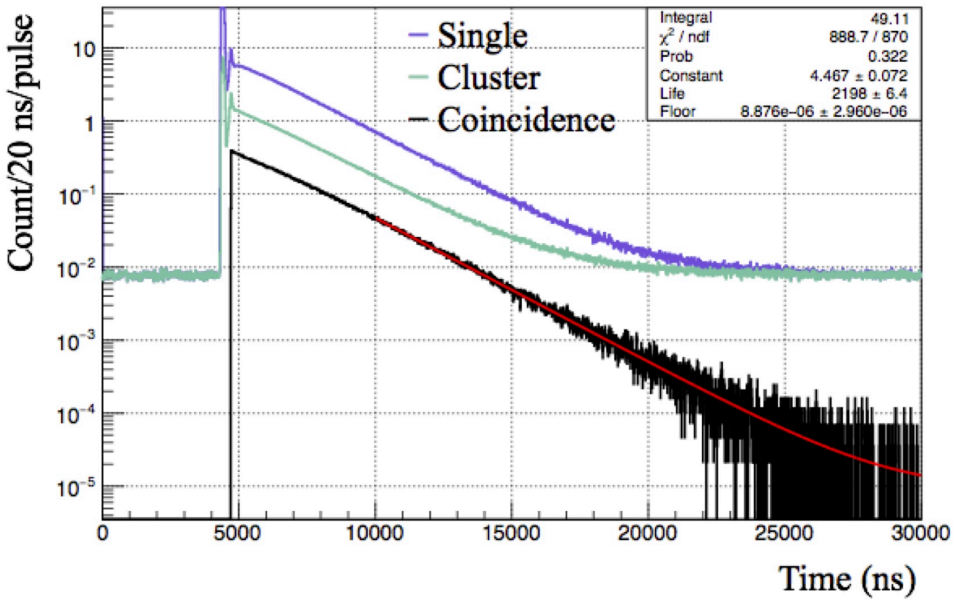

Figure 8-24: Time spectra of the detector hits. The histograms in blue, green, and black lines correspond to all single hits, cluster merged hits, and coincidence hits, respectively. Red line indicates the fitting result with an exponential function on a constant background. The event selection of $\Delta t \leq 3\sigma$ and $\Delta r \leq 2$ cm were applied to the coincidence time spectrum.

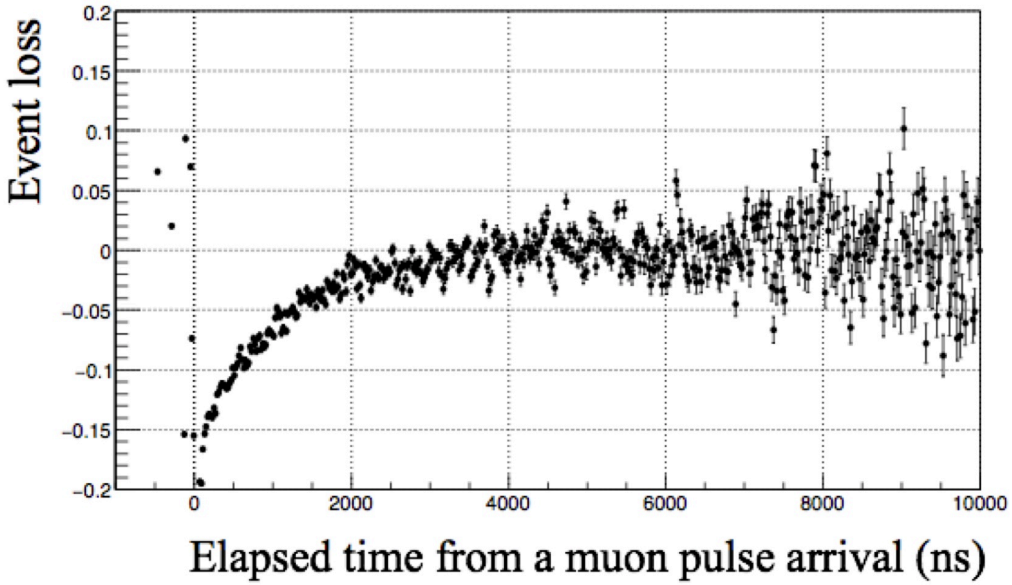

Figure 8-25: Pileup event loss of the coincidence hits as a function of elapsed time from a muon pulse arrival. The event loss was estimated based on the difference between the positron coincidence time spectrum and the fitting result shown in Fig. 8-24.

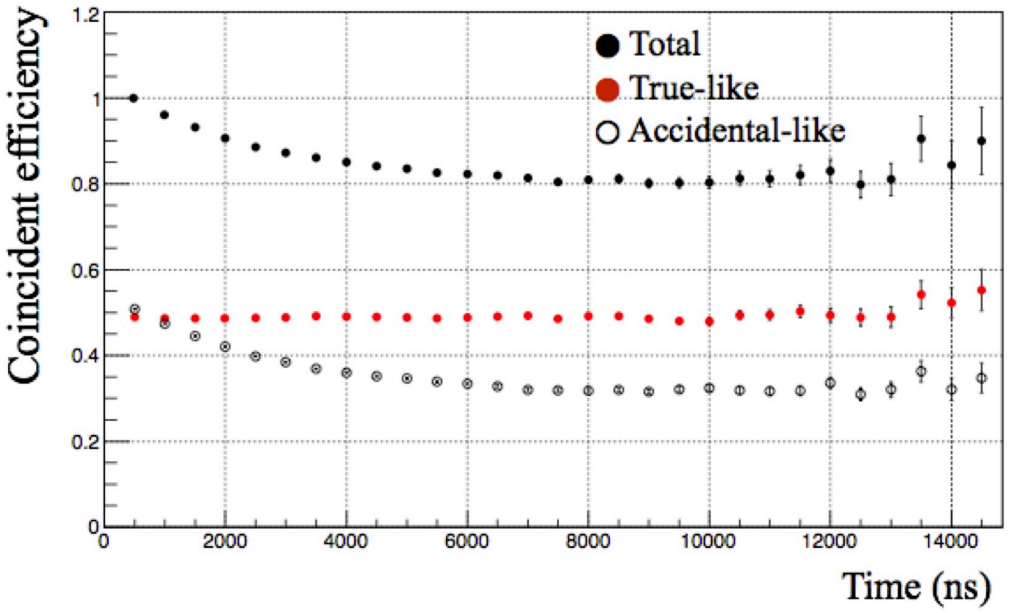

Figure 8-26: Coincidence finding efficiency as a function of elapsed time from a muon pulse arrival. Red, black and outlined circles correspond to all events, true-like events, and accidental-like events, respectively. The event selection of $\Delta t \leq 3\sigma$ and $\Delta r \leq 2$ cm were applied for the true-like coincidence time spectrum.

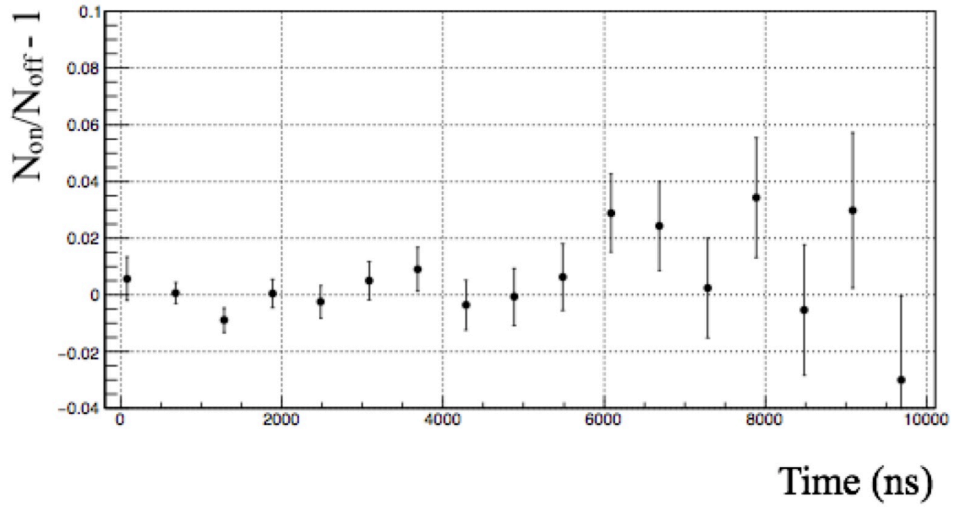

Figure 8-27: Off resonance result of the time dependent spin flip signal analysis. The vertical axis indicates the time spectrum ratio $N_{\mathrm{ON}}/N_{\mathrm{OFF}} - 1$ where N_{ON} and N_{OFF} correspond to the positron time spectra with the microwave ON and OFF, respectively. The horizontal axis indicates elapsed time from a muon pulse arrival.

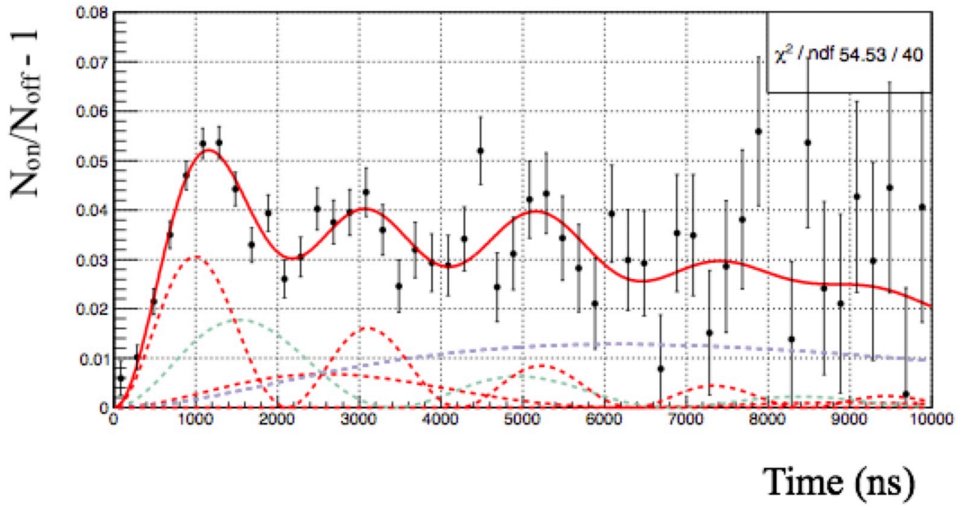

Figure 8-28: Time dependent spin flip signal at the microwave frequency of 4463.3 MHz. The vertical axis indicates the time spectrum ratio $N_{\mathrm{ON}}/N_{\mathrm{OFF}} - 1$ where N_{ON} and N_{OFF} correspond to the positron time spectra with the microwave ON and OFF, respectively. The horizontal axis indicates elapsed time from a muon pulse arrival. Red solid line represents the fitting result with the theoretical expression of the signal. Each of dashed lines in colors corresponds to the different microwave field strength.

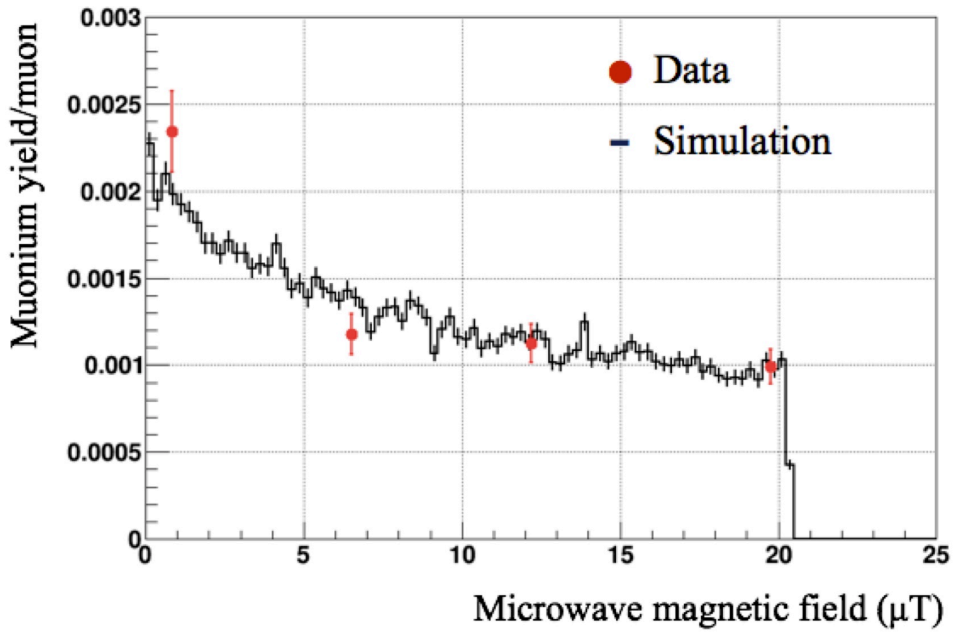

Figure 8-29: Comparison of the effective microwave strength distribution. Red circles represent the fitting result while the histogram in black line indicates the simulation result.

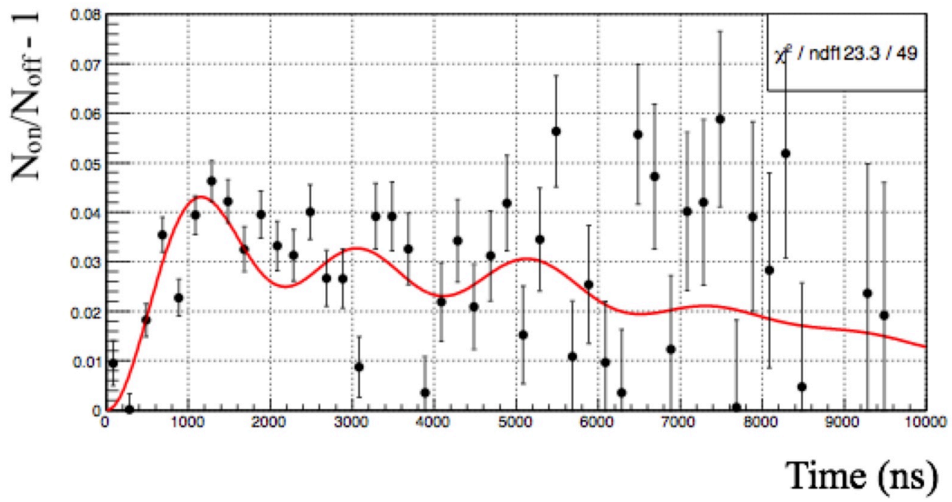

Figure 8-30: Time dependent spin flip signal at 200 kHz detuned microwave frequency. The analysis was performed in the same manner as one for Fig. 8-28. The red line corresponds to the fitting result with the theoretical expression of the signal. The parameters in the theoretical curve were fixed at the results shown in Fig. 8-28 except for the microwave frequency and an arbitrary scaling parameter.

Chapter 9

Results and Discussion

This chapter describes the results obtained through the experiment and its understanding. The first section summarizes the measurement result of muonium HFS resonance spectroscopy. Systematic uncertainties are discussed in the second section. Sources of systematic uncertainties are sorted out and each contribution was estimated. Comparisons with precursor experiments and further improvements are included. The last section describes prospects for the future, particularly, expected statistical precision with higher-intensity muon beam. For a case of the existing facility and one of the new facility under construction are discussed.

9.1 Results

This section summarizes the experimental result of muonium spectroscopy obtained by the data analysis described in the previous chapter.

9.1.1 Muonium spin flip induced by a microwave magnetic field

Figure 9-1 shows time dependent spin flip signals extracted from decay positron time spectra. A solid circle corresponds to the result with on-resonance microwave while an outlined circle corresponds to one with off-resonance microwave. The detail of data

analysis is described in Chapter 8. Under an excitation of microwave resonance in the cavity, clear oscillating spin flip signal was observed. On the contrary, no significant spin flip signal was observed for a case of off-resonance tuning.

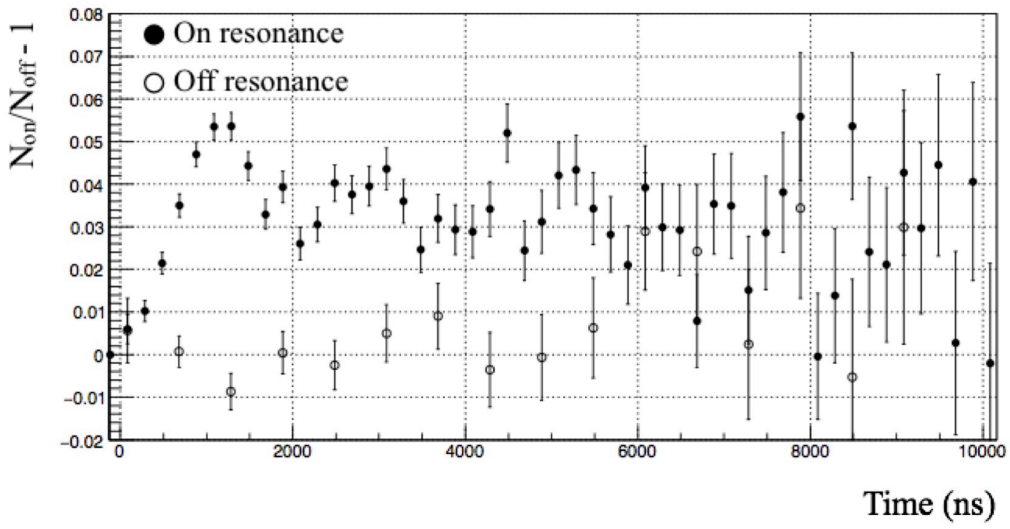

Figure 9-1: Time dependent signal of the muonium spin flip. Black solid circles and outlined circles correspond to the signal at on-resonance tuning and off-resonance tuning, respectively. The microwave frequency for the on-resonance measurement was tuned at 4463.3 MHz.

9.1.2 Resonance lineshape

As a result of decay positron counting with microwave frequency scan, a resonance lineshape of muonium HFS transition was obtained. This was the first observation of muonium HFS resonance as an experimental result with pulsed muon beam. Figure 9-2 shows a measured resonance lineshape. Frequency dependence of the microwave characteristics was corrected. Fitting was performed by a theoretical expression of lineshape derived in Chapter 2. For a case of wide timing range of positron integration, the function form is approximated by a Lorentzian. The obtained frequency center was -41 ± 22 kHz. This result corresponds to a relative uncertainty of 4.9 perts per million. An expected resonance frequency based on zero-extrapolation of gas pressure is -33 kHz.

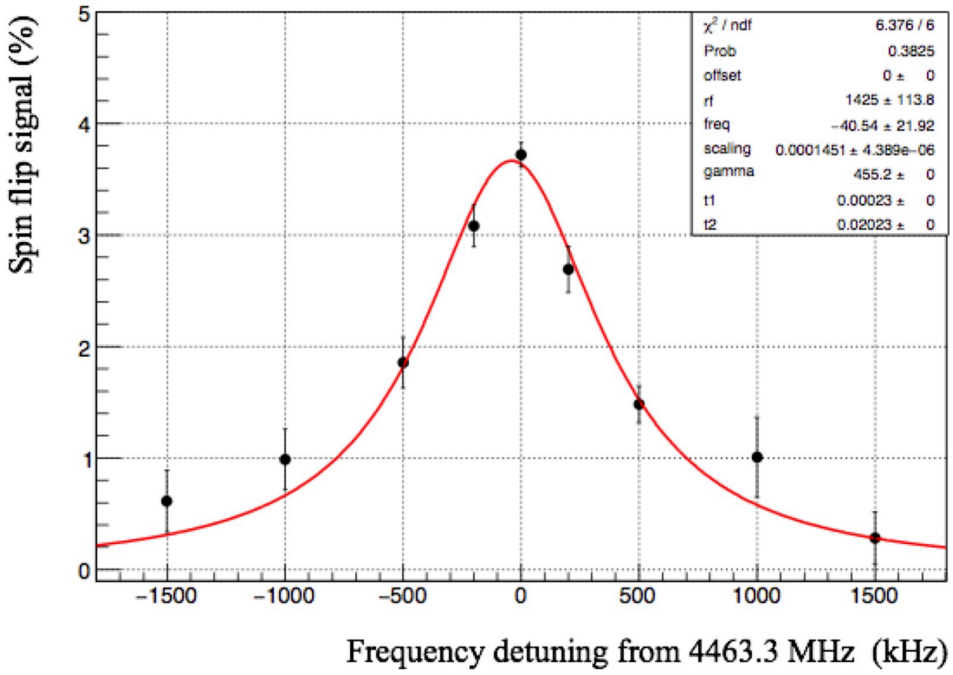

Figure 9-2: Resonance lineshape of the muonium HFS transition. Red line corresponds to the result of Lorentzian fitting. The vertical axis indicates the time integrated signal of the muonium spin flip. The frequency center of the resonance lineshape was evaluated to be 4463 259 (22) kHz.

9.2 Systematic Uncertainties

In this section, the systematic uncertainties in the measurement are discussed.

9.2.1 Static magnetic field

Static magnetic field causes a splitting of muonium sub-levels and broadening of the resonance lineshape. Figure 9-3 shows measured static magnetic field distribution in the microwave cavity. The magnetometer was placed on the beam axis and translated along the axis.

By combining the muonium spacial distribution and magnetic field map, an effective magnetic field distribution was obtained. Fig. 9-4 shows the obtained magnetic field which muonium feels in the microwave cavity. Shift of the resonance lineshape was estimated by using the numerical resonance simulator as described in Chapter 4. As a result of numerical simulation, no significant systematic shift of a lineshape was

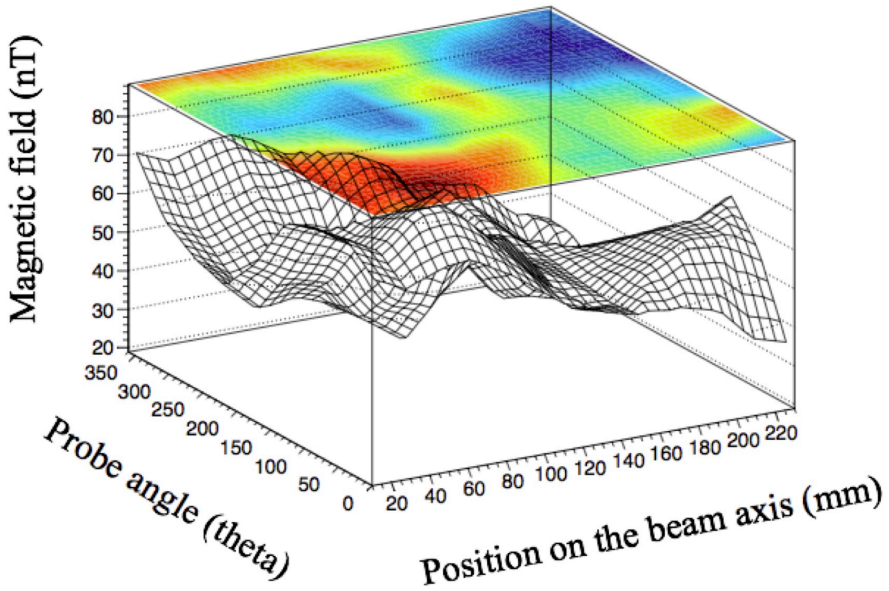

Figure 9-3: Static magnetic field map inside the microwave cavity. The magnetometer was placed on the longitudinal axis (beam axis). A local magnetization on the upstream side.

observed.

9.2.2 Microwave power fluctuation

Drift of microwave power causes signal fluctuation. Stability of microwave power was monitored by using a small loop antenna attached to the microwave cavity. Figure 9-5 shows measured trends in monitored microwave power.

During the measurement, a gradient detuning of the microwave resonance was observed. This detuning was caused by a local temperature drift on the microwave cavity. Changing in a temperature gives a slight deformation of the microwave cavity. Periodic switching of microwave output was effective to suppress the temperature drift. However, a temperature stability of the cavity was imperfect.

Figure 9-6 shows a magnified fluctuation of the microwave power. It consists of a short-term component and a long-term component. The fast fluctuation is supposed to be a contribution from a stability of the signal generator. On the other hand, the slow fluctuation is to be one from the temperature drift. This long-term drift was

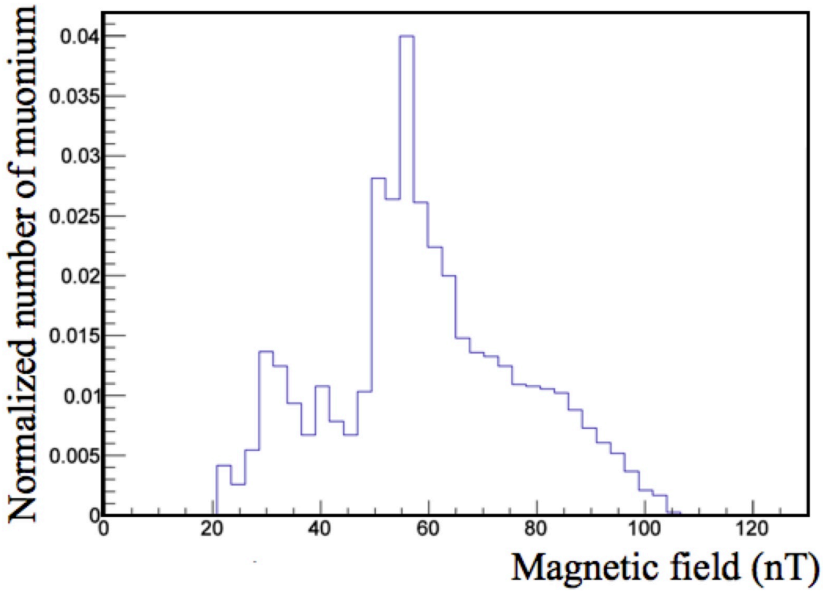

Figure 9-4: Effective magnetic field strength surrounding the muonium. The distribution was obtained from the magnetic field map and three-dimensional muon stopping distribution which was measured by the muon beam imager.

evaluated by linear-approximation and corresponds to a power decrease of 6.3%. The short-term drift corresponds to a power changing of 0.5% on average.

In the analysis, a correction to a long-term fluctuation was implemented by using a liner approximation. Table 9.1 summarizes estimated long-term drift at each microwave frequency. In the beginning of a measurement at each frequency data point, input microwave power to the cavity was measured directly via an attenuator. No significant change in input power was observed. This supports that power fluctuation origins from a change in the microwave cavity. Systematic uncertainties arising from short-term fluctuation was estimated by using the resonance simulator. At each frequency point, 0.5% of random fluctuation was assumed. As a result of numerical calculation, the systematic uncertainty in a resonance frequency was estimated to be 26 Hz. To suppress the systematic uncertainty arising from microwave power drift, addition of feedback to the system and temperature control of the microwave cavity are considered. Feedback to a microwave power was studied by using another synthesizer which has lower frequency range. As a result of feedback trial, power fluctuation of 0.02 % was achieved in laboratory test. While some modifications are

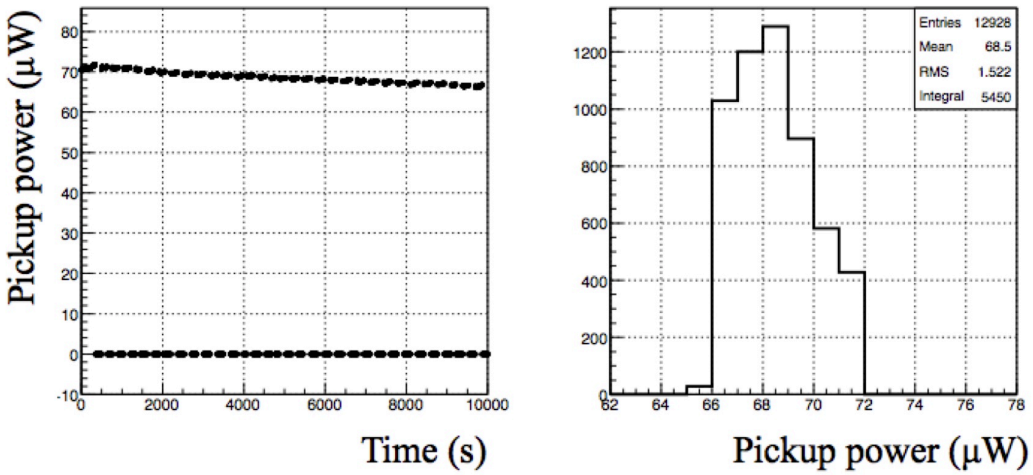

Figure 9-5: Drift of the microwave power: (left) monitored microwave power as a function of measurement time; (right) microwave power distribution. During the measurement, the microwave signal was switched ON/OFF periodically.

necessary, developed feedback system is planned to be implemented to the signal generator which is utilized in the experiment. For a case of feedback with 0.02 % of accuracy, systematic uncertainty due to a microwave power instability is estimated to be 3 Hz.

9.2.3 Muon beam intensity fluctuation

During the measurement, systematic drift of a proton beam intensity was observed. Figure 9-7 shows measured proton beam intensity as a function of time. The left figure corresponds to the number of protons estimated by using the current monitor located before the muon production target. The right figure corresponds to the proton beam intensity distribution. By switching the microwave output ON and OFF in a minute interval, the muonium spin flip signal is free from a systematics arising from long-periodic temporal variations.

Figure 9-8 shows a trends in the proton beam intensity pulse-by-pulse. In a period of minutes, drift of beam intensity was 1.6 ppm. This level of intensity drift is safely negligible in extraction of muonium spin flip signal.

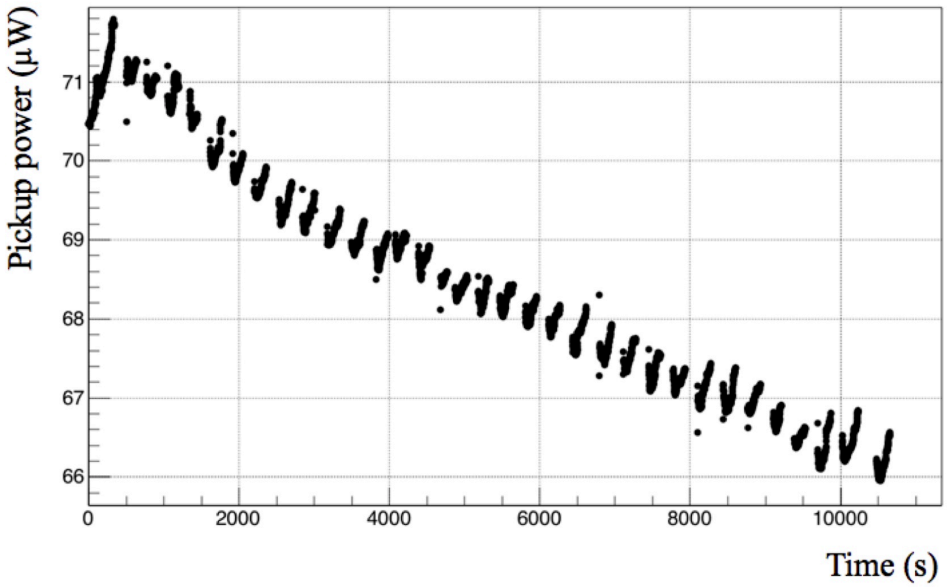

Figure 9-6: Magnified fluctuation of the microwave power. The slow component of the drift was caused by thermal deformation of the microwave cavity. The fast one was caused by microwave circuit instability after the ON/OFF switching. The slow microwave power changing was corrected by a linear-approximation.

9.2.4 Muon beam profile fluctuation

Through the microwave frequency scan, a possible fluctuation of muon beam profile was estimated. Figure 9-9 shows beam parameters measured by using the muon beam imager. The left figure corresponds to a beam width, while the right figure corresponds to a beam center. In both figures, a black circle indicates vertical parameter, a red circle indicates horizontal parameter. Dashed lines are averages of the values. For both parameter cases, no significant fluctuation larger than 1 mm was observed.

In addition, similar study was performed by using the two-dimensional fiber beam profile monitor. Due to an unexpected operation failure in a readout electronics, only a certain period of measurement was performed. However, no significant fluctuation of beam profile was observed during the measurement. Figure 9-10 shows measured beam width and center as a function of accumulated trigger number. Fluctuation of the muon beam profile affects spin flip signal via a changing of effective microwave power. A systematic shift of 1 mm in a beam center gives 0.03% of changing in

Table 9.1: Microwave power drift in the measurement.

Microwave frequency (MHz)	Drift (%)
4463.3	6.3
4463.5	0.9
4463.8	1.1
4464.3	0.8
4464.8	2.5
4463.1	4.3
4462.8	3.1
4462.3	2.5
4461.8	5.6
Off Resonance	2.1

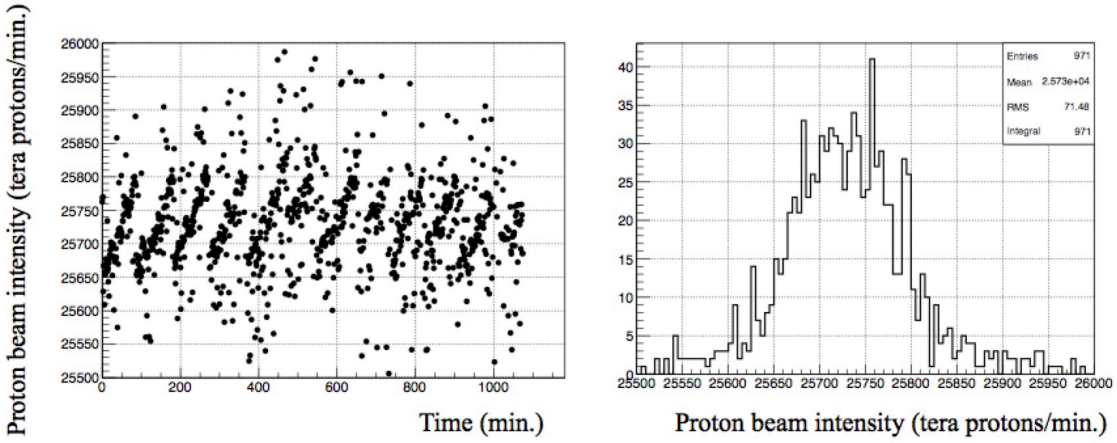

Figure 9-7: Proton beam intensity per minutes: (left) proton beam intensity as a function of measurement time; (right) beam intensity distribution.

effective microwave power. By using the resonance simulator, systematic uncertainty due to the beam profile fluctuation was calculated. A linear drift of 1 mm in a muon beam profile center during the frequency scan was assumed. As a result of numerical simulation, the uncertainty was estimated to be 9.8 Hz. In order to suppress this systematic effect, an iterative measurement with randomized measurement order is effective. When an iterative frequency scan with randomized measurement order is performed, this systematic effect is suppressed to be 2.5 Hz.

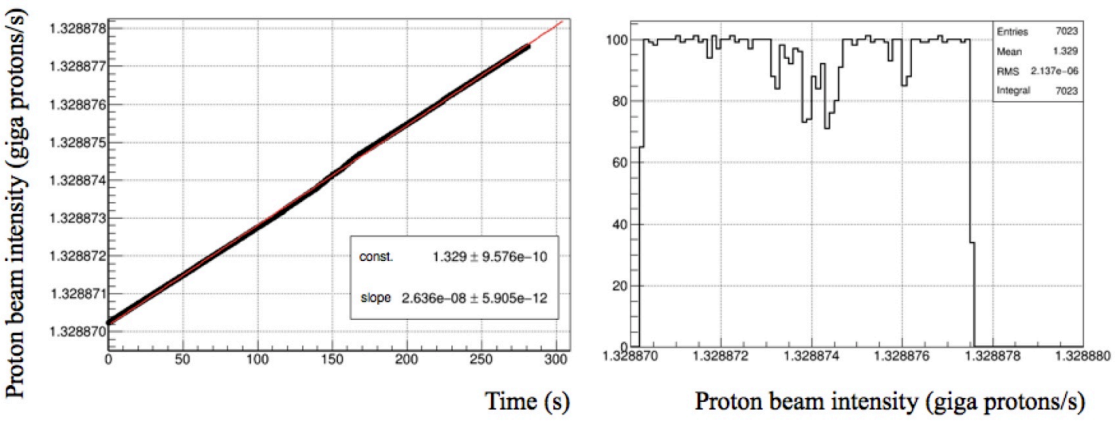

Figure 9-8: Proton beam intensity pulse-by-pulse: (left) proton beam intensity as a function of measurement time; (right) beam intensity distribution. Red line in the left figure corresponds to the linear fitting result.

9.2.5 Gas pressure zero-extrapolation

As discussed in Chapter 4, the zero-extrapolation of gas pressure arises the systematic uncertainty depends on absolute value of the gas pressure. Estimated systematic uncertainty was 66 Hz. To suppress the systematic uncertainty origins from gas pressure extrapolation, a silicon gauge which has higher measurement precision is going to be adopted. Typical precision of a silicon gauge is 0.02 %, ten-folds better than a capacitance gauge. After an upgrade of a pressure gauge, uncertainties in pressure dependence parameters are to be improved. To determine gas density dependence of HFS frequency more precisely, a new measurement at several values of the gas pressure is planned.

9.2.6 Gas pressure fluctuation

Figure 9-11 shows a trend in gas pressure measured by the capacitance gauge. The left figure corresponds to gas pressure in a period of 3 hours. The right figure corresponds to gas pressure distribution in entire duration of the experiment. Fluctuation of the gas pressure was estimated to be 0.03%. Changing in the muon stopping distribution and the magnetic permeability of the target gas are negligible. Systematic uncertainty arising from the gas pressure fluctuation was evaluated by using the resonance

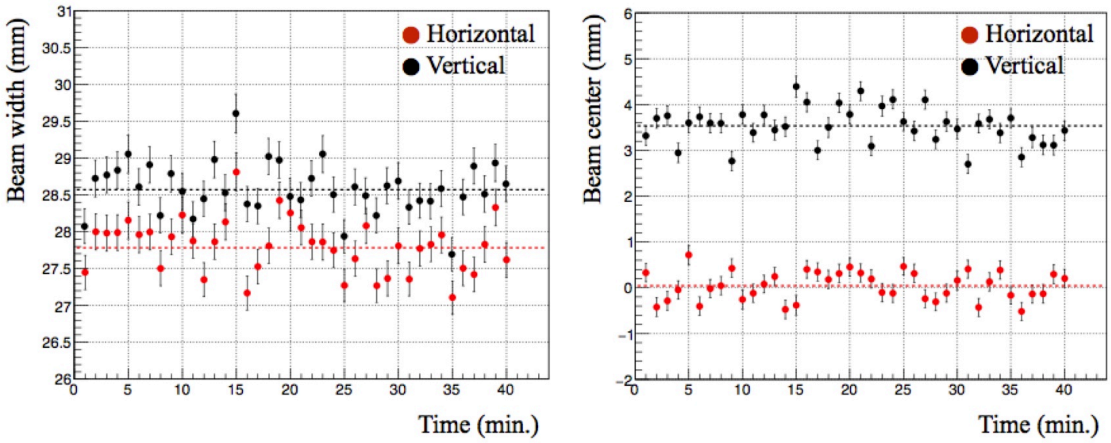

Figure 9-9: Muon beam profile stability measured by the three-dimensional muon beam imager: (left) beam width; (right) beam center. In both figures, red and black circles correspond to the horizontal beam parameters and the vertical ones, respectively.

simulator via the fluctuation of HFS frequency shift due to the atomic collision. As a result of numerical simulation, uncertainty in the resonance frequency was estimated to be 6 Hz. For a case of an improved experiment with the randomized iteration of a frequency scan, this systematic effect would be negligible.

9.2.7 Gas impurity effect

Para-magnetic impurity causes muon spin depolarization. Measured pressure increase rate was 0.002 Pa per minute. In a period of 20 hours, 2.4 Pa of pressure increase was expected. For a case of para-magnetic molecules, 0.4 ppm of oxygen and 0.5 ppm of nitrogen oxide were expected. According to the cross-sections of spin exchange interaction between a muonium and a magnetic molecule [65, 66], expected decrease of the signal due to the spin depolarization was estimated to be 0.5 % at maximum. Systematic uncertainty due to this depolarization effect was evaluated by using the resonance simulator. A linear increase of impurity during a microwave frequency scan was assumed. As a result of numerical simulation, uncertainty in the resonance frequency was estimated to be 12 Hz. Non-magnetic gas impurity causes a collisional shift of the resonance frequency. However, even for a case of water vapor, the most

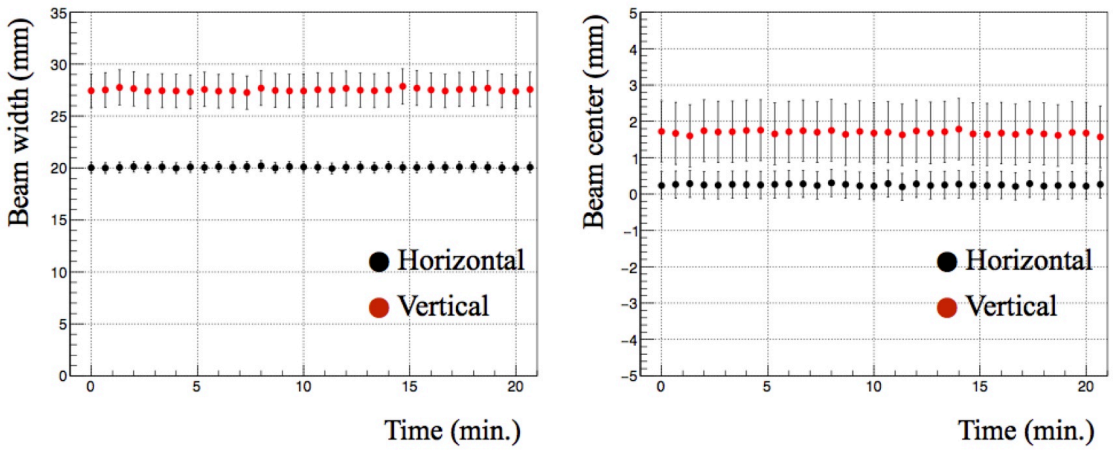

Figure 9-10: Muon beam profile stability measured by the two-dimensional muon beam monitor. (left) beam width; (right) beam center. In both figures, red and black circles correspond to the vertical beam parameters and the horizontal ones, respectively. Dashed lines indicate the average.

abundant impurity, expected collisional shift is safely ignored relatively to a collisional shift by krypton atoms. The depolarization effect origins from magnetic impurities is suppressed by a frequent exchange of the target gas and a randomization of the measurement order. In the experiment, a longest duration of gas containment was 20 hours. For a case of a gas exchange in every six hours, the signal decrease due to the magnetic impurities is suppressed to be 0.15 %. When an iterative frequency scan with randomized measurement order is performed, this systematic effect is estimated to be 1.1 Hz.

9.2.8 Detector pileup

A rate-dependent efficiency of the positron detector was estimated in the previous chapter. At the immediate after a muon pulse arrival, event loss due to signal pileup was about 20 %. By using the event generator and resonance simulator, this systematic effect was evaluated numerically. A rate-dependent event loss probability was implemented based on a measurement result. Figure 9-13 shows simulated pileup loss of the time dependent spin flip signal at the HFS resonance. A histogram in red lines corresponds to a result with pileup loss while one in black lines corresponds to

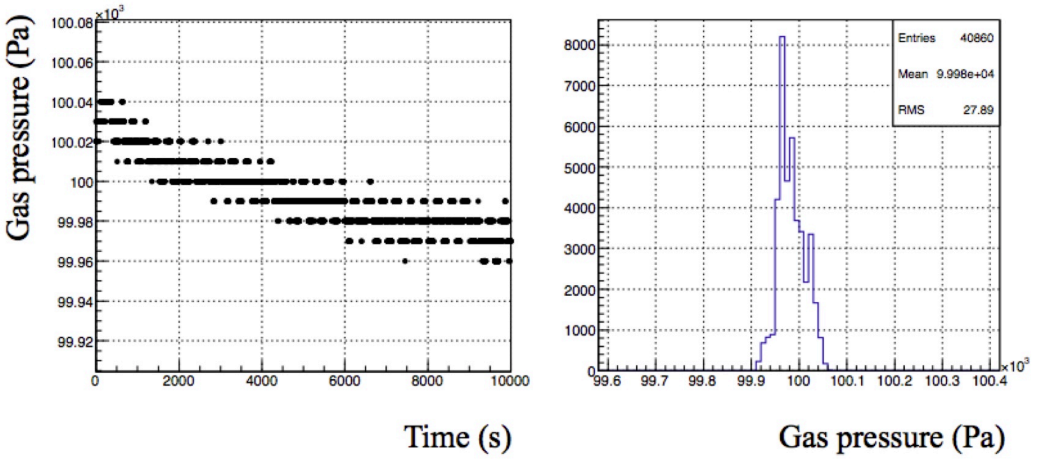

Figure 9-11: Target gas pressure measured by the capacitance gauge: (left) gas pressure as a function of measurement time; (right) gas pressure distribution.

a result without pileup loss. The pileup loss at each microwave frequency detuning was calculated and the systematic uncertainty was estimated to be 2 Hz.

9.2.9 Total systematics

Estimated systematic uncertainties in the experiment were estimated as shown in Table 9.2. With the present apparatuses, systematic uncertainty is dominated by a measurement precision of the capacitance gauge. The second largest contribution is arising from an instability of the microwave power. For both sources of uncertainty, an order of magnitude improvements are expected by upgrades.

9.3 Statistical extrapolation and studies for improvement

A high-intensity pulsed muon beam is capable to generate an extremely large number of muonium relative to a continuos muon beam. However, only a well-designed, robust measurement system is able to accept the benefit of high-intensity pulsed beam because of pileup loss and beam-related background. Studies for proof of principle and improvements to overcome the high-rate environment are discussed.

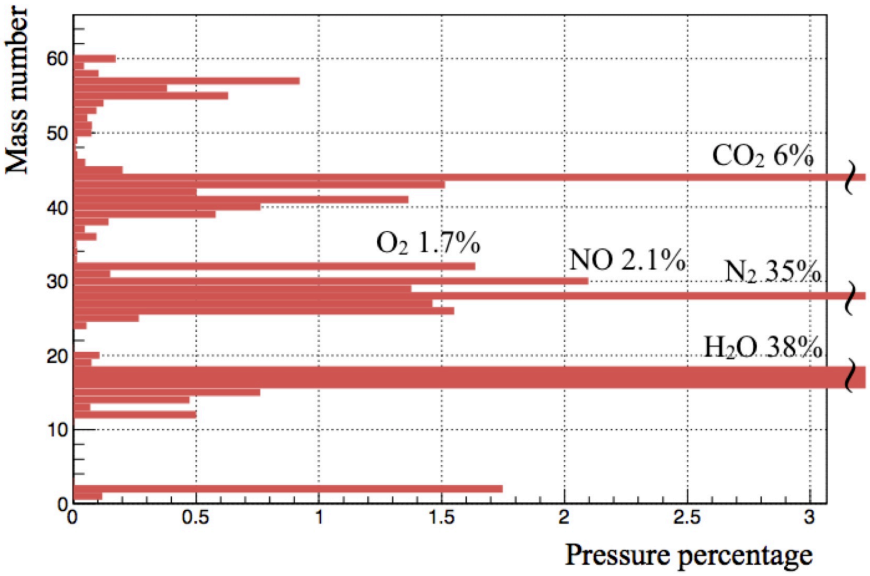

Figure 9-12: Abundance of impurities measured by the Q-mass spectrometer. The horizontal axis indicates a pressure percentage of each mass number in total impurities. Oxygen and nitrogen oxide were considered as the sources of muon spin depolarization.

9.3.1 Statistical precision at the existing facility

At J-PARC MLF MUSE D-Line, the highest beam intensity achieved in the past is about 9×10^6 muon per second at 600 kW of accelerator operation power. For a case of 600 kW operation, the beam intensity would be tripled.

In the experiment, half of incident muons stopped on the wall of the microwave cavity. These wall-stopped muons were major sources of background and to be suppressed. Development of a microwave cavity with larger inner radius is under study. To enlarge a size of microwave cavity, higher order mode of a microwave resonance should be excited. The first higher-order candidate is TM220 mode which corresponds to a diameter of 17.8 cm. The second candidate is TM330 mode corresponds to one of 27.7 cm. Figure 9-14 shows simulated muon stopping distribution projected on the cavity section. For a case of a TM330 mode cavity, wall-stopped positrons would be suppressed to a negligible level.

Figure 9-15 shows simulated the number of positron detection for each diameter

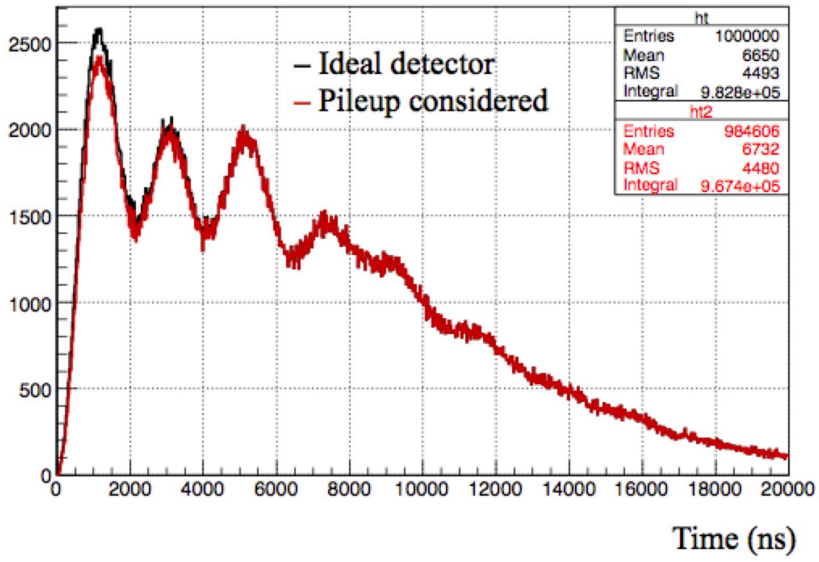

Figure 9-13: Pileup loss of the muonium spin flip signal as a function of elapsed time from a muonium formation. The histograms in red and black lines correspond to the results with and without signal pileup, respectively.

of the cavity. A red circle indicates the number of detected positron from target gas while a black circle corresponds to one from the cavity wall. For a case of the cavity with the diameter of 277 mm, a factor of four enhancement of signal yield and 400-fold of suppression of the wall-stopped positron are expected.

Due to the spacial restriction in the magnetic shield, the thickness of an aluminium absorber was smaller than optimum. To suppress the duct streaming positrons, an additional absorber is to be installed inside of the gas chamber. An additional aluminium absorber with the thickness of 20 mm gives almost no duct streaming positron to be detected.

To study the detail of duct streaming positrons, a supplemental experiment was performed at J-PARC MLF MUSE D-Line. Figure 9-16 depicts the experimental setup. A stainless-steel plate was placed in front of the beam window as a muon stopping target. Two pairs of scintillation counters were placed beside and behind of the stopping target. The detectors beside the target is denoted as the side counter while ones behind the target is denoted as the downstream counter. The downstream counter detects both duct streaming and decay positrons. On the other hand, the side

Table 9.2: Systematic uncertainties in the measurement.

Source	Contribution (Hz)	Future upgrade (Hz)
Microwave power drift	26	3
Gas pressure extrapolation	66	7
Gas pressure fluctuation	6	0
Gas impurity	12	1.1
Muon beam intensity	0	0
Muon beam profile	9.8	2.5
Static magnetic field	0	0
Detector pileup	2	2
Total	73	8.3

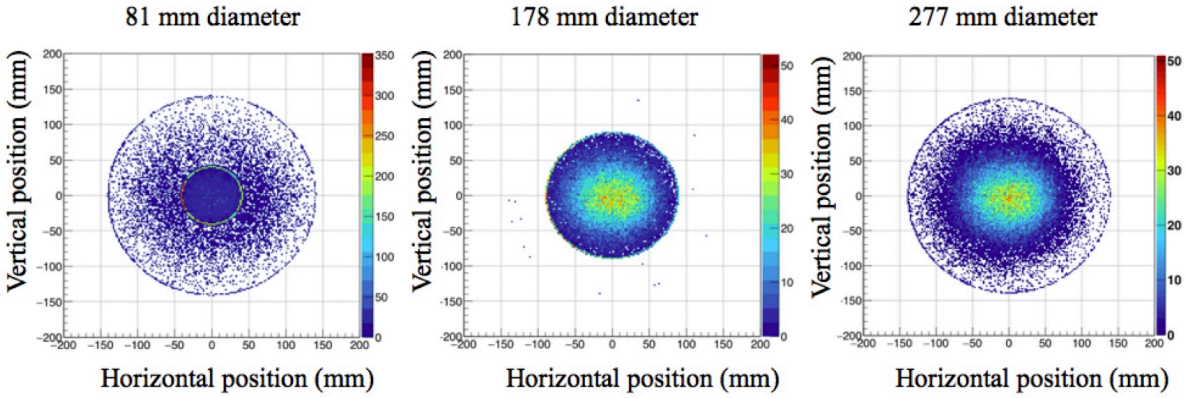

Figure 9-14: Muon stopping distribution projected on the microwave cavity section for three types of the cavity radius.

counter detects only decay positrons except for few scattered streaming positrons.

Figure 9-17 shows a relative yield of positron measured by the downstream counter and the side counter. A red circle indicates a result by the downstream counter, a black circle indicates one by the side counter. For a case of an absorber with the thickness of 30 mm, contributions from decay positron and duct streaming positron are mostly equivalent. For a case of the thickness of 60 mm, no significant contribution from duct streaming positron was observed.

In the spectroscopy experiment, a trial for high-rate measurement was performed at the microwave frequency of 4462.3 kHz. Figure 9-18 shows a comparison of extracted muonium spin flip signal between a high-rate case and a moderate-rate case.

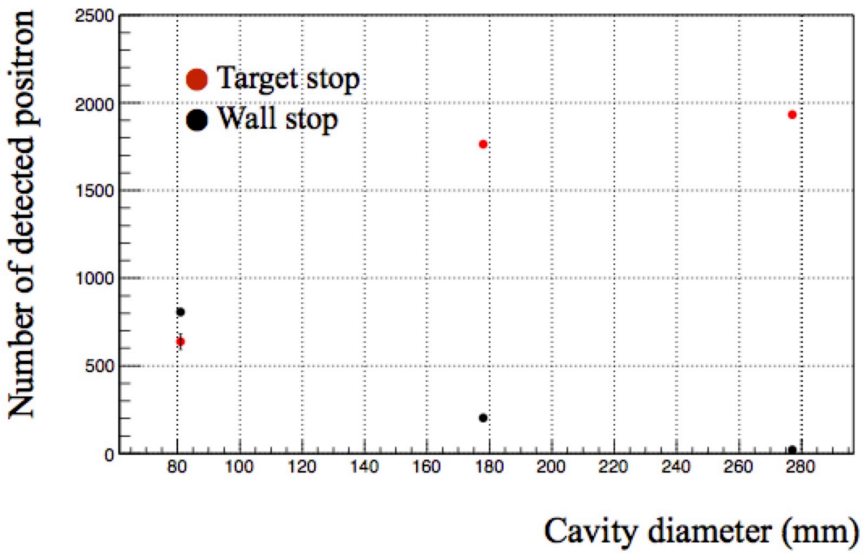

Figure 9-15: The number of muon stopping as a function of the cavity diameter. Red and black circles correspond to the number of muon stopped in the target gas and inner wall of the microwave cavity, respectively.

Extracted spin flip signal was consistent with each other. Hence, the positron counter is capable of an experiment in a three-fold of high-rate environment. This result corresponds to the highest beam intensity at the existing facility.

When these improvements are collected, more than a ten-fold of improvement in statistical precision is expected. Table 9.3 summarizes improvements arising from each upgrade. The resonance lineshape shown in Fig. 9-2 was obtained in a period of

Table 9.3: Expected improvement in statistical precision.

Modification	Improvement in precision
Beam power 600 kW	1.7
Duct streaming elimination by an absorber	2
Enhancement of target stop by a larger cavity	1.7
Suppression of wall-stop contribution by a larger cavity	2
Total	11.6

8 hours. On the other hand, the precursor experiment achieved 1.4 kHz of statistical precision in a span of 600 hours [46]. When a similar measurement duration to the precursor experiment is assumed, a factor of one hundred improvement in statistical

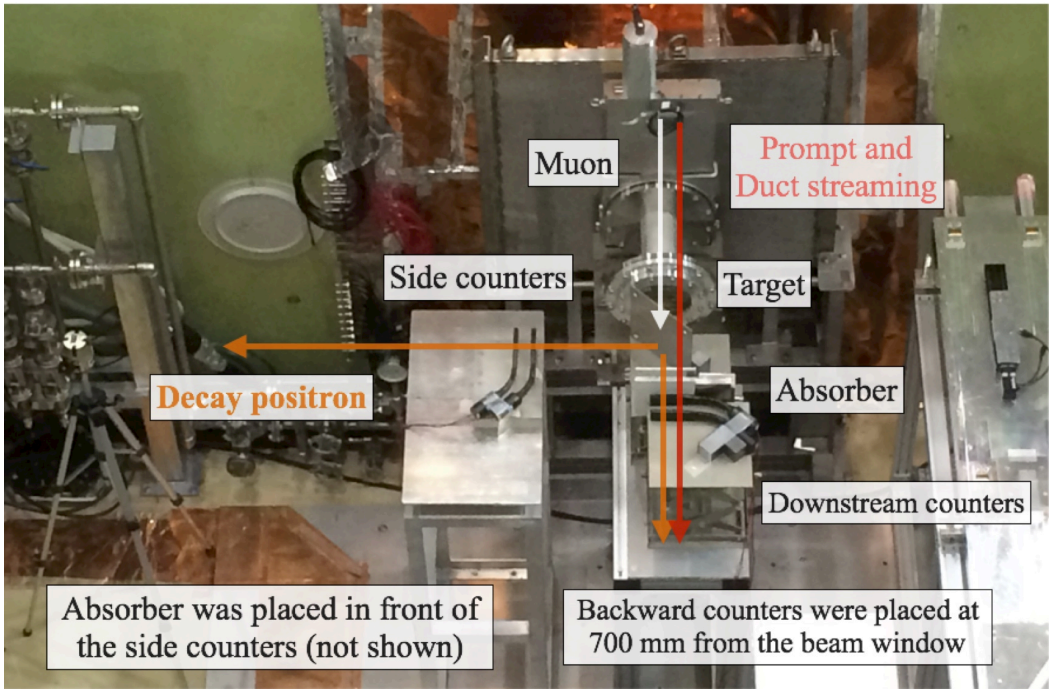

Figure 9-16: Experimental setup for the duct streaming positron measurement. Two pairs of the scintillation counters were placed in the downstream side and beside the muon stopping target. An aluminum absorber was placed between the target and the detectors.

precision is expected. This improvement corresponds to the statistical precision of 218 Hz, i.e., the world highest precision in direct determination of muonium HFS.

9.3.2 Future prospects at the new facility under construction

At J-PARC MLF MUSE, a brand-new beamline H-Line is under construction. H-Line has a large solid angle and expected to have a well focused beam spot [64]. For a case of a mega-watt proton beam power, 1×10^8 muons per second is expected at H-Line. This highest-intensity muon beam provides 33-fold of incident muons relative to the case of 200 kW beam power at D-Line.

To overcome the extreme-high event rate, several types of measures were considered as follows.

1. The timing structure of the muonium spin flip signal is adjustable by the optimization of the microwave power. Especially, a peak position of the oscillating

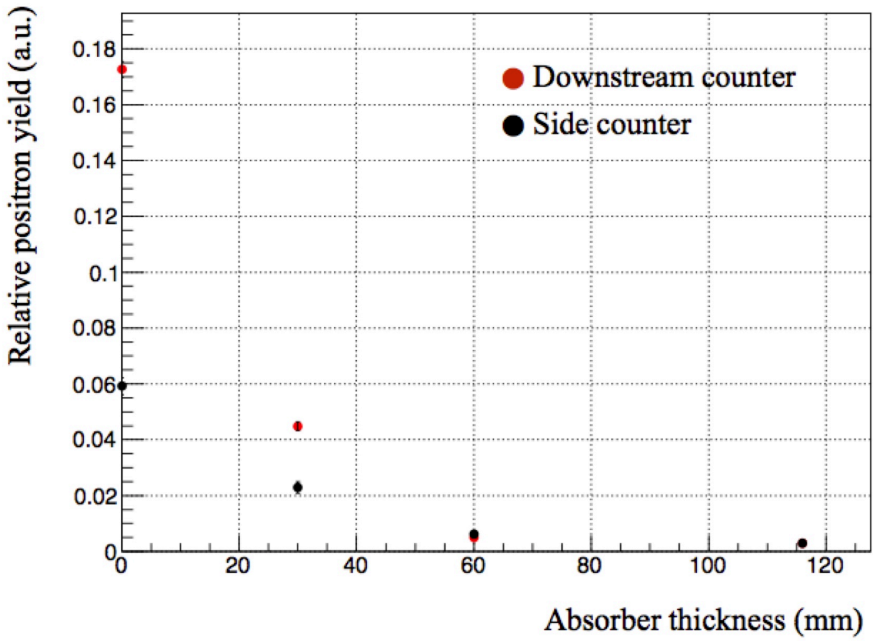

Figure 9-17: Suppression of the duct streaming positron by an aluminum absorber. Red and black circles indicate the positron yield measured by the downstream counter and the side counter, respectively. The downstream counter measured the duct streaming positron and the decay positron from muon stopping target. The side counter measured only the decay positron from the target.

signal depends on the maximum strength of the microwave field. The relatively low microwave power makes the peak position being late in time. Even the signal intensity is reduced at the low microwave power, the width of the resonance lineshape becomes narrower at the same time.

2. The timing integration range for the time dependent spin flip signal analysis can be optimized. For a case of the signal shown in Fig. 8-28, the second peak in the oscillating signal is about 2 μs later than the first one. The analysis utilizing only long-lived muons in a finite time interval leads a narrower resonance linewidth than a natural linewidth [67].

3. Upgrade of the readout electronics for the positron detector in under study. A new version of the ASIC was developed in order to improve the high-rate capability of the detector. Pole-zero-cancelation was implemented in the amplifier and no signal undershoot is expected.

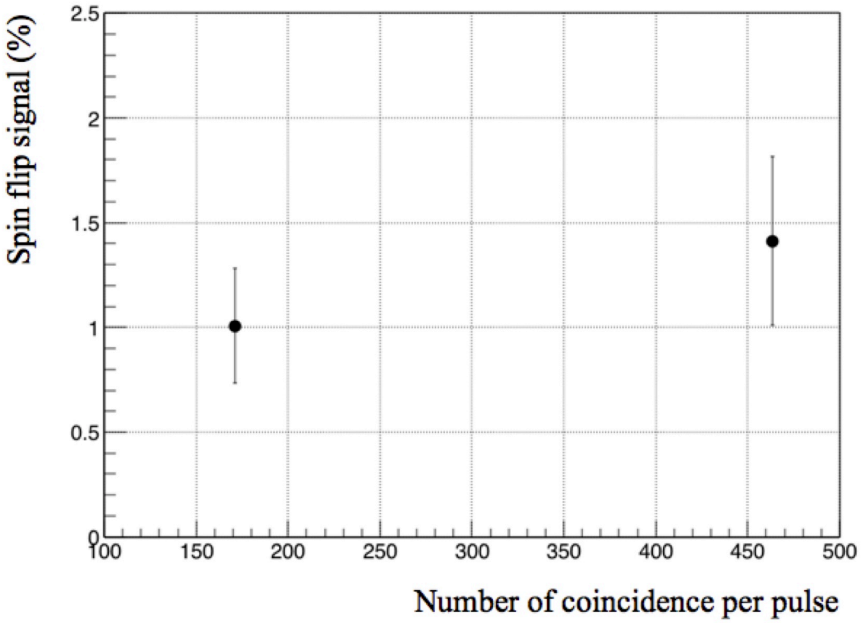

Figure 9-18: Comparison of the muonium spin flip signal as a function of event rate. The horizontal axis indicates the number of coincidence hit per muon pulse. The vertical axis indicates the time integrated signal of the muonium spin flip.

4. Pileup correction under a high rate environment was studied. Figure 9-19 shows simulated event loss as a function of the maximum event rate at each detector segment. The muon beam intensity of 1.2×10^7 muons per second was assumed. The ordinate axis indicates the number of lost positrons per pulse. A pileup correction function was obtained by polynomial fitting. Figure 9-20 presents a result of the pileup correction where the abscissa indicates the relative statistics normalized by the total number of incident positrons. After the pileup correction, the systematic uncertainty in the resonance frequency determination was estimated to be 2 Hz.

For instance, by combining the measures 2 and 4, the muon beam intensity of 2.4×10^7 muons per second is acceptable. This result corresponds to an eight-fold of the current beam intensity. Further improvements are possible with the measures 1 and 4.

As medium-to-long term prospects, an indirect measurement of muonium HFS in a high magnetic field is under study. Similar to the experiment reported the highest precision of muonium HFS [10], a super-conducting solenoidal magnet is utilized

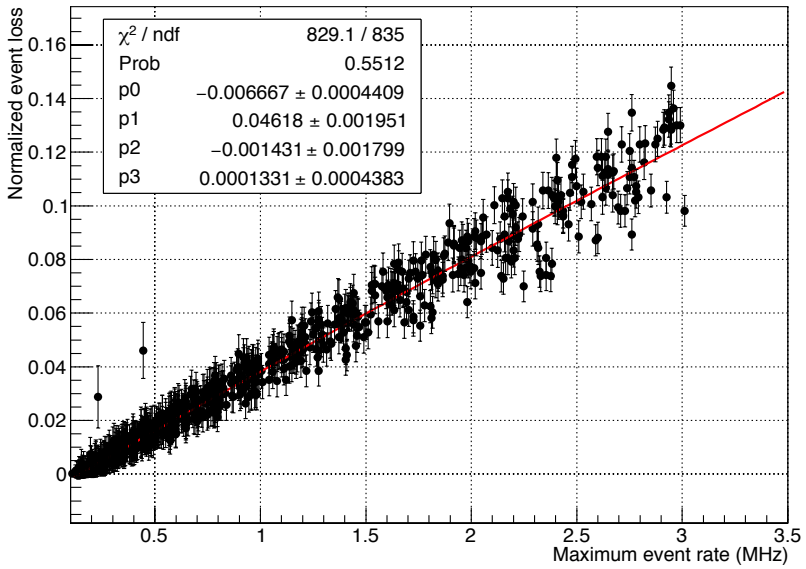

Figure 9-19: Simulated pileup loss as a function of the maximum instantaneous event rate. Red line indicates the fitting result with a polynomial function.

to generate a magnetic field of 1.7 T. A magnetic field causes Zeeman splitting of muonium energy levels. Two transition frequencies between sub-levels are measured. Experimental principle and for the most part of the apparatuses are common with the experiment at zero magnetic field. In particular, the positron detector and the fiber beam profile monitor described in this thesis are applicable as it is because they are tolerant to a presence of high magnetic field. The three-dimensional beam imager is also utilized after minor modifications for use in a magnetic field.

For a case of an experiment in a high magnetic field, positrons from muonium decay are converged by the magnetic field. This focusing effect gives the quadruple of positron statistics relative to a case at zero magnetic field. An external magnetic field recovers the muon spin polarization. Mostly, 100% of spin polarization is expected at the magnetic field of 1.7 T. The signal height at the resonance is twice as large as one at zero magnetic field because the muonium energy levels are completely degenerated and no mixing of the states is expected. The experiment at a high field requires twice longer of measurement period for two independent transition frequencies. The most precise value of muonium HFS obtained ever is 53 Hz. In order to realize an expected precision with the highest-intensity pulsed muon beam, an upgrade of the positron

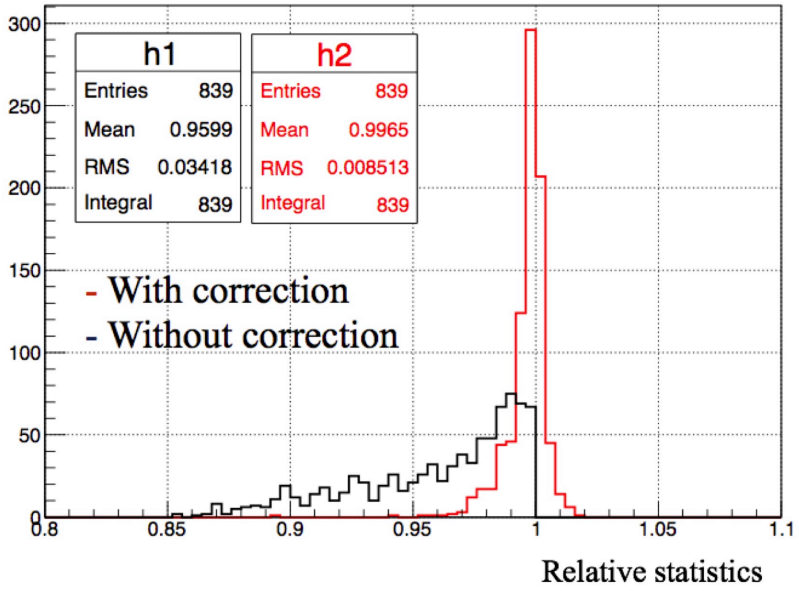

Figure 9-20: Simulated pileup correction. The histograms in red and black lines correspond to the results with the pileup correction and without the correction, respectively.

detector and optimization of measurement condition are in progress. In contrast to the zero field case, the uniformity of static magnetic field is one of the major sources of systematic uncertainty in a high field experiment. A passive shimming is applied to the super conducting solenoid to prevent the non uniformity of the magnetic field [68].

The measurement at zero magnetic field and one in a high field are complementary experiments because they have different types of systematic uncertainties and sensitivities to a Lorentz violating interaction [69]. Therefore, both experiments will be prepared as an exploration of the frontier in precision muonium spectroscopy at the new facility to be constructed.

Chapter 10

Conclusion

Through the studies described in this thesis, a new precision spectroscopy of the muonium ground state hyperfine splitting was explored. To overcome a limitation in the statistical precision achieved by the precursor experiment, the world highest-intensity pulsed muon beam was utilized. The development of the high-rate capable positron detector enabled to accept the statistical benefit of the high-intensity pulsed muon beam without increase of systematic uncertainties. Both experimental and computational approaches to the estimation of systematic uncertainties provided an understanding of the uncertainties and a suitable means to control the systematics. The reconstruction of the three-dimensional muon stopping distribution in the target gas by the muon beam imager was highly effective to optimize the beam and target conditions. The magnetic shield provided a static magnetic field sufficiently close to zero from the aspect of muonium energy levels splitting.

The muonium HFS resonance was successfully observed and the essential foundation of the new methodology was established. Obtained result of the muonium HFS interval was $\Delta\nu = 4.463292(22)$ GHz which corresponds to 4.9 ppm of relative uncertainty. The result was consistent with one by the precursor experiment. Simulation study bolsters that more than tenfold of improvement is expected from the suppression of the wall-stopped muons and the duct streaming positrons. These improvements are achieved by the simple modifications of the apparatuses; enlargement of the microwave cavity and increase of the absorber thickness. The positron

detection system is able to accept a higher beam intensity at least not less than eight times. This high-rate capability is good enough to accept the highest beam intensity at existing facility and further improvement was studied towards the future upgrade of the beamline. It is feasible to exceed the result of the precursor experiment by an accumulation of unequivocal steps. Furthermore, the developed methodology has a large potential for the expansion of precision muon physics where the high-intensity pulsed muon beam is applicable.

Systematic uncertainty in the measurement was estimated to be 73 Hz. This value is sufficiently smaller than statistical errors in both this experiment case and the precursor experiment case [46]. However, it is nearly equivalent to the order of total uncertainty in the most precise result obtained by an indirect measurement at a high magnetic field [10]. Towards the realization of the highest precision, room for improvement in major sources of the systematic uncertainty were studied. An order of magnitude improvement is expected by adaptation of the microwave power feedback and a precise silicon pressure gauge.

In conclusion, the experiment succeeded in the world's first demonstration of muonium HFS spectroscopy utilizing the high-intensity pulsed muon beam.

Bibliography

[1] V. W. Hughes, D. W. McColm, K. Ziock, and R. Prepost, "Formation of Muonium and Observation of its Larmor Precession", Phys. Rev. Lett. 5 (1960) 63-65.

[2] P. J. Mohr, D. B. Newell, and B. N. Taylor, "CODATA recommended values of the fundamental physical constants: 2014", Rev. Mod. Phys. 88, 035009 (2016).

[3] D. Hanneke, S. Fogwell, and G. Gabrielse, "New Measurement of the Electron Magnetic Moment and the Fine Structure Constant", Phys. Rev. Lett. 100, 120801 (2008).

[4] L. Essen *et al.*, "Hydrogen Maser Work at the National Physical Laboratory", Metrologia 9 (1973) 128.

[5] L. Essen *et al.*, "Frequency of the Hydrogen Maser", Nature, 229 110 (1971).

[6] J. R. Sapirstein and D.R. Yennie, "Quantum Electrodynamics", edited by T. Kinoshita (World Scientific, Singapore, 1990) 560.

[7] A. Ishida *et al.*, "New precision measurement of hyperfine splitting of positronium", Physics Letters B 734 (2014) 338-344.

[8] B. A. Kniehl, A.A. Penin, "Order $\alpha^7 \ln(1/\alpha)$ Contribution to Positronium Hyperfine Splitting", Phys. Rev. Lett. 85 (2000) 5094.

[9] D.E. Casperson *et al.*, "A New High Precision Measurement of the Muonium Hyperfine Structure Interval $\Delta\nu$", Phys. Lett. (1975).

[10] W. Liu *et al.*, "High Precision Measurements of the Ground State Hyperfine Structure Interval of Muonium and of the Muon Magnetic Moment", Phys. Rev. Lett. (1999).

[11] E. Fermi, "Uber die magnetischen Momente der Atomkerne", Zeitschrift fusr Physik. 60 (1930) 5-6.

[12] M. I. Eides, H. Grotch, and V. A. Shelyuto, "Theory of Light Hydrogenlike Atoms", Phys. Rep. 342, 63 (2001). arXiv:hep-ph/0002158

[13] G. Breit, "Dirac's Equation and the Spin-Spin Interactions of Two Electrons", Phys. Rev. 39, 616 (1932) 616-624.

[14] H. A. Bethe, and E. E. Salpeter, "A Relativistic Equation for Bound State Problems" Phys. Rev. 82 (1951) 309-310.

[15] J. Schwinger, "On Quantum Electredynamics and the Magnetic Moment of the Electron", Phys. Rev. 73 (1948) 416-417.

[16] W. E. Caswell and G. P. Lepage, "Effective Lagrangians for bound state problems in QED, QCD, and other field theories", Phys. Lett. 167B, 437 (1986) 437-442.

[17] N. Kroll, F. Pollock, "Radiative Corrections to the Hyperfine Structure and the Fine Structure Constant", Phys. Rev. 84 (1951) 594; ibid. 86 (1952) 876.

[18] R. Karplus and A. Klein, "Electrodynamic Displacement of Atomic Energy Levels. I. Hyperfine Structure", Phys. Rev. 85 (1952) 972.

[19] D. Zwanziger, "Radiative corrections to hyperfine structure in hydrogen", Nuovo Cim. 34 (1964) 77.

[20] S.G. Karshenboim, "Leading logarithmic corrections and uncertainty of Muonium hyperfine splitting calculations", Z. Phys. D 36 (1996) 11.

[21] T. Kinoshita, "NRQED Approach to the Hyperfine Structure of the Muonium Ground State", arXiv:hep-ph/9808351 (1998).

[22] R. Arnowitt, "The Hyperfine Structure of Hydrogen", Phys. Rev. 92 (1953) 1002.

[23] T. Fulton, P.C. Martin, "Two-Body System in Quantum Electrodynamics. Energy Levels of Positronium", Phys. Rev. 95 (1954) 811.

[24] W.A. Newcomb, E.E. Salpeter, "Mass Corrections to the Hyperfine Structure in Hydrogen", Phys. Rev. 97 (1955) 1146.

[25] E.A. Terray, D.R. Yennie, "Radiative-Recoil Corrections to Muonium Hyperfine Splitting", Phys. Rev. Lett. 48 (1982) 1803.

[26] M. I. Eides, "Weak-interaction contributions to hyperfine splitting and Lamb shift", Phys. Rev. A 53, 2953 (1996).

[27] A. Czarnecki, S. I. Eidelman, and S. G. Karshenboim, "Muonium hyperfine structure and hadronic effects", Phys. Rev. D 65, 053004 (2002).

[28] S.G. Karshenboim, V.A. Shelyuto, and A.I. Vainshtein, "Hadronic light-by-light scattering in muonium hyperfine splitting", Phys. Rev. D 78, 065036 (2008).

[29] T. Kinoshita and M. Nio, "Improved Theory of the Muonium Hyperfine Structure", Phys. Rev. Lett. 72, 3803 (1994) 3803-3806.

[30] T. Kinoshita and M. Nio, "Radiative corrections to the muonium hyperfine structure: The $\alpha^2(Z\alpha)$ correction", Phys. Rev. D 53 (1996) 4909-4929.

[31] M. Nio and T. Kinoshita, "Radiative corrections to the muonium hyperfine structure: The $\alpha(Z\alpha)^2$ correction", Phys. Rev. D 55 (1997) 7267-7290.

[32] M. I. Eides, H. Grotch, and V. A. Shelyuto, "Second order in mass ratio radiative-recoil corrections to hyperfine splitting in muonium", Phys. Rev. D 58, 013008 (1998).

[33] D. Nomura and T. Teubner, "Hadronic contributions to the anomalous magnetic moment of the electron and the hyperfine splitting of muonium", Nuclear Physics B 867 (2013) 236-243.

[34] G. Breit and I. I. Rabi, "Measurement of Nuclear Spin", Phys. Rev. 38 (1931) 2082-2083.

[35] S. Sturn *et al.*, "High-precision measurement of the atomic mass of the electron", Nature 13026 (2014).

[36] G.W. Bennett *et al.*, "Final report of the E821 muon anomalous magnetic moment measurement at BNL", Phys. Rev. D73, 072003 (2006).

[37] K. Hagiwara *et al.*, "$(g-2)\mu$ and $\alpha(M_Z^2)$ re-evaluated using new precise data", JPHGB G38, 085003 (2011).

[38] R. Bluhm, V.A. Kostelecky, and C.D. Lane, "CPT and Lorentz Tests with Muons", Phys. Rev. Lett. 84, 1098 (2000).

[39] W. Hughes, M. G. Perdekamp, D .Kawall, W. Liu, K. Jungmann, and G. zu Putlitz, "Test of CPT and Lorentz Invariance from Muonium Spectroscopy", Phys. Rev. Lett. 87, 111804 (2001).

[40] S. G. Karshenboim, "Constraints on muon-specific dark forces", Phys. Rev. D90, 073004 (2014).

[41] R. Pohl, R. Gilman, G. A. Miller, and K. Pachucki, "Muonic Hydrogen and the Proton Radius Puzzle", Annual Review of Nuclear and Particle Science 63 (2013) 175-204.

[42] S. G. Karshenboim, "Precision Physics of Simple Atoms and Constraints on a Light Boson with Ultraweak Coupling", Phys. Rev. Lett. 104, 220406 (2010).

[43] V. W. Hughes *et al.*, "Muonium. I. Muonium Formation and Larmor Precession", Phys. Rev. A, 1, 595 (1970). ; Erratum Phys. Rev. A 2, 551 (1970).

[44] J. M. Bailey, W. E. Cleland, V. W. Hughes, R. Prepost, and K. Ziock, "Muonium. II. Observation of the Muonium Hyperfine-Structure Interval", Phys. Rev. A 3, 871 (1971).

[45] W. E. Cleland, J. M. Bailey, M. Eckhause, V. W. Hughes, R. Prepost, J. E. Rothberg, and R. M. Mobley, "Muonium. III. Precision Measurement of the Muonium Hyperfine-Structure Interval at Strong Magnetic Field", Phys. Rev. A 5, 2338 (1972).

[46] P. A. Thompson, P. Crane, T. Crane, J. J. Amato, V. W. Hughes, G. zu Putlitz, and J. E. Rothberg, "Muonium. IV. Precision Measurement of the Muonium Hyperfine-Structure Interval at Weak and Very Weak Magnetic Fields", Phys. Rev. A 8, 86 (1973).

[47] M. Arai *et al.*, "Present Status of the Materials & Life Science Experimental Facility of J-PARC", JPS Conf. Proc. 8 (2015) 036021(1-10).

[48] Y. Miyake *et al.*, "J-PARC muon facility, MUSE", Nucl. Inst. and Methods in Phys. A, 600 (2009) 22-24.

[49] P. Strasser *et al.*, "J-PARC decay muon channel construction status", J. Phys.: Conf. Ser. 225 (2010) 012050(1-8).

[50] S. Makimura *et al.*, "Development of muon rotating target at J-PARC/MUSE", J. Radioanal. Nucl. Chem. 305 (2015) 811-815.

[51] H. D. Amold and G. W. Elmen, "Permalloy, an alloy of remarkable magnetic properties", Journal of the Franklin Institute, 195, 5 (1923) 621-632.

[52] R. D. Enoch and A. D. Fudge, "High magnetic permeability in Ni-Fe alloys", British Journal of Applied Physics, 17, 5 (1966) 623-634.

[53] F. Primdahl, "The fluxgate magnetometer", Journal of Physics E (1979).

[54] D. G. Fleming, R. J. Mikula, and D. M. Garner, "μ^+ charge exchange and muonium formation in low-pressure gases", Phys. Rev. A, 26, 5 (1982) 2527-2544.

[55] A. Lassise, P. H. A. Mustaers and O. J. Luiten, “Compact, low power radio frequency cavity for femtosecond electron microscopy”, Rev. Sci. Instrum. 83 043705 (2012).

[56] G. K. Wertheim, M. A. Butler, K. W. West, and D. N. E. Buchanan, "Determination of the Gaussian and Lorentzian content of experimental line shapes", Review of Scientific Instruments 45, 1369 (1974).

[57] National Instruments, http://www.ni.com/labview/

[58] T. J. Roberts, http://g4beamline.muonsinc.com

[59] S. Agostinelli *et al.*, "Geant4 - a simulation toolkit", Nucl. Inst. and Methods in Phys., A, 506, 3 (2003) 250-303.

[60] C. Brunnèe, "The ideal mass analyzer: Fact or fiction?", Int. J. Mass. Spectrom. Ion Proc. 76, 125 (1987).

[61] I. Nakamura *et al.*, "A 64ch readout module for PPD/MPPC/SiPM using EASIROC ASIC", Nucl. Inst. and Methods in Phys. A, 787, 1 (2015) 376-379.

[62] K. M. Kojima *et al.*, "New μSR spectrometer at J-PARC MUSE based on Kalliope detectors", Journal of Physics: Conference Series 551 (2014) 012063.

[63] N. Inadama *et al.*, “Performance of a PET detector with a 256ch flat panel PS-PMT”, IEEE Trans. Nucl. Sci., 51 (2004) 58-62.

[64] N. Kawamura *et al.*, "H line; a beam line for fundamental physics study", Journal of Physics: Conference Series 551 (2014) 012062.

[65] R. M. Mobley, J. M. Bailey, W. E. Cleland, V. W. Hughes, and J. E. Rothberg, "Muonium chemistry", The Journal of Chemical Physics, 44, 11 (1966) 4354-4355.

[66] R. M. Mobley, J. J. Amato, V. W. Hughes, J. E. Rothberg, and P. A. Thompson, "Muonium chemistry ii", The Journal of Chemical Physics, 47, 8 (1967) 3074-3075.

[67] M. G. Boshier *et al.*, "Observation of resonance line narrowing for old muonium", Phys. Rev. A 52, 1948 (1995).

[68] Y. Higashi, Master thesis, The University of Tokyo (2015).

[69] A. H. Gomes, V. A. Kostelecky, and A. J. Vargas, "Laboratory tests of Lorentz and CPT symmetry with muons", Phys. Rev. D 90, 076009 (2014).